Characterization of Irradiated Depleted Monolithic Active Pixel Sensors in 150 nm and 180 nm CMOS Technology for High-Rate and High-Radiation Environments

Dissertation
zur
Erlangung des Doktorgrades (Dr. rer. nat.)
der
Mathematisch-Naturwissenschaftlichen Fakultät
der
Rheinischen Friedrich-Wilhelms-Universität Bonn

vorgelegt von
Lars Philip Schall
aus
Herrenberg

Bonn 2025

Angefertigt mit Genehmigung der Mathematisch-Naturwissenschaftlichen Fakultät
der Rheinischen Friedrich-Wilhelms-Universität Bonn

Gutachter/Betreuer: Prof. Dr. Jochen Dingfelder
Gutachterin: Prof. Dr. Ingrid-Maria Gregor

Tag der Promotion: 06. März 2026
Erscheinungsjahr: 2026

Contents

1 Introduction **1**

2 Interactions of particles with matter **3**
2.1 Energy loss of charged particles in matter . . . 3
2.2 Fluctuations in energy deposition . . . 7
2.3 Multiple scattering . . . 7
2.4 Interaction of photons with matter . . . 9

3 Semiconductor particle detectors **13**
3.1 Characteristic properties of semiconductors . . . 13
3.1.1 Doping of semiconductors . . . 16
3.1.2 P-n junction and space-charge region . . . 17
3.1.3 MOS transistors . . . 20
3.1.4 Charge carrier transport in semiconductors . . . 21
3.2 Signal processing . . . 23
3.2.1 Signal generation . . . 23
3.2.2 Readout electronics . . . 25
3.3 Silicon detectors for tracking applications . . . 28
3.3.1 Hybrid pixel detectors . . . 29
3.3.2 Monolithic pixel detectors . . . 30
3.3.3 Depleted monolithic active pixel sensors . . . 32
3.4 Application of DMAPS in high-energy physics experiments . . . 36

4 Radiation damage in semiconductors **39**
4.1 Bulk damage . . . 39
4.1.1 Displacement damage . . . 39
4.1.2 NIEL hypothesis and hardness factor . . . 40
4.1.3 Impact on detector properties . . . 42
4.1.4 Annealing of bulk defects . . . 46
4.2 Surface damage . . . 46
4.2.1 Defect classification in silicon oxide . . . 47
4.2.2 Formation mechanisms of radiation induced defects in MOS devices . . . 50
4.2.3 Effect on electrical parameters of a MOS transistor . . . 52

5 The Monopix chips 55
5.1 The LF-Monopix chips . . . 55
5.1.1 LF-Monopix2 . . . 56
5.2 The TJ-Monopix chips . . . 59
5.2.1 TJ-Monopix2 . . . 62
5.3 Data acquisition systems . . . 65

6 Measurement methodologies 69
6.1 X-ray irradiation campaigns . . . 69
6.1.1 Irradiation setup . . . 70
6.1.2 Irradiation campaign measurements . . . 71
6.2 Test beam measurements . . . 72
6.2.1 Beam telescope setup . . . 73
6.2.2 Test beam analysis and hit-detection efficiency . . . 76
6.2.3 Error estimation of the hit-detection efficiency . . . 79

7 Characterization of the Monopix2 DMAPS 81
7.1 Characterization of LF-Monopix2 . . . 81
7.1.1 Laboratory characterization . . . 82
7.1.2 X-ray irradiation of LF-Monopix2 . . . 87
7.1.3 Beam test results of LF-Monopix2 . . . 93
7.1.4 Conclusion . . . 104
7.2 Characterization of TJ-Monopix2 . . . 106
7.2.1 Laboratory characterization . . . 106
7.2.2 X-ray irradiation of TJ-Monopix2 . . . 114
7.2.3 Beam test results of TJ-Monopix2 . . . 117
7.2.4 Conclusion . . . 122
7.3 Performance comparison . . . 124

8 Summary 129

9 Appendix 131
9.1 Synchronous column-drain readout architecture . . . 131
9.2 Supplementary figures on irradiated LF-Monopix2 results . . . 132
9.3 Supplementary information on threshold fluctuation of TJ-Monopix2 . . . 132

Bibliography 135

List of Figures 149

List of Tables 153

Acronyms 155

1 Introduction

Particle physics and, in particular, the field of high-energy physics concentrates on gaining a complete understanding of the fundamental constituents of matter and the forces between them. The Standard Model of particle physics has emerged as the most complete description of these elementary building blocks to date [1–4]. In 2012, the discovery of the Higgs boson provided the final piece of the Standard Model [5]. Although it is the most accurate theoretical description of particle physics and has been thoroughly tested, some phenomena remain unexplained by the Standard Model. Nowadays, the focus has shifted towards precision measurements of Standard Model parameters and the search of physics beyond this model. Particle collisions at accelerator facilities are produce under well-defined experimental conditions to study interactions of interest in this field of research. The Large Hadron Collider (LHC) is the largest and most powerful accelerator that enables research in energy ranges up to several TeV at very high rates [6]. Complex detector systems built around the interaction point of the proton-proton collisions in the case of the LHC are required to accurately measure and reconstruct the induced interactions. Both precision measurements and the search for new physics demand a large amount of data for new discoveries. This is achieved by higher collision rates at the accelerator, which pose increasing challenges for the detector systems. Tracking detectors are employed to measure particle trajectories and identify decay vertices with very good spatial resolution. To accomplish the required vertex resolution, high-precision tracking systems often based on segmented silicon sensors are installed closest to the interaction point. Based simply on geometric considerations, this sub-detector receives the most radiation and has to cope with the highest rates.

Hybrid pixel detectors have advanced as the current standard for precision tracking and vertexing applications in such high-rate and high-radiation environments. The separation of readout electronics and sensor into two entities of silicon facilitates the individual optimization of both while requiring a complex and expensive electrical interconnection step. Monolithic active pixel sensors comprise both components in one entity of silicon. Technological advances in commercial CMOS processes and increased accessibility of high-resistivity substrates for these processes sparked ongoing developments of such monolithic active pixel sensors with high radiation tolerance and high rate capabilities. Motivated by the demand for extremely precise particle tracking, the employment of monolithic detectors reduces the introduced material in an experiment, which results in fewer distorting scattering effects. The high throughput available for commercial processes and lower production cost without the complex interconnection step are further benefits of the monolithic approach. However, the design of monolithic active pixel

sensors with a radiation tolerance to the levels faced at the LHC is far from trivial.

Advances in the bias-voltage capabilities of commercial CMOS processes, combined with the increasing availability of high-resistivity silicon substrates, have initiated the development of monolithic active pixel sensors with large depleted sensitive volumes. Over the past decades, many developments by various groups in this field have resulted in such depleted monolithic active pixel sensors becoming a worthy alternative to hybrid pixel detectors even in high-rate and high-radiation environments. The Monopix2 chips constitute two large-scale deplete monolithic active pixel sensors fabricated in 150 nm and 180 nm CMOS technology. The two chips employ conceptually different design approaches with respect to the size of the collection electrode, and consequently the integration of the in-pixel electronics. Both devices are designed to satisfy the radiation tolerance and hit-rate requirements of high-precision tracking detectors at the LHC.

This thesis studies the radiation tolerance of both Monopix2 chips. A general introduction into the interaction mechanisms of particles with matter is given in Chapter 2. The first part of Chapter 3 discusses basic properties of semiconductor materials and their functionality as particle detectors. The second part describes general pixel detector technologies from hybrid to monolithic implementations, where the focus is put on the latter. Chapter 4 provides a detailed breakdown of radiation damage to semiconductor materials. This includes the various categorizations of damages caused by different types of radiation. The two pixel detectors, which are characterized in the scope of this thesis, are introduced in Chapter 5. A brief overview of their development history is given before the latest iterations are presented. In addition, the respective data acquisition system of each detector is described. Chapter 6 outlines the elaborate measurement methods for irradiation campaigns and beam tests containing both hardware setup and analysis software information. The characterization of the Monopix2 chips after irradiation is presented in Chapter 7. First, the performance of each chip at various radiation levels is analyzed and discussed. Afterwards, a brief performance comparison between the two detectors is conducted, although this is limited by the comparability of the two chips. Finally, Chapter 8 summarizes the research performed in the scope of this thesis.

2 Interactions of particles with matter

To detect particles, their interaction with matter must be leveraged, while the specific interaction process varies depending on the type and energy of the incoming particle. When developing detectors, these characteristics are exploited to design the most efficient detection system for a distinct application. In addition, the correct choice of the detector medium is essential, as the material dependence of interaction processes can be used to efficiently force the necessary process. This chapter introduces the interaction mechanisms and processes of different particles with matter that are relevant for tracking applications with semiconductor detectors.

The interaction probability of a traversing particle with an atom of the medium is described by the cross-section. For a given particle rate $\dot{N}_{\mathrm{in}}$ impinging on a medium, the cross-section is given as [7]

$$\sigma = \frac{\dot{N}_{\mathrm{R}}}{\dot{N}_{\mathrm{in}}} \frac{1}{nd} \quad , \tag{2.1}$$

where $\dot{N}_{\mathrm{R}}$ denotes the scattered particle rate. The particle number density $n = \frac{\rho}{A} N_{\mathrm{A}}$ depends on the material's mass density ρ and its mass number A, while d is the thickness of the medium. Here, the medium is assumed to be sufficiently thin such that no particle is absorbed within. In general, a particle can interact multiple times with the medium before it has traversed completely or lost all its energy within the medium and is absorbed. The latter is especially important for thick media.

Furthermore, Eq. (2.1) yields a linear proportionality between cross-section and scattered particle rate [7]:

$$\dot{N}_{\mathrm{R}} = \dot{N}_{\mathrm{in}} n d \sigma = \mathcal{L} \sigma \quad . \tag{2.2}$$

The introduced proportionality factor $\mathcal{L} = \dot{N}_{\mathrm{in}} nd$ is called *luminosity*. The luminosity is a characteristic property used in high-energy collider experiments to quantify the interaction rate of two particle beams or a particle beam and a fixed target.

2.1 Energy loss of charged particles in matter

When traversing matter, charged particles scatter off shell electrons resulting in energy transfers and, therefore, excitation or ionization of the medium's atoms. The quantum mechanical calculation to describe the underlying physics was performed by Bethe [8] and Bloch [9]. This applies exclusively to *heavy* charged particles, since light charged particles (electrons and

positrons) require the consideration of additional interaction processes. For a given differential cross-section $\frac{d\sigma}{dT}$ of a collision with the medium resulting in the kinetic energy loss T, the average energy loss of a particle with mass M and velocity β per path length [7]

$$-\left\langle \frac{dE}{dx} \right\rangle = n_{\mathrm{e}} \int_{T_{\mathrm{min}}}^{T_{\mathrm{max}}} T \frac{d\sigma}{dT}(M, \beta, T) dT \tag{2.3}$$

is defined by the integral over all possible energy transfers. The target density $n_{\mathrm{e}} = \frac{Z\rho N_{\mathrm{A}}}{A}$ is given by the material-dependent electron density of the medium.

To calculate the average energy loss, the integral is split into two relevant energy regimes [7]: For large energy transfers compared to the electrons binding energy, the electron is considered quasi-free. Thus, the interaction is described by the classical Rutherford scattering [10]. The maximum energy transfer occurs for central collisions and is determined by considering an elastic collision of a particle and a shell electron with negligible binding energy. In case the binding energy is not negligible in the scattering process, quantum mechanical considerations are necessary. Due to the discrete nature of an atom's energy levels, the minimum energy transfer is never arbitrarily small but depends on the mean excitation energy of the material. Taking the aforementioned considerations of the integral's limits into account and inserting the Rutherford cross-section in Eq. (2.3) yields the *Bethe-Bloch* formula ([7] and therein)

$$-\left\langle \frac{dE}{dx} \right\rangle = K \frac{Z}{A} \rho \frac{z^2}{\beta^2} \left[\frac{1}{2} \ln \left(\frac{2 m_{\mathrm{e}} c^2 \beta^2 \gamma^2 T_{\mathrm{max}}}{I^2} \right) - \beta^2 - \frac{\delta(\beta\gamma)}{2} - \frac{C(\beta\gamma, I)}{Z} \right] \tag{2.4}$$

with the following parameters:

- Charge z, relativistic velocity β, and Lorentz factor γ of the impinging particle.
- Atomic number Z, atomic mass A, and mass density ρ of the medium.
- Constant $K = 4\pi N_{\mathrm{A}} r_{\mathrm{e}}^2 m_{\mathrm{e}} c^2 = 0.307\,\mathrm{MeVcm^2/mol}$ given for the classical electron radius $r_{\mathrm{e}} \approx 2.8\,\mathrm{fm}$.
- Mean excitation energy I of an interaction.
- Maximum energy transfer T_{max} to a shell electron in the case of a central collision.
- Density correction $\delta(\beta\gamma)$ relevant for high particle energies.
- Shell correction $C(\beta\gamma, I)/Z$ important for low particle energies.

Typically, the quantity is standardized to the density of the medium and expressed in units of $\mathrm{MeV/gcm^{-2}}$. The resulting dependence of the average energy loss on the energy of the incident particle is visualized in Figure 2.1. Since the *Bethe-Bloch* formula describes the average energy lost per path length, it effectively characterizes the *stopping power* of a material for a particle and is often referred to as such [11]. Between the $1/\beta^2$ decrease at low energies and the logarithmic $\ln(\beta\gamma)$ rise towards high energies, a broad minimum in the average energy loss

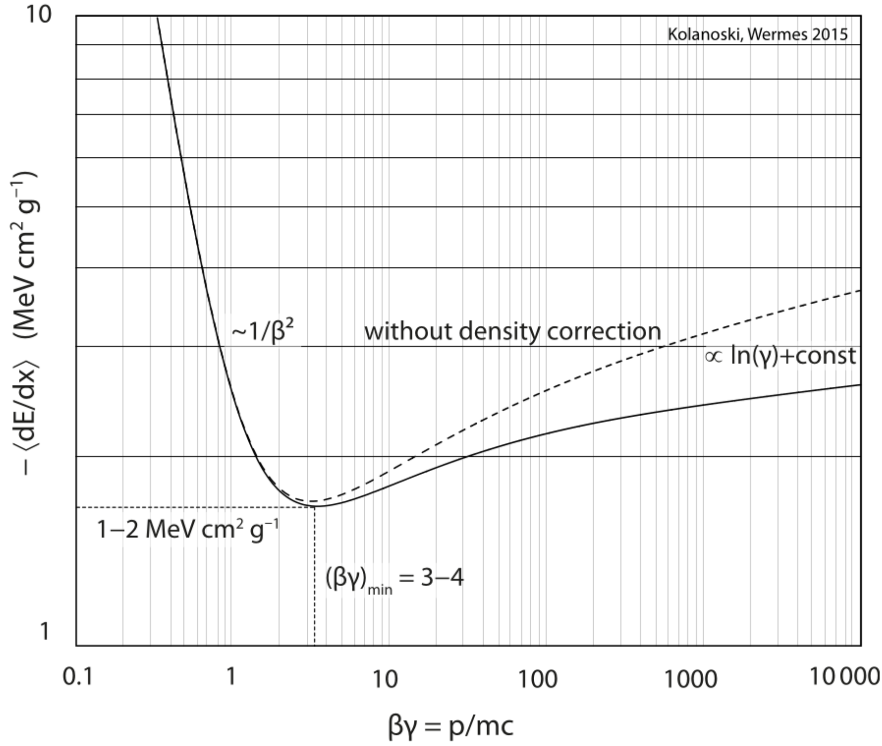

Figure 2.1: Average energy loss of a pion in silicon as a function of the particle's $\beta\gamma = p/mc$. A minimum energy loss of around $1 - 2\,\text{MeV/gcm}^{-2}$ occurs at $\beta\gamma = 3 - 4$. This data point is mostly independent of impinging particle and material type. The total *stopping power* is dominated by the $\ln(\beta\gamma)$ term towards high energies and by the $1/\beta^2$ term at low energies. From [7].

exists in the region of $\beta\gamma = 3 - 4$. Thus, particles in this energy range are referred to as minimum-ionizing particle (MIP). Due to the moderate logarithmic rise, this classification also approximately holds for more energetic particles.

For a sufficiently thick medium, a heavy charged particle will deposit all its energy and is completely stopped within the material. Assuming a mono-energetic beam of heavy charged particles, the number of beam particles remains constant until a certain distance is traversed. Upon reaching this depth, all particles are stopped and absorbed relatively rapidly. Considering the *Bethe-Bloch* equation, the exact depth depends on the particle type and energy as well as the medium. Due to the dominant $1/\beta^2$ dependence at low energies, most of the energy is deposited right before the particle is stopped completely. Thus, there is a spike in the amount of deposited energy per path length towards the maximum depth reached, which is referred to as *Bragg peak*.

Energy dependence of the average energy loss

The inverse correlation of the effective interaction time with the particles velocity and the proportionality of the energy transfer to the squared momentum transfer yields the $1/\beta^2$ dependence of the average energy loss at low energies [7]. The shell correction term $C(\beta\gamma, I)/Z$ describes the decreasing contribution of inner shell (K, L, ...) electrons to the stopping power at low energies close to the shell electron velocities [11]. This adjustment starts to become relevant for velocities of $\beta < 0.3$. Consequently, the average energy loss reaches a maximum before dropping rapidly and diverging from the $1/\beta^2$ dependence at very low energies.

The increase in stopping power towards high energies can be explained by considering the kinematics and the resulting larger maximum energy transfer. In addition, the electric field of the impinging particle extends transversally for large γ and facilitates large impact parameter collisions [7]. However, screening effects of nearby atoms due to polarization of the medium limit this extension which is described in the density correction term $\delta(\beta\gamma)$.

Energy loss of electrons and positrons

Due to the difference in mass, spin, and kinematics, the calculation of the ionizing energy loss requires some adjustments when considering electrons or positrons. In the case of electrons, the indistinguishability of incoming and scattered particle limits the maximum energy transfer to $T_{\max}/2$, since the electron with less energy is defined as the 'scattered' one [7]. For large energy transfers, the collision process is described by Møller scattering ($e^-e^- \to e^-e^-$) or Bhabha scattering ($e^+e^- \to e^+e^-$). This causes a reduction of about 10 % in the average energy loss by ionization close to the minimum and differs even more towards small and large particle velocities [7]. Additionally, positrons can transfer all their energy into a photon undergoing e^+e^- annihilation with a shell electron.

Furthermore, a non-negligible amount of energy is lost by bremsstrahlung at relatively low energies already due to their small mass. Bremsstrahlung describes the energy loss by radiation of a photon due to bending of the charged particle's trajectory by an electric field. Since the cross-section of this interaction scales with the inverse of the squared mass m of a particle with charge q [12]

$$\sigma_{\text{Brems}} \propto \left(\frac{q^2}{mc^2}\right)^2 \tag{2.5}$$

it is mainly relevant for electrons, positrons or slightly heavier particles such as muons. Due to the dependence on the electric field, the cross-section is also impacted by the medium and, in particular, possible screening effects. Consequently, the *critical energy* at which radiative energy loss is equal to the collision one depends on the particle and the medium. In solid state silicon, this is the case for 48 MeV electrons [13] or 581 GeV muons [14]. For even larger particle

velocities, the energy loss is dominated by bremsstrahlung and can be approximated as [11, 12]

$$-\frac{dE}{dx}_{\text{Brems}} \approx \frac{E}{\chi_0} \quad \Rightarrow \quad E(x) = E_0 \exp\left(-\frac{x}{\chi_0}\right) \quad . \tag{2.6}$$

The material characteristic radiation length χ_0 is defined as the mean distance which an electron has to traverse such that its energy is reduced to 1/e.

2.2 Fluctuations in energy deposition

As described in Section 2.1, the energy loss of a charged particle in matter is a statistical process dependent on the number of collisions and the amount of energy transferred per collision. Consequently, the total energy lost is subject to statistical fluctuations within these two factors. For thin detectors, typically used in tracking applications, the number of ionizations follows Poisson statistics. In addition, the energy transferred through an individual collision can range between the minimum excitation or ionization energy of the material up to the maximum energy transfer T_{max}. Although the majority of interactions yield an energy transfer close to the mean excitation energy of the material, collisions with large energy transfers cause a non-negligible tail towards high total energy deposition. This leads to a distortion of the average value, making the most probable value (MPV) a more characteristic quantity of the underlying statistical behavior. The resulting distribution of the deposited energy is described by the highly asymmetric Landau function [7, 15]

$$P(\lambda) = \frac{1}{\pi} \int_0^\infty \exp(t \ln(t) - t\lambda) \sin(\pi t) dt \tag{2.7}$$

where

$$\lambda(\Delta E_{\text{MPV}}, \xi) = \frac{\Delta E - \Delta E_{\text{MPV}}}{\xi} - 0.22278 \tag{2.8}$$

is used to scale and shift the function according to the observed energy loss distribution. Here, E_{MPV} describes the MPV of the deposited energy statistic, whereas $\xi = \frac{1}{2} K \frac{Z}{A} \rho \frac{z^2}{\beta^2} \Delta x$ is the pre-factor of the logarithmic term in Eq. (2.4) multiplied by the path length Δx. An exemplary Landau function is shown in Figure 2.2. The indication of the average value and MPV in the figure emphasized the difference between them due to the asymmetric tail towards large energies. According to the central limit theorem of statistics, the distribution of the energy deposition becomes Gaussian for sufficiently thick detectors and many collisions.

2.3 Multiple scattering

As charged particles traverse through matter, they scatter on the Coulomb fields of nuclei. The Coulomb scattering process of a particle on a single nucleus is described by the Rutherford cross-section [7]. In the case of light particles compared to the nucleus mass, only a small

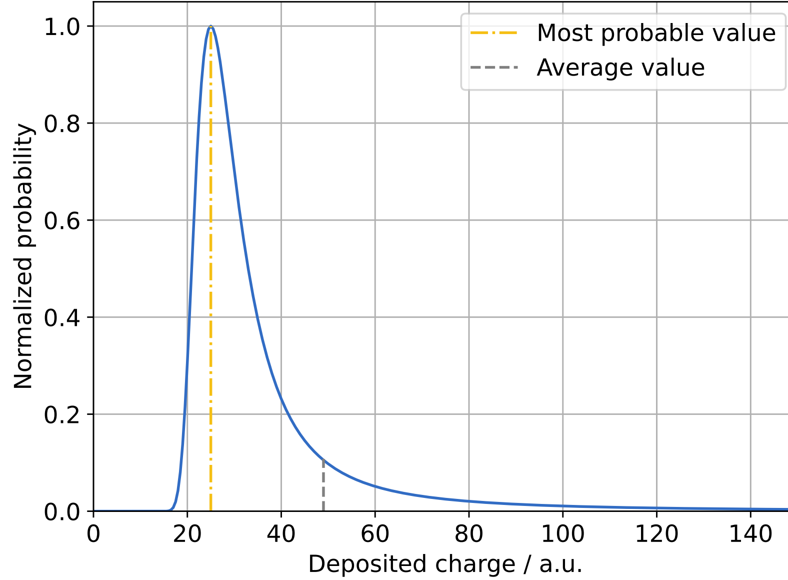

Figure 2.2: Exemplary characteristic Landau-shaped probability of the energy deposited by a charged particle traversing matter. The most probable value and the average value are indicated to highlight their difference due to the asymmetric nature of this distribution.

amount of energy is transferred to the nucleus through the deflection. This is further facilitated by the large range of the electromagnetic interaction. For large particle energies $E \gg m_\mathrm{e}c^2$, the scattering of shell electrons results in small deflections only.

In case the medium is thick enough to cause multiple scattering interactions, the number of deflections and the final deflection angle depend on the underlying statistical processes. *Multiple scattering* refers to scenarios with a finite number of deflections (typically ≥ 20) [7]. An illustration of a particle subject to multiple deflections while traversing a medium is shown in Figure 2.3. The corresponding fundamental concept was established by Molière [16, 17]. This general description of multiple scattering yields an approximately Gaussian distribution for the total angular distribution in most practical cases. However, measurements have shown that the Gaussian prediction is not entirely accurate, especially for large scattering angles [18]. This observation is contrary to the *central limit theorem* of statistics. Instead, a generally approved approximation of the standard deviation of the multiple scattering angle distribution θ_ms in a plane is given by the Highland formula and subsequent adjustment of its parameters [19, 20]:

$$\theta_\mathrm{ms} = \frac{13.6\,\mathrm{MeV}/c}{p\beta} z \sqrt{\frac{x}{X_0}} \left(1 + 0.038 \ln \frac{x}{X_0}\right) \quad . \tag{2.9}$$

Here, p and β describe the momentum and velocity of the particle with charge z, whereas X_0 denotes the radiation length and x is the thickness of the scattering material.

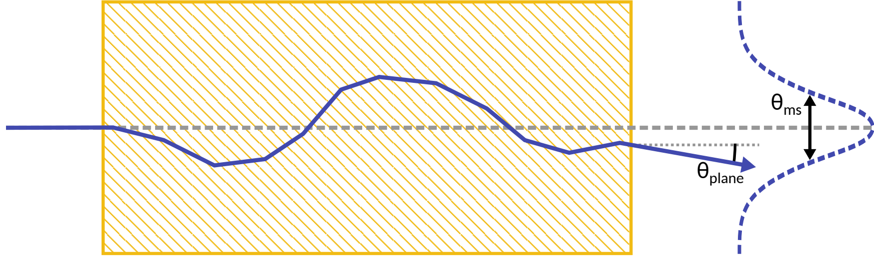

Figure 2.3: Particle traversing matter and being deflected multiple times by Coulomb scattering. The final deflection angle θ_{plane} and the standard deviation θ_{ms} of the total angular distribution are determined by the underlying statistical interaction processes. Adapted from [7].

2.4 Interaction of photons with matter

Since photons are electrically neutral, massless particles, they do not lose energy according to the Bethe-Bloch formula. Instead, photons are either absorbed completely or scatter elastically in the medium. The dominant interactions for photons above the ionization threshold are [7, 21]:

- The **photoelectric effect**, which describes the complete absorption of a photon by an atom of the medium and the resulting release of a shell electron through the energy transfer.
- **Compton scattering**, which describes the electromagnetic scattering of a traversing photon and a shell electron.
- **Pair production**, which is defined as the conversion of a photon into an electron-positron pair under the influence of a sufficient electric field.

While the photoelectric effect is the most probable interaction at low energies, the photon must have a minimum energy of twice the electron mass ($2 \cdot m_{\mathrm{e}}$) to undergo pair production. Figure 2.4 shows the attenuation of a photon beam in silicon and highlights the individual contributions of each interaction process.

In the case of a monochromatic photon beam containing N_0 photons, the number of photons decreases exponentially

$$N(x) = N_0 \cdot \mathrm{e}^{-\mu x} \tag{2.10}$$

with the distance x traveled through a medium. The factor μ in the exponent,

$$\mu = \rho \frac{N_{\mathrm{A}}}{A} \sigma \quad , \tag{2.11}$$

is the attenuation factor and quantifies the absorption probability of a single photon in the material [7, 21]. This probability is medium-dependent, as it is calculated from the density ρ

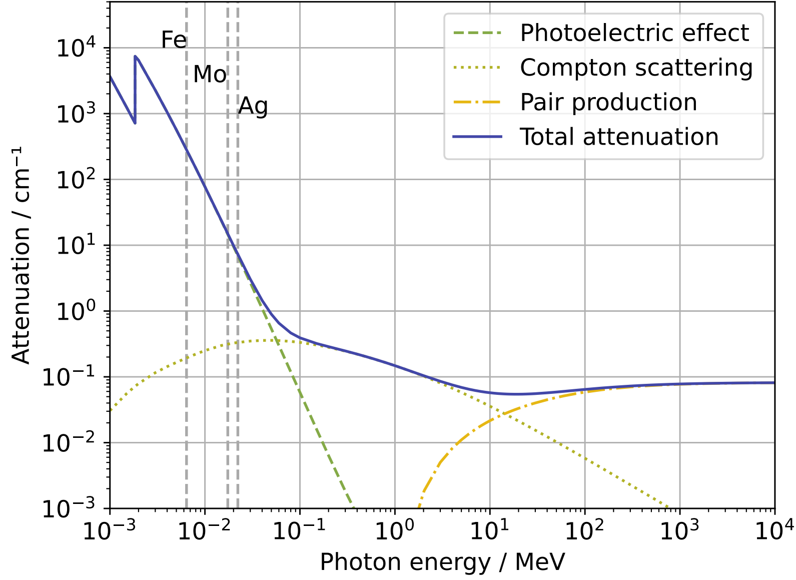

Figure 2.4: Total attenuation of photons in silicon across the relevant energy range. The individual contributions of each ionizing interaction process are emphasized. Data from [22]. In addition, exemplary K_α emission lines of Molybdenum (Mb), silver (Ag), and iron (Fe) typically used in laboratory measurements are shown. Emission energies from [23].

and mass number A of the medium, Avogadro's constant N_A, and the total interaction cross-section σ. Therefore, the energy deposition of photons in matter follows a continuous depth profile, in contrast to the *Bragg peak* observed for charge particles (see Section 2.1).

Photoelectric effect

The complete absorption of a photon with energy $E_\gamma = h\nu$ by an atom under the release of a shell electron is referred to as the photoelectric effect. Accordingly, the photon energy must exceed the binding energy E_B of the electron in the atom. To conserve energy and momentum, the atom, which is significantly heavier than the electron, takes up a negligible amount of recoil energy. Thus, the kinetic energy of the electron [7]

$$T = E_\gamma - E_\mathrm{B} \tag{2.12}$$

results from the difference in photon energy and binding energy of the electron. This process is the dominant photon interaction at lower keV energy ranges, while it becomes insignificant for high energies. Moreover, the release of an inner shell electron results in an excited atom that can relax through quantum mechanical transitions. Apart from relaxation through the emission of a photon, the atom can also readjust itself into a non-excited state by releasing one or more

additional shell electrons referred to as *Auger electrons* [21].

For a given photon energy, the photoelectric cross-section is strongly material dependent as it increases proportionally to Z^{4-5}. The emission of electrons with high binding energies such as present in the K-shell are most probable. This also accounts for the characteristic *absorption edges* [21] in the cross-section at the material dependent binding energies of each shell (see Figure 2.4). Furthermore, the likelihood of a photoelectric interaction decreases proportionally to $1/E_\gamma^{3.5}$ for higher photon energies in the associated dominant energy range. For very large photon energies ($E_\gamma \gg m_\mathrm{e}$), the relativistic limit alters this dependency to $\sigma_\mathrm{photo}(E_\gamma \gg m_\mathrm{e}) \propto Z^5/E_\gamma$ [7]. However, the photoelectric effect is already suppressed by Compton scattering and pair production at such energies.

Compton scattering

Incident photons in a medium can scatter on an atom as a whole or on a single shell electron. Coherent scattering processes on the whole atom are dominant for low photon energies and result in a typically small energy transition between photon and atom which is converted into recoil momentum. For photon energies significantly larger than the binding energy ($E_\gamma \gg E_\mathrm{B}$), the shell electrons of an atom can be considered quasi-free. If such a highly energetic photon scatters on an electron, which is kicked out of the atom's shell as a result of this process[1], it is referred to as Compton scattering [21]. In this case, the transferred energy is transformed into the recoil momentum of the released electron.

The kinematics of Compton scattering are given by the energy and momentum conservation of the scattering process of the incident photon on a quasi-free electron at rest. Figure 2.5 provides an illustration of such a process including the initial and final state energies and momenta. Consequently, the photon energy in the final state [7]

$$E'_\gamma = \frac{E_\gamma}{1 + \frac{E_\gamma}{m_\mathrm{e}c^2} \cdot (1 - \cos\theta_\gamma)} \tag{2.13}$$

depends on the scattering angle θ_γ, while the kinetic energy of the scattered electron $T = E_\gamma - E'_\gamma$ corresponds to the energy transferred by the photon. In the case of backward scattering ($\theta_\gamma = 180°$), the maximum energy transferred to the electron is [7]

$$T_\mathrm{max} = E_\gamma \frac{2\epsilon}{1 + 2\epsilon} \quad . \tag{2.14}$$

Here, $\epsilon = \frac{E_\gamma}{m_\mathrm{e}c^2}$ indicates the photon energy in relation to the rest energy of the electron (i.e. its mass). Hence, the measured energy spectrum of Compton scattering is cut off at an energy below the photoelectric peak, also referred to as *Compton edge*. For $E_\gamma \gg m_\mathrm{e}c^2$, the maximum

[1]It is possible, that the electron is bound to the atom after the scattering process even though the photon is sufficiently energetic. Such cases also classify as coherent scattering [7].

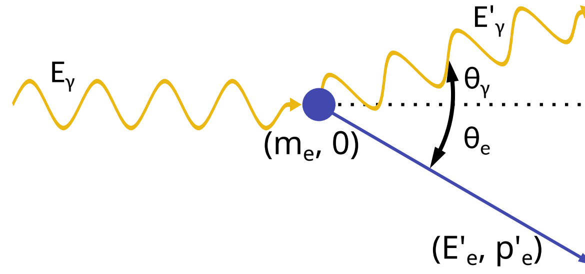

Figure 2.5: Schematic drawing of Compton scattering of an incident photon on a quasi-free electron at rest. The initial and final state energies and momenta of both particles are indicated. Adapted from [7].

energy transfer can be approximated as $T_{\mathrm{max}} = E_\gamma - E'_{\gamma,\mathrm{min}} \approx E_\gamma - m_\mathrm{e}c^2/2$ [7].

Compton scattering is the dominant interaction process for photon energies around 1 MeV [7]. The interaction cross-section of Compton scattering on a free electron integrated over all possible scattering angles was described by Klein and Nishina [24]. For low photon energies, the classical limit described by the *Thomson cross-section* is approached. In the relativistic approximation ($E_\gamma \gg m_\mathrm{e}$), the cross-section of a single, free electron is proportional to $\sigma_{\mathrm{Compton}} \propto 1/E_\gamma$. Additionally, materials with more shell electrons introduce more possible scattering options as the binding energy of each shell electron becomes negligible for large photon energies. Thus, the total cross-section increases with the atomic number $\sigma^{\mathrm{Atom}}_{\mathrm{Compton}} = Z\sigma_{\mathrm{Compton}}$, where $\sigma_{\mathrm{Compton}}$ denotes the cross-section for scattering of a single, free electron [7].

Pair production

The conversion of a photon into an electron-positron pair in the presence of a Coulomb field is called pair production. This process is predominantly stimulated by the electric field of a nucleus and requires a minimum photon energy of twice the electron mass $E_\gamma \geq 2m_\mathrm{e}$. Additional recoil effects for energy- and momentum conservation are generally negligible due to the large mass of the nucleus [7]. Furthermore, the physical process of pair production is closely associated with the energy loss of electrons through bremsstrahlung (see Section 2.1) [25]. Consequently, screening effects are equally relevant for pair production.

For very high photon energies of $\epsilon = \frac{E_\gamma}{m_\mathrm{e}c^2} \geq 10$, pair production is the dominant interaction process [21]. Nevertheless, the interaction cross-section of pair production does not depend on the photon energy but on the material. Since the electric field of the nucleus is determined by the number of charges within, the cross-section is dependent on the atomic number $\sigma_{\mathrm{pair}} \propto Z^2$ [7]. Combined with bremsstrahlung, pair production generates electromagnetic showers.

Apart from pair production in the field of a nucleus, the process can also happen in the electric field of a shell electron. However, this interaction is rare in comparison, except for very light atoms, and requires an even larger photon energy [21].

3 Semiconductor particle detectors

Due to their electrical properties, semiconductors have become indispensable in modern electronics. In addition, their low ionization energies and high charge carrier mobilities make semiconductor materials excellent particle detectors. As a result of the technological advances over the last decades, semiconductor detectors have become an essential tool in medical imaging, space instrumentation, and high-energy physics. This chapter provides an overview on semiconductors and how they are applied in the context of high-energy physics. Section 3.1 introduces the most important characteristic properties of semiconductors. In Section 3.1.2 and Section 3.1.3 examples of key electrical applications of semiconductors are showcased. Section 3.2 describes the signal generation in semiconductors as well as the subsequent signal processing by readout electronics. The second half of the chapter focuses on the use of silicon detectors as particle trackers in high-energy physics applications. Section 3.3 covers the current standard of hybrid pixel detectors for radiation-intensive environments with high rates and reviews the evolution of monolithic pixel detectors as an alternative. Finally, the applications of radiation-hard depleted monolithic active pixel sensors in high-energy physics experiments are discussed in Section 3.4.

3.1 Characteristic properties of semiconductors

In their solid state, crystalline semiconductors form a structure in which each atom establishes a covalent bond with four neighboring atoms. This crystalline structure results in a periodic arrangement of atomic nuclei and, consequently, a periodic potential throughout the crystal. Solving the Schrödinger equation of such potentials is described in textbooks such as [26, 27] and provides information about the energy eigenvalues of the overall system. In a pure semiconductor crystal, the energy levels of each individual atom are the same. Since the Pauli exclusion principle forbids the occupation of an energy level by more than two electrons[1], the material's characteristic energy levels split according to the number of atoms in the crystal. The resulting new energy levels only deviate marginally from the original one [27]. In the case of many-atom systems[2], the density of discrete energy levels becomes so large that a quasi-continuous range of occupiable energy exists, referred to as an energy band. A schematic illustration of a periodic potential and the corresponding energy levels is given in Figure 3.1. According to the solution of the Schrödinger equation, different energy bands are separated by regions of

[1] Two electrons which occupy the same energy level are required to have opposite spins.

[2] Within a cubic centimeter of crystal, the number of atoms is in the order of 5×10^{22} [27].

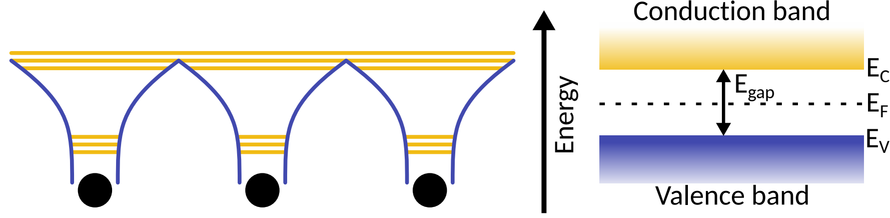

Figure 3.1: Schematic illustration of a periodic potential and the corresponding discrete energy levels of a one dimensional crystal (left). For a many-atom crystal, the energy levels are so dense that they can be considered as quasi-continuous energy bands (right). The gap energy E_{gap} is a characteristic property relevant for the electrical conductivity of a material and describes the region of forbidden energies between valence and conduction band. Adapted from [28].

forbidden energy values. The highest energy band containing electrons in the ground state is defined as the valence band, while the next higher group of permitted energy levels is referred to as the conduction band [27]. The conduction band of a semiconductor is completely unoccupied at temperatures close to absolute zero. In semiconductors, the two bands are separated by a region devoid of permitted energy levels called the band gap. The energy range covered by the band gap is a material dependent property referred to as gap energy E_{gap}. The characteristic attribute of semiconductors is the small gap energy of 1 or a few eV[3] [7], which can be overcome by additional (thermal) energy at higher temperatures. Typical elemental semiconductors are silicon ($E_{\mathrm{gap}}^{\mathrm{Si}} = 1.12\,\mathrm{eV}$) or germanium ($E_{\mathrm{gap}}^{\mathrm{Ge}} = 0.66\,\mathrm{eV}$), while gallium arsenide ($E_{\mathrm{gap}}^{\mathrm{GaAs}} = 1.424\,\mathrm{eV}$) is a frequently used compound semiconductor. All corresponding gap energies are taken from [7] and given at 300 K.

When an electron from the valence band is excited into the conduction band, it creates a vacancy in the crystal lattice referred to as a hole. Electrons in the conduction band are only lightly bound to nuclei and, thus, can be considered quasi free within the crystal. Similarly, electrons involved in the covalent bonds can *fill* vacancies left behind in the valence band, also allowing holes to move quasi freely within the band. Although holes are not physical particles, they contribute to the electrical conductivity by effectively carrying charge in quantities of $+e$.

Furthermore, semiconductors are categorized as direct or indirect based on the energy-momentum relationship of the band structure. For direct semiconductors such as gallium arsenide, the maximum of the valence band coincides with the minimum of the conduction band with respect to the wave vector of the crystal. Indirect semiconductors like silicon or germanium require a change of the wave vector and, thus, additional energy in form of lattice vibrations to accomplish the transition between valence and conduction band. An illustrative comparison of the two types is shown in Figure 3.2. The reader is referred to [29] for a more detailed explanation of this topic.

The electrical conductivity of a material rises with the number of (quasi) free charge carriers.

[3] In contrast, insulators have a factor 4 – 5 larger gap energy at which thermal excitation at room temperature is impossible, while the valence and conduction band are touching or even overlapping in the case of conductors.

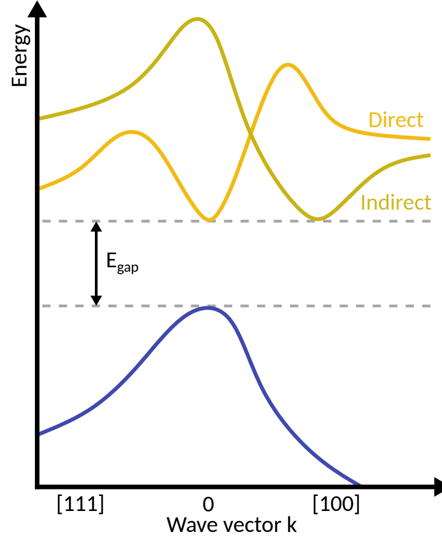

Figure 3.2: Schematic illustration of the difference between direct and indirect semiconductors. The origin of the x-axis is set arbitrarily and the Miller indices [klm] define designated directions within the crystal structure. Here, the gap energy is the same for both, however, the indirect type requires an additional shift of the wave vector to accomplish the transition. Adapted from [7].

In the case of intrinsic semiconductors, which contain very few impurities, the occupation probability of an electronic state in thermal equilibrium is given by the Fermi-Dirac statistics [30]

$$f(E) = \frac{1}{1 + \exp\left(\frac{E - E_\mathrm{F}}{kT}\right)} \tag{3.1}$$

where k is the Boltzmann constant and T is the absolute temperature. The Fermi energy E_F is defined as the energy at which the occupation probability of a state is exactly 50 %. Considering intrinsic semiconductors, the Fermi level characteristically lies in the middle of the band gap (see Figure 3.1). The free electron concentration

$$n_\mathrm{e} = \int_{E_\mathrm{C}}^{\infty} N_\mathrm{C}(E) f(E) dE \tag{3.2}$$

is then given by integrating the effective density of states $N_\mathrm{C}(E)$ in the conduction band multiplied by the corresponding occupation probability over all energies of the conduction band and above. Similarly, the hole concentration in the valence band can be determined. Under the assumption of thermal equilibrium, the free electron and hole concentrations are equivalent and the free charge carrier density is given as [30]

$$n_\mathrm{i} = \sqrt{N_\mathrm{C} N_\mathrm{V}} \cdot \exp\left(-\frac{E_\mathrm{C} - E_\mathrm{V}}{2kT}\right) = \sqrt{N_\mathrm{C} N_\mathrm{V}} \cdot \exp\left(-\frac{E_\mathrm{gap}}{2kT}\right) \quad . \tag{3.3}$$

Here, N_C and N_V are the effective densities of states in the conduction and valence band, respectively, which imply a strong temperature dependence ($N_\mathrm{C}, N_\mathrm{V} \propto T^{3/2}$) in the free charge carrier density [7]. Consequently, the current density and resistivity of intrinsic semiconductors depend significantly on temperature.

3.1.1 Doping of semiconductors

The selective insertion of other materials into the natively very pure semiconductor lattice is a common procedure to alter the electrical properties of a semiconductor. Injecting intended impurity atoms referred to as *dopants* into the pure lattice structure is called doping and creates energy levels within the forbidden band gap. To achieve the desired electrical modification, the *dopants* are required to have either one more or one less valence electron compared to the four valence electrons of elementary semiconductors. When introducing an element with five valence electrons (such as phosphorus or arsenic), only four of these form covalent bonds with the neighboring silicon atoms. Consequently, energy levels close to the conduction band are created, which are occupied by the remaining electrons. Thus, such a *dopant* is called donor and correspondingly doped semiconductors are categorized as n-type due to the electron excess. On the contrary, the introduction of atoms with three valence electrons (such as boron) into the crystal results in missing electrons in the covalent bonds and the formation of energy levels close to the valence band. These *dopants* are called acceptors and the resulting excess of holes is characteristic for correspondingly doped p-type semiconductors. It is important to note that the crystal remains electrically neutral in both cases due to the charge of the inserted atomic nucleus. Figure 3.3a schematically depicts the effects of doping on the band structure of semiconductors. For typical donors and acceptors, the created energy levels are in the order of $\mathcal{O}(0.05\,\mathrm{eV})$ below the conduction or above valence band, respectively [30]. Due to this very small energy difference, room temperature is sufficient to cause ionization of donor states and occupation of acceptor states resulting in an increase of free charge carriers in both bands, independently. Since holes are the numerically dominant free charge carriers in a p-type crystal, they are referred to as majority charge carriers. Likewise, electrons are the majority charge carriers in an n-type crystal. Furthermore, the additional energy states cause a shift of the Fermi level towards their energetic position (e.g. the Fermi energy for an n-type semiconductor shifts towards the conduction band). The extent of change depends on the donor or acceptor concentration. When high enough, this can even result in the Fermi level lying within the conduction or valence band, respectively [7].

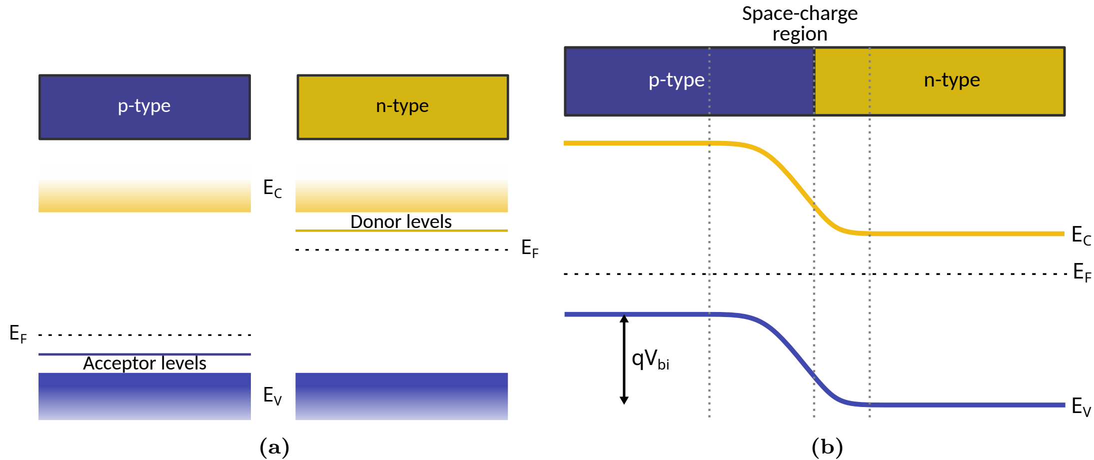

Figure 3.3: (a) Schematic band structure of p- and n-type semiconductors, respectively. The additional energy levels introduced by the doping and the resulting shift of the Fermi energy are visualized. (b) Brought into contact, the band structure of an abrupt p-n junction bends. This is caused by the diffusion of charge carriers due to gradients in their density and the resulting built-in voltage V_{bi} created by space charge that offsets the diffusion in thermal equilibrium. Physical constraints require that the Fermi level remains constant across the whole crystal. Adapted from [30].

3.1.2 P-n junction and space-charge region

Fabricating adjacent p-n-type semiconductors and, thus, creating a p-n-diode[4] is essential for the particle detection application of semiconductors. Due to the concentration gradients of the two different charge carriers across the combined entity, electrons from the n-type diffuse into the p-type region to recombine with holes and vice versa. As a result, a zone without free charge carriers forms around the boundary area of both crystals typically called depletion zone or space-charge region. After recombination, ionized atoms remain in the crystal, creating space charge and thus an electric field that generates drift which counteracts the diffusion. Because of the difference in *dopants*, negative space charge builds up in p-type and positive space charge in n-type semiconductors. In thermal equilibrium, the diffusion is counterbalanced by the created electric field, the magnitude of which is referred to as the built-in voltage, and the accompanying drift. This potential difference leads to a bending of the energy bands proportional to the built-in voltage while the Fermi level stays constant across the whole crystal as visualized in Figure 3.3b.

The following derivations of characteristic properties of a p-n junction are based on [7] if not stated otherwise and kept one-dimensional for the sake of simplicity. Since the combined semiconductors must be electrically neutral overall, the number of charge carriers that recombine must originate equally from p- and n-type. Thus, the spatial extension of the depletion zone into the respective doping type $x_{\mathrm{p,n}}$ depends on the concentration of donors N_{D} and acceptors N_{A}

[4]Other diode types share the same fundamental principles but have different specific properties. Particularly noteworthy is the Schottky diode, which consists of a metal-semiconductor interface and is widely used in modern electronics for its fast switching speeds.

as described by the *neutrality condition*:

$$N_{\mathrm{A}} x_{\mathrm{p}} = N_{\mathrm{D}} x_{\mathrm{n}} \quad . \tag{3.4}$$

Furthermore, the charge carrier density in thermal equilibrium, in which diffusion and drift offset each other,

$$\rho(x) = \begin{cases} -eN_{\mathrm{A}} & \text{for} \quad -x_{\mathrm{p}} < x < 0 \\ +eN_{\mathrm{D}} & \text{for} \quad 0 < x < x_{\mathrm{n}} \end{cases} \tag{3.5}$$

is also obtained from the doping concentrations directly. Applying Maxwell's equations, the electric field across the crystal

$$E(x) = \int \frac{1}{\epsilon_0 \epsilon} \rho(x) dx = \begin{cases} \frac{-eN_{\mathrm{A}}}{\epsilon_0 \epsilon}(x + x_{\mathrm{p}}) & \text{for} \quad -x_{\mathrm{p}} < x < 0 \\ \frac{+eN_{\mathrm{D}}}{\epsilon_0 \epsilon}(x - x_{\mathrm{n}}) & \text{for} \quad 0 < x < x_{\mathrm{n}} \end{cases} \tag{3.6}$$

is determined by integrating the space-charge density over the spatial parameter normalized to the permittivity ϵ. Outside the depletion zone, the electric field is zero as specified by the *neutrality condition*. The behavior of the aforementioned parameters along an abrupt p-n junction is illustrated in Figure 3.4. In addition, the built-in voltage is calculated from the electrical potential difference at the edges of the depletion zone

$$V_{\mathrm{bi}} = \phi_{\mathrm{n}} - \phi_{\mathrm{p}} = -\int_{-x_{\mathrm{p}}}^{x_{\mathrm{n}}} E(x) dx = \frac{e}{2\epsilon_0 \epsilon}(N_{\mathrm{A}} x_{\mathrm{p}}^2 + N_{\mathrm{D}} x_{\mathrm{n}}^2) \quad . \tag{3.7}$$

Typical built-in voltages of silicon diodes are in the range of $0.4 - 0.8\,\mathrm{V}$.

The additional supply of an external voltage V_{ext} to the p-n junction changes the characteristic properties and puts the system out of its thermal equilibrium. The polarity of this voltage is relevant: In case the external voltage counteracts the built-in voltage (specified as forward bias), the space-charge region reduces and disappears completely when the two voltages compensate each other. From this point, charge carriers can move freely throughout the crystal and the diode current increases exponentially with the external voltage [31]. In contrast, the depletion region grows larger with the applied voltage if the external voltage is of the same polarity as the built-in potential (reverse bias scenario). Rearranging Eq. (3.7) reveals a proportionality to $\sqrt{V_{\mathrm{ext}}}$

$$x_{\mathrm{p,n}} \approx \sqrt{\frac{2\epsilon_0 \epsilon}{eN_{\mathrm{A,D}}}(V_{\mathrm{bi}} + V_{\mathrm{ext}})} \overset{V_{\mathrm{ext}} \gg V_{\mathrm{bi}}}{\approx} \sqrt{\frac{2\epsilon_0 \epsilon}{eN_{\mathrm{A,D}}} V_{\mathrm{ext}}} \tag{3.8}$$

as the approximation of $V_{\mathrm{ext}} \gg V_{\mathrm{bi}}$ holds for the small built-in voltage of silicon and the typically large external voltage. Also in the reverse bias scenario, a small current referred to as leakage current is measurable for a p-n junction. The magnitude of leakage current is dominated by thermal generation of electron-hole pairs in the space-charge region and, thus, proportional to the depleted volume. Before exposure to radiation, leakage currents are typically in the order

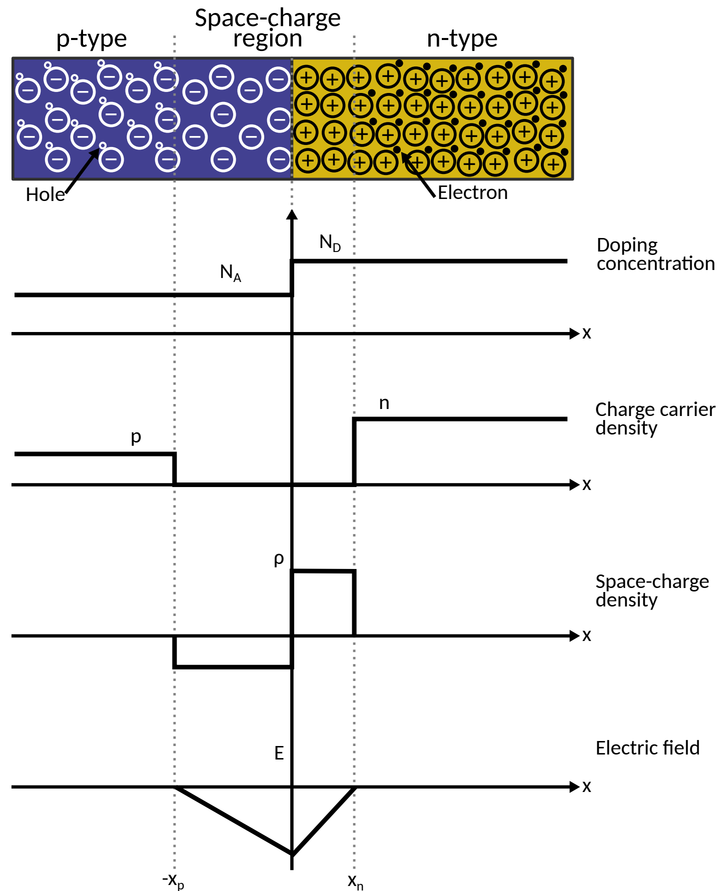

Figure 3.4: Change of characteristic properties across an abrupt p-n transition. Adapted from [7].

of nA/cm^{-2} [7]. Furthermore, the capacitance of the diode decreases as the depletion zone increases.

Silicon detectors are operated in reverse bias to extend the depletion zone over the entire sensitive area, if possible. Traversing charged particles generate electron-hole pairs (see Section 2.1), which would recombine quickly in non-depleted regions of a p-n junction and, consequently, could not be detected[5]. In addition, strong electric fields across the depletion zone combined with low leakage currents are desired to facilitate fast charge collection and low noise in the sensor. Typical external bias voltages range between 1 V and 1000 V depending on sensor properties (doping concentration, thickness, etc.) and application.

[5]This is not as critical for semiconductors with significantly smaller intrinsic charge carrier density such as gallium arsenic [7].

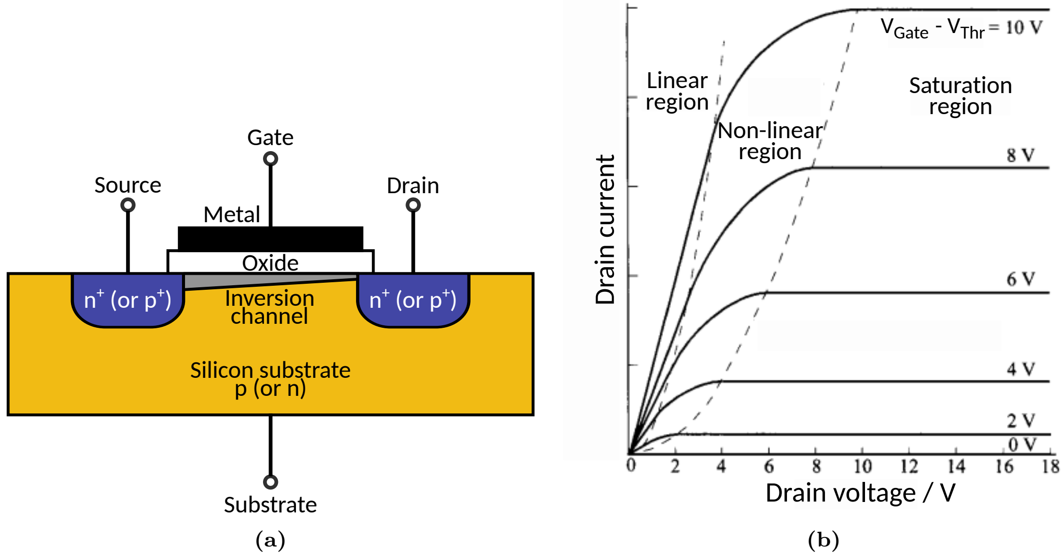

Figure 3.5: (a) Schematic illustration of a generic MOSFET structure. The structure features four contact points: drain, source, gate, and substrate. The insulating oxide layer between gate and substrate prevents direct-current flow between the two components. Adapted from [7]. (b) The idealized drain current characteristics emphasize the effect of the gate voltage V_{Gate}, drain voltage V_{Drain}, and their relation on the current flow of a MOSFET. The dashed lines separate the different operational regions. Modified from [29].

3.1.3 MOS transistors

One of the most important applications of semiconductors are so-called metal-oxide-semiconductor (MOS) transistors, which are used to realize complex integrated circuits on the sub-micrometer level. As the name suggests, the interface between metals, insulating oxides, and semiconductors is exploited to achieve the desired electrical properties in such circuits. A detailed derivation of the underlying physics is beyond the scope of this thesis, and it is referred to [7, 29]. Nevertheless, the most commonly used metal-oxide-semiconductor field-effect transistor (MOSFET) is introduced, as it plays an essential role in the high-density readout electronics of detectors.

A MOSFET structure comprises two highly doped channels called drain and source embedded in an oppositely lowly doped silicon substrate [7], as shown in Figure 3.5a. The surface between drain and source is interfaced to a metal, referred to as gate, via an insulating oxide, which prevents direct-current flow towards the gate. In total, the structure contains four electrical contact points: drain, source, gate, and substrate.

A MOSFET has different modes of operation based on the applied voltages at the contact points, while keeping the drain at a higher absolute potential than the source. If the gate voltage V_{Gate} is kept below an intrinsic threshold voltage V_{Thr}, almost no current will flow from source to drain[6] and the device is effectively off. For gate voltages above this threshold, a conductive

[6] A small current referred to as *sub-threshold current* continues to flow [29].

inversion layer of charge carriers forms below the oxide and a so-called *drain current* flows. This current increases for larger gate voltages and is proportional to the geometrical length and width of the gate contact [7]. If the potentials applied to source and drain is not identical, the conductive inversion channel is not symmetric below the gate and the current flow can also be manipulated by the drain voltage V_{Drain}. For small drain voltages ($V_{\mathrm{Drain}} < V_{\mathrm{Gate}} - V_{\mathrm{Thr}}$), the drain current is proportional to the drain voltage and the MOSFET is operated in the linear region. If the drain voltage exceeds the effective gate voltage ($V_{\mathrm{Drain}} \geq V_{\mathrm{Gate}} - V_{\mathrm{Thr}}$), the inversion channel at the drain contact is (close to) zero and the drain current saturates [29]. Between the operation in saturation and in linear relation, there is a transition region generally referred to as *non-linear region*. The idealized drain current characteristics for different gate and drain voltages are shown in Figure 3.5b.

For MOSFET devices, a distinction is made between NMOS structures, where the substrate is of p-type silicon, and PMOS structures, where the substrate is of n-type silicon. Depending on the substrate type, the free charge carriers below the gate change (electrons for p-type substrate and holes for n-type substrate) [7]. Integrated circuits that employ both types of structures are categorized as complementary metal-oxide-semiconductor (CMOS) devices. They are realized through the implantation of additional deep wells oppositely doped than the substrate that provide a local bulk for complementary devices.

3.1.4 Charge carrier transport in semiconductors

The transport of charge carriers in materials originates either from intrinsic states of non-equilibrium or from the application of external fields. Diffusion occurs whenever the charge carrier concentration is non-uniform across the semiconductor as in the case of local charge carrier injection or inhomogeneous exposure to radiation. It describes the movement of free charge carriers from the highest towards the lowest concentration region to balance this discrepancy and does not require an external electric field. According to Fick's law of diffusion, the carrier flux is proportional to the respective concentration gradient $\vec{\nabla} p$ or $\vec{\nabla} n$ and results in a diffusion current [29]

$$\vec{j}_{\mathrm{p}}^{\mathrm{diff}} = -eD_{\mathrm{p}}\vec{\nabla} p \quad \text{or} \quad \vec{j}_{\mathrm{n}}^{\mathrm{diff}} = eD_{\mathrm{n}}\vec{\nabla} n \tag{3.9}$$

depending on the charge carrier type. The proportionality factor $D_{\mathrm{p,n}}$ is defined as the diffusion coefficient and is related to the respective charge carrier mobility $\mu_{\mathrm{p,n}}$ as well as the temperature based on the Einstein relation [29]:

$$D_{\mathrm{p,n}} = \mu_{\mathrm{p,n}} \frac{kT}{e} \quad . \tag{3.10}$$

If an electric field E is applied, free charge carriers are accelerated and drift with or against the direction of the field, depending on charge polarity. While drifting, the charge carriers scatter off impurities and phonons in the lattice structure resulting in momentum and direction

changes. The average equation of motion for a charge carrier with drift velocity $\vec{v}_\mathrm{D}$ in such a scenario is given by [7]

$$m_\mathrm{eff}\left(\dot{\vec{v}}_\mathrm{D} + \vec{v}_\mathrm{D}/\tau\right) = q\vec{E} \tag{3.11}$$

where m_eff is the effective mass of the charge carrier with charge q and τ is the mean time between collisions. Under the assumption of constant drift velocities ($\dot{\vec{v}}_\mathrm{D} = 0$), the equation of motion yields a direct dependency between drift velocity and electric field [29]

$$\vec{v}_\mathrm{D} = \frac{q\tau}{m_\mathrm{eff}}\vec{E} = \mu\vec{E} \quad , \tag{3.12}$$

while the proportionality factor is summarized as the charge carrier mobility. For increasing electric field strengths, the charge carriers start to scatter inelastically, and, in the case of very high electric fields, can ionize lattice atoms causing a charge carrier avalanche. Consequently, the drift velocity becomes progressively independent of the electric field and saturates eventually. Studies have shown that the assumption of a field strength-dependent mobility [32]

$$\vec{v}_\mathrm{D} = \mu(\vec{E})\vec{E} = \frac{\mu_0}{\left[1 + \left(\frac{\mu_0}{v_\mathrm{sat}}\right)^\beta\right]^{1/\beta}}\vec{E} \tag{3.13}$$

accurately describes the drift velocity over a wide electric field range. Here, μ_0 is the mobility at low electric fields and v_sat refers to the drift velocity in saturation, while β is an empirically determined parameter ranging between 1 and 2 depending on the charge carrier type. In silicon, the mobility of electrons and holes at low fields are $1450\,\mathrm{cm^2/Vs}$ and $500\,\mathrm{cm^2/Vs}$ at $300\,\mathrm{K}$, respectively, whereas saturation velocities are in the order of $\mathcal{O}(1\times10^7\ \mathrm{cm/s})$ [7]. Furthermore, the motion due to drift results in a drift current [7]

$$\vec{j}^\mathrm{drift} = e(p\mu_\mathrm{p} - n\mu_\mathrm{n})\vec{E} = \sigma\vec{E} \tag{3.14}$$

proportional to the electric conductivity σ, which comprises charge, density, and mobility of the free charge carriers. Thus, the total current within the semiconductor is obtained by the sum of both contributions

$$\vec{j}^\mathrm{total} = \vec{j}^\mathrm{diff} + \vec{j}^\mathrm{drift} \quad . \tag{3.15}$$

Charge clouds

Assuming multiple charge carriers are generated at a point-like location without an external field present, diffusion causes the charge carriers to disperse into a Gaussian shaped *cloud* over time. The width of such a charge cloud in one dimension is given by $\sigma = \sqrt{2D_\mathrm{p,n}t}$ [7], where t denotes the time. In a realistic scenario, the multitude of charge carriers generated along the trajectory of an impinging MIP are swept away by an electric field. Thus, the charge carriers are also subject to diffusion for the duration of the drift time spreading the signal around the

particle's trajectory. At constant drift velocities, the spatial extension orthogonal to the drift direction $\sigma = \sqrt{2D_{\mathrm{p,n}}\vec{x}/\vec{v}_{\mathrm{D}}}$ can be associated with the drift distance $\vec{x}$.

3.2 Signal processing

The deposited energy by traversing particles in a semiconductor detector must be converted into an electrical signal for further processing. To understand the signal processing chain, the following section describes how the deposited energy generates a measurable signal in a semiconductor. Subsequent readout electronics for amplification, shaping, and digitization of the generated signal are described in Section 3.2.2.

3.2.1 Signal generation

Impinging particles and radiation are detected by energy deposited inside the detector, which generates electron-hole pairs. Semiconductor detectors maximize the depletion zone of differently doped junctions to prevent immediate recombination. In addition, the applied bias voltage to deplete the sensitive area causes the created charge carriers to drift in opposite directions.

One common misconception is the physical relationship between signal charge and potential at the collection electrode. In fact, the movement of the charge carriers relative to the electrode already induces a measurable signal. The coupling of a charge at any position to a given electrode is expressed by the weighting potential of the specific electrode, while the drift direction and velocity are defined by the existing electric field [33]. Therefore, a charge carrier does not necessarily need to reach the electrode to be detected.

The general concept of weighting potentials and the induced signals due to moving charges is described by the *Shockley-Ramo theorem* [34, 35]: Considering a system with k electrodes in which all except electrode i are at the potential $\phi_{k\neq i}(\vec{r}) = 0$, the weighting potential and the corresponding weighting field of electrode i are

$$\phi_{\mathrm{w},i}(\vec{r}) = \frac{\phi_i(\vec{r})}{V_i} \quad \text{and} \quad \vec{E}_{\mathrm{w},i} = -\vec{\nabla}\phi_{\mathrm{w},i}(\vec{r}) \quad . \tag{3.16}$$

For simplicity, the voltage V_i is usually normalized to one. An exemplary simulation of the weighting potential and weighting field lines for a segmented, multi-electrode system is shown in Figure 3.6. When a charge q moves by $d\vec{r}$ within this system, the induced charge signal in electrode i is determined by the respective weighting field

$$dQ_i = -q\vec{E}_{\mathrm{w},i}d\vec{r} \quad . \tag{3.17}$$

Consequently, the corresponding induced signal current depends on the drift velocity

$$i_i = q\vec{E}_{\mathrm{w},i}\vec{v}_{\mathrm{D}} \tag{3.18}$$

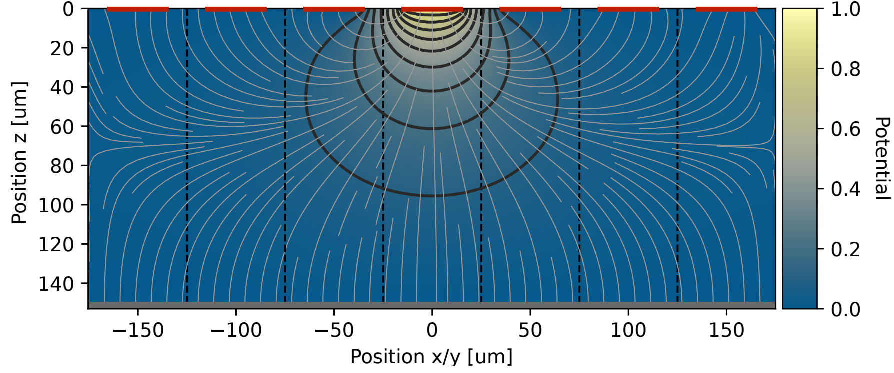

Figure 3.6: Two-dimensional simulation of the weighting potential (color gradient) and field shaping (gray lines) of a segmented, multi-electrode configuration. The center electrode lies on potential $V_i = 1$ while all other electrodes are set to ground. From [28].

and thus, according to Eq. (3.12) and Eq. (3.13), on the electric field. Depending on the application, the induced current is measured through a resistor or integrated over a capacitor to convert the signal to a voltage or charge, respectively. If the space-time relation $\vec{r}(t)$ of the drifting charge is known, integrating over its trajectory yields the total induced signal charge [7]

$$Q_i = -q \int_{\vec{r}(t_0)}^{\vec{r}(t_1)} \vec{E}_{\mathrm{w},i} d\vec{r} = -q[\phi_{\mathrm{w},i}(\vec{r}(t_1)) - \phi_{\mathrm{w},i}(\vec{r}(t_0))] \tag{3.19}$$

which is proportional to the difference between the weighting potential at starting position $\vec{r}(t_0)$ and final position $\vec{r}(t_1)$.

The following is a simple example of the introduced concept using an unsegmented silicon detector in the form of a p-n junction with two electrodes. The derivation is based on [7]. If the external voltage exceeds the depletion voltage $V_{\mathrm{dep}} \approx \frac{eN_{\mathrm{eff}}}{\epsilon_0 \epsilon} \frac{d^2}{2}$, given by the effective doping concentration N_{eff} and thickness d of the detector, the electric field between the electrodes exhibits a constant offset proportional to the applied voltage. For sufficiently large external voltages, the configuration effectively resembles a parallel plate detector with space charge in the depleted area. Choosing the coordinate system in such a way that $\vec{e}_x$ is the direction vector of the shortest distance between the electrodes, the electric field along this axis is described by

$$\vec{E}(x) = -\left(\frac{V_{\mathrm{ext}} + V_{\mathrm{dep}}}{d} - \frac{2V_{\mathrm{dep}}}{d^2} x\right) \vec{e}_x = -\left(a - bx\right) \vec{e}_x \quad . \tag{3.20}$$

The parameterization of $a = \frac{V_{\mathrm{ext}}+V_{\mathrm{dep}}}{d}$ and $b = \frac{2V_{\mathrm{dep}}}{d^2}$ is useful for simplifying equations in later steps. Since the weighting field is not affected by the space charge created due to full depletion of the volume, it stays constant across this configuration:

$$\vec{E}_{\mathrm{w}} = -\frac{1}{d} \vec{e}_x \quad . \tag{3.21}$$

Generated e-h pairs are separated by the external voltage and drift towards a respective electrode. The corresponding characteristic drift time

$$\tau_{\mathrm{e,h}} = \frac{d^2}{2\mu_{\mathrm{e,h}} V_{\mathrm{dep}}} \tag{3.22}$$

depends not only on the charge carrier mobility and maximum drift distance, but also on the depletion voltage. For a fully depleted configuration, charge carriers created at the location of the opposing electrode experience the maximum drift time

$$T_{\mathrm{max}}^{\mathrm{e,h}} = \tau_{\mathrm{e,h}} \cdot \ln \frac{V_{\mathrm{ext}} + V_{\mathrm{dep}}}{V_{\mathrm{ext}} - V_{\mathrm{dep}}} \tag{3.23}$$

determining the duration of signal generation. Once the charge carrier reaches its destination electrode, it no longer contributes to the signal. Based on the above considerations and neglecting diffusion, the signal current induced in the sensitive electrode by N equally distributed e-h pairs can be expressed by

$$\begin{aligned} i_{\mathrm{e}}(t) &= -\frac{qN}{d^2}\frac{1}{\tau_{\mathrm{e}}} e^{-t/\tau_{\mathrm{e}}} \left(\frac{a}{b} x_{\mathrm{max}}^{\mathrm{e}} - \frac{1}{2} x_{\mathrm{max}}^{\mathrm{e}} \right) && \text{for} \quad 0 < t < T_{\mathrm{max}}^{\mathrm{e}} \\ i_{\mathrm{h}}(t) &= -\frac{qN}{d^2}\frac{1}{\tau_{\mathrm{h}}} e^{+t/\tau_{\mathrm{h}}} \left(\frac{a}{b} (d - x_{\mathrm{min}}^{\mathrm{h}}) - \frac{1}{2} (d^2 - x_{\mathrm{min}}^{\mathrm{h2}}) \right) && \text{for} \quad 0 < t < T_{\mathrm{max}}^{\mathrm{h}} \end{aligned} \tag{3.24}$$

where

$$x_{\mathrm{max}}^{\mathrm{e}}(t) = \frac{a}{b} + \left(d + \frac{a}{b} \right) e^{+t/\tau_{\mathrm{e}}} \quad \text{and} \quad x_{\mathrm{min}}^{\mathrm{h}}(t) = \frac{a}{b} \left(1 - e^{-t/\tau_{\mathrm{h}}} \right) \tag{3.25}$$

denote the time dependent position of the charge carriers with the longest drift distances. The integration of the signal current over time directly yields the collected signal charge. Figure 3.7 shows the calculated signal current and charge for typical values and operational conditions of pixel detectors. Besides the longer drift duration of holes compared to electrons due to differing mobilities, a dependence of the signal on the external voltage is apparent. To ensure complete signal collection within a finite time interval, over-depletion ($V_{\mathrm{ext}} > V_{\mathrm{dep}}$) of the detector is assumed for this calculation. If this is not the case, charge carrier motion by diffusion becomes crucial and can no longer be neglected.

3.2.2 Readout electronics

The processing of analog signals into digital data is done by the front-end readout electronics. A generic readout channel comprises multiple stages for signal amplification, signal filtering and shaping, and signal digitization as is shown in Figure 3.8. In pixelated semiconductor detectors, each pixel is electrically coupled to an individual front-end circuit. Since the initial signal in such detectors has a very small amplitude, its amplification at an early stage in the readout chain is essential. This so-called *pre-amplification* provides high internal gain and configurable

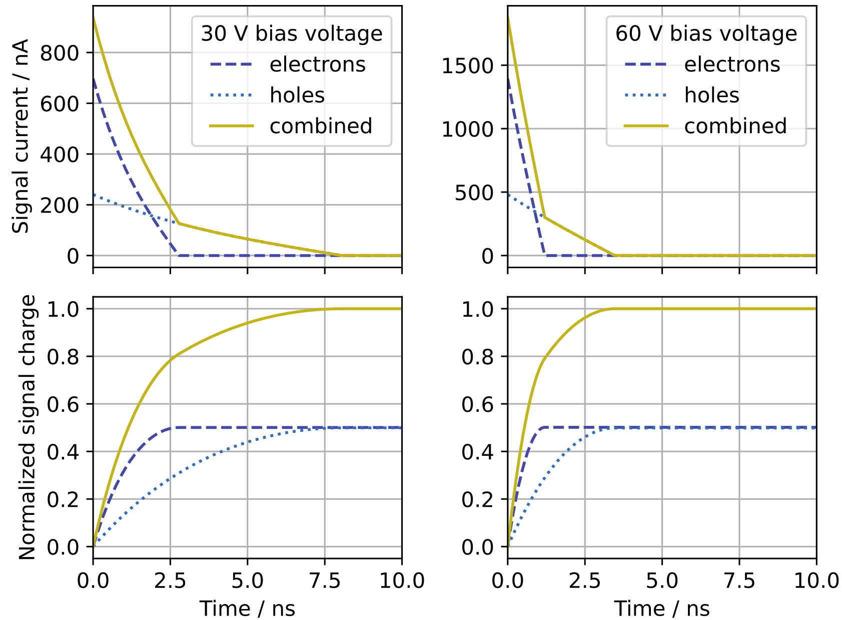

Figure 3.7: Signal current (top) and normalized signal charge (bottom) induced by charge movement and accumulation in an unsegmented silicon detector. This example assumes 10 000 e-h pairs generated uniformly along the track of a MIP traversing a 100 µm thick detector perpendicularly. The complete charge collection is ensured by bias voltages greater than the depletion voltage $V_{\mathrm{dep}} = 20\,\mathrm{V}$ of the detector. The dependence of the signal duration on the external voltage and over-depletion is visualized between $V_{\mathrm{ext}} = 30\,\mathrm{V}$ (left) and $V_{\mathrm{ext}} = 60\,\mathrm{V}$ (right).

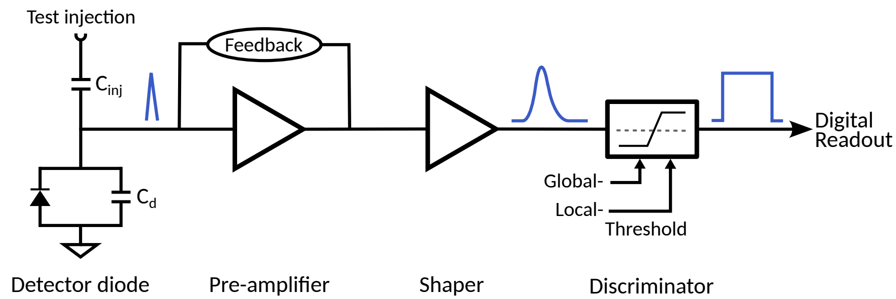

Figure 3.8: A generic analog front-end readout chain used for pixelated detector systems. The generated signal is amplified and shaped before being digitized by the discriminator stage. The transformation of signal shape is indicated in blue. To verify the functionality of the readout electronics, an injection circuit is implemented to induce artificial signals at the pre-amplifier input. Adapted from [36].

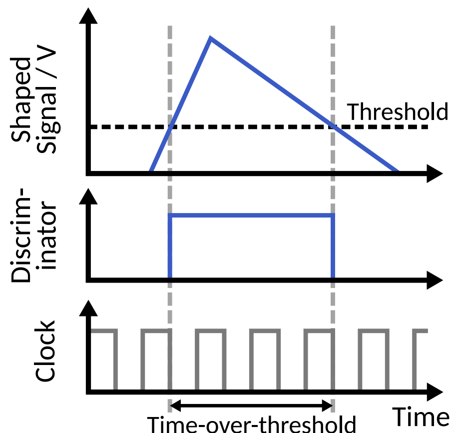

Figure 3.9: Time-over-threshold method utilized to measure the deposited charge which is proportional to the amplitude of the shaped signal pulse. The sampling rate and, thus, resolution of this method depends on the provided clock of the system.

operation through the external circuit [36]. As the pre-amplifier is the first stage of the readout, it must have a high signal-to-noise ratio while respecting the allowed power budget and heat dissipation. Depending on the detector type and application, the most efficient input signal can be a current, a voltage, or a charge. Thus, the subsequent amplification stage is implemented as a current-, a voltage-, or a charge-sensitive amplifier, correspondingly, with the latter being most common. In addition to the resistive feedback required in any amplification stages, charge-sensitive amplifiers typically also have capacitive feedback to integrate the collected charge. In this case, a constant feedback current source yields the discharge of the feedback capacitor at a constant slope. For any amplification stage, the width of the resulting amplified pulse is proportional to its amplitude and, thus, to the deposited energy in the sensitive volume. Typical pulse widths after the amplification stage range from several 10 ns up to several 1 µs [7]. Further pulse shaping in the filter and shaping stage may be necessary to minimize the noise contributions or shorten the output signals to prevent *pile-up* effects in high-rate environments. *Pile-up* effects describe the indistinguishability of two (or more) signals overlapping timewise within the readout electronics, because the signals are not processed quickly enough.

Finally, the discriminator stage compares the amplified and shaped signal to an adjustable threshold and digitizes it. In the case of a constant feedback current, the duration for which the shaped signal pulse exceeds the discriminator threshold is proportional to the initial signal amplitude and can be used to measure the deposited energy. This method, referred to as *time-over-threshold*, is commonly used in high-energy physics applications and illustrated in Figure 3.9. The resolution of the time-over-threshold measurement depends on the sampling rate of the discriminator given by the provided clock frequency. In addition to a global register controlling all readout channels, the threshold of each pixel's discriminator can, typically, be individually tuned (see Figure 3.8) to compensate for manufacturing process deviations. The

digitized data is then passed on to further digital logic, where it is aggregated into a detector specific data stream and transmitted to the data acquisition system (see Section 5.3).

To validate the functionality of the front-end electronics, readout chains are equipped with a test-injection circuit to induce artificial signals at the pre-amplifier input node. This feature is implemented by a well-defined injection capacitance C_{inj}, across which a known voltage is applied [36].

3.3 Silicon detectors for tracking applications

Tracking detectors play an essential role in high-energy physics collider experiments as they are responsible for the accurate reconstruction of particle tracks. This is necessary to verify particle decays and locate their so-called vertex position at a high precision. For this purpose, the tracking detector is installed as close as possible to the interaction point of the experiment. As a result, it receives the highest particle rates and the most radiation damage of any sub-detector. The constantly increasing demands on tracking detectors over the last decades raise the indispensability of semiconductor trackers, which results in a continuous development. The combination of precise spatial resolution and fast signal readout in the order of $\mathcal{O}(\mu\mathrm{m})$ and $\mathcal{O}(\mathrm{ns})$ across multiple channels provided by silicon detectors is ideally suited for tracking applications in high-luminosity environments. To reach the required spatial resolution, the electrodes of a semiconductor detector are segmented where each electrode functions as an individual readout channel. Consequently, a particle's trajectory can be associated with the location of the electrode in which the signal is induced.

Micro-strip detectors are a straight forward example of the realization of segmented electrodes in one dimension. Early studies were able to demonstrate less than 5 µm spatial resolution in the direction of their segmentation for strip pitches of 60 µm [37, 38]. A schematic illustration of such a sensor layout is shown in Figure 3.10. Multiple approaches for measuring the position in all three dimensions exist: The simplest method utilizes two layers of single-sided strip detectors tilted towards each other. A more novel option implants an additional set of strips perpendicular to the initial set at the rear side of the same silicon bulk. The fabrication of such double-sided micro-strip sensors is very complex and, thus, expensive at the benefit of minimizing the supplementary material of the detector [30]. Single-sided strip sensors are a popular concept of semiconductor trackers for current and planned experiments to cover large areas at comparatively low cost and complexity [39, 40]. The induced signals are typically routed to the periphery of the sensor[7] where a dedicated readout application specific integrated circuit (ASIC) is connected to handle the data processing of all channels. Another common concept is the segmentation of the electrode into pixelated areas yielding two-dimensional spatial information within a single sensor. Modern pixel detectors in the high-energy physics field rely

[7] In general, the sensitive area of a semiconductor detector is referred to as sensor while the signal processing part is referred to as front-end or readout.

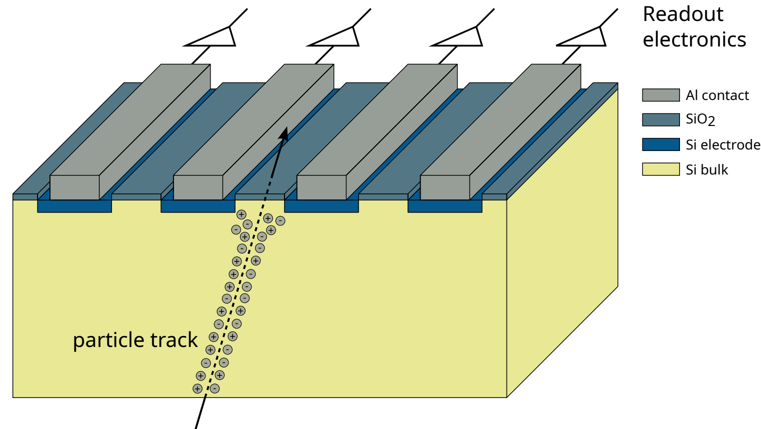

Figure 3.10: Schematic visualization of segmented electrodes implemented in a single-sided micro-strip detector. Each electrode is connected to an individual readout channel and functions as an independent detector. From [28].

on pitches in the order of $\mathcal{O}(10-100\,\mu\text{m})$ per segment which results in $\mathcal{O}(10^4)$ separate readout channels per square centimeter [36]. Consequently, it is not feasible to route each individual signal to the periphery of the sensor and an alternative method is required.

3.3.1 Hybrid pixel detectors

The concept of hybrid pixels describes combining an electrically passive sensor with an active readout ASIC on a per-pixel level and its functionality was validated by the RD19 collaboration at CERN [41]. To realize this, the segmentation of both sensor and readout chip must match precisely[8]. Furthermore, the small sizes and high density of individual pixels require a sophisticated and expensive connectivity procedure on micrometer level called *fine pitch bump bonding*. This procedure includes preparation of the contact points in form of *under bump metallization*, deposition of the connecting *bump bond*, and high-precision alignment of the contact points between both chips. For a detailed description of the bump bonding process it is referred to [36]. Due to the large number of channels, readout chips are usually with per channel front-end electronics to digitize the induced signals and a global logic and communication block (typically located at the chip's periphery) to process and transmit the data. A schematic layout of the hybrid pixel concept is illustrated in Figure 3.11. While the sensor does not require active electronic components, high-resistivity substrates with thicknesses in the order of $\mathcal{O}(100\,\mu\text{m})$ are necessary for efficient charge collection[9]. Front-end chips utilize commercial CMOS technology

[8] In this case, precise matching describes a one-to-one connection between a sensor pixel and a front-end pixel, while the individual pixel size can differ between the two. For example, it is possible to match $50\,\mu\text{m} \times 50\,\mu\text{m}$ front-end pixels with $25\,\mu\text{m} \times 100\,\mu\text{m}$ sensor pixels.

[9] Due to their requirements on substrate resistivity and thickness, sensors wafers were previously not available from commercial vendors. However, studies have shown, that passive sensors manufactured in commercially available CMOS processes form a promising alternative [42].

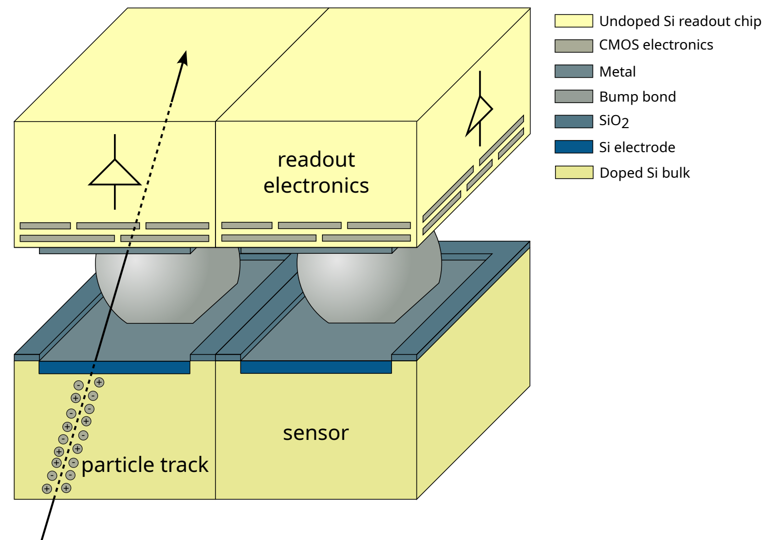

Figure 3.11: Schematic layout of hybrid pixel cells consisting of precisely aligned sensor- and readout pixel connected via a bump bond. From [28].

and low-resistivity silicon allowing the implantation of many active components and high wafer throughput but limit the feasible reticle size permitted by the manufacturer. Thus, often more than one readout chip is connected to a single sensor tile forming a so-called multi-chip module to cover more area efficiently.

The major advantage of the hybrid pixel concept is the possibility of optimizing both, sensor and readout chip, separately towards their application. This facilitates a large signal-to-noise ratio at fast operating and readout frequencies [36]. Therefore, hybrid pixel detectors are the current state-of-the-art technology for applications in the harshest radiation environments with tremendous data rates [7]. With regard to the high-luminosity upgrade of the ATLAS and CMS experiments at the LHC, a readout ASIC tolerating up to 1 Grad in ionizing dose was successfully developed within the RD53 collaboration [43]. The separate optimization of the sensors successfully ensured efficient charge collection up to $1 \times 10^{16}\,\mathrm{n_{eq}\,cm^{-2}}$ fluences [44]. The drawback of the hybrid pixel concept, however, is the expensive and complex *bump bonding* procedure as well as the additional material that is installed in the experiment because both chips require a certain thickness for handling. The latter is especially important for high precision measurements since more material increases multiple scattering and, thus, reduces tracking precision.

3.3.2 Monolithic pixel detectors

Since the main components of hybrid pixel detectors are typically fabricated in silicon, the attempt of combining both sensor and front-end electronics in a single entity of silicon is a logical enhancement to simplify manufacturing. This significantly reduces the thickness of the

detector, as the additional material of the ASIC chip substrate and the bump bonds become obsolete. Furthermore, the monolithic approach facilitates designs with pixels that are smaller than the 50 µm pixel pitch currently available by standard bump-bonding techniques in this field[10]. The developments of such monolithic pixel detectors already started in the 1980s [46, 47] and produced different strategies of integrating the active electronics partially or fully. The latter are generally referred to as monolithic active pixel sensors (MAPS). DEPFET[11] pixel structures incorporate a single transistor per pixel to allow an immediate internal amplification before routing the signal to a separate readout chip. This *semi-monolithic* technology is used in the pixel detector of the current vertex detector of the Belle II experiment [48]. Utilizing the *silicon-on-insulator* (SOI) technology, a micrometer thick silicon-oxide insulating layer separates the active front-end electronics from the high-resistivity passive sensor volume and functions as shielding of potential cross-talk [49]. The connection between the different layers is established by vertical connections through the insulator.

The concept of exploiting commercial CMOS technologies without an additional insulating layer proves to be very popular due to the potential for low-cost and high-throughput production. In this case, additional highly doped (deep) wells shield the electronics from the sensitive volume to mitigate cross-talk between one another. It must be emphasized that MAPS are significantly more susceptible to cross-talk between front-end and sensitive volume making shielding of the electronics essential even at the expense of the individual optimization of each. Since the silicon substrate used for these technologies is typically of p-type, the collection electrode is realized as a strongly doped n-well. The complex in-pixel electronics are shielded by additional p-wells as other n-wells would distort the charge collecting electric field. The cross-section of a generic MAPS implementation is visualized in Figure 3.12. Such commercial manufactures commonly use low-ohmic substrate wafers onto which a $1-20$ µm thick, high-resistivity epitaxial silicon layer is grown [7]. This limits the generated signal amplitude and requires very little noise in the readout electronics to function efficiently. Some vendors also allow the production on custom, commercially unavailable high-resistivity wafers enhancing the signal charge generation at higher production costs. Both options were investigated and delivered successful results [50, 51]. Furthermore, early developments of MAPS were restricted in the maximum applicable bias voltage needed to deplete the sensitive volume, since the protection of the front-end electronics from these voltages is not trivial. Thus, the sensitive volume is only depleted close to the collection electrode and the charge collection is dominated by diffusion. Due to this, charge collection times are long, and such designs are prone to charge carrier trapping reducing the already small signal further after irradiation. This yields the technology particularly inappropriate for radiation-harsh environments with large particle rates or precise timing measurements. Nevertheless, for suited requirements, MAPS implemented in commercial CMOS technologies have been successfully operated in the field of high-energy physics [52] and further applications

[10] Studies on decreasing the achievable pixel pitch by adjusting the bump-bonding technique are ongoing [45] but are currently not in high demand in the field of high-energy physics.

[11] Depleted field-effect transistor

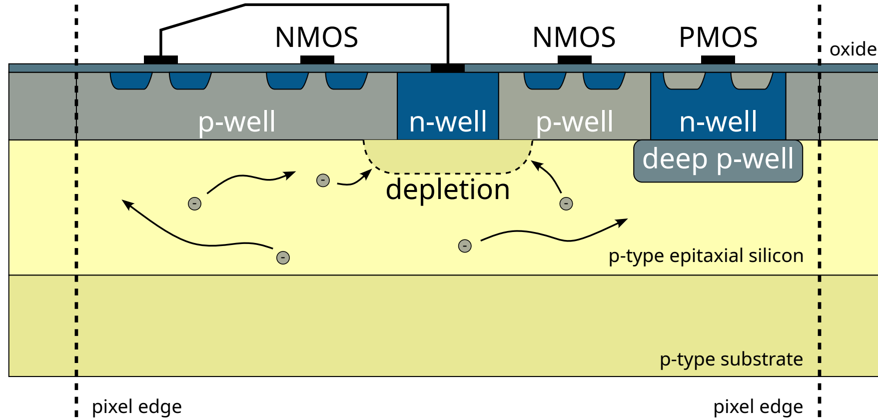

Figure 3.12: Cross-section of a monolithic active pixel cell. The complex front-end electronics are shielded by deep p-wells while a deep n-well functions as the charge collection electrode inside the p-type silicon substrate. Due to the small depleted volume, the charge collection relies significantly on diffusion. From [28].

are planned [53].

3.3.3 Depleted monolithic active pixel sensors

Increasing the depleted volume of MAPS to rapidly collect the entire charge signal by drift is essential to render monolithic pixels viable for high-rate and high-radiation environments such as those faced in the LHC. Since the expansion d of the depletion zone depends not only on the external voltage but also on the resistivity ρ of the silicon substrate (see also Section 3.1.2) [7]

$$d \propto \sqrt{\rho V_{\mathrm{ext}}} \quad \text{for} \quad V_{\mathrm{ext}} \gg V_{\mathrm{bi}} \quad , \tag{3.26}$$

there are two possible adjustments for enhancing the initial concept by the desired effect: The use of the aforementioned custom high-resistivity wafer substrates and the capability of applying external voltages to the substrate which are larger than the usually allowed $\leq 3.3\,\mathrm{V}$ in CMOS technologies. Both strategies were pursued (also in combination) [54, 55] and modern developments achieve a substrate resistivity of $1-10\,\mathrm{k\Omega\,cm}$ and high voltage capabilities up to $10-500\,\mathrm{V}$ depending on manufacturer, sensor design, and target application. Such depleted monolithic active pixel sensors (DMAPS) yield similar signals amplitudes and fast charge collection times compared to conventional hybrid pixel detectors at lower material budgets. In addition, the benefits of using commercial CMOS technologies and the non-necessity of complex interconnection techniques generates a low-cost alternative to the hybrid pixel design. However, the monolithic approach loses the advantage of separately optimizing both readout ASIC and sensor chip as described in Section 3.3.2. This poses a considerable challenge when trying to achieve the same radiation hardness of state-of-the-art hybrid pixel detectors in particular.

Many prototypes and demonstrators have been developed over the recent years [54, 56–59] which can generally be divided into two design concepts:

- **Large-collection-electrode** designs fully integrate the front-end electronics inside the deep n-well charge collection electrode that covers nearly the entire pixel area.
- **Small-collection-electrode** designs utilize small charge collection electrodes compared to the pixel size which requires the separation of the electronics inside deep-p wells at the pixel edges.

Both design concepts experience performance trade-offs which are optimized specific to their application. The small collection electrode yields a lower detector capacitance C_d and, thus, facilitates low-noise operation and fast signal processing. In contrast, a large collection electrode ensures a more homogeneous electric field across the sensitive volume improving the prerequisites for radiation hardness. A more detailed discussion of both design concepts is given in the following.

Large-collection-electrode design

As the name implies, this design utilizes a large collection electrode of similar size as the pixel in which all in-pixel electronics are implemented. The charge collection electrode is implanted very deep (up to 20 µm) within the substrate ensuring enough space for electronics and shielding. Typically, high-resistivity p-substrate wafers are chosen in which the collection electrode is realized as n-type implant, although other configurations are also available. The schematic cross-section of a generic pixel cell with large collection electrode is shown in Figure 3.13. The realization of CMOS electronics within the collection electrode requires an additional deep p-well layer to isolate the n-wells of PMOS transistors from the very deep n-well. Furthermore, the proper shielding of the readout electronics is extremely important to prevent possible cross-talk into the collection electrode in this design approach. The external bias voltage to deplete the sensitive volume is either applied through a vertical connection from the topside or through a backside contact to the p-type substrate. The latter requires backside metallization of the wafer, which poses an additional processing step. The collection electrode stays at or close to ground depending on coupling from voltages supplied to the in-pixel electronics. Additional p-type implants in between the collection electrodes improve the electric field shaping in the pixel edges and separate the individual pixels from each other.

Due to the large fill factor, a uniform electric field and short drift distances across the entire sensitive volume are facilitated and reduce charge trapping probabilities after irradiation. Thus, large-collection-electrode designs naturally have a higher radiation tolerance than their counterpart designs. This can be enhanced by providing high breakdown capabilities through design that ensure full depletion and high charge collection efficiency even after irradiation. Dedicated guard ring designs achieve breakdown voltages of several 100 V and are implemented in modern

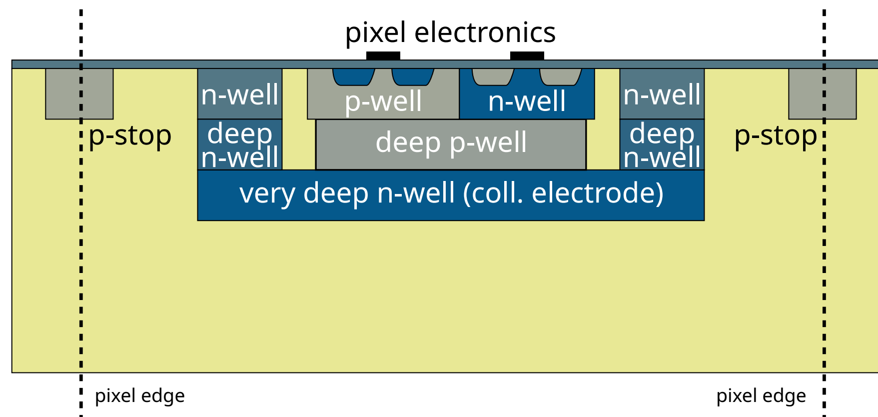

Figure 3.13: Cross-section of a depleted monolithic active pixel cell designed with a large collection electrode. All front-end electronics are located inside the deep n-well collection electrode close to the size of the pixel pitch. Deep p-wells shield the electronic from cross-talk into the collection electrode. Individual pixel cells are separated by p-stop implants which also direct the electric field in the inter-pixel region towards the pixel center. Typically, the external bias voltage is applied at the back of the substrate requiring backside metallization. From [28].

DMAPS prototypes [60]. However, the sheer size of the collection electrode combined with the additional capacitance created by the neighboring very deep n-well and deep p-well implants result in a very large detector capacitance in the order of several 100 fF [61]. This is larger than typical equivalents of modern planar hybrid pixel sensors and induces an increase in noise and a decrease in timing performance of the signal readout [7]. Typically, this disadvantage is compensated by increasing the power of the readout electronics, which in return requires better cooling and consequently adds to the material budget. Furthermore, minimizing the pixel size in this design is complicated since all in-pixel electronics are placed within the charge collection electrode and require sufficient shielding. To achieve pixel pitches close to $50\,\mu\text{m} \times 50\,\mu\text{m}$, in-pixel electronics would have to be reduced[12]. Efforts to develop a high-granularity DMAPS with such pixel pitches and a large collection electrode are pursued by the RD50 collaboration [62].

Small-collection-electrode design

In this design approach, the charge collection electrode is small compared to the pixel size which makes it unfeasible to place all in-pixel electronics within the electrode. Consequently, the in-pixel electronics are separated and placed at the pixel edges. In contrast to the MAPS design, the CMOS electronics are not placed directly next to the collection electrode to mitigate coupling between the two due to larger bias voltages. As in the other design approach, the n-type charge collection electrode is implanted into the high-resistivity p-type substrate. The latter is

[12]Alternatively, the use of smaller technology feature sizes would allow to implement the same amount of transistors in less space. However, smaller technologies are significantly more expensive, differ in radiation tolerance (especially with respect to single event effects), and may not be open to customization (e.g. high-resistivity wafer substrates).

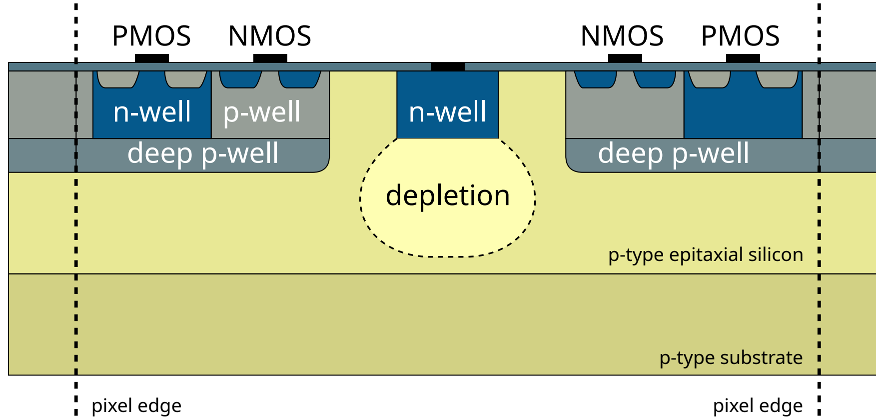

Figure 3.14: Cross-section of a depleted monolithic active pixel cell designed with a small collection electrode. The front-end electronics are placed in the pixel edges and separated from the small n-well collection electrode relative to the pixel size. Deep p-wells shield the electronics from the sensitive material and prevent distortions of the electric field in the sensitive volume due to the n-well transistor substrates. Typically, the external bias voltage is applied through the p-type substrate. From [28].

again used as contact for the external bias voltage. Figure 3.14 illustrates a generic pixel cell of the small-collection-electrode design. Here, the additional deep p-wells at the pixel edges not only shield the electronics but also permit the use of PMOS transistors without introducing distortions of the electric field. However, this geometry limits the applicable bias voltage since the deep p-wells for shielding must be at a similar potential as the substrate (typically within 1 V) to prevent punch-through. If the applied voltage exceeds the permissible range of the electronics, the transistors will be irreversibly destroyed. Due to the difference in boundary area, the small collection electrode restricts the growth of the depletion zone to less than 50 µm [28] compared to the large-collection-electrode design. Thus, the use of high-resistivity epitaxial silicon with a maximum thickness of 25 – 30 µm grown on low-ohmic substrate is sufficient.

As no additional shielding between the small collection electrode and electronics is required, this design approach benefits from a very small detector capacitance of only a few 1 fF. Considering the dependency between generated voltage signal dV and detector capacitance C_D [7]

$$dV = \frac{dQ}{C_\mathrm{D}} \tag{3.27}$$

for the generated charge dQ, voltage amplification is well suited for this design and compensates the small charge signal available due to the restricted depleted volume. In addition, the small detector capacitance reduces noise facilitating very high signal-to-noise ratios and enhances the timing performance of the detector. Contrary to the large-collection-electrode design, the long drift distances towards the small collection electrode make the design prone to charge carrier trapping. The challenging electric field shaping especially in the pixel corners due to the relatively large distance to the collection electrode enhances this impairment. Studies have shown

that this becomes particularly problematic after irradiation and supplementary modifications to the pixel cell are required [63], which is discussed in more detail in Section 5.2. Since the more complex biasing conditions cannot always guarantee full depletion of the sensitive volume, a part of the charge collection may also rely on diffusion. The aforementioned challenges are more severe for larger pixel sizes due to increasing distances within a pixel cell. Thus, small pixel pitches of, typically, less than 50 µm are advantageous making the small-collection-electrode design well suited for high-granularity and timing applications.

3.4 Application of DMAPS in high-energy physics experiments

In the context of the high-luminosity LHC upgrade, the ATLAS experiment considered the deployment of DMAPS developments in the new tracking detector [64]. This energized the ongoing advancements of verifying radiation hard monolithic pixel detectors with high-rate capabilities. More specifically, DMAPS were proposed as an option for the outermost layer of the ATLAS Inner Tracker (ITk) barrel region. The environment of this layer requires radiation tolerance up to $1.5 \times 10^{15}\,\mathrm{n_{eq}\,cm^{-2}}$ non-ionizing energy loss (NIEL) fluence and 100 Mrad total ionizing dose (TID) as well as high-rate capabilities up to $2\,\mathrm{MHz/mm^2}$. Furthermore, the detector must comply with the available power budget of $0.7\,\mathrm{W/cm^2}$ while being equipped with a readout architecture that is fast enough for the 40 MHz bunch-crossing frequency of the ATLAS experiment [64–66]. As part of this progress, a dedicated CMOS collaboration realized multiple DMAPS prototypes based on several CMOS technologies and different design concepts, including the Monopix development lines [64]. Although the different prototypes produced promising results, it was decided against integrating DMAPS in the ATLAS ITk as the developments were not yet mature enough.

However, DMAPS are already a well-suited technology to be used in high-precision lepton collider experiments. Since leptons are elementary particles, the generation of wanted production channels can be controlled much more accurately and is affected by fewer extremely dense hadronic background events. Furthermore, lepton colliders produce less pileup[13] per event compared to hadron colliders such as the LHC. Both facts imply that the detector system receives significantly less hit-rate and total radiation, which additionally simplifies the event reconstruction and complexity substantially. This considerably eases the requirements for the pixel detector on both radiation tolerance and time resolution. In return, the detector systems of lepton experiments require an extremely high spatial resolution for vertex reconstruction. Thus, the material budget of the corresponding tracker must be reduced to a minimum, such that the track of a traversing particle is barely distorted by multiple scattering effects (see Section 2.3). This is especially important for low momenta particles. It favors the application of thinner monolithic pixel detectors, while also imposing challenges on the power consumption

[13] Pileup describes the number of collisions within a single bunch-crossing as particles are accelerated in bunches to increase the collision probability.

Requirements	ATLAS ITk[14]		Belle II	Mu3e
	Inner	Outer	VTX	Phase I
Integrated luminosity in fb^{-1}	2000	4000	50 000	N/A
Material budget in $\%\chi_0$ / layer	0.67		0.2 – 0.7	0.1
Time resolution in ns	25		25 – 100	< 20
Total ionizing dose in Mrad	1000	100	100	N/A
NIEL fluence in $n_{eq}\,cm^{-2}$	1×10^{16}	$2 - 5 \times 10^{15}$	5×10^{14}	$< 1 \times 10^{13}$
Power consumption in mW/cm^2	≤ 700		≤ 200	≤ 350

Table 3.1: Requirements to the silicon tracking detector of multiple planned experiments and upgrades. The Belle II experiment expects a run time of five years for the VTX upgrade. Some information on the Mu3e experiment could not be found and is marked with N/A. The data was collected from multiple sources [66–69] and this table was created to the author's best knowledge at the time.

since complex cooling systems contribute to the overall material budget. A comparison between different high-energy physics experiments and their requirements for the tracking detector is given in Table 3.1. Here, the hadronic dominated ATLAS ITk environment [66] is compared to two lepton collider experiments: the Belle II VTX upgrade [67] and the Mu3e experiment [69]. Most notable is the extremely high radiation tolerance required by the ATLAS ITk environment while it is almost negligible in the case of Mu3e. Since ATLAS ITk also demands good timing and tracking resolution, compensation by a relaxed limit on the power consumption is inevitable, which increases the material budget due to the necessary cooling. In contrast, the lepton collider experiments pose much stricter requirements on the material budget and power consumption. While hadron collider experiments must prioritize the radiation tolerance of the tracking detector, lepton collider experiments focus on the vertexing performance by minimizing the material budget. For now, the latter is the better suited application of DMAPS. As part of the Belle II VTX upgrade, a new DMAPS named OBELIX [70] is being developed that is based on the TJ-Monopix2, which is partly characterized in this thesis.

[14] The ATLAS ITk requirements with respect to radiation hardness include a 1.5 safety factor.

4 Radiation damage in semiconductors

This chapter contains an overview of radiation damage relevant for the application of semiconductors as particle detectors. In this context, radiation damage can be categorized into the deterioration of the passive sensitive detector volume or the active readout electronics. The degradation of the passive silicon bulk and its properties for particle detection is discussed in Section 4.1. Further, Section 4.2 describes the underlying effects and challenges faced when active MOS devices are operated under exposure to radiation. In addition, traversing (heavy) particles can disrupt the electronic circuit operation or alter stored information. These phenomena are referred to as single event effects [71]. However, such single event effects are not relevant for this work and are only mentioned for the sake of completeness.

4.1 Bulk damage

Non-ionizing radiation leads to the displacement of atoms from the lattice structure and, consequently, changes in electrical properties of the material. Furthermore, this radiation induced alteration of the silicon bulk affects macroscopic sensor properties such as the bulk leakage current or the effective doping concentration [71]. Thus, the sensing capabilities of silicon deteriorate with increasing radiation exposure. The amount of non-ionizing energy loss (NIEL) depends on the impinging particles type and energy.

4.1.1 Displacement damage

Incoming high energy particles interact with the atoms in the silicon bulk which can cause the displacement of a primary knock-on atom (PKA) from the crystal creating point-like defects in the lattice structure. Such initial defects consist of a vacancy at the position of the PKA and an atom in an interstitial position (typically referred to as an interstitial). Thus, this process distorts the crystalline lattice structure which defines the name of displacement damage. The created interstitials and vacancies become mobile within the silicon lattice for temperatures above 150 K [72] and can form more complex point-like defects upon combination with other impurities[1] in the silicon. An overview of common point-like defects such as vacancies and interstitials of silicon or impurities are shown in Figure 4.1. The combination of a silicon interstitial with the corresponding vacancy is defined as Frenkel pair. However, a significant

[1]Typical impurities that are introduced to the silicon through its growing process are oxygen and carbon.

fraction of point-like defects already recombine instantly after their production which prevents them from contributing to long-term bulk damage [73]. Furthermore, the recovery of existing bulk damage can be stimulated by increased temperature, which is efficiently exploited in so-called annealing (see Section 4.1.4).

In silicon, a minimum recoil energy of approximately 25 eV is required to knock an atom out of its lattice structure [74]. If the PKA receives sufficient energy from the initial collision, additional interactions of the PKA with the lattice leading to further displacements are possible. The localized loss of large energy amounts through several interactions (either from the impinging particle or subsequently from the PKA) and the resulting multiple displacement defects are referred to as a cluster. Given the non-relativistic relation of the maximum recoil energy

$$E_{\mathrm{R,max}} = 4E_{\mathrm{particle}} \frac{m_{\mathrm{particle}} \cdot m_{\mathrm{Si}}}{(m_{\mathrm{particle}} + m_{\mathrm{Si}})^2} \tag{4.1}$$

transferred through the collision of an incoming particle with mass m_{particle} to the PKA, a threshold energy of around 5 keV for the production of clustered defects can be estimated. In addition to the energy of the incoming particle, its type can also favor either point-like or clustered defects[2], although this preference is balanced by secondary interactions of the PKA [36, 75]. Both, point-like and clustered defects, contribute to the total bulk damage in silicon and result in macroscopic property changes [76].

4.1.2 NIEL hypothesis and hardness factor

Since bulk damage depends on the incoming particle's type and energy, a method for standardizing and comparing displacement damage from different types of radiation is required. The NIEL hypothesis accomplishes this by making the assumption that the induced radiation damage scales linearly with the amount of NIEL irrespective of the spatial displacement distribution of PKA relative to the energy of the particle [77]. However, the NIEL hypothesis is only an approximation and the underlying physical processes have yet to be fully understood at a microscopic level [75, 78]. To calculate the NIEL, several variables need to be considered:

- The cross-section $\sigma_\nu(E)$ of an interaction between an incoming particle with the energy E and an atom in the silicon bulk
- The probability $f_\nu(E, E_{\mathrm{R}})$ of generating a PKA with a certain recoil energy through this interaction
- Possible additional NIEL causing interactions of a PKA with a given recoil energy represented by the *Lindhard partition function* $P(E_{\mathrm{R}})$ [79]

[2] Since charged particles scatter via electromagnetic interaction with the nuclei, which is partially screened by their electron clouds, they are more likely to produce point-like defects. Neutrons instead are not affected by the electromagnetic interaction and, thus, have a higher chance of producing clustered defects compared to charged particles.

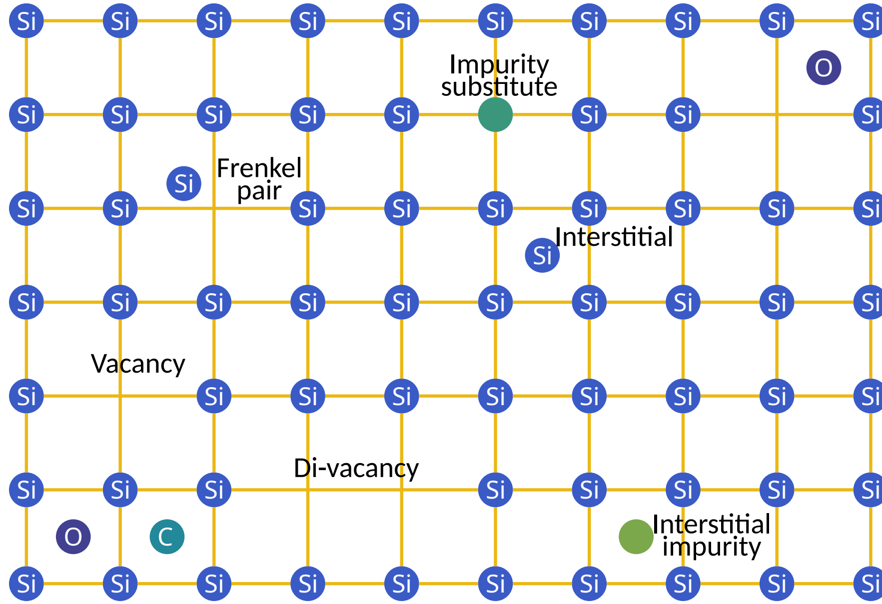

Figure 4.1: Exemplary overview of point-like defects in the silicon lattice generated by displacement damage. The combination of a silicon interstitial and a corresponding vacancy is referred to as *Frenkel pair*. Furthermore, impurities can substitute a lattice atom or form additional interstitials. A more complex point-like defect called Di-vacancy consists of two adjacent vacancies. Adapted from [76].

With these considerations, the total displacement damage cross-section [76]

$$D(E) = \sum_{\nu} \sigma_\nu(E) \cdot \int_0^{E_{\mathrm{R,max}}} f_\nu(E, E_\mathrm{R}) P(E_\mathrm{R}) dE_\mathrm{R} \tag{4.2}$$

can be calculated by taking the sum over all potential interactions ν between the incoming particle and the silicon lattice leading to a displacement damage.

Finally, the hardness factor κ is introduced to compare the induced damage across different particle types and energy spectra. Within high-energy physics, NIEL damage is standardized to the equivalent fluence of 1 MeV neutrons with a displacement damage cross-section of $D(E_\mathrm{n} = 1\,\mathrm{MeV}) = 95\,\mathrm{MeV\,mb}$. Hence, the hardness factor [76]

$$\kappa = \frac{\int D(E)\Phi(E)dE}{95\,\mathrm{MeV\,mb} \cdot \Phi} = \frac{\Phi_\mathrm{eq}}{\Phi} \tag{4.3}$$

is defined by the ratio between the irradiation fluences of a given particle and energy spectrum and the 1 MeV neutron equivalent. Here $\Phi = \int \Phi(E)dE$ denotes the irradiation fluence of an energy spectrum $\Phi(E)$. The 1 MeV neutron equivalent fluence Φ_eq is measured in units of $\mathrm{n_{eq}\,cm^{-2}}$. It must be emphasized that point-like and clustered defects affect certain sensor properties differently, which is not yet accurately accounted for within the NIEL hypothesis [77].

Since irradiation facilities rely on complex systems, the energy spectra and beam conditions

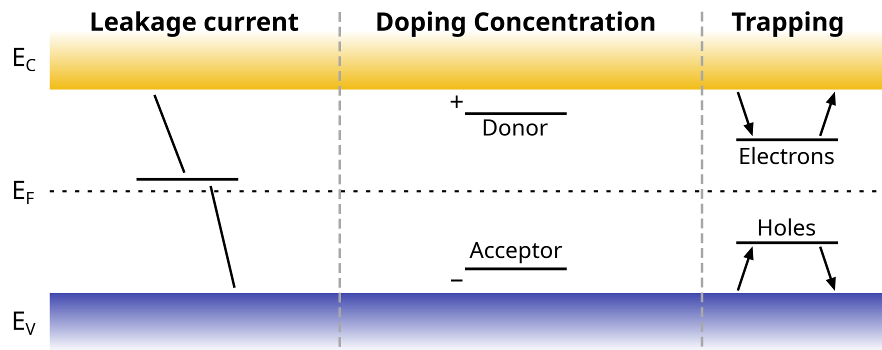

Figure 4.2: NIEL induced defect levels and their location within the silicon band gap. The affected detector properties are featured above. Defect states close to the Fermi level facilitate the transition from valence into conduction band and, thus, increase the leakage current. Deeper level defect states (i.e. energy levels within the band gap but not as close to the Fermi level) act as charge traps, which can distort the charge collection in case of sufficiently long trapping duration. Charged defect levels close to the valence or conduction band effectively function as acceptors or donors respectively and alter the effective doping concentration. Adapted from [76].

are custom properties requiring a separate hardness factor calibration per site [80]. Ideally, the calibration is repeated before each beam time to ensure accuracy of the irradiation.

4.1.3 Impact on detector properties

In general, radiation damage is uniformly distributed across the silicon bulk and generates energy levels in the band gap referred to as defect states. These radiation induced defects are categorized into three main types affecting different properties of the silicon sensor which are summarized in Figure 4.2. Considerations regarding the impact of each defect type are based on the Shockley-Read-Hall statistics discussed subsequently. Defect states close to the middle of the band gap act as generation-recombination centers and effectively increase the leakage current in the silicon bulk. The formation of charged defect states close to either the valence or conduction band, which effectively act as acceptors or donors respectively, impacts the effective doping concentration and space charge. Furthermore, charge carriers can get trapped in defect states. If the trapping duration exceeds the detector electronic characteristics, the charge appears to have been lost and the charge collection efficiency decreases. A qualitative description of the underlying statistical process behind the defect properties is given by the Shockley-Read-Hall statistics [81, 82].

Shockley-Read-Hall statistics

The model comprises only single energy level defects and their interaction with the conduction and valence band on a statistical basis. Based on the Fermi-Dirac statistics, the probability

that a quantum state of the energy E is occupied is given by [81]

$$f(E) = \frac{1}{1 + \exp[(E - E_\mathrm{F})/k_\mathrm{B}T]}\,, \tag{4.4}$$

where E_F is the Fermi level, k_B the Boltzmann constant, and T the temperature. Within the model, only a total of four interactions with a defect state are taken into consideration [7]:

- The **emission of a trapped electron** into the conduction band. The corresponding emission rate $R_\mathrm{e}^\mathrm{em} = \epsilon_\mathrm{e} \cdot N_\mathrm{t} \cdot f(E_\mathrm{t})$ depends on the defect state concentration N_t and the probability of a trap at the energy E_t to be occupied by an electron.
- The **capture of an electron** from the conduction band in a non-occupied defect state. In addition to the defect state concentration and the corresponding occupation probability, the capture rate $R_\mathrm{e}^\mathrm{cap} = c_\mathrm{e} \cdot n \cdot N_\mathrm{t} \cdot (1 - f(E_\mathrm{t}))$ is affected by the number of free electrons n.
- The **emission of a trapped hole** into the valence band, which is equivalent to the capture of an electron from the valence band. Analog to the electron emission, the hole emission rate is defined as $R_\mathrm{p}^\mathrm{em} = \epsilon_\mathrm{p} \cdot N_\mathrm{t} \cdot (1 - f(E_\mathrm{t}))$.
- The **capture of a hole** from the valence band in a non-occupied defect state, which is equivalent to the emission of an electron into the valence band. Similarly, the number of free holes p in the valence band and the defect state concentration and their occupation probability by electrons determine the capture rate $R_\mathrm{p}^\mathrm{cap} = c_\mathrm{p} \cdot p \cdot N_\mathrm{t} \cdot f(E_\mathrm{t})$

The proportionality factors of the above equations are defined as emission $\epsilon_\mathrm{e/p}$ and capture $c_\mathrm{e/p}$ coefficients. The capture coefficients are given as the product of the thermal velocity of the charge carrier v^th and its capture cross section σ^cap:

$$c_\mathrm{e} = v_\mathrm{e}^\mathrm{th} \cdot \sigma_\mathrm{e}^\mathrm{cap} \quad \text{and} \quad c_\mathrm{p} = v_\mathrm{p}^\mathrm{th} \cdot \sigma_\mathrm{p}^\mathrm{cap} \tag{4.5}$$

Additionally, the *principle of detail balancing* requires that capture and emission rates must be equal within a thermal equilibrium state [81].

Leakage current

An increase in bulk leakage current is one of the main challenges imposed by bulk damage to the detector. Radiation induced defect levels close to the middle of the band gap effectively facilitate the current generation as the defect state enables a two-step transition from valence to conduction band or vice versa requiring less thermal energy per transition. Utilizing the Shockley-Read-Hall statistics, the occupancy of a defect can be approximated to [77]

$$f_\mathrm{t} = \frac{c_\mathrm{e} \cdot n + \epsilon_\mathrm{p}}{c_\mathrm{e} \cdot n + \epsilon_\mathrm{p} + c_\mathrm{p} \cdot p + \epsilon_\mathrm{e}} \approx \frac{\epsilon_\mathrm{p}}{\epsilon_\mathrm{e} + \epsilon_\mathrm{p}} \tag{4.6}$$

in the case of thermal equilibrium and a negligible amount of free charge carriers, such as given in the depleted region of a detector. Based on these assumptions, the generation rate of an individual trap type

$$G_{\mathrm{t}} = N_{\mathrm{t}} f_{\mathrm{t}} \epsilon_{\mathrm{e}} = N_{\mathrm{t}} \frac{\epsilon_{\mathrm{e}} \epsilon_{\mathrm{p}}}{\epsilon_{\mathrm{e}} + \epsilon_{\mathrm{p}}} \tag{4.7}$$

can be expressed simply by the trap density and the fraction of emission rates. Finally, the total leakage current of a detector with volume V is obtained by summing over all defect types [77]

$$I = eV \sum_{\mathrm{defects}} G_{\mathrm{t}} = eV \sum_{\mathrm{defects}} N_{\mathrm{t}} \frac{\epsilon_{\mathrm{e}} \epsilon_{\mathrm{p}}}{\epsilon_{\mathrm{e}} + \epsilon_{\mathrm{p}}} \tag{4.8}$$

where e denotes the elementary charge.

Furthermore, the increase in leakage current scales according to the NIEL hypothesis for hadron damage

$$I_{\mathrm{leak}} = I_{\mathrm{leak}}^{\Phi=0} + \alpha \Phi_{\mathrm{eq}} V \tag{4.9}$$

and increases linearly with the equivalent fluence. The introduced proportionality factor α is defined as the *current-related damage rate*, which is largely independent of bulk material properties or particle type and energy of the irradiation [83]. However, the *current-related damage rate* depends on the intrinsic charge carrier density n_{i} and, therefore, on the measurement temperature and annealing routine (see Section 4.1.4) [36]. The increase in bulk leakage current leads to a higher noise rate (shot noise) in the readout amplifier as well as higher power consumption [72]. Since the leakage current scales exponentially with temperature, irradiated devices hold an increased risk of experiencing a fatal thermal runaway due to continuously growing temperature and leakage current. Hence, cooled operation of irradiated devices is a practical solution or even essential.

Effective doping concentration

For non-irradiated silicon, the doping concentration is controlled by the density of impurities in the lattice structure (see Section 3.1). However, radiation induced defect states act as electrically active donor-like states when located in the upper half or acceptor-like states in the lower half of the band gap [76]. Thus, they impact the effective doping concentration. In addition, the removal of donor or acceptor atoms[3] as a result of bulk damage changes the space charge during irradiation [7]. When neglecting free charge carriers[4], the effective space charge of an irradiated device is given by the sum over all donors and acceptors as well as all donor-like and acceptor-like defect states [77]:

$$N_{\mathrm{eff}} = \sum_{\mathrm{donors}} (1 - f_{\mathrm{t}}) N_{\mathrm{t}} - \sum_{\mathrm{acceptors}} f_{\mathrm{t}} N_{\mathrm{t}} \tag{4.10}$$

[3]The initial impurity either interacts with a mobile defect or is knocked out of the lattice structure and captured by another interstitial. In both cases, the impurity becomes electrically neutral and does not contribute to the space charge anymore.

[4]Under reverse bias conditions, it can be assumed that all free charge carriers are swept away.

Consequently, bulk damage alters the electric field distribution across a silicon device and, thus, leads to a shift in the depletion voltage. Depending on the initial doping concentration, this radiation induced change in space charge either enhances or counteracts the initial configuration. In the case of n-type silicon, the removal of donors combined with the generation of acceptor-like defect states can even lead to an effective type inversion for large enough fluences [84]. Moreover, the change in effective doping concentration depends on the irradiation particle type and energy as well as bulk properties such as oxygen content[5]. Thus, it does not scale according to the NIEL hypothesis [77].

In general, the change in effective space charge and doping concentration after irradiation to high fluences of $\mathcal{O}(1 \times 10^{15}\,\mathrm{n_{eq}\,cm^{-2}})$ requires larger bias voltages[6] to fully deplete the silicon bulk. At very high fluences $\geq 5 \times 10^{15}\,\mathrm{n_{eq}\,cm^{-2}}$, reaching full depletion of a planar sensor is typically no longer feasible [7].

Charge carrier trapping

The signal creation in the detector depends on the charge carrier propagation through the depleted volume and its duration (see Section 3.2.1). Radiation induced defect levels can trap charge carriers for a characteristic trapping time and, thus, decrease the effective charge carrier mobility. If the trapping time is long compared to the typical readout time of the detector or the trap density within the bulk is very high, charge carriers generated by ionizing radiation may not be detected by the device. Thus, the overall signal will be reduced. This loss is generally quantified as the *charge collection efficiency* [7]

$$CCE \approx \frac{Q_{\mathrm{det}}}{Q_{\mathrm{ion}}} \tag{4.11}$$

where Q_{det} describes the detected charge while Q_{ion} is the actually generated charge.

The trapping time τ of an individual charge carrier is given by its inverse capture rate

$$\tau_{\mathrm{e}} = \frac{1}{c_{\mathrm{e}} \cdot N_{\mathrm{t}}(1 - f(E_{\mathrm{t}}))} \quad \text{and} \quad \tau_{\mathrm{p}} = \frac{1}{c_{\mathrm{p}} \cdot N_{\mathrm{t}} \cdot f(E_{\mathrm{t}})} \tag{4.12}$$

Therefore, the effective trapping probability [77, 85]

$$\frac{1}{\tau_{\mathrm{eff}}} = \sum_{\mathrm{defects}} \left(\frac{1}{\tau_{\mathrm{e}}} + \frac{1}{\tau_{\mathrm{p}}} \right) = \sum_{\mathrm{defects}} \left(R_{\mathrm{e}}^{\mathrm{cap}} + R_{\mathrm{p}}^{\mathrm{cap}} \right) \tag{4.13}$$

is defined as the sum of the inverse trapping time over all defect states and charge carrier types. Furthermore, NIEL scaling applies to the effective trapping probability as it increases linearly with the equivalent fluence [85]. Charge carrier trapping becomes increasingly relevant for large

[5] The capture of displaced boron atoms by oxygen interstitials and the subsequent formation of a boron-oxygen interstitial complex is a typical acceptor removal process [7].

[6] For a 100 µm thick silicon bulk with a resistivity of $\mathcal{O}(1\,\mathrm{k\Omega\,cm})$, typical bias voltages of $\mathcal{O}(100\,\mathrm{V})$ are required.

fluences $\geq 1 \times 10^{15}\,n_{eq}\,cm^{-2}$ and, combined with the increase in leakage current and change in effective doping concentration, eventually limits the use of silicon sensors [36, 76].

4.1.4 Annealing of bulk defects

Since defect states are not locally bound in the silicon lattice, they can interact with other defects and still alter the macroscopic detector properties over time. When migrating through the lattice structure, an interstitial can recombine with a vacancy or vice versa (Frenkel pair recombination). However, the defect can also fuse with further defects of the same or even different types to form a more complex, multi-constituent defect state [72]. If sufficient lattice vibrational energy is given, existing complex defects can even dissociate into their constituents and migrate through the bulk. Because the defects' mobility scales with temperature, this so-called annealing process is thermally activated and can be utilized to recover a part of the radiation induced displacement damage [76].

Overall, the impact of annealing to the detector properties comprises three contributions [7]: The stable component describes bulk damage that does not change over time after the irradiation. The beneficial component, which represents the recovery of part of the displacement damage, is dominant after relatively short annealing durations. Thus, it is often also referred to as *short-term* annealing. The *reverse annealing* component describes the degradation of detector properties due to activation of previously non-influencing defect states. Reverse annealing becomes dominant after long annealing times for instance several hours to days at 60 °C [7]. In addition to the intentional annealing after the irradiation, self-annealing of the device occurs already during irradiation [72].

A very important recovery achieved by annealing an irradiated device is the reduction of leakage current. Studies of the *current related-damage rate* for different annealing temperatures are summarized in Figure 4.3 and emphasize the temperature dependence of this process. Within the detector physics community, an annealing of 80 min at 60 °C is regarded as the standard procedure and yields a *current-related damage rate* of $\alpha_{80/60} = (3.99 \pm 0.03) \times 10^{-17}$ A/cm [83]. While further annealing will continue to reduce the *current-related damage rate*, it results in reverse annealing as it worsens other properties such as the effective doping concentration.

4.2 Surface damage

In contrast to the silicon bulk, the surface and interface regions of MOS devices are primarily sensitive to ionizing radiation. Defects in the silicon oxide (SiO_2) or the Si-SiO_2 interface region are categorized as surface damage [36]. Due to its already irregular structure, displacement damage has little effect on the silicon oxide [7]. When exposed to ionizing radiation, the intrinsic defects in the oxide and the Si-SiO_2 interface region of a MOS transistor interact with the created charge carriers and become electrically relevant. Two primary effects arise from surface damage

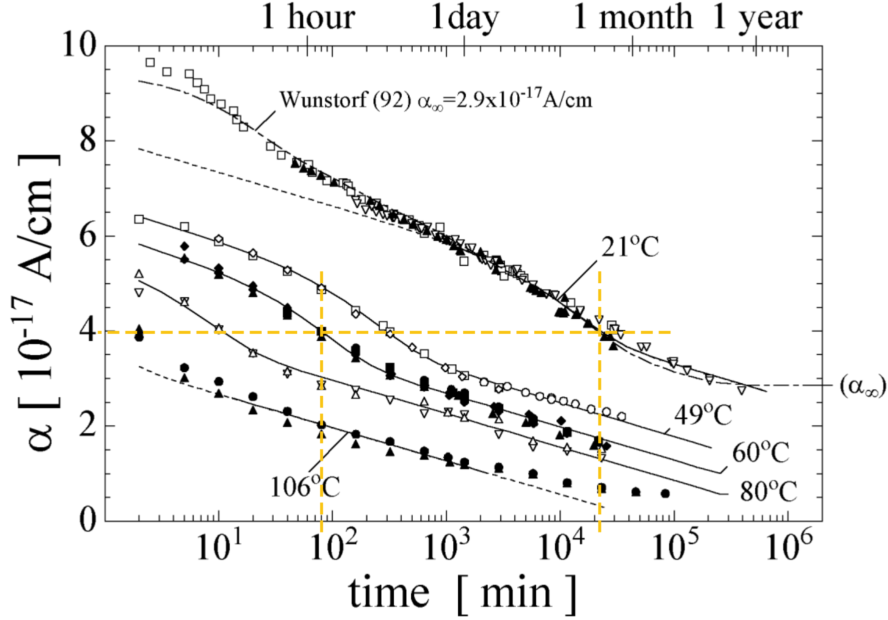

Figure 4.3: Studies of the *current-related damage rate* α for different annealing temperatures and accumulated annealing times. The common annealing procedures within the detector physics community are either 80 min at 60 °C or two weeks at room temperature (21 °C). The corresponding data points are highlighted. Modified from [72].

in MOS devices: positive charge buildup leading to a shift in the threshold voltage as well as an increase of the leakage current [86, 87].

The amount of ionizing energy loss (IEL) to which a device is exposed is typically quantified by the total ionizing dose (TID) measured in units of 1 rad = 0.01 Gy. Due to the large band gap of 8.06 eV in thermally grown SiO_2 on silicon, an average energy of (17 ± 1) eV is required for electron-hole pair creation [88]. Based on this value, the average amount of electron-hole pairs created per volume and TID can be calculated to 8.1×10^{12} pairs/cm^3/rad [86]. Charge carriers generated this way can subsequently lead to radiation-induced defects in MOS transistors which impair the functionality of the device.

4.2.1 Defect classification in silicon oxide

The exposure to radiation and IEL increases the electrical relevance of intrinsic defects and leads to the formation of further defects in silicon oxide. These (radiation induced) defects are categorized into five different types with distinctive characteristics. The naming convention of these defect types in MOS devices were fixed in [89, 90]:

- **Mobile ionic charges** are generated primarily due to ionic impurities such as Na^+ or K^+ in the oxidation process [89]. Measurements have shown that the generation density

of this defect is largest at the Si-SiO_2 interface for a MOS device [91]. As the name suggests, mobile ionic charges are freely moveable, and their mobility is enhanced by an applied electric field or increased temperature. Thus, they can influence the electrical characteristics of the device.

- **Oxide trapped charges** classify charge carriers that are trapped in the oxide bulk and do not interact electrically with the underlying silicon [90]. Depending on the type of trap and the type of the trapped charge carrier, the defect can contribute negatively or positively to the total space charge[7]. Apart from ionizing radiation, this defect type can also result from avalanche injection or similar processes [89].

- **Fixed oxide charges** describe structural defects in the oxide close to the Si-SiO_2 interface (less than 2.5 nm [89]). They result in deep hole traps which contribute positively to the total space charge upon trapping holes and do not interact electrically with the underlying silicon. The increased likelihood of intrinsic defects near the Si-SiO_2 interface explains the resulting higher concentration of fixed oxide charges in this region compared to the SiO_2 bulk.

- **Interface trapped charges (or interface traps)** are positive or negative charge states right at the Si-SiO_2 interface [86]. Since they interact electrically with the underlying silicon and have a continuous distribution of defect levels across the silicon band gap, charging or discharging of the traps is possible depending on the surface charge. Additional to radiation induced bond breaking processes, interface traps can originate from metal impurities or structural, oxidation induced defects [89]. They contribute either in form of traps as part of the oxide charge to the total space charge or in form of generation centers to leakage current.

- **Border traps** depict defects located within the oxide at a distance of up to 3 nm from the Si-SiO_2 or gate-SiO_2 interface [90]. Like interface traps, these traps interact electrically with the underlying silicon as they can exchange charge carriers with the silicon bulk via tunnelling. However, border traps differ from interface traps in the depth of the tunnelling process and their characteristic response time.

Figure 4.4 visualizes the different defect types and their location inside the extended interface region. In addition, the band structure of the SiO_2-Si interface and underlying physical processes behind the defect formation are illustrated in the same figure. A more detailed description of the formation mechanisms of the listed defects caused by IEL are explained in the following Section 4.2.2.

[7] E.g. a hole trap contributes as positive space charge upon trapping a hole

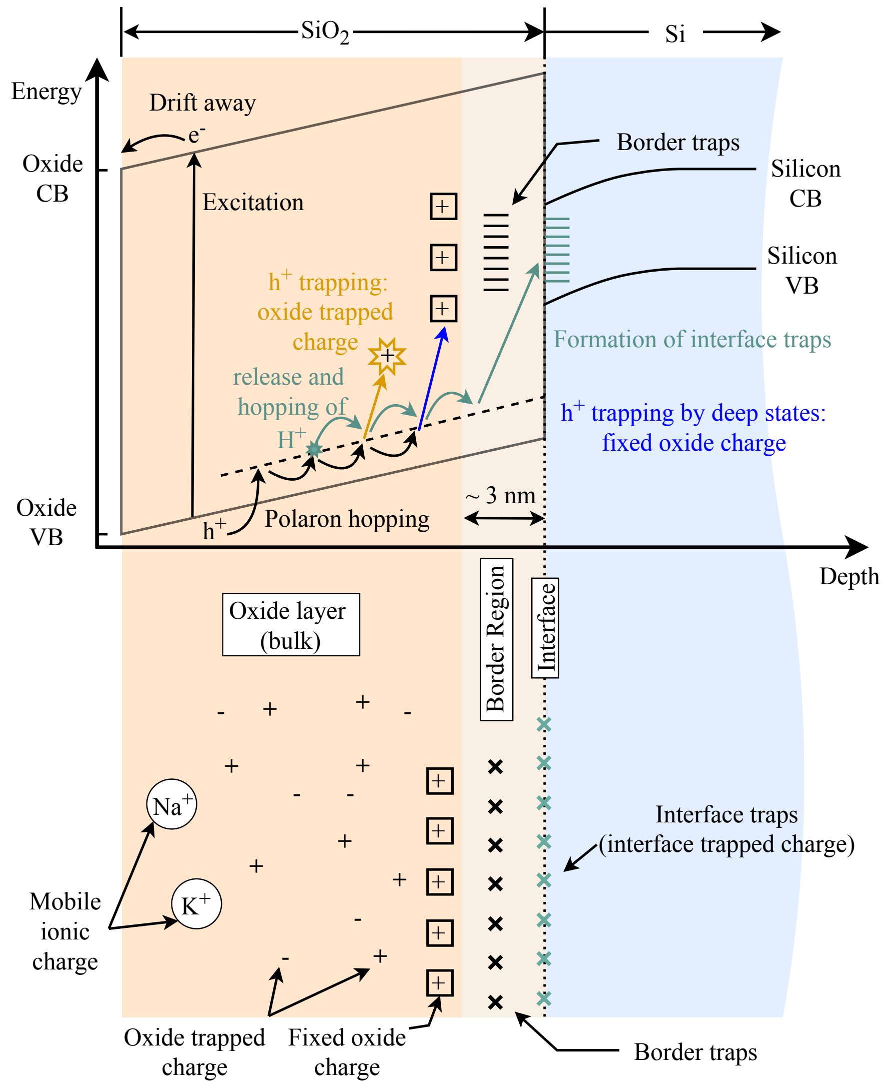

Figure 4.4: Visualization of IEL caused defects and their propagation in a MOS structure. The silicon oxide is represented by the orange area (left) whereas the silicon is shown in blue (right). The lower part of the figure illustrates the location of the different defect types inside the extended interface region. In the upper part, the physical processes behind the formation of the defects is displayed based on the energy band diagram of the SiO_2-Si interface region. From [60].

4.2.2 Formation mechanisms of radiation induced defects in MOS devices

The formation of surface damage depends on multiple steps including interaction of different defect types with each other, which have direct impact on the threshold voltage of the MOS device. The time-dependent change of the threshold voltage after a radiation pulse is shown in Figure 4.5 and highlights the individual contributions. In the following, the respective processes contributing to the formation are introduced.

Initial charge yield

Following the exposure to radiation and IEL, electron-hole pairs are created in the SiO_2 medium of a MOS transistor. If an electric field is applied, the charge carriers start to separate. Due to their high mobility in SiO_2, electrons are swept away on a picosecond timescale [92, 93] making them less relevant for the formation of surface damage. Yet, a fraction of the created charge carriers recombine immediately before the electric field can separate them. The amount of initial recombination depends on two factors: The strength of the applied electric field as well as the type and energy of the impinging particle [86, 87]. While the impact of the former factor is clear, the latter defines the spatial distance between individual electron-hole pairs created. This distance is important since closer or even overlapping charge carrier pairs are more likely to take part in the initial recombination. Promptly recombined charge carriers do not contribute to the formation of defects. However, holes that did not take part in the initial recombination remain near their point of creation and cause a (negative) threshold voltage shift of the transistor as shown by (1) in Figure 4.5. The initial charge yield describes the fraction of charge that escaped the initial recombination [86, 87].

Hole propagation

The process of hole propagation in SiO_2 is best modelled by the Continuous-Time Random Walk hopping transport formalism, which considers the time-dependent and stochastic nature of the process [86, 94, 95]. As the holes interact strongly with the SiO_2 medium, they create local lattice distortions in their immediate proximity that lead to self trapping of the holes. The coupled state of a hole with its lattice distortion increases the effective mass of the hole and deceases its mobility. This state is commonly referred to as a polaron in the context of solid-state physics [86, 87]. When propagating through the medium, the holes carry their local lattice distortion with them resulting in so-called *polaron hopping*.

The duration of hole propagation in SiO_2 is dependent on many factors and can vary by several orders of magnitude [86]. It is directly affected by temperature as temperatures above 140 K activated the propagation while it stays inactive for lower temperatures. Around room temperature, the process lasts seconds or less [86]. Furthermore, the hole propagation time depends on the oxide thickness of the transistor and is activated by applying an electric field [96]. Because of their slow propagation, excess holes in oxide bulk contribute to the positive space

charge, similar to the trapped holes which form oxide trapped charge. As the holes propagate, they cause a shift of the threshold voltage on the given timescale, which is considered as a recovery (see (2) in Figure 4.5).

Interaction of holes with Si-SiO_2 interface traps

The formation of deep hole traps originates from the incomplete oxidation in the Si-SiO_2 interface region. Vacancies of oxygen atoms in the standard SiO_2 lattice configuration lead to weak bonds between silicon atoms, while each silicon atom is back-bonded to three oxygen atoms [86]. Upon trapping of a positive charge carrier (hole), the weak Si-Si bond breaks and the lattice relaxes asymmetrically[8] [97]. These oxide trapped charges in the interface regions posses a (relatively) long-term stability as their annealing process is in the order of hours up to years. Their dominant annealing mechanisms are either tunnelling at around room temperature [98] or thermal excitation at sufficiently high temperatures [99] of electrons into the oxide to recombine with the trapped hole. The longevity of oxide trapped charges at the Si-SiO_2 interface generates a persistent negative threshold voltage shift as indicated by (3) in Figure 4.5 [86].

Radiation-induced interface traps at the Si-SiO_2 transition region

Exposure of MOS devices to radiation leads to the formation of interface traps in the Si-SIO_2 transition region, the energy levels of which lie within the silicon band gap. Although the formation mechanisms of these traps are not experimentally proven, several models have been proposed to explain this process. While all models converge on the assumption that the formation of interface traps is a secondary effect subsequent after radiation induced electron-hole pair creation, they can primarily be put into three categories [71]:

1. **Hydrogen based models**: The bond of a trivalent silicon atom in the Si-SiO_2 interface region to hydrogen is broken by a radiation induced process resulting in a *dangling* bond that acts as the interface trap.

2. **Injection based models**: An injected electron from the silicon or the oxide bulk recombines with a trapped hole in the transition region in such a way, that structural changes at the interface are caused, and an interface trap is created.

3. **Stress based models**: Stress at the Si-SiO_2 interface leads to strained Si-O bonds which are broken by radiation induced holes. The created oxygen defects mitigate towards the interface region and form interface traps upon reaching it.

Interface traps are amphoteric defects[9] consisting of a trivalent silicon atom that is bound to three other silicon atoms while the last bond extends into the oxide as an electrically active

[8]One silicon atom relaxes into a planar lattice configuration while the other remains in a tetrahedral lattice configuration.

[9]The interface state is negatively charged above, neutral close to, and positively charge below the Fermi-level within the energy regime.

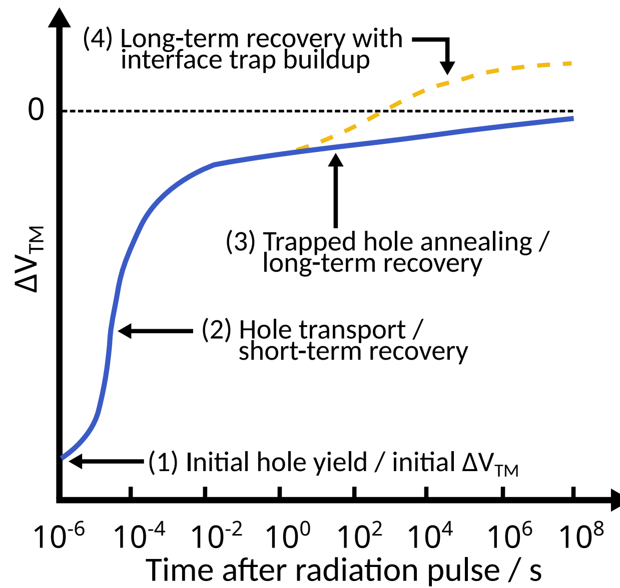

Figure 4.5: Schematically illustrated recovery of the threshold voltage of an n-channel MOS-transistor over time after an irradiation pulse. The initial threshold voltage shift arises from holes that escaped the instant recombination (1). The propagation of the holes in the SiO_2 results in a recovery of the threshold voltage shift within a very short time (2). Since holes are trapped in the process, a long-lasting threshold voltage shift of comparatively small amplitude remains (3). The build up and occupation of radiation-induced interface traps causes a further shift in threshold voltage, which can lead to additional recovery or even overshoot (4). Adapted from [86].

defect [86, 100]. The accumulation of such traps depends on the applied electric field to the transistor, where positive fields facilitate the build up while negative fields counteract it [71]. Since the occupancy of interface traps is regulated by the Fermi level as well as the applied electric field, they cause a voltage-dependent shift of the transistor threshold voltage [86]. This shift can lead to additional recovery or even overshoot of the threshold voltage as displayed by (4) in Figure 4.5. Furthermore, the density of created interface traps and trapped oxide charges (holes) are approximately equal and both share the same annealing characteristics [100].

4.2.3 Effect on electrical parameters of a MOS transistor

Surface damage affects the electrical properties of MOS devices and, thus, impacts its performance and lifetime. The effects on two of the most important properties, the threshold voltage and leakage current, are introduced in the following for the relevant technologies of this work.

Threshold voltage shift

Radiation induced defects directly affect the threshold voltages and, thus, the stable operation of transistors. The threshold voltage shift ΔV_{Thr} of a MOS transistor due to radiation damage

can be separated into the sum of shifts originating from interface traps V_{Int} and oxide trapped charges V_{Ox} [101]:

$$\Delta V_{\mathrm{Thr}} = V_{\mathrm{Int}} + V_{\mathrm{Ox}} \tag{4.14}$$

Trapped positive charges in the oxide form *quickely* during the irradiation and are already relevant for TID of a few (hundred) krad. The accumulation of trapped positive charges cause a threshold voltage shift proportional to the trapped charge density and their position relative to the Si-SiO_2 interface[10] [102]. Since oxide trapped charges are predominantly positive, they cause a negative threshold voltage shift independent of the transistor type. Due to the biasing difference in NMOS and PMOS transistors, this effect is more relevant for NMOS devices, as the radiation induced holes are sucked towards the Si-SiO_2 interface instead of the SiO_2-gate interface in the case of PMOS devices.

The formation of interface traps is a slower process with time compared to the formation of oxide trapped charges [102, 103]. Depending on the transistor type and its respective biasing, either negative or positive charges are caught in the interface traps. The trapping of negative charges in the case of NMOS transistors counteracts the threshold voltage shift due to oxide trapped charges resulting in a well-known rebound effect [102]. The exact TID at which the effect of the interface traps becomes dominant depends among other things on the technology feature size, the properties of the transistor (length and width), and the dose rate of the irradiation [102, 104]. Technology nodes of $100-200$ nm and dose rates of less than 1 Mrad/h relevant for this thesis report a peak in the threshold voltage shift between $1-10$ Mrad[102, 105–107]. In the case of PMOS transistors, positive charges are caught in the interface traps and add to the threshold voltage shift caused by oxide trapped charges [102]. Therefore, the shape of the total threshold voltage shift rises continuously instead of peaks with an increasing TID for PMOS compared to NMOS transistors.

Leakage current

Similarly to the threshold voltage of a transistor, its leakage current is also affected by radiation induced defects. The flow of additional leakage currents not only leads to a higher power consumption, but can cause complete failure of the device. There are two different formation mechanisms for a radiation induced increase in leakage current of a transistor.

The first type causes an increase in the gate leakage current observed at low electric fields close to and below the threshold voltage for ultra-thin gate oxides [87]. This leakage current is typically referred to as radiation induced leakage current (RILC) [108] and originates from trap assisted, inelastic tunnelling of electrons [87, 109]. The formation of radiation induced neutral electron traps in the oxide is necessary to allow electrons to first tunnel into these trap states and eventually into the gate. Due to the required tunnelling of electrons, this process is directly dependent on the oxide thickness [110]. The contribution of RILC becomes negligible for gate

[10] The closer the trapped charge is to the interface, the large the effective threshold voltage shift.

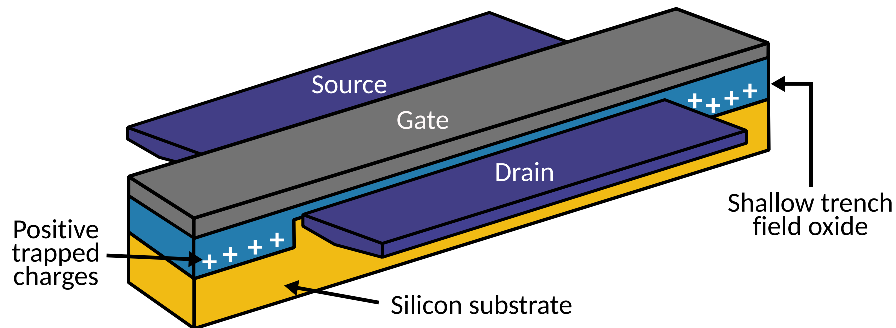

Figure 4.6: Schematic example of the positive charge accumulation within the field oxide of a transistor that leads to the build up of an inversion channel and, thus, parasitic currents. Adapted from [87].

voltages well above the threshold voltage of the transistor.

The second type is the formation of parasitic currents in the field oxide with increasing TID [104]. Based on the same principles as previously discussed, positive charges accumulate not only in the gate oxide of the transistor but also in the field oxide of isolation areas at the transistor edges. Isolation regions need to be considered as parasitic transistors with a significantly higher threshold voltage due to the large thickness of the field oxide. Radiation induced positive charges accumulate in the field oxide and cause a large shift in the threshold voltage of the parasitic transistor that eventually leads to an inversion channel and parasitic current flow from source to drain [87, 111]. A schematic illustration of the charge accumulation and its position within the transistor is given in Figure 4.6. This contribution is dominant at higher dose rates and larger TID and potentially becomes a failure mechanism of the transistor. In agreement with the threshold voltage shift, the leakage current of NMOS transistors also shows a peaking behavior with the total dose [102].

5 The Monopix chips

The Monopix chips are a realization of DMAPS designed and fabricated in commercial CMOS technologies for high-radiation and high-rate environments. There are two independent development lines, LF-Monopix and TJ-Monopix, comprising two iterations of designs named Monopix1 and Monopix2 each. As described in Section 3.4, they have been developed to comply with the requirements posed by the outermost layer of the ATLAS ITk pixel detector (see Table 3.1). Despite having the same application in mind, the development lines differ fundamentally in design approach and, thus, characteristic properties. The most recent versions, LF-Monopix2 and TJ-Monopix2, are large-scale monolithic demonstrators with fully integrated readout electronics within each pixel cell and a synchronous column-drain readout architecture, as described in Section 9.1. This chapter introduces both development lines in Section 5.1 and 5.2, while a focus is put on the latest iterations. In addition, the individual data acquisition (DAQ) systems for readout of and communication with each chip are presented in Section 5.3.

5.1 The LF-Monopix chips

The LF-Monopix development line is fabricated in the 150 nm LFoundry[1] CMOS imaging process and utilizes the large-collection-electrode design approach (see Section 3.3.3). As starting point of these developments, two DMAPS prototypes, CCPD_LF [112] and LF-CPIX [113], successfully demonstrated radiation-hard sensor design with this technology and design approach. However, both chips did not include highly complex digital logic or fast readout architecture. In the first iteration of LF-Monopix, exactly these features were implemented in the form of the column-drain readout, while the sensor design and analog electronics were mostly inherited. All chips are manufactured on high-resistivity ($\geq 2\,\mathrm{k\Omega\,cm}$) Czochralski substrate wafers. LF-Monopix1 is a $1\,\mathrm{cm} \times 1\,\mathrm{cm}$ chip with a pixel pitch of $50\,\mathrm{\mu m} \times 250\,\mathrm{\mu m}$. It was designed to prove the functionality of a DMAPS equipped with the aforementioned features that also meets the required radiation tolerances. At the time of submission in 2016, LF-Monopix1 was (one of) the first DMAPS prototypes with the fast column-drain readout architecture. The chip comprises a total of nine different pixel variants in four columns each to efficiently characterize the effect of specific changes to the in-pixel electronics. Studies have proven the radiation hardness of LF-Monopix1, as hit-detection efficiencies of 98.9 % after $1 \times 10^{15}\,\mathrm{n_{eq}\,cm^{-2}}$ NIEL fluence were measured and full functionality throughout the irradiation up to 100 Mrad TID was

[1] http://www.lfoundry.com/

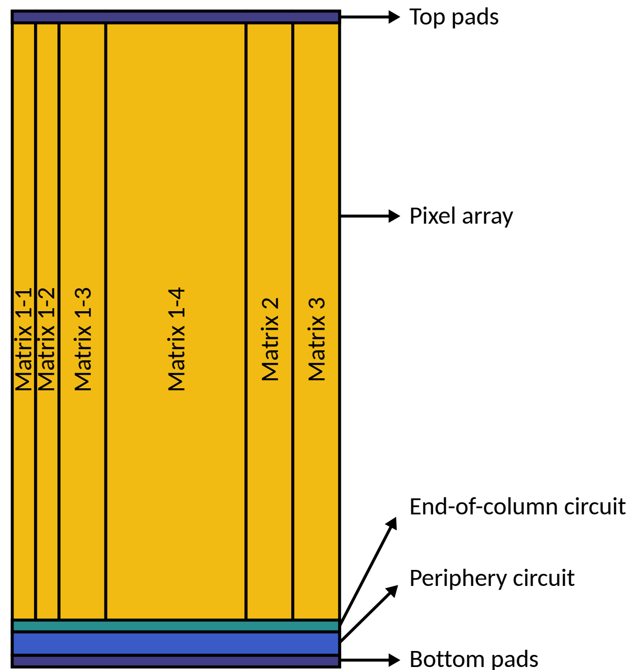

Figure 5.1: Schematic illustration of the LF-Monopix2 layout. Wire-bonding pads for powering, biasing, and communication are situated at the top and bottom of the chip. The periphery circuit above the bottom pads comprises the digital logic, global registers, and analog buffers for monitoring purposes. The sensitive area of the chip is divided into six different pixel variations for efficient testing of individual changes to the in-pixel electronics.

confirmed [107, 114, 115]. These results fueled the design and submission of a second iteration LF-Monopix2, in which the column length was increased while the pixel size was minimized.

5.1.1 LF-Monopix2

Submitted in 2020, LF-Monopix2 is the second iteration of the LF-Monopix development line employing the large-collection-electrode concept. With a chip size of 2 cm × 1 cm, it is a large-scale DMAPS with implemented fast column-drain readout architecture over a *full column length*[2]. A careful redesign of the in-pixel layout allowed the implementation of the same amount of electronics as its predecessor within smaller pixels of 50 µm × 150 µm [116]. The decrease of the detector capacitance to around 250 fF from the resulting smaller collection electrode improves the signal-to-noise ratio, timing performance, and power consumption of the detector. Furthermore, cross-talk effects observed in the predecessor LF-Monopix1, originating from digital signal switching, were mitigated in LF-Monopix2 through enhanced substrate potential connections and better shielding of the sensing node against digital transients [117].

[2] In this context, the term *full column length* refers to the maximum reticle size available on a wafer of this process.

Matrix	1-1	1-2	1-3	1-4	2	3
Columns	4	4	8	24	8	8
CSA version	V1				V2	V3
Feedback capacitance	1.5 fF	5 fF			1.5 fF	
Discriminator tuning	Bidirectional		Unidirectional		Bidirectional	
Logic	Falling		Rising	Falling		

Table 5.1: Overview of the different pixel variants implemented in LF-Monopix2.

Figure 5.1 shows a schematic illustration of the LF-Monopix2 layout. The top and bottom of the chip are covered with wire-bonding pads required to supply power and biasing voltages as well as a digital data interface. However, the pads at the top are only necessary because the chip is not wide enough to fit all pads at the bottom[3]. The chip periphery and end-of-column logic are situated above the bottom pads and include global registers for the whole chip, sensing amplifiers, digital logic and buffers, and analog buffers for signal monitoring. Similar to LF-Monopix1, the LF-Monopix2 chips are successfully thinned to 100 µm and backside processed. Studies on dedicated test structures initiated the adjustment of the guard-ring design [4] compared to the predecessor, which improved the breakdown voltage from around 200 V to more than 450 V before irradiation [116]. In LF-Monopix2, the sensitive area of 1.7 cm × 0.84 cm comprises 340 × 56 pixels, which are split into six different pixel variants listed in Table 5.1. A detailed introduction to the implemented front-end electronics and their variations is given in the following.

Analog front-end circuit and in-pixel logic

As introduced in Section 3.2.2, the analog front-end circuit consists of an amplifier stage and a discriminator stage. Due to the large charge signals and high detector capacitance, charge-sensitive amplification is generally used for large-collection-electrode designs, which also applies to LF-Monopix2. The collected charge is integrated over a feedback capacitance C_{f}. Two different feedback capacitance sizes are chosen across the pixel variants, as a lower AC feedback results in a larger gain. The resistive feedback of the amplifier is realized by a current mirror with a globally adjustable feedback current, that continuously discharges the feedback capacitance while also stabilizing the operation point of the amplifier. In total, three pre-amplifier versions are implemented in LF-Monopix2. The largest part of the matrix is equipped with version V1, which is the single-stage folded cascode NMOS amplifier design of its predecessor

[3]The LF-Monopix2 design prioritized the *full column length* over the width of the chip. In another, larger iteration of the LF-Monopix, they could be moved to the bottom reducing the insensitive area.

[4]Sensor guard-rings are floating, concentric implants that surround the pixel matrix. They are used to smooth the potential gradient between the high-voltage pixel matrix and low-voltage chip edges, and thus prevent early breakdown [60].

chip [118]. Version V2 introduces a telescopic cascoded structure that requires isolating the resistive feedback from the high-impedance gain stage. While a similar telescopic cascoded structure is used for version V3, the current into the input transistor is adjustable by two independent registers. Both adaptions facilitate control over the trade-off between the gain and bandwidth of the pre-amplifier stage.

The subsequent discriminator stage is connected to the pre-amplifier output via a coupling capacitor that decouples the working points of both, as the baseline of the discriminator is set by a MOS transistor pedestal. A global register controls the biasing current of this pedestal resulting in an adjustable baseline [118]. Two different versions of discriminators are implemented within LF-Monopix2. Similar to the pre-amplifier, the majority of the matrix features the proven design of the predecessor referred to as *unidirectional*. It comprises a self-biased differential amplifier [119] followed by a CMOS inverter providing high gain and fast operation. The upgraded *bidirectional* discriminator optimized transistor dimensions and swapped the input nodes of threshold and signal to achieve faster operation. However, the swapped inputs require an additional inverter to obtain a positive output pulse. This implementation provides a larger dynamic range of the discriminator tuning at the cost of larger noise.

In addition to the global discriminator threshold register, LF-Monopix2 features a four-bit local threshold tuning register referred to as *TDAC*. The step size of the latter is adjustable via another global register digital-to-analog converter (DAC). Furthermore, the bidirectional discriminator circuit introduces an improved implementation of the local tuning circuit that covers a larger threshold range at the cost of a broader step size. Each pixel is equipped with two memory cells of 6 bit each that store the digitized data in form of time-of-arrival (leading edge) and time-over-threshold (trailing edge). The corresponding gray-coded timing reference distributed to the pixels runs at a frequency of 25 ns according to the LHC-based design requirements. For one sub-matrix, the in-pixel readout logic clears the `Token` signal on the rising edge of the `Read` signal instead of the falling edge (see Section 9.1). An injection circuit is implemented for testing purposes, which induces a pulse proportional to the difference between two externally provided voltages (V_{Hi} and V_{Lo}) at the input of the pre-amplifier. The implemented injection capacitance was measured to be around 2.73 fF before irradiation matching the results of the predecessor [116].

Readout logic and peripheral design

As mentioned before, LF-Monopix2 is equipped with the synchronous column-drain readout architecture described in Section 9.1 without trigger functionality. The chip contains only one readout controller for the entire matrix and can be seen as one *super column*. In this concept, readout priority proceeds from lower to higher column and higher to lower row within a single column. The highest priority hit will generate a `Token` signal that triggers a global `Freeze` signal across the whole matrix and a local `Read` signal sent only to the specific column. After the hit is read out, the `Token` signal is cleared and the cycle repeats to read out additional hits,

	Column (6 bit)	Leading edge (6 bit)	Trailing edge (6 bit)	Row (9 bit)
Bits	26 ... 21	20 ... 15	14 ... 9	8 ... 0

Table 5.2: Bit-wise structure of the LF-Monopix2 serialized hit data. The leading and trailing edge information of the discriminator are gray-encoded.

if necessary. For each hit, a pixel sends out a total of 27-bit serialized data words that comprise column and row information as well as the gray-encoded leading and trailing edge information of the discriminator. The structure of the serialized data is shown in Table 5.2. The readout of each column can be enabled and disabled by a global register. Furthermore, the chip is equipped with an analog monitoring circuit that can forward the analog hit signal output of each pixel after the pre-amplifier stage.

In total, the chip comprises eleven global current DAC registers with 6 bit each in its periphery that define the required biasing conditions. For debugging purposes, each register current is mirrored to a single analog monitoring pad that allows for the measurement of a single register output at a time. For registers with very small output currents, the mirroring gain is increased making the analog monitoring only reliable for relative changes after irradiation.

5.2 The TJ-Monopix chips

The TJ-Monopix development line uses the 180 nm Tower Semiconductor[5] CMOS imaging technology. It comprises two iterations of chips designed in the small-collection-electrode design approach. Motivated by the excellent results of the ALPIDE MAPS designed for the ALICE ITS upgrade [53], the target of this development is the conversion of the technology into the radiation-harder DMAPS designs. The TJ-Monopix chips were developed in close collaboration with the MALTA project managed by CERN [120, 121], which share the same sensor design and analog front-end, but pursue different concepts of readout architecture. The Monopix and MALTA sensor layout is based on an improved version of an early demonstrator called TJ-Investigator [122]. As described in Section 3.3.3, the long drift distances and complex electric field configuration compromise the radiation hardness of the sensor design. In joint efforts with the foundry, an additional low-dose n-type implant beneath the collection electrode was added to increase the surface of the p-n junction and, consequently, the depleted region under reverse bias conditions [63]. A schematic illustration of this modification is shown in Figure 5.2. Simulations have shown not only the expected expansion of the depleted volume, but also a significantly increased electric field at the pixel edges [123]. However, studies with the first iterations of TJ-Monopix and MALTA revealed a significant drop of hit-detection efficiency after irradiation to $1 \times 10^{15}\,\mathrm{n_{eq}\,cm^{-2}}$ in the pixel corners [120, 124]. Further simulations have proven

[5] `https://towersemi.com/`,formerly known as TowerJazz

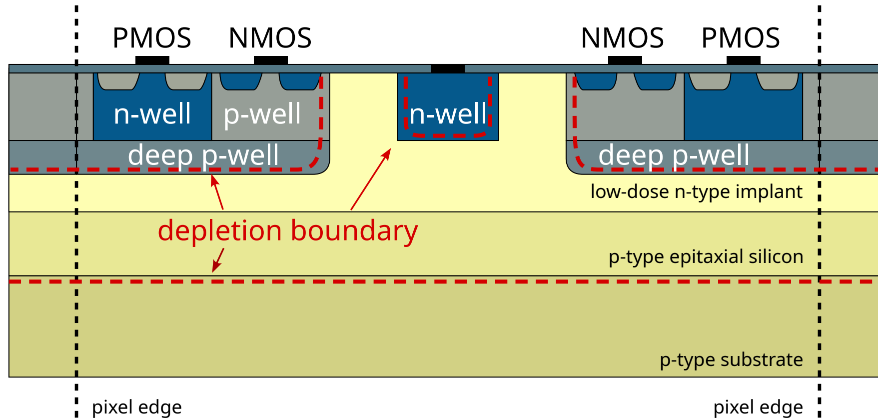

Figure 5.2: Schematic illustration of the low-dose n-type implant modification to the small collection electrode design. This modification increases the effective p-n junction and, consequently, enlarges the depleted region across the pixel volume. From [28].

that this effect originates from a lateral electric field minimum in the pixel corners that results in longer charge collection times [125]. Consequently, the probability of charge trapping increases drastically after irradiation resulting in the observed decrease of charge collection. Based on these observations, two methods for improving the performance after irradiation were identified:

For one, adjustments to the geometry of the process modifications allow for an enhancement of the lateral electric field in the pixel edges. To achieve this, two possible implementations were identified by simulations [125]: introducing a gap in the low-dose n-type implant below the deep p-wells at the pixel edges shapes the potential distribution, and therefore enhances the lateral electric field towards the collection electrode in this region. This modification is commonly referred to as n-gap (NGAP). The same can be achieved by adding another p-type implant below the deep p-well, called extra-deep p-well (XDPW), at the same location instead of the n-gap modification. Both process modifications are visualized in Figure 5.3.

The second method relies on increasing the generated signal charge. This is accomplished by substituting the high-ohmic epitaxial layer and its low-ohmic substrate handling wafer with a high-ohmic Czochralski wafer that provides a larger sensitive thickness. The resistivity of both utilized silicon types is larger than $2\,\mathrm{k\Omega\,cm}$, while the thickness of a Czochralski wafer is typically $725\,\mu\mathrm{m}$ but can be thinned below $100\,\mu\mathrm{m}$. In the case of TJ-Monopix chips, Czochralski wafers were thinned to $100\,\mu\mathrm{m}$ and $300\,\mu\mathrm{m}$ thickness. As a result, the depleted volume extends beyond the accessible volume of a chip fabricated on an epitaxial wafer. However, due to the limited bias voltage capabilities, a $100\,\mu\mathrm{m}$ thick Czochralski wafer cannot be fully depleted in this design [28].

In the first iteration, TJ-Monopix1, both improvement methods were implemented and tested. TJ-Monopix1 is a $1\,\mathrm{cm} \times 2\,\mathrm{cm}$ chip with a pixel pitch of $36\,\mu\mathrm{m} \times 40\,\mu\mathrm{m}$. Submitted in 2017, it was designed to demonstrate the functionality of a large-scale DMAPS with small collec-

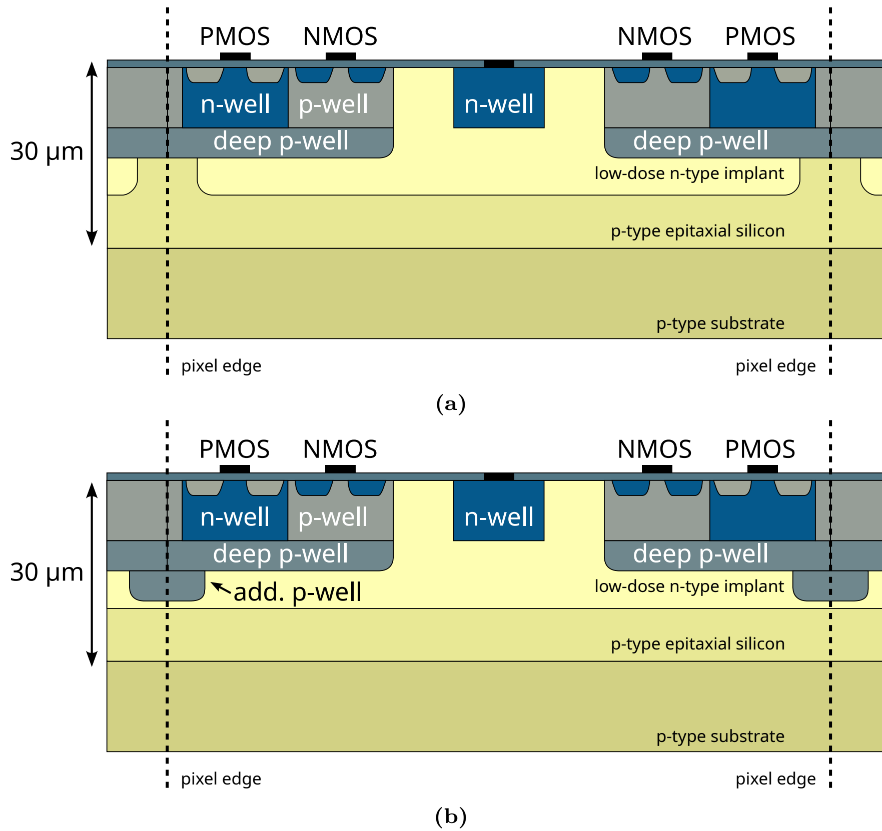

Figure 5.3: Schematic illustration of the (a) NGAP and (b) XDPW modifications to the small collection electrode design. Simulations and measurements have proven that both modifications enhance the charge collection efficiency after irradiation. From [28].

tion electrode and sophisticated column-drain readout architecture for high-radiation environments [126]. The chip comprises a total of four different in-pixel electronics variations to efficiently characterize changes in the data bus and front-end input configuration. Beam tests of TJ-Monopix1 with modified sensor geometry confirmed an improved hit-detection efficiency of 87.29 % for 30 µm epitaxial sensors and 98.28 % for 300 µm Czochralski sensors after irradiation to $1 \times 10^{15}\,\mathrm{n_{eq}\,cm^{-2}}$ [28]. Furthermore, full functionality after 100 Mrad TID of X-ray irradiation was verified [127]. To maximize the hit-detection efficiency after irradiation (also for epitaxial wafers) with this technology and design approach, necessary adjustments were identified and implemented in a second iteration called TJ-Monopix2 [126].

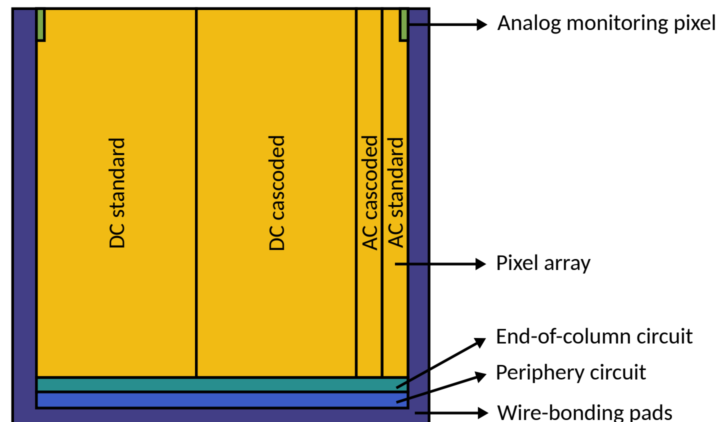

Figure 5.4: Schematic illustration of the TJ-Monopix2 layout. Wire-bonding pads for powering, biasing, and communication are situated at the top and both sides of the chip. The periphery circuits above the bottom pads comprise the end-of-column logic, global registers, and digital logic. The sensitive area of the chip is divided into four different pixel variations for efficient testing of individual changes to the in-pixel electronics. A total of eight analog monitoring pixels are implemented in two groups of four on each side of the chip.

5.2.1 TJ-Monopix2

Submitted in 2020, TJ-Monopix2 is a full-scale 2 cm × 2 cm DMAPS designed in the small-collection-electrode concept. Featuring a *full column length*[6], the chip is equipped with the same synchronous column-drain readout architecture (see Section 9.1) as all Monopix chips. The pixel size was reduced to 33.04 µm × 33.04 µm while more in-pixel electronics were implemented compared to the predecessor. These changes address necessary key adjustments identified in TJ-Monopix1 to enhance the performance after irradiation. A schematic illustration of the TJ-Monopix2 layout is shown in Figure 5.4. Three sides of the chip are covered with wire-bonding pads. The bottom pads include connections for data transmission and powering of the peripheral circuits, while the in-pixel powering (analog and digital) and biasing voltages are supplied via the left and right connections. In the case of TJ-Monopix2, the sensitive region covers a total area of about 1.69 cm × 1.69 cm with 512 × 512 pixels and is divided into four pixel variations. Wafers of this chip were submitted in both n-gap and extra-deep p-well sensor modifications and manufactured on both 30 µm epitaxial and up to 300 µm Czochralski silicon substrates. Consequently, TJ-Monopix2 has been fabricated in a total of four variants, corresponding to the different combinations of pixel modification and silicon substrate.

Analog front-end circuit and in-pixel logic

The small pixel size of TJ-Monopix2 assists to minimize the detector capacitance to around 3 fF [126], which creates large voltage signals (see Eq. (3.27)). Instead of a charge sensitive

[6] Again, the term *full column length* refers to the maximum reticle size available for this process.

Matrix	DC standard	DC cascoded	AC cascoded	AC standard
Columns	224	224	32	32
Source-drain follower	Standard	Cascoded	Cascoded	Standard
Signal input coupling	DC		AC	

Table 5.3: Overview of the different pixel variations implemented in TJ-Monopix2.

amplifier, a single-stage voltage amplifier is more suitable in the small-collection-electrode design to take advantage of this signal. The implemented voltage amplifier is a modified version of the analog front-end designed for the ALPIDE chip, which is based on a source-drain follower approach [128, 129]. Enlarging the transistor size at the amplifier input facilitated an improvement in gain by 50 % and a significant decrease of the noise performance compared to its predecessor. In addition, the size of the coupling transistor and, thus, its capacitance was increased by a factor of 7.5 to raise the gain by a factor of 2 and enhance the signal-to-noise ratio [28, 65]. Among its pixel variations, TJ-Monopix2 features a cascoded version of the source-drain follower to improve the pre-amplifier gain. Furthermore, both the standard and the cascoded versions are implemented with a DC- and an AC-coupled signal input node to the pre-amplifier. While the sensitive volume of the DC-coupled pixels is depleted by applying a negative bias voltage to the substrate (PSUB) and shielding p-well (PWELL) contacts, the AC-coupled pixels allow to apply a positive biasing voltage to the n-type collection electrode. This raises the maximum applicable voltage before irradiation from around −6 V in DC-coupled case to 50 V for the AC-coupled case. An overview of the different pixel variations is given in Table 5.3. For a more detailed description of the changes in the TJ-Monopix2 design and its pixel variations, it is referred to [65].

TJ-Monopix2 is designed in a 2×2 pixel core layout that shares as much functionality of the analog and digital in-pixel electronics as possible between the respective pixels to save area. One enhancement compared to the predecessor is the addition of a 3-bit local threshold tuning circuit to reduce the threshold dispersion. In case all tuning bits are set to zero, the discriminator of the respective pixel is disabled. Each pixel is equipped with two 7-bit memory cells to sample the digitized hit information in form of leading edge and trailing edge. The corresponding sampling rate, nominally set to 40 MHz, is derived from the command clock and distributed across the matrix in gray code. Due to the long column length, TJ-Monopix2 features a delay compensation that reduces the propagation delay of the timing reference clock along a column. A test injection circuit is included in the chip that imitates charge deposition proportional to a voltage difference controlled by two 8-bit registers `VH` and `VL`. The corresponding injection capacitance, over which the voltage is applied, is designed to be 230 aF to not increase the total detector capacitance [126]. Furthermore, the sophisticated injection circuit of TJ-Monopix2 can induce signals in eight phases relative to the timing reference clock. This is equivalent to 3.125 ns

	Column (8 bit)	Leading edge (7 bit)	Trailing edge (7 bit)	Row (10 bit)
Bits	31 ... 24	23 ... 17	16 ... 10	9 ... 0

Table 5.4: Bit-wise structure of the TJ-Monopix2 digitized hit data. Due to the double-column structure, the 256 double columns comprise 1024 pixels each. The leading and trailing edge information of the discriminator are gray-encoded.

steps in the case of the nominal 40 MHz clock. For detailed debugging purposes, TJ-Monopix2 provides eight analog monitoring pixels, which are not included in the digital readout and sit in groups of four at the top left and right of the pixel matrix (see Figure 5.4). These pixels provide the analog output signal of all individual front-end variations as well as the initial voltage signal across the sensor for both types of coupling.

Readout logic and digital periphery

TJ-Monopix2 features an existing pseudo-LVDS driver [130] combined with a sophisticated command decoder that minimizes the necessary low voltage differential signaling (LVDS) signals for data and command transmission. The command decoder is operated at a nominal command clock frequency of 160 MHz and the respective command decoder is copied from the RD53B readout ASIC [131]. This facilitates the use of LVDS signals for command, clock, and data transmission to simplify the DAQ hardware. Nevertheless, the chip is equipped with an additional single-ended CMOS output for HitOr signals.

The chip comprises a total of twelve global registers (for voltages and currents) with 8 bit each to control the biasing conditions of the front-end and two injection-related registers that define the amplitude of a test injection pulse. Dedicated wire-bonding pads enable monitoring and even overwriting of the output currents or voltages of these global and injection-related registers. Like all Monopix chips, TJ-Monopix2 is equipped with the synchronous column-drain readout architecture (see Section 9.1). In the case of the TJ-Monopix development line, the pixel matrix is designed in a double-column structure implementing one readout controller per 1024 pixels (e.g. two full columns) in the end-of-column logic. Consequently, data words comprising the pixel address as well as the gray-encoded 7-bit time-of-arrival and trailing edge information require a total length of 32 bit as summarized in Table 5.4. The corresponding timing reference clock is derived within the chip and can be enabled and disabled on a double-column basis. For data transmission to the DAQ, TJ-Monopix2 uses a DC-balanced 8b10b transmission protocol [132]. It is referred to [28] for a more detailed description of the digital design of TJ-Monopix2.

5.3 Data acquisition systems

In general, DAQ systems can be divided into three main constituents: hardware, firmware, and software. Modern DAQ systems try to be as modular as possible to avoid redundant work across multiple projects. For tests on a single chip basis, a chip is glued to an individualized printed circuit board (PCB) and wire-bonded to establish connection. If the device is equipped with sophisticated readout electronics, an FPGA-based DAQ board is typically used for data transmission and communication. The firmware of the FPGA must be customized for the chip and its communication protocol, while the software contains the comprehensive control over the communication. The DAQ systems of both Monopix2 chips are structured in the same way and the constituents relevant for this thesis are introduced in the following.

Hardware

To test a chip, the bare silicon is glued onto a customized PCB and wire-bonded to establish the required connections for powering and communication. The PCB area below the chip is cut out and the chips are only glued to the PCB at their edges, since supplementary material can degrade the resolution of certain measurements (i.e. for beam tests). In general, the chip PCB is equipped with low voltage power connectors and multiple pin headers to set and monitor supplied voltages to the on-chip electronics. Different LEMO connectors provide inputs for the supply of the external biasing voltages and outputs for the analog monitoring signals. For chips that are not yet in the final version, the possibility of externally monitoring or even overwriting applied voltages by DAC registers can contribute significantly to the characterization of the device. The chip PCB is connected to a DAQ board that houses a commercial FPGA module, which handles the communication and data transmission between chip and DAQ computer. Typically, a low voltage power connector supplies the voltage to power the FPGA and an Ethernet connection is used for data transmission between DAQ board and computer. Multiple LEMO connectors and an additional RJ45 port on the board facilitate the transmission of signals directly to the FPGA, which is particularly relevant for external trigger information (see Section 6.2).

Figure 5.5 shows the DAQ hardware of LF-Monopix2. The chip PCB is connected to the custom-made multi-IO board named MIO3 via the general purpose analog card called GPAC, which routes the data to the FPGA accordingly. Since LF-Monopix2 transmits single-ended CMOS signals, short connections are relevant to avoid signal distortions. The MIO3 board houses the commercial Mercury KX1[7] FPGA daughter board. The GPAC provides a multi-pin connection with active and passive components between the FPGA mother board and the chip PCB that requires a separate 5 V low-voltage power supply. Due to these features, the adapter card can be used for communication and data transmission between chip and DAQ system as well as the supply of required voltages.

[7] `https://www.enclustra.com/en/products/fpga-modules/mercury-kx1/`

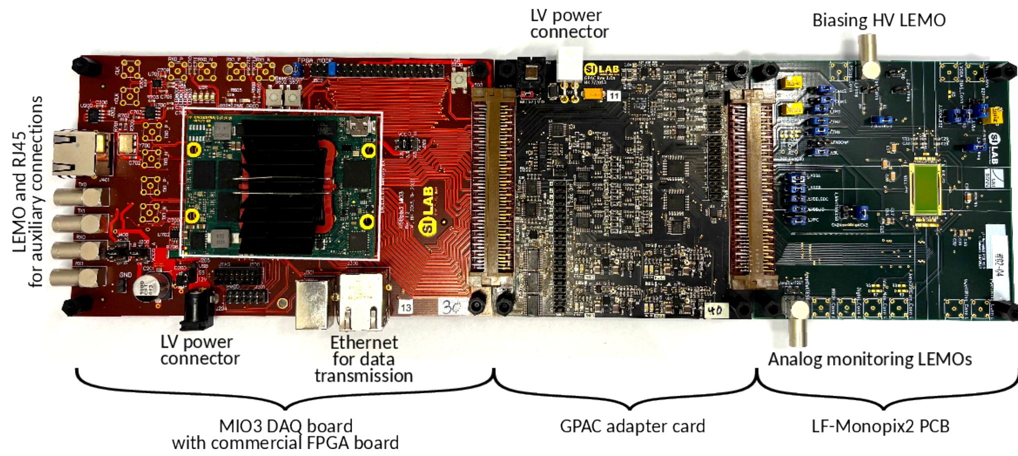

Figure 5.5: LF-Monopix2 data acquisition hardware consisting of MIO3 base board, FPGA daughter board, GPAC adapter, and the LF-Monopix2 chip PCB. The most important connectors and components of each constituent are highlighted.

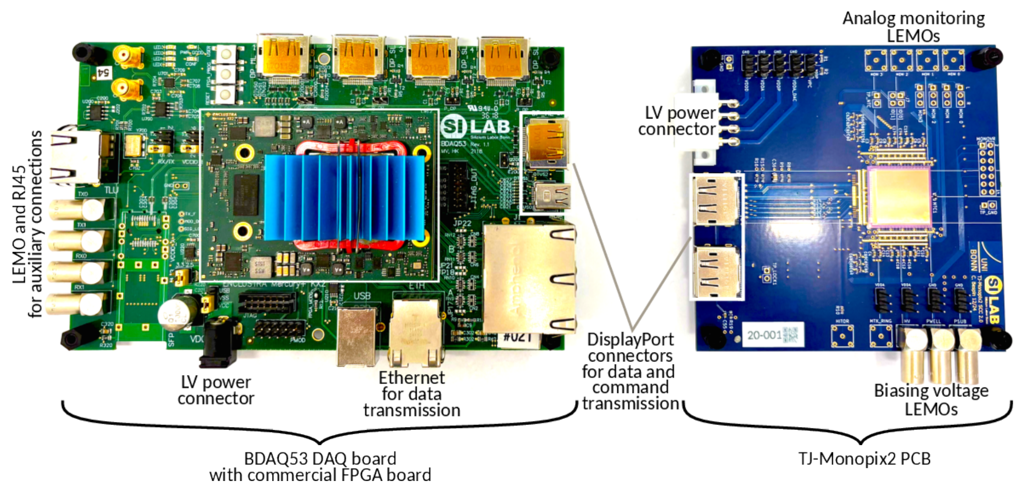

Figure 5.6: TJ-Monopix2 data acquisition hardware consisting of BDAQ53 base board, FPGA daughter board, and the TJ-Monopix2 chip PCB. The most important connectors and components of both constituents are highlighted.

The DAQ hardware of TJ-Monopix2 is shown in Figure 5.6 and offers a much simpler design based around the available LVDS communication. In this case, the BDAQ53 hardware [133] developed in Bonn for RD53 testing as part of the ATLAS Inner Tracker upgrade is taken as DAQ base board, which houses a commercial Mercury+ KX2 FPGA[8]. Since TJ-Monopix2 transmits LVDS signals instead of single-ended ones, the customized chip PCB is connected to the BDAQ53 board via DisplayPort cables. As no power is supplied via DisplayPort in this case, the chip PCB requires a separate low-voltage power connection for the required 1.8 V.

Firmware and software

For both Monopix projects, the `python`-based control software for chip communication and data taking is structured around `basil` [134]. `basil` provides common firmware modules shared between projects and the corresponding software interface. This includes modules for data transmission between chip, FPGA, and DAQ computer, as well as measurement specific supplementary modules. Two examples of the latter are a trigger logic unit (TLU) module, which is required to receive trigger signals for beam test measurements (see Section 6.2), or a time-to-digital converter (TDC) module for timing measurements. For identification, a specific header is assigned to the data of each module before it is stored in respective FIFO registers. The FPGA merges all received data (including hit information from the chip and data from supplementary modules) into a continuous data stream and stores it in another FIFO register that is read by the DAQ computer.

The core of the object-oriented software is the `ScanBase`, which is accessed for every scan routine to trigger the initialization of all necessary instances specific to the scan. Such instances are additional classes comprising software for controlling hardware components or for interpreting and analyzing raw data sent by the chip. The schematic structure of the DAQ software is illustrated in Figure 5.7. In a typical scan routine, the `ScanBase` first initializes the DAQ hardware class, that configures the DAQ board for the scan. Subsequently, the chip class is initialized. It contains the respective commands to control the chip and initiates communication. The actual measurement procedure is programmed in an individual scan script, which inherits instantiated objects from the `ScanBase`. Each scan routine is written as a scan class, which contains the scan-specific configuration and commands for both DAQ board and chip. Exemplary common scans for both Monopix2 chips are listed in Table 5.5. For each scan, the data is stored in `hdf5` file format[9]. Finally, the supplementary classes for data analysis and plotting are accessed to interpret the raw data sent by the chip and graphically display the results. The DAQ software for both LF-Monopix2 and TJ-Monopix2 is both publicly available on GitHub [135, 136].

[8] `https://www.enclustra.com/en/products/fpga-modules/mercury-kx2/`
[9] `https://www.hdfgroup.org/solutions/hdf5/`

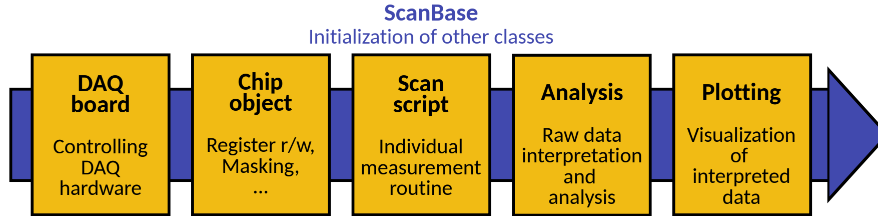

Figure 5.7: Schematic illustration of the modular data acquisition software based around the `ScanBase` class. Supplementary classes for different tasks are initialized and called by the `ScanBase`.

Scan	Description
Threshold scan	For an adjustable charge scan range, N hits per charge step Q are injected into a pixel. The distribution of detected hits per charge step follows the error function. The threshold Q_{thr} of a pixel is defined as the charge where 50 % of the injected hits are detected. The width σ of the pixel response distribution is interpreted as the noise performance of the pixel and referred to as equivalent noise charge (ENC).
Injection based tuning	The target threshold charge is injected N times and the pixel response is measured. If the pixel detects more than half of the injected hits, the (global or local) tuning register is adjusted such that the threshold increases and vice versa. To decrease the scan duration, the registers are adapted according to the binary search principle.
Noise based tuning	The pixel readout is activated, and its threshold is lowered using the (global or local) tuning register until the pixel detects a target noise rate.
Source scan	Activate the pixel readout and detect incident particles from radioactive sources. This measurement also supports handling of external trigger data by the TLU module for beam tests (see Section 6.2).

Table 5.5: Description of common scan routines between the Monopix2 chips.

6 Measurement methodologies

The characterization and testing of new pixel detectors for tracking applications is a complex process with many milestones. Upon receiving chips from the manufacturer, electrical tests of non-irradiated devices are conducted to verify their functionality. This includes the characterization of important parameters such as the threshold, ENC, I-V characteristics, power consumption, and many more relevant detector properties. Ultimately, the most important criteria for any tracking device are the spatial resolution and hit-detection efficiency within a given time interval. Once the functionality of non-irradiated chips is verified, the radiation tolerance is investigated based on the same parameters. For this purpose, samples are deliberately exposed to radiation at dedicated irradiation facilities. Radiation hardness is often tested separately for bulk damage to the sensitive volume (see Section 4.1) and surface damage to the active electronics (see Section 4.2). The reason for this is that the device needs to be powered during the irradiation to receive surface damage, which cannot be provided at every facility. The main focus of this thesis is the characterization of the performance of two separate DMAPS after irradiation. This chapter presents the employed measurement methods relevant for this thesis. In Section 6.1, the available X-ray irradiation setup is introduced and the measurement routine during an X-ray irradiation campaign is described. Section 6.2 depicts the complex procedure of test beam measurements and the subsequent elaborate data analysis. A necessary discourse on the error estimation of the test beam analysis is also addressed.

6.1 X-ray irradiation campaigns

To characterize the radiation hardness of an ASIC, the device under test (DUT) is exposed to X-rays (see Section 4.2). Due to the extreme demands on radiation tolerance in high-energy physics experiments, dedicated radiation sources with large dose rates are required to perform the measurement within a reasonable duration. Since surface damage in transistors forms exclusively under biased conditions, it is important to power the circuitry during the entire irradiation to ensure that the device receives radiation damage. The irradiation setup employed in the scope of this thesis is described in the following.

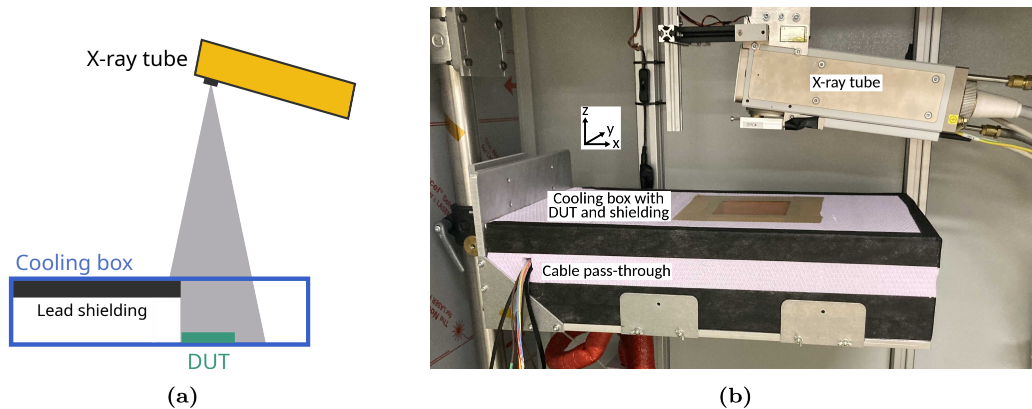

(a) (b)

Figure 6.1: (a) Schematic illustration and (b) picture of the X-ray irradiation setup.

6.1.1 Irradiation setup

The available irradiation setup is based around a commercial X-ray irradiation cabinet. It is equipped with an X-ray tube that accelerates an electron beam onto a tungsten target and generates a photon beam. The cabinet supports acceleration voltages up to 60 kV at variable tube currents up to a maximum power output of 3 kW. The resulting X-ray beam is filtered and collimated. The opening angle of the beam is measured to be 0.144 rad behind the collimator [137]. A schematic illustration and a picture of the setup are shown in Figure 6.1. In addition, the setup contains a cooling box for mounting and cooling the DUT during the irradiation. The latter is important to prevent thermal runaway caused by the leakage current increase due to the high intensity beam. The water based cooling system comprises a chiller, tubing, and cooling plate on which the DUT is mounted. For all irradiation campaigns performed in the scope of this thesis, the corresponding device is cooled to 0 °C at all times. Dry air is supplied to the inside of the cooling box to avoid condensation. To minimize the attenuation of the X-ray beam, the cooling box has a cut-out at the location of the device, which is only covered by Kapton tape. Lead shielding can be installed in the remaining area such that other active electronic devices in the cabinet do not receive radiation damage. The entire cooling box is placed on a manual stage to adjust the distance to the collimator exit before an irradiation. This is important to ensure a complete and uniform illumination of the DUT.

Before each irradiation campaign, the setup requires a calibration to precisely know the beam profile, spectrum, and dose rate at the chosen machine settings. The analysis and calibration of the X-ray spectrum were done in [137] and are used to calculate the respective dose rate. As calibration procedure of beam profile and dose rate, the leakage current of a commercial PIN diode is measured while scanning the x-y plane within the X-ray cabinet at a chosen height. Due to the opening angle of the photon beam behind the collimator and the attenuation of its intensity with distance (see Eq. (2.10)), the maximum dose rate depends on the variable height at which the diode (and later the DUT) is installed. Figure 6.2 shows an exemplary

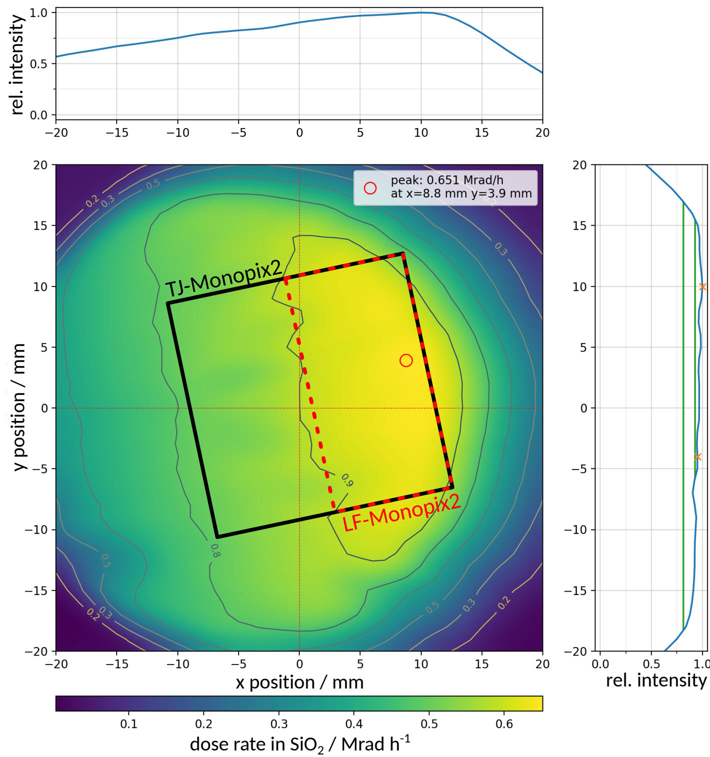

Figure 6.2: Calibration of the X-ray irradiation setup using a commercial PIN diode. The DUT is placed such that it receives a homogeneous dose rate across the larges possible area. The on-chip electronics are positioned in the region of the highest dose rate. The placement of each Monopix2 chips is indicated in the figure, respectively.

beam profile of the X-ray tube. Permanent lasers installed in the cabinet help to align the DUT to the measured beam profile. Since the Monopix2 chips are large-scale DMAPS, the given beam profile requires a trade-off between a reasonably high and homogeneous dose rate across the entire area of the chip. Each chip is positioned such that the largest possible section of it receives a homogeneous dose rate (see Figure 6.2). For all irradiation campaigns, the on-chip periphery electronics are placed in the region with at least 90 % of the maximum dose rate. Consequently, the mean dose rate of the irradiation across the device is assumed to be 90 % of the calibrated peak dose rate. Accordingly, a rather large error of 10 % is estimated on the received TID of the chip.

6.1.2 Irradiation campaign measurements

X-ray irradiation campaigns comprise multiple irradiation steps to characterize the functionality of the DUT in between each step. The specific measurement routine depends on the tested device and its application. The irradiation to a total dose of 100 Mrad alone takes close to a week at rates around 0.6 Mrad/h typical for the available setup. A waiting period of 30 minutes

after each irradiation step is added to allow for short-term annealing of surface damage (see Section 4.2.2). Thus, the measurement routine must be well-prepared and optimized not to unnecessarily prolong the duration of the irradiation campaign.

In the case of complex devices like the Monopix2 chips, it is virtually impossible to measure direct changes in behavior with increasing TID at the level of individual transistor. Consequently, primary focus is put on the general functionality of the device. This is qualitatively accomplished by measuring the change in threshold and noise and evaluating the possibility of compensating the effects by adjusting certain chip parameters. The latter is only done extensively after the entire irradiation campaign, since optimizing the performance of an irradiated chip is a lengthy process and time slots of the X-ray irradiation setup are limited. Another important measurement is the monitoring of power consumption of the DUT versus TID due to the alteration of threshold voltage and leakage current within the transistors (see Section 4.2.3). The corresponding results indicate which power domain, and thus which transistors are affected by surface damage. Furthermore, the analog monitoring options of the Monopix2 chips (see Chapter 5) are utilized to measure the signal shape of representative pixels throughout the irradiation. This provides information about deviations in the response of the amplifier circuit.

6.2 Test beam measurements

The hit-detection efficiency describes the probability of a detector to detect an impinging particle. It is the most important property of a silicon pixel detector as silicon trackers should ideally register all traversing particles. To study this performance parameter, a beam of MIPs referred to as *test beam* is directed at a beam telescope setup comprising the DUT that is to be characterized. The beam telescope functions as a reference detector system, which is used to reconstruct a traversing particle's trajectory and compare it to the measurement of the DUT. The structure of a beam telescope setup is described in detail in the following section. The particle energy is an important beam property in these measurements since larger beam energies reduce multiple scattering (see Section 2.3), which improves the spatial resolution and facilitates a precise reconstruction of the particle trajectory. In addition, multiple scattering is reduced by introducing as little supplementary material as possible into the beam in form of the measurement setup. Since the generation of such a test beam is cost-intensive and far from trivial, dedicated test beam facilities provide sites to perform beam measurements. Consequently, time slots at these facilities are highly requested and need to be booked well in advance.

Within this thesis, measurements are performed at the DESY[1] II [138] and ELSA[2] [139] test beam facilities in Hamburg and Bonn, respectively. While both facilities use electrons, DESY II implemented a tertiary beam generation allowing for variable energies between 1 and 6 GeV and particle rates of a few kHz. The ELSA facility is equipped with a primary beam extraction

[1] Deutsches Elektronen-Synchrotron
[2] Elektronen-Strechter-Anlage

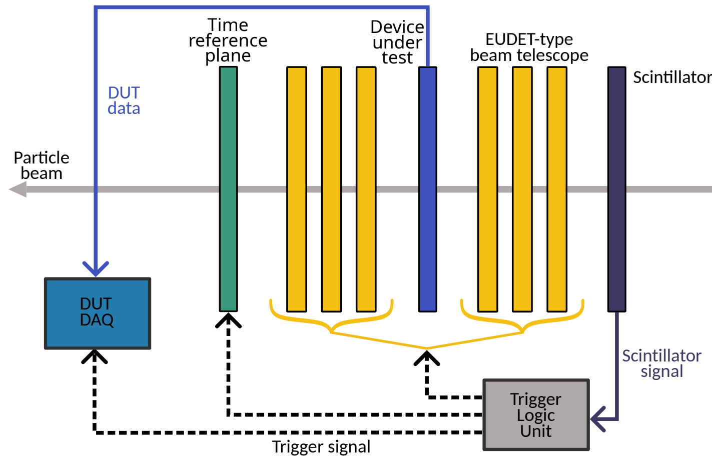

Figure 6.3: Schematic illustration of a beam telescope setup. The beam telescope itself comprises six planes of a well-characterized pixel detector with high spatial resolution. The DUT is placed in the middle of the beam telescope to facilitate a precise track reconstruction at the location of the device. A scintillator in front of the beam telescope detects impinging particles and sends a signal to the trigger logic unit, which in return forwards a trigger signal to all devices. The fast time reference plane (relative to the telescope) eliminates ambiguities due to track multiplicities in the later track reconstruction.

providing beam energies up to 3.2 GeV at adjustable particle rates across a wide range of a few kHz up to several hundred MHz. Typically, particle rates of a few kHz are preferred in test beam measurements from the user's side to prevent saturation of the DAQ systems for the entire setup. Furthermore, higher rates will result in a larger track multiplicity, which compromises the data quality.

6.2.1 Beam telescope setup

Measuring the hit-detection efficiency of a DUT relies on the detection of traversing particles and reconstruction of their trajectories referred to as tracks using a beam telescope. The beam telescope consists of multiple planes of a well-characterized detector with high spatial resolution providing precise tracking information. A schematic illustration of a common beam telescope setup is shown in Figure 6.3. In this thesis, EUDET-type beam telescopes [140] are used for particle tracking and operated with the `python`-based readout framework `pymosa`[3]. Such a telescope comprises six planes of 50 µm thick `MIMOSA26` MAPS [141] with a pixel pitch of 18.4 µm × 18.4 µm. Studies have shown that the intrinsic resolution of 3.2 µm per `MIMOSA26` plane facilitates a precise pointing resolution of less than 2 µm on the DUT [142]. The continuous rolling-shutter readout implemented in the detector limits its readout frequency to frames of 115.2 µs, which is significantly slower than most DUTs. At high particle rates, this leads to a high track multiplicity within a single frame and, thus, ambiguities in event reconstruction of the EUDET-type telescope. These ambiguities are resolved by adding a time reference plane

[3] `https://github.com/SiLab-Bonn/pymosa`

with a more precise time resolution to the back of the telescope. In this case, single-chip modules of either the `FE-I4` [143] or the `ITKPixv1.1` [144] chips are used as a time-reference plane. Both provide a time stamping resolution of 25 ns. The DUT is positioned in the middle of the six telescope planes to optimize the pointing resolution at the device. To minimize the material budget, the DUT PCB is equipped with a cut-out below the sensitive area (see Section 5.3). A portable cooling system specifically designed for test-beam measurements to cool irradiated DUTs is described in the upcoming section.

A scintillator is mounted in front of the telescope and sends a signal to the EUDET trigger logic unit (TLU) [145] once a particle traverses it. The TLU converts this signal into a digitized pulse and distributes this trigger pulse to all connected devices. The trigger data contains a trigger number to synchronize all devices to a common event basis and timeline. For triggerless devices such as the Monopix2 chips, an additional timestamp is assigned to each trigger word by the FPGA before it is inserted into the continuous data stream (see Section 5.3) to facilitate subsequent event building. Consequently, the TLU forms the centerpiece of the beam telescope setup and test-beam measurements.

Portable cooling system

As described in Chapter 4, irradiated devices require cooling during operation to prevent thermal runaway and, consequently, permanent damage. Since beam tests are performed at dedicated test-beam facilities, the cooling setup needs to be portable. In this case, the cooling system is based on a controllable nitrogen flow cooled by dry ice, which is directly blown onto the backside of the DUT [146]. A schematic overview of the entire system is given in Figure 6.4. The cooling box houses the DUT and is equipped with pass-throughs for powering, communication, and nitrogen. By using polystyrene foam, the walls of the box add as little material as possible to minimize the scattering of beam particles and, thus, the uncertainty on track reconstruction. The temperature and humidity inside the cooling box is monitored by an `SHT` sensor[4] and recorded by an Arduino. In addition, this data is used to control the nitrogen flow using an electrical valve that is connected to the DAQ computer. The setup ensures a constant environmental temperature inside the cooling box with variations of less than 1 °C over multiple hours of runtime. This is important as it reduces fluctuations in the response of the device due to (significant) changes in chip temperature. The control software of the system is publicly available[5]. A supply of warm nitrogen controlled by a manual valve prevents condensation during cooling or heating periods inside the cooling box. The tested operational range of this cooling system is between −25 °C and 15 °C. Figure 6.5 displays the cooling box installed in a beam telescope setup at the DESY II test-beam facility.

[4] https://sensirion.com/de/search/products?q=SEK-SHTxx
[5] https://github.com/SiLab-Bonn/n2_cooling

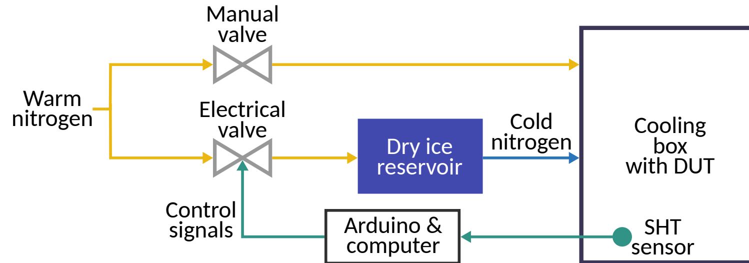

Figure 6.4: Schematic illustration of the portable cooling system. The nitrogen flow is controlled via an electrical valve and cooled using a dry ice reservoir before being fed into the cooling box. Made of polystyrene foam, the cooling box houses the DUT and is equipped with pass-throughs for cables and tubes. Monitoring of temperature and humidity inside the cooling box is done by an `SHT` sensor.

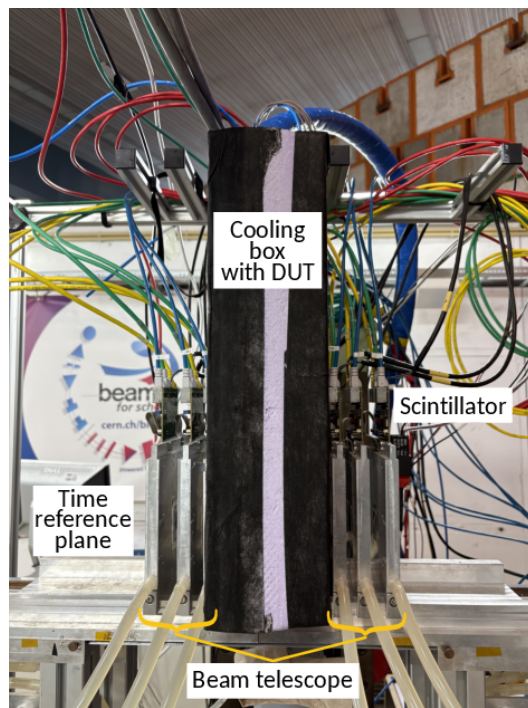

Figure 6.5: Picture of the beam telescope setup including a DUT inside a cooling box. The particle beam orientation is from right to left. Time reference plane and scintillator are barely visible in this picture.

6.2.2 Test beam analysis and hit-detection efficiency

Analyzing the complex test beam data requires many analysis steps from combining the raw hit data of each device to finally calculating the hit-detection efficiency of the DUT. Multiple sophisticated software frameworks exist for this purpose, which share a common analysis procedure. Within this thesis, the `python`-based analysis framework `Beam Telescope Analysis` [147] is used. Selected measurement results are verified by employing the popular `Corryvreckan` software [148]. The common key steps of such an analysis are briefly discussed in the following [42, 149]:

Event building and data formatting
An event is defined as each incident when a particle generates a scintillator signal which results in a TLU trigger signal. In the first step, possible events of a single particle traversing the beam telescope setup need to be identified. The TLU trigger signal is used to assign hit data of each device to a corresponding event. In the case of triggered devices, the assignment of hits to an event is straightforward as hit data is only read out upon arrival of a trigger. For triggerless devices, a cut on the timestamp difference between hit words and trigger words in the continuous data stream is used to assign hits to an event. Due to misassignment, both overestimation and underestimation of detected events are possible. Subsequently, the event-based data of each device is formatted into a common data structure (containing information such as event number, timestamp, column, row, charge, ...) before being passed to the analysis framework.

Noisy pixel removal and clustering
Noisy pixels are identified and removed from further analysis steps since they can artificially alter and improve the hit-detection efficiency. The identification is achieved by comparing the occupancy of each pixel to its neighbors. Furthermore, charge sharing can lead to multiple pixels detecting the traversing particle. In such cases, these hits corresponding to a single event are group into a cluster based on the center-of-gravity approach, if they are within a reasonable distance to each other. This enhances the hit position information of the device. The considered cluster distance of the procedure depends on the pixel pitch of the device and can be chosen variably (typically up to 5 times the pixel pitch). If charge information (time-over-threshold) is available, the clustering algorithm applies charge weighting. This step is performed separately for each detector in the beam telescope setup as preparation for the subsequent analysis.

Alignment
The track reconstruction and efficiency analysis require a global coordinate system for the entire measurement setup. Since the mechanical installation of the setup is not accurate on a micrometer level, it must be assumed that the detector planes are inadvertently displaced and rotated against each other. The alignment step consists of multiple iterations in which the translation and rotation between the different planes are identified and corrected. To

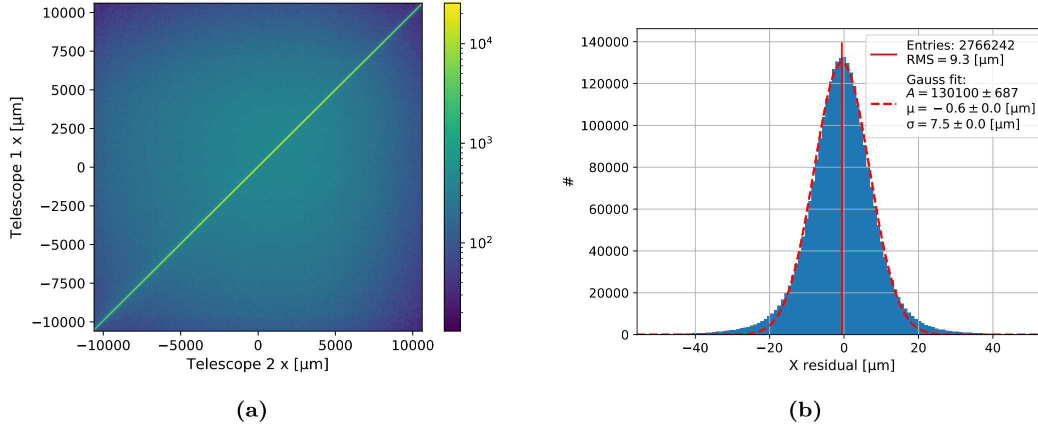

(a) **(b)**

Figure 6.6: (a) Exemplary correlation between the neighboring telescope planes 1 and 2, and (b) unbiased residual distribution of a `MIMOSA26` sensor, both in x direction. The deviations of the residual data towards the tails of the Gaussian distribution are due to multiple scattering effects. Both plots are created by the `Beam Telescope Analysis` framework.

achieve this, the cluster positions of each plane within an event are compared to a preselected reference plane, which defines the origin of the global coordinate system. If the event building is done correctly, the detected cluster positions within an event will show a strong correlation between all planes. The exemplary correlation between two neighboring `MIMOSA26` telescope planes is shown in Figure 6.6a. The alignment process continues until no further adjustments to the plane positions are made within a single iteration, and all iterations are complete. It relies on the track finding, track fitting, and data selection steps introduced in the following. For each iteration, cuts on the track quality and data selection are subsequently tightened to ensure the best possible alignment.

Track finding and fitting

The track finding algorithm assigns clusters of the different detector planes within a single event to a track candidate. This association is based on the shortest distance between the clusters of two neighboring planes assuming perpendicular tracks. In the next step, the found track candidates are reconstructed based on a χ^2-minimization fitting method. It is important that the DUT is excluded from the track reconstruction since this would bias the final results. Typically, multiple scattering effects are negligible and a general broken-line fit model is sufficient for the track reconstruction. In case the setup introduces considerable material, fit models like the Kalman Filter [42] also take multiple scattering into account. The χ^2 value provides an important parameter that describes the quality of the reconstructed track and can be used to discard events based on the track quality.

Track residuals

Track residuals refer to the spatial difference between the reconstructed track intersection and the recorded hit position assigned to the event. They are used as verification of the

track reconstruction and alignment procedure. Simplified to one dimension, the residual can be expressed as

$$\Delta x = x_{\text{hit}} - x_{\text{track}} \quad . \tag{6.1}$$

In the case of successful alignment and track reconstruction, the residual distribution of a device is centered around zero. The shape of the distribution depends strongly on the pixel size. For small pixel pitches of $\leq 25\,\mu\text{m}$, the residuals are Gaussian distributed, while larger pixel sizes require an additional convolution with a box function. An exemplary residual distribution of a `MIMOSA26` telescope plane is shown in Figure 6.6b. Deviations from the expected Gaussian shape of the distribution are explained by multiple scattering effects (see Section 2.3), while the uniform background is the consequence of incorrectly reconstructed tracks. Neglecting biases from the analysis framework, the width of the residual distribution is described by [149]

$$\sigma_{\text{res}} = \sqrt{\sigma_{\text{det}}^2 + \sigma_{\text{point}}^2} \quad , \tag{6.2}$$

where σ_{point} denotes the pointing resolution at the detector plane and σ_{det} is the intrinsic resolution of the device. In the case of binary hit information, the latter is defined by the pixel pitch p of the device [7]:

$$\sigma_{\text{det}}^{\text{binary}} = \frac{p}{\sqrt{12}} \tag{6.3}$$

Results

In the final step, the performance of the DUT is analyzed in depth using the reconstructed tracks. The most important property is the hit-detection efficiency ϵ_{hit} of the device. It is defined as the ratio

$$\epsilon_{\text{hit}} = \frac{N_{\text{tracks}}^{\text{DUT}}}{N_{\text{tracks}}^{\text{total}}} \tag{6.4}$$

of the number of detected tracks by the DUT, $N_{\text{tracks}}^{\text{DUT}}$, and the total number of reconstructed tracks, $N_{\text{tracks}}^{\text{total}}$. Tracks are considered as detected if the DUT measured hit(s) within the vicinity of the reconstructed track in space and time. The latter was already handled by the event building step. A search radius around the reconstructed track intersection point based on the residual distribution is chosen to prevent overestimation of the hit-detection efficiency (see Section 6.2.3). Incorrectly reconstructed tracks (noticeable as the uniform background in the residual distribution) are discarded. Furthermore, the good pointing resolution of the telescope facilitates an investigation of the hit-detection efficiency within a single pixel cell of the DUT. This is relevant since certain in-pixel areas are of greater interest such as the pixel corners due to a higher probability of charge sharing. If high resolution timing information of the trigger and DUT hit arrival times are available, the behavior of the hit-detection efficiency against the hit arrival time can be investigated. Especially high-rate experiments like ATLAS require high hit-detection

efficiencies within a short duration after a trigger signal.

6.2.3 Error estimation of the hit-detection efficiency

The error estimation of such a challenging measurement and analysis as given in beam tests is complex. Several factors contribute systematically to the uncertainty of the estimation of the number of reconstructed tracks in the setup and measured events in the DUT. According to Eq. (6.4), these errors directly affect the measured hit-detection efficiency and can lead to an underestimation or even overestimation of the result, the latter being more severe. They can be separated into four categories, which differ in their impact [149]:

- **Increase of** $N_{\text{tracks}}^{\text{total}}$: Noise hits in the telescope planes can result in the reconstruction of fake track candidates. Also, the reconstruction of tracks based on hits that do not belong to the same incident particle is an issue. Both cause an overestimation of the number of reconstructed tracks, which artificially decreases the measured hit-detection efficiency. This error can be mitigated by using more telescope planes and requiring hits in most of them for the track reconstruction.

- **Decrease of** $N_{\text{tracks}}^{\text{total}}$: The hit-detection efficiency of the telescope planes and the track reconstruction efficiency of the analysis framework lead to an underestimation of the reconstructed tracks. Not reconstructed tracks will lead to an overestimation of the hit-detection efficiency (except for the trivial cases of $\epsilon_{\text{hit}} = 1$ and $\epsilon_{\text{hit}} = 0$) as a corresponding DUT hit can be incorrectly assigned to a different reconstructed track. Simulations have shown that tight cuts on the association distance in the track reconstruction limit the overestimation of the efficiency to less than 0.03 % [149].

- **Increase of** $N_{\text{tracks}}^{\text{DUT}}$: Noise hits in the DUT can lead to an artificial overestimation of its hit-detection efficiency, if the noise hits are assigned to tracks which were not detected by the device. The impact of this contribution strongly depends on the noise occupancy of the detector. Here, the noise occupancy refers to the average detected noise hit rate per readout channel and scan duration. In case of triggerless devices, the association distance to the trigger signal in the event building also influences the size of this uncertainty. For typical noise levels, studies have shown an overestimation of the hit-detection efficiency of less than 0.01 % due to association errors in the event building [28]. Especially for irradiated devices, it is important to reduce the noise of the DUT as much as possible by cooling it during the measurement.

- **Decrease of** $N_{\text{tracks}}^{\text{DUT}}$: Events with large scattering angles can result in an artificial decrease of the detected hits in the DUT and, thus, its hit-detection efficiency. This effect is more prominent at the sensor edges, since it is more likely that the particle is scattered outside the sensitive area. It can be mitigated by employing track fitting models that take into

account multiple scattering. In addition, only pixels in the center of the sensor should be considered in the analysis.

Additional uncertainties are introduced by the chosen cuts on the reconstructed track quality χ^2_{red} and the association distance during the alignment procedure [42]. The size of both is in the order of 0.02 %. Furthermore, the statistically based event building for triggerless devices causes an uncertainty that is strongly dependent on the noise rate of the device [28]. The exact noise rate varies between samples and depends on the front-end settings. Thus, it needs to be evaluated for each measurement independently. Based on this discussion and considering typical noise rates of the studied devices, a systematic uncertainty of 0.05 % is estimated for test beam measurements performed in the scope of this thesis.

The statistical uncertainty of such a test beam analysis is described by a binomial distribution and depends on the number of tracks as well as the hit-detection efficiency. Typical data sets contain more than 10^6 events, of which at least 10^5 tracks are assumed to be reconstructed. For hit-detection efficiencies $\epsilon_{\mathrm{hit}} > 98\,\%$ and such a number of track, this yields a 1σ uncertainty interval of less than 0.05 % [149]. In case of lower efficiencies, the statistical uncertainty increases. Due to the large amount of data, the statistical uncertainty is typically negligible compared to the systematic one, especially considering high hit-detection efficiencies.

7 Characterization of the Monopix2 DMAPS

The main goal of this thesis is the characterization of the LF- and TJ-Monopix2 chips after irradiation. The effects of bulk and surface damage on both chips were investigated separately since a powered NIEL irradiation could not be realized. This chapter describes the characterization results of both chips after irradiation. The results obtained with LF-Monopix2 are presented in Section 7.1, while the TJ-Monopix2 results are shown in Section 7.2. The general performance based on laboratory measurements of both chips at different irradiation levels is reviewed in Sections 7.1.1 and 7.2.1. For TJ-Monopix2, the investigation of an unexpected fluctuation in threshold during operation is also discussed. Sections 7.1.2 and 7.2.2 summarize the X-ray irradiation campaigns performed with LF- and TJ-Monopix2, respectively. The results of beam tests conducted with each chip and at different irradiation levels are presented in Sections 7.1.3 and 7.2.3. Finally, Section 7.3 compares the performance of both Monopix2 chips and highlights their respective advantages.

7.1 Characterization of LF-Monopix2

For the characterization of the radiation tolerance, LF-Monopix2 samples were irradiated up to 400 Mrad TID and $5 \times 10^{15}\,\mathrm{n_{eq}\,cm^{-2}}$ NIEL fluence, separately. The X-ray irradiation was performed at the laboratory setup in Bonn described in Section 6.1. As bulk damage depends on particle type and energy (see Section 4.1), multiple facilities were selected to irradiate chips to fluences ranging from 1×10^{15} to $5 \times 10^{15}\,\mathrm{n_{eq}\,cm^{-2}}$. Table 7.1 gives an overview of the available NIEL-irradiated LF-Monopix2 samples that were measured in the scope of this thesis. All samples measured were 100 µm thin and backside processed. Irradiation with protons were conducted at the Bonn isochronous cyclotron [150]. The TRIGA Mark II research reactor in Ljubljana [151] was employed for neutron irradiation. All devices were not powered during and annealed for 80 min at 60 °C after irradiation. Since MOS devices need to be powered to receive surface damage, the precise TID during NIEL irradiation is unknown but assumed to be negligible. The Bonn isochronous cyclotron facility is preferred due to logistic advantages that facilitate stepwise irradiations. As no long-distance shipping is necessary between the facilities in Bonn, the risk of uncontrolled annealing during transportation is significantly reduced. Furthermore, the custom beam diagnostic system implemented in the Bonn facility [80] enables

Sample	Fluence / $n_{eq}\,cm^{-2}$	Particle energy and type	Irradiation facility
A	1×10^{15}	14 MeV protons	Bonn isochronous cyclotron
B	2×10^{15}	14 MeV protons	Bonn isochronous cyclotron
C	3×10^{15}	14 MeV protons	Bonn isochronous cyclotron
D	5×10^{15}	14 MeV protons	Bonn isochronous cyclotron
E	1×10^{15}	Reactor neutron spectrum	TRIGA Mark II research reactor, Ljubljana
F	2×10^{15}	Reactor neutron spectrum	TRIGA Mark II research reactor, Ljubljana

Table 7.1: Overview of available NIEL-irradiated LF-Monopix2 samples. The received TID is assumed to be negligible since all chips were not powered during the irradiation. Each sample was annealed for 80 min at 60 °C after the irradiation.

homogeneous irradiation at relative uncertainties of less than 2 % NIEL fluence across a device. Conventional dosimetry methods applied by the other facilities have uncertainties in the order of 10 %.

7.1.1 Laboratory characterization

This section discusses the results of laboratory measurements with NIEL-irradiated LF-Monopix2 samples. The respective results after X-ray irradiation are covered in Section 7.1.2.

I-V characteristics

The I-V characteristics summarize the change in leakage current relative to the reverse bias voltage supplied to the chip. As described in Section 4.1.2, the NIEL scaling predicts a linear increase of the leakage current with fluence. Figure 7.1 shows the change in I-V characteristic with increasing NIEL fluence for LF-Monopix2. Here, no data is available for the $3 \times 10^{15}\,n_{eq}\,cm^{-2}$ sample. A reference measurement of a non-irradiated sample confirms the high breakdown above 450 V [116] and the low overall leakage current at this fluence level. After irradiation, no breakdown is observed up to 500 V at $5 \times 10^{15}\,n_{eq}\,cm^{-2}$. To prevent irreparable damage to the chips, the bias voltage was only increased up to 410 V for lower fluence levels. Subsequent detailed analysis on the change in depletion depth with NIEL fluence in Section 7.1.3 will show that the applied bias voltages were sufficient to fully deplete the sensitive volume. The expected increase in leakage current with fluence level due to bulk damage is visible across all samples. The linear nature of this increase (at around $7\,\mu A/cm^2$ per $1 \times 10^{15}\,n_{eq}\,cm^{-2}$ fluence at

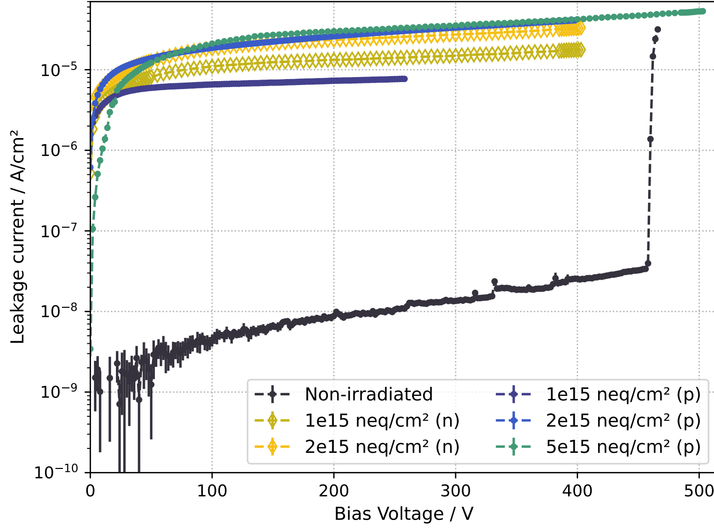

Figure 7.1: I-V characteristics of LF-Monopix2 at different NIEL fluences scaled to cm^{-2}. Due to the large increase in leakage current, the y-axis is shown on a logarithmic scale. The non-irradiated sample was measured at room temperature while all irradiated chips were cooled to $-20\,°\mathrm{C}$. Proton (p) and neutron (n) irradiated samples are marked accordingly. No data is available for the $3 \times 10^{15}\,\mathrm{n_{eq}\,cm^{-2}}$ sample.

150 V) for proton-irradiated samples up to $2 \times 10^{15}\,\mathrm{n_{eq}\,cm^{-2}}$ is in agreement with NIEL scaling (see Section 4.1.2). At $5 \times 10^{15}\,\mathrm{n_{eq}\,cm^{-2}}$ fluence, this step size predicts a leakage current of $35\,\mathrm{\mu A/cm^2}$ at 150 V. The measured $28\,\mathrm{\mu A/cm^2}$ at 150 V deviate by 20 % from the expected value for the highest fluence. In contrast, the coincidence within the error margin between proton- and neutron-irradiated I-V characteristics at $2 \times 10^{15}\,\mathrm{n_{eq}\,cm^{-2}}$ is consistent with the NIEL hypothesis. At $1 \times 10^{15}\,\mathrm{n_{eq}\,cm^{-2}}$ fluence, the leakage current of the neutron-irradiated sample exceeds the proton-irradiated one by almost a factor of two. The main source for deviations are uncertainties in the dosimetry during irradiation and, thus, the received fluence by the sample. In addition, devices such as DMAPS, that exceed the complexity of a simple diode which is used as reference for NIEL scaling, may sustain localized damage (e.g. in the periphery) that distort the scaling. This may also contribute to the presumably restricted increase in leakage current at $5 \times 10^{15}\,\mathrm{n_{eq}\,cm^{-2}}$, which is not consistent with the linear increase observed at lower fluences.

Threshold and ENC performance

Apart from the I-V characteristics, threshold and ENC are key parameters that affect the performance of a detector. As described in Section 5.3, both are extracted from a threshold scan. For each pixel, the error function of the form $N_{\mathrm{det}}(Q) = N/2\left(\mathrm{erf}\left(\frac{Q-Q_{\mathrm{thr}}}{\sqrt{2}\sigma}\right)+1\right)$ is fitted to the respective registered hit distribution. Figure 7.2 shows the resulting hit occupancy

with increasing injected charge for multiple pixels after tuning and the corresponding threshold distribution. An exemplary s-curve fit to the mean response across all pixels is visualized by

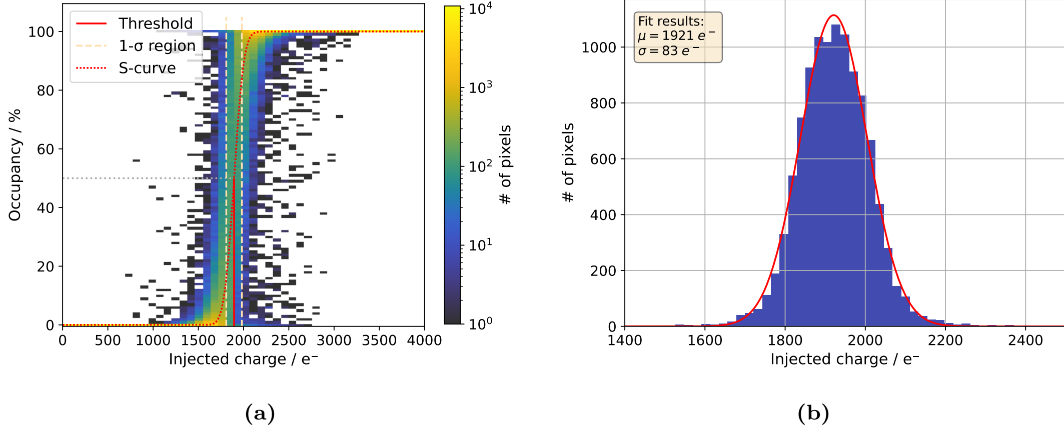

(a) **(b)**

Figure 7.2: (a) Exemplary hit occupancy with increasing injected charge for multiple pixels and (b) resulting threshold distribution measured with LF-Monopix2. As demonstrations, an s-curve is fitted to the mean hit occupancy. Additional markers visualize how threshold and ENC (1-σ region) are determined from the exemplary s-curve fit. The threshold dispersion is estimated by the Gaussian fit to the threshold distribution.

the red dotted line. If noisy pixels complicated the tuning procedure, about 0.5 %[1] of pixels are allowed to be masked. This is particularly important after irradiation, since individual pixels may become very noise due to radiation damage. In the worst case, such pixels permanently detect noise hits which spam the DAQ system and render the chip inoperable. A summary of the mean achievable operational threshold and ENC for the different matrices of LF-Monopix2 at each NIEL fluence is given in Table 7.2. Here, *achievable operational threshold* refers to front-end settings that allowed a stable operation (in test-beam conditions) across multiple hours. All measurements were performed at $-20\,°\mathrm{C}$ ambient temperature and bias voltages in the range of 100 to 200 V which sufficiently deplete the sensitive volume for all fluences. The threshold dispersion is used to quantify the error on the threshold, while the error on the ENC is estimated accordingly by the width of the noise distribution. The percentage of disabled pixels during the tuning procedure is stated for each measurement. For each fluence and front-end variant, the global registers were adjusted to achieve the best possible performance. Most importantly, the global register regulating the local tuning step size must be adapted to compensate the increased threshold variance between individual pixels after irradiation. From here on, Matrix 1-3 and Matrix 1-4 are treated as one, since no difference in performance was observed between them across non-irradiated and irradiated results. Due to time constrains, Matrix 1-2 could not be measured at the $2 \times 10^{15}\,\mathrm{n_{eq}\,cm^{-2}}$ fluence step of the proton-irradiated sample.

Up to $2 \times 10^{15}\,\mathrm{n_{eq}\,cm^{-2}}$ fluence, a systematic increase in threshold and ENC with irradiation

[1] This limit originates from the ATLAS ITk outer layer requirements.

	Fluence / $n_{eq}\,cm^{-2}$	Threshold / e^-	ENC / e^-	Disabled pixels
Matrix 1-1	0	2089 ± 52	105 ± 17	0.3 %
	1×10^{15} (p)	1990 ± 73	139 ± 13	0.1 %
	2×10^{15} (p)	2411 ± 83	188 ± 15	0.3 %
	3×10^{15} (p)	2318 ± 89	125 ± 12	0.4 %
	5×10^{15} (p)	2174 ± 78	135 ± 11	0.5 %
	1×10^{15} (n)	1845 ± 61	127 ± 13	0.4 %
	2×10^{15} (n)	2506 ± 85	174 ± 17	0.5 %
Matrix 1-2	0	2458 ± 113	117 ± 20	0.4 %
	1×10^{15} (p)	2107 ± 136	142 ± 14	0.6 %
	2×10^{15} (p)	N/A	N/A	N/A
	3×10^{15} (p)	2535 ± 148	140 ± 15	0.7 %
	5×10^{15} (p)	2373 ± 184	155 ± 19	0.3 %
	1×10^{15} (n)	1993 ± 127	148 ± 16	0.1 %
	2×10^{15} (n)	2636 ± 183	181 ± 17	0.3 %
Matrix 1-34	0	1922 ± 85	88 ± 13	0.4 %
	1×10^{15} (p)	2091 ± 114	121 ± 13	0.9 %
	2×10^{15} (p)	2051 ± 106	157 ± 26	0.3 %
	3×10^{15} (p)	2616 ± 140	130 ± 17	0.6 %
	5×10^{15} (p)	2631 ± 214	133 ± 17	0.6 %
	1×10^{15} (n)	1757 ± 102	112 ± 14	0.6 %
	2×10^{15} (n)	2432 ± 131	140 ± 14	0.5 %
Matrix 2	0	1899 ± 62	106 ± 16	1.0 %
	1×10^{15} (p)	1940 ± 90	132 ± 14	0.8 %
	2×10^{15} (p)	2174 ± 91	192 ± 17	0.7 %
	3×10^{15} (p)	2250 ± 89	121 ± 13	0.5 %
	5×10^{15} (p)	2447 ± 95	130 ± 14	0.5 %
	1×10^{15} (n)	1785 ± 75	130 ± 14	0.6 %
	2×10^{15} (n)	2280 ± 89	160 ± 18	0.4 %
Matrix 3	0	2055 ± 53	128 ± 17	0.8 %
	1×10^{15} (p)	1941 ± 77	143 ± 15	0.8 %
	2×10^{15} (p)	2391 ± 77	200 ± 17	0.6 %
	3×10^{15} (p)	2235 ± 98	124 ± 12	0.5 %
	5×10^{15} (p)	2420 ± 88	140 ± 12	0.6 %
	1×10^{15} (n)	1917 ± 65	139 ± 13	0.5 %
	2×10^{15} (n)	2316 ± 85	169 ± 17	0.5 %

Table 7.2: Mean threshold and ENC results after tuning for the individual matrices implemented in LF-Monopix2 (see Table 5.1) at all available NIEL fluences. Proton (p) and neutron (n) fluences are marked accordingly. All measurements were performed at $-20\,°C$ environmental temperature.

level is observable independent of front-end variation or particle type. The reason for this is the increase in leakage current (see Figure 7.1) and, consequently, a larger shot noise contribution with fluence [7]. While the ENC already increases at $1 \times 10^{15}\,\mathrm{n_{eq}\,cm^{-2}}$, the achievable threshold stays the same within the respective error margins. Accordingly, the operational thresholds listed in Table 7.2 are not the absolute noise limit. Early tests with non-irradiated samples showed, that operation at the noise limit in test-beam environments was not feasible. Due to the activity in the matrix, pixels would become very noisy and fire continuously. However, detailed studies on the analog monitoring signals did not show any particular cross-talk from the in-pixel electronics and this issue remains not fully understood. For fluences of 3×10^{15} and $5 \times 10^{15}\,\mathrm{n_{eq}\,cm^{-2}}$, the ENC worsens in contrast to the non-irradiated case, but stagnates or even improves compared to lower fluences. At the same time, the threshold and threshold dispersion deteriorate. It was observed, that operation at higher bias voltages noticeably increased the noise level and permanent firing of individual pixels in this case. This hints at an increased contribution of shot noise, which is also in agreement with the higher leakage currents present at these fluences. Furthermore, it needs to be considered that the adjustments of the (global) front-end settings required by large radiation damage at these fluences impacts the threshold and ENC performance. At larger fluences, an increase in feedback current is necessary to counteract the longer charge collection times due to bulk damage effects (see Section 4.1). This adjustment can partially compensate the higher leakage currents by stabilizing the baseline at the amplifier input node. Nevertheless, there is a higher probability that the radiation damage received by individual pixels at such fluences cannot be compensated by adjustments to the front-end settings anymore. The threshold of such pixels may not be recoverable by the local tuning and will require masking of pixels in the tuning procedure.

Comparing the threshold dispersion between the different front-end variants highlights the performance enhancement from the bidirectional discriminator tuning. While the threshold dispersion increases to more than $200\,\mathrm{e^-}$ for the unidirectional tuning after irradiation, it remains below $100\,\mathrm{e^-}$ for all fluences in the case of the bidirectional tuning. A lower threshold dispersion directly implies an improvement in the mean threshold through the (local) tuning procedure. This degradation explains the significant increase in threshold experienced already at $3 \times 10^{15}\,\mathrm{n_{eq}\,cm^{-2}}$ NIEL fluence in the case of the unidirectional tuning front-end variants. Furthermore, the advantage of a lower ENC in the case of the unidirectional tuning circuit ($88\,\mathrm{e^-}$ for Matrix 1-34) before irradiation is reduced as the radiation level increases.

The comparison between proton- and neutron-irradiated samples up to a fluence of $2 \times 10^{15}\,\mathrm{n_{eq}\,cm^{-2}}$ shows consistent behavior of both threshold and ENC within the margin of error. Only the achieved thresholds of Matrix 1-34 deviate beyond the error margin for each respective fluence. At $1 \times 10^{15}\,\mathrm{n_{eq}\,cm^{-2}}$ fluence, the proton-irradiated sample required an unusually high number of $0.9\,\%$ of pixels masked during tuning, compared to $\leq 0.6\,\%$ for all other tuned configurations of this matrix. This may be caused by deviating operational conditions or chip configurations due to the complex nature of the measurement. Thus, it is no explicit indicator

Front-end variant	Analog / mW	Digital / mW	EoC logic / mW	VPC / mW	DAC reference / mW
Matrix 1-1	20.19	9.39	16.82	0.18	8.9×10^{-3}
Matrix 1-2	20.19	9.39	16.83	0.18	9.5×10^{-3}
Matrix 1-34	59.92	7.77	16.82	0.18	8.8×10^{-3}
Matrix 2	24.51	9.39	16.83	0.18	9.5×10^{-3}
Matrix 3	23.97	9.75	16.83	0.18	8.9×10^{-3}

Table 7.3: Power consumption of the low-voltage power domains for all front-end variants in LF-Monopix2 before X-ray irradiation.

for the performance degradation of the chip at this fluence. At $2 \times 10^{15}\,\mathrm{n_{eq}\,cm^{-2}}$ fluence, the threshold of the neutron-irradiated sample exceeds the one of the proton-irradiated sample with respect to the respective error margins while similar amounts of pixels were disabled. In both cases, it seems likely that the adjustment of the global front-end settings and, thus, the tuning procedure was not optimized for the individual samples.

7.1.2 X-ray irradiation of LF-Monopix2

The X-ray irradiation of LF-Monopix2 was split into two separate campaigns, both of which were performed at the irradiation setup described in Section 6.1. In the scope of the first campaign, a sample was irradiated to 100 Mrad in accordance with the design target. This campaign was split into 16 irradiation steps logarithmically distributed across the TID range, between which a standardized measurement procedure was performed. After 100 Mrad was reached, the sample was annealed for 80 min at 60 °C to replicate the post-irradiation procedure of NIEL-irradiated chips. Subsequently, extensive tests on the recovery of the surface damaged front-end performance were conducted. Planned beam tests at this TID could not be realized due to limitations of available beam times at the respective facilities. Subsequently, the same chip was irradiated further to 400 Mrad in seven steps to investigate the maximum radiation tolerance of the electronics. During both irradiation campaigns, the sample was cooled to 0 °C.

Throughout the entire irradiation campaign, the power consumption of all low-voltage power domains was monitored. Apart from digital and analog supply voltages for the matrix, LF-Monopix2 requires powering of the end-of-column (EoC) logic and the pre-charge (VPC) for the column bus. In addition, a reference current for the DAC registers is provided. The power consumption of each domain before X-ray irradiation is listed in Table 7.3 for each front-end variant. The peripheral power domains (EoC logic, VPC, and DAC reference) show no difference between the individual front-ends, as is expected. The analog and EoC logic domains are the dominant contributors to the overall power consumption. It needs to be considered that the former scales with the number of enabled pixels, which explains the noticeably larger value measured for Matrix 1-34.

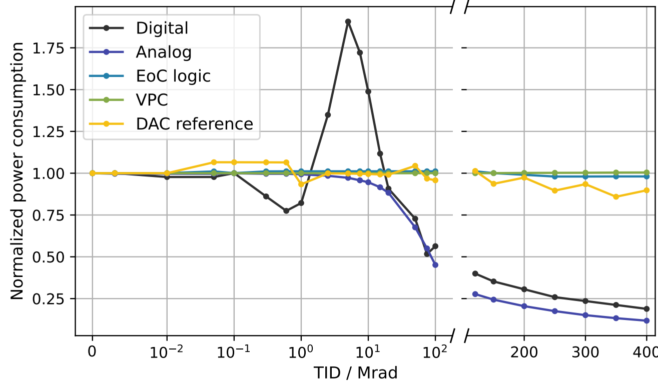

Figure 7.3: Normalized power consumption of all power domains of LF-Monopix2 throughout the X-ray irradiation measured with Matrix 1-34. The separation of the x-axis indicates the break between the two irradiation campaigns.

The relative change of each low-voltage power domain with increasing TID is visualized in Figure 7.3 for Matrix 1-34 as an example. Up to 100 Mrad TID, no changes in power consumption are observed for the peripheral power domains. From these three domains, only the consumption of the DAC reference starts to decrease slightly during the irradiation to 400 Mrad. Significantly more change with increasing TID is measured for the analog and digital power supplied to the matrix. Between 0.1 and 1 Mrad, the digital power consumption decreases around 25 % before almost doubling between 1 and 10 Mrad. Subsequently, this value drops continuously as the irradiation continues. At 400 Mrad TID, less than a quarter of the initial digital power is consumed by the matrix. In the case of the analog power domain, only the reduction in power consumption starting around 10 Mrad is observed. Similar to its digital counterpart, the measured consumption drops below a quarter of the initial value.

Changes in threshold voltage of MOS transistors due to surface damage alter the leakage current of the device and, thus, its power consumption. As described in Section 4.2.3, NMOS transistors of the relevant technology feature size first experience a decrease in threshold voltage caused by the accumulation of oxide trapped charges. Subsequently, trapping of negative charges at the Si-SiO_2 interface counteracts this decrease and becomes dominant for larger TID. In the case of PMOS devices, both effects contribute to an increase of the threshold voltage. Since the digital in-pixel electronics of LF-Monopix2 uses NMOS transistors, the resulting characteristic spike in power consumption caused by the described rebound effect is observed [102]. The analog in-pixel electronics is implemented with PMOS transistors exclusively, which only lead to the decrease of the power consumption. This behavior is also in agreement with measurements of the predecessor LF-Monopix1 [107].

For the significantly changing matrix power domains, a comparison between the respective relative change for all front-end variants is shown in Figure 7.4. For both power domains,

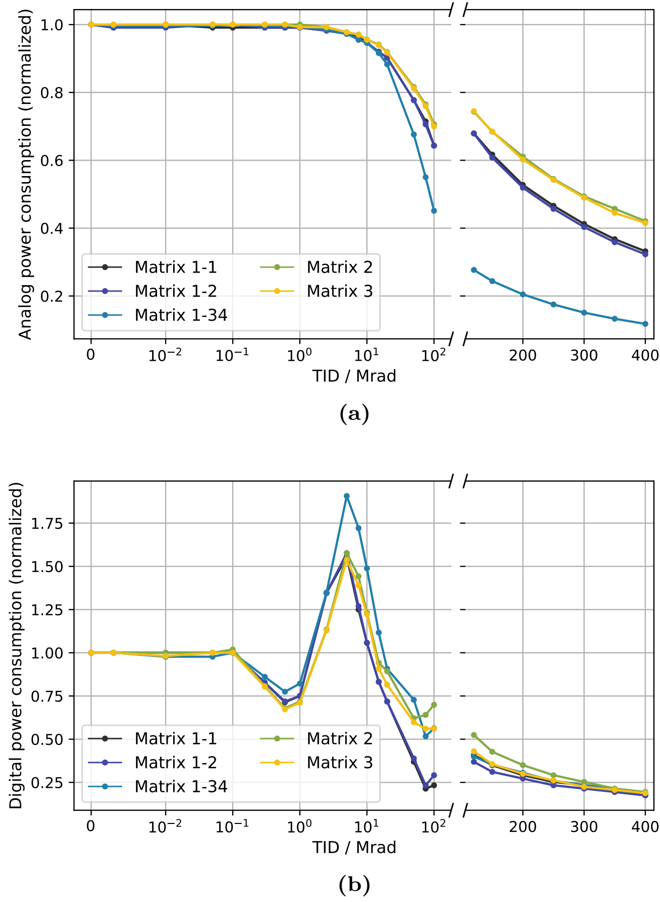

Figure 7.4: Normalized power consumption of the (a) analog and (b) digital power domain for all front-end variants of LF-Monopix2 throughout the X-ray irradiation. The separation of the x-axis indicates the break between the two irradiation campaigns.

inconsistencies in the relative change are noticeable between 100 and 120 Mrad TID. This is explained by the break between the two individual irradiation campaigns, in which additional controlled and uncontrolled annealing happened. In the case of the digital power domain, the largest relative spike in power consumption is measured for Matrix 1-34. For the other front-end variants, the relative increase is only about 50 %. After irradiation to 400 Mrad TID, all variations experience the same drop below 25 % of the initial digital power consumption. The analog power consumption shares the same trend for all front-ends, but differs in the extent of the decrease. For larger absolute values before irradiation, a greater relative drop is observed. As stated previously, the absolute consumption of this power domain depends also on the amount of enabled pixels. This correlation can be recognized again in the graph. Consequently, it cannot be concluded that Matrix 1-34 is more prone to surface damage from these results.

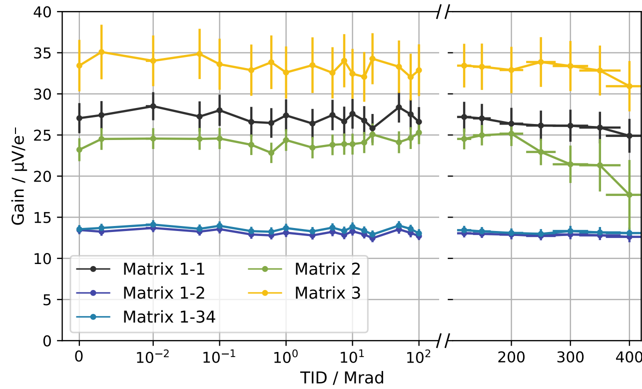

Figure 7.5: Measured gain of all front-end variants of LF-Monopix2 throughout the X-ray irradiation. The impact of the lower feedback capacitance (see Table 5.1) on the amplifier gain is evident. The separation of the x-axis indicates the break between the two irradiation campaigns.

Apart from the power consumption, the gain and threshold configuration of the front-end electronics is monitored throughout the irradiation campaign. Figure 7.5 displays the amplifier gain with increasing TID measured for each front-end variant. Here, the gain was determined on a per-pixel basis from the change in unbiased[2] threshold scans at different global discriminator threshold settings. The width of the resulting Gaussian distribution is interpreted as the corresponding uncertainty. The increase in amplifier gain by reduction of the feedback capacitance is clearly visible in the figure. Up to 100 Mrad TID, the gain stays constant within the uncertainty for all front-end variations. During the continuation of the irradiation to 400 Mrad TID, a tendency of gain degradation is apparent for variants equipped with the smaller feedback capacitance. Most affected is Matrix 2, which also exhibits the largest increase in per-pixel fluctuations. The latter is evident in the increasing uncertainty towards the end of the irradiation campaign. For front-end variants with larger feedback capacitance, the gain remains constant even at this TID.

Since the time for an X-ray irradiation campaign is limited by the availability of the setup, it was decided against the optimization of the front-end parameter settings after each irradiation step. Instead, the change of an initial threshold configuration tuned before the irradiation was monitored, where the threshold dispersion was used as an indicator for the received surface damage. Retuning of the threshold configuration was used to test the potential for compensation of the received radiation damage by adjustment of global register settings. With respect to the threshold dispersion, the adjusted register was the local tuning step size. Figure 7.6 shows the degradation in initial threshold dispersion and the retuned one after each irradiation step. Due to the increasing extent of surface damage, the initial threshold configuration was only measured

[2] In this case, unbiased refers to the local threshold tuning transistors which, in return, do not influence the threshold of a pixel.

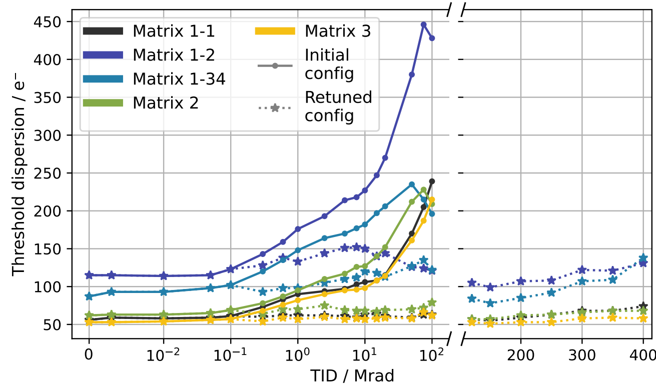

Figure 7.6: Measured threshold dispersion of all front-end variants of LF-Monopix2 throughout the X-ray irradiation. The change of the initial front-end configuration and a retuned one with adjusted global and local chip settings were measured after each irradiation step. The separation of the x-axis indicates the break between the two irradiation campaigns.

throughout the first irradiation campaign. A degradation of close to 50 % is observed for all front-end variations starting at an ionizing dose of 0.6 Mrad. This is consistent with the change monitored in the digital power domain due to the implemented NMOS transistor. At 100 Mrad TID, the threshold dispersion of the initial configuration doubled for Matrix 1-34 and increased by at least a factor of 3.5 for all other front-end variants. The lower power consumption in both digital and analog domain suggests that the front-end transistors are no longer operated at their intended operating points. Retuning the threshold configuration facilitated a reduction of this rise to around 50 % in the worst case of Matrix 1-34 after 400 Mrad. It needs to be emphasized that this measurement does not include a detailed optimization of the global front-end settings to compensate the received surface damage. This analysis is a quantitative characterization of the change in performance of the readout electronics and the possibility to counteract it. Thus, similar investigations on the ENC and threshold degradation after each irradiation step are not very meaningful.

The time-consuming optimization of the front-end settings to readjust the operating points of the transistors was only performed after reaching the maximum TID of each individual campaign and annealing the chip for 80 min at 60 °C. Adjustments to the reference current for the DAC registers proved to be most effective to recover the performance degradation. To restore the non-irradiated performance of the transistors, the reference current was increased from 8 µA to 10 µA or 11 µA depending on the front-end variant. Table 7.4 summarizes the change in mean achievable threshold and ENC after 100 Mrad and 400 Mrad TID. Again, the threshold dispersion and the width of the ENC distribution define the respective uncertainties. At an ionizing dose of 100 Mrad, the ENC increased between 18.5 % and 33.3 % depending on the front-end variant. Due to surface damage (see Section 4.2), the working point of each

TID	Front-end	Threshold / e^-	ENC / e^-	Disabled pixels
0 Mrad	Matrix 1-1	2089 ± 52	113 ± 15	0.3 %
	Matrix 1-2	2448 ± 113	117 ± 16	0.4 %
	Matrix 1-34	2076 ± 85	90 ± 11	0.1 %
	Matrix 2	1993 ± 59	105 ± 18	0.4 %
	Matrix 3	2188 ± 47	124 ± 19	0.3 %
100 Mrad	Matrix 1-1	2087 ± 56	136 ± 14	0.3 %
	Matrix 1-2	2092 ± 132	146 ± 18	0.3 %
	Matrix 1-34	1915 ± 100	120 ± 12	0.2 %
	Matrix 2	1908 ± 68	135 ± 14	0.3 %
	Matrix 3	1990 ± 50	147 ± 15	0.3 %
400 Mrad	Matrix 1-1	2145 ± 69	184 ± 18	0.9 %
	Matrix 1-2	2868 ± 128	215 ± 13	0.7 %
	Matrix 1-34	1865 ± 142	140 ± 14	0.6 %
	Matrix 2	1723 ± 65	145 ± 12	0.4 %
	Matrix 3	2123 ± 53	150 ± 12	0.4 %

Table 7.4: Mean threshold and ENC results after tuning for each front-end variant implemented in LF-Monopix2 (see Table 5.1) after X-ray irradiation to 100 Mrad and 400 Mrad TID, respectively. All measurements were conducted at 0 °C and after annealing of 80 min at 60 °C.

individual transistor is distorted. This leads to changes in response of each front-end readout electronics, which cannot entirely be compensated by adjustments to the global chip. Additional leakage currents in the transistors (as described in Section 4.2.3) implemented in the front-end electronics contribute to this degradation. Despite the higher ENC, comparable thresholds were achieved within the uncertainty across all front-ends while disabling a similar amount of pixels. Also, the corresponding threshold dispersions were close to the non-irradiated values. The front-end variants equipped with the unidirectional discriminator tuning circuit suffered the worst degradation at around 17 % increase. A recalibration of the charge injection circuit at 100 Mrad TID revealed no alteration of the injection circuit at this dose.

After X-ray irradiation to 400 Mrad TID, a further increase of the ENC between 21.0 % and 83.8 % compared to the non-irradiated values was observed. The largest increase was measured for Matrix 1-2, which is also the only front-end that experienced a substantial increase in threshold. For all other front-end variants, similar thresholds as before irradiation were achieved within the margin of error. However, the matrices equipped with the original charge-sensitive amplifier of the predecessor (see Table 5.1) required more masked pixels to accomplish this compared to the non-irradiated case. This is also emphasized by the larger increase in threshold dispersion observed for these front-end variants. In the case of Matrix 2 and Matrix 3, no

significant change in threshold dispersion and required masked pixels was observed throughout the second irradiation campaign. Correspondingly, both front-ends suffered the smallest increase in ENC between 100 to 400 Mrad. It must be noted, that no recalibration of the charge injection circuit was performed at 400 Mrad TID. Consequently, the actual values of threshold and ENC may differ. Since the injected charge is set by the difference between two independent voltages, which are predicted to degrade similarly, the effective change of the calibration result is expected to be small.

7.1.3 Beam test results of LF-Monopix2

This section evaluates the radiation hardness of LF-Monopix2 based on the performance in beam test environments. A focus is put on the measured hit-detection and in-time efficiencies that were achieved at the different irradiation levels. All irradiated devices were cooled using the portable cooling setup described in Section 6.2.1. While the X-ray-irradiated chip was cooled to $-10\,°\mathrm{C}$ environmental temperature, the NIEL-irradiated samples were measured at $-20\,°\mathrm{C}$ to reduce the significantly increased leakage current induced by bulk damage.

Depletion depth measurement after NIEL irradiation

As described in Section 4.1, bulk damage degrades the charge collection capabilities of semiconductor sensors. Due to the increased charge carrier trapping probability with higher fluences, depleting the sensitive volume is essential to optimize the tracking performance. However, the change in effective doping concentration requires larger bias voltages to reach similar depletion depths as before irradiation. Studies on the depletion depth against applied bias voltage are relevant to understand the performance of sensors after NIEL irradiation. In the case of LF-Monopix2, these studies were conducted utilizing an electron beam at the introduced test-beam facilities in Section 6.2. The depletion depth is calculated from the Landau-shaped charge spectrum (see Section 2.2) of an electron beam, in which the electrons can be considered as MIPs. Such an exemplary charge spectrum measured with a fully depleted LF-Monopix2 chip is shown in Figure 7.7a. The charge MPV is extracted by fitting the convolution of a Landau and a Gaussian distribution to the spectrum. The Gaussian contribution is needed due to smearing effects due to electrical noise or digitization artifacts in the detector readout. As discussed in Section 2.1, the average energy loss depends on the thickness of the detector. Rearranging Eq. (2.4) provides the correlation between detector thickness and most probable energy deposition for a given material and particle type and energy [11]. Figure 7.7b shows the most probable number of electron-hole pairs created for different thicknesses of silicon in the case of an impinging 5 GeV electron beam. Considering that the value must be an integer, this yields an MPV of 71 electron-hole pairs created in 100 µm thick LF-Monopix2 sensors. Thus, a depletion thickness of $\frac{6021\,\mathrm{e}^-}{71\,\mathrm{e}^-/\mu\mathrm{m}} = 84.8\,\mu\mathrm{m}$ is estimated for the exemplary charge spectrum. The dominant uncertainty contribution in this analysis is the binning of the charge spectrum

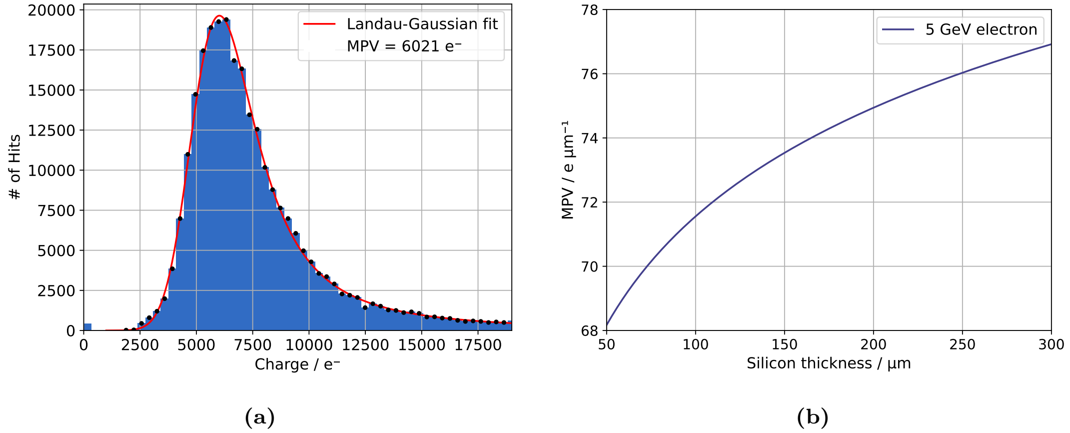

(a) **(b)**

Figure 7.7: (a) Exemplary charge spectrum of a 5 GeV electron beam measured with LF-Monopix2 and (b) estimation of the number of generated electron-hole pairs by an impinging particle for different silicon thicknesses. The convolution of a Landau and a Gaussian distribution is fitted to the spectrum to extract the most probably charge value. For 100 µm thick silicon detectors, 71 electron-hole pairs are most probably created by a traversing 5 GeV electron.

defined by the time-over-threshold resolution of the detector. In this case, the bin width of 342 e^- results in an uncertainty of 2.4 µm on the calculated depletion depth.

The resulting depletion depth against bias voltage measured across multiple test-beam campaigns is shown in Figure 7.8a collectively for all available NIEL fluences. Previous measurements with LF-Monopix2 have shown that passivation and metal layers occupy about 15 µm of the total thickness [116]. Thus, the maximum achievable depletion depth is around 85 µm for 100 µm thin samples, which is indicated in the figure. The graph demonstrates that the sensitive volume of LF-Monopix2 can be fully depleted up to fluences of $3 \times 10^{15}\,\mathrm{n_{eq}\,cm^{-2}}$. An essential factor for this is the improved guard-ring design and the associated increase in breakdown voltage compared to the predecessor. In the non-irradiated case, 20 V bias voltage are sufficient to fully deplete the sensitive volume. After irradiation to $3 \times 10^{15}\,\mathrm{n_{eq}\,cm^{-2}}$ fluence, more than 250 V are necessary, which is above the breakdown voltage of the predecessor chip [116]. At $5 \times 10^{15}\,\mathrm{n_{eq}\,cm^{-2}}$ fluence, the received bulk damage is so severe that charge trapping and changes in the effective doping concentration prevent full depletion. The latter also explains the systematic increase in the required bias voltage to reach maximum depletion with NIEL fluence.

Furthermore, different characteristics in the depletion depth are measured between proton- and neutron-irradiated samples at the same fluence. The results shown in Figure 7.8a imply that the radiation damage caused by $3 \times 10^{15}\,\mathrm{n_{eq}\,cm^{-2}}$ NIEL fluence of protons coresponds to between 1×10^{15} and $2 \times 10^{15}\,\mathrm{n_{eq}\,cm^{-2}}$ NIEL fluence of neutrons. This is contrary to the expectation of NIEL scaling. However, the NIEL hypothesis is based on the comparison of changes in leakage currents against fluence for simple diodes, as described in Section 4.1.2.

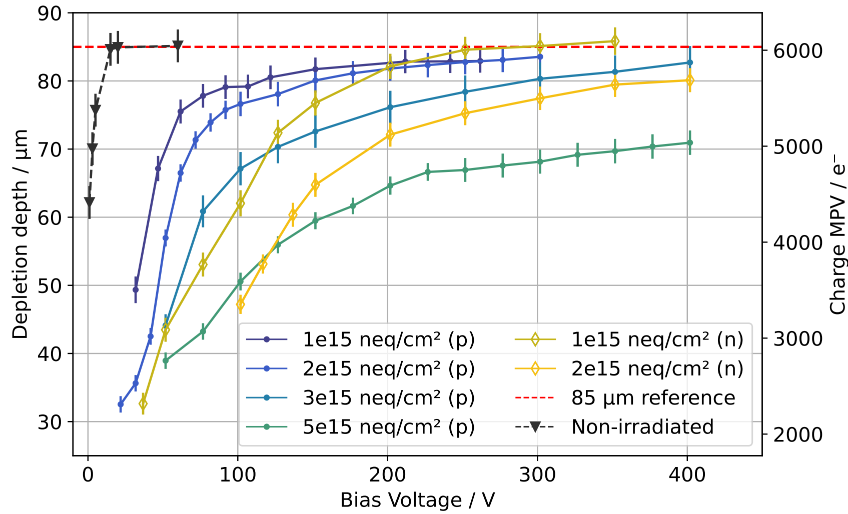

(a)

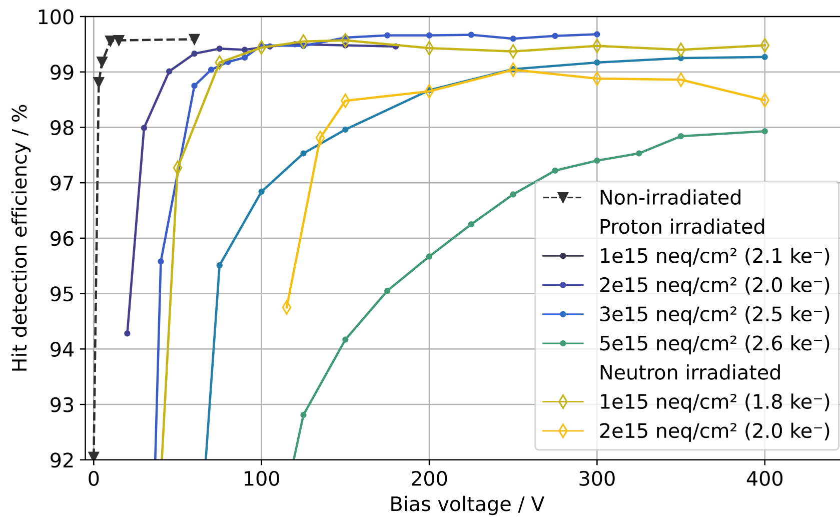

(b)

Figure 7.8: (a) Depletion depth and (b) corresponding hit-detection efficiency versus bias voltages for all available NIEL fluences. Since the depleted volume is a sensor property independent of the front-end variant, this measurement is only performed for Matrix 1-34. The mean threshold of each sample is given in parentheses in the efficiency plot. There is a clear correlation between depletion depth and hit-detection efficiency.

For complex devices and measurements not related to leakage current as presented here, it is apparent that the NIEL hypothesis does not sufficiently account for distinctions in radiation damage caused by different particle types or energies [75].

The extent of the depleted volume significantly affects the (fast) charge collection and, thus, the hit-detection efficiency of the silicon detector (see Section 3.3). The corresponding hit-detection efficiency at different bias voltages of the aforementioned depletion depth study is shown in Figure 7.8b. For all fluences, an improvement in hit-detection efficiency with increased depletion depth is observed. The corresponding threshold and ENC settings are listed in Table 7.2. The hit-detection efficiencies were calculated for the activated pixels only of each tuning, respectively. At (close to) full depletion, hit-detection efficiencies larger than 99 % were measured for fluences up to $3 \times 10^{15}\,\mathrm{n_{eq}\,cm^{-2}}$ protons and $2 \times 10^{15}\,\mathrm{n_{eq}\,cm^{-2}}$ neutrons. The sample irradiated to $5 \times 10^{15}\,\mathrm{n_{eq}\,cm^{-2}}$ fluence still achieved close to 98 % hit-detection efficiency at 400 V bias voltage. This is a very promising result considering that it is more than three times the initial fluence target and the threshold of $(2631 \pm 214)\,\mathrm{e^-}$ is relatively high.

Similar to the measured depletion depths, the hit-detection efficiency curves with bias voltage differ between proton- and neutron-irradiated samples of the same fluence. In this case, the performance of the $1 \times 10^{15}\,\mathrm{n_{eq}\,cm^{-2}}$ neutron- and $2 \times 10^{15}\,\mathrm{n_{eq}\,cm^{-2}}$ proton-irradiated samples are relatively equal. The results of the $2 \times 10^{15}\,\mathrm{n_{eq}\,cm^{-2}}$ neutron sample would correspond to a NIEL fluence between 3×10^{15} to $5 \times 10^{15}\,\mathrm{n_{eq}\,cm^{-2}}$. This is expected since the change in effective doping concentration (see Section 4.1.3) is different for point-like and clustered defects, and, thus, also for proton and neutron irradiation [77]. It also supports the previous observation that NIEL scaling cannot accurately quantify complex parameters beyond leakage current. In addition, for both neutron-irradiated samples the hit-detection efficiency drops slightly for increasing bias voltages, after reaching its respective maximum. In the worst case, the difference is 0.5 % between 250 and 400 V for a NIEL fluence of $2 \times 10^{15}\,\mathrm{n_{eq}\,cm^{-2}}$. Especially for the latter, it was difficult to find appropriate front-end settings and maintain stable operation throughout a beam test. Activity in the matrix repeatedly led to rapidly, firing noisy pixels which disturbed the data acquisition. This got progressively worse for larger bias voltages and the corresponding increased leakage currents.

It needs to be considered that the samples vary up to $700\,\mathrm{e^-}$ in threshold within this measurement, which is more than 10 % of the charge MPV at full depletion. While charge collection degrades after irradiation, the hit-detection performance is also impaired by higher thresholds. The latter is equally an effect of radiation damage as discussed in Section 7.1.1. Studies have shown that the hit-detection efficiency starts to drop at thresholds larger than $3000\,\mathrm{e^-}$ for 100 µm thick LF-Monopix2 chips before irradiation [116]. This effect is expected to increase after irradiation as the charge collection efficiency decreases.

In addition, the noise hit rate affects the threshold configuration and hit-detection efficiency of the detector. The noise hit rate is calculated for the number of noise hits detected per pixel over a given time period (here 300 s) [28]. Figure 7.9 visualizes the measured noise hit rates

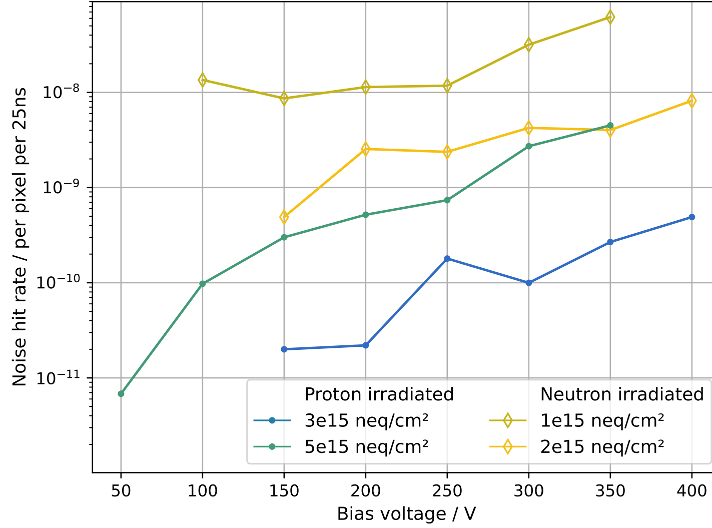

Figure 7.9: Noise hit rate of Matrix 1-34 of LF-Monopix2 for different bias voltages after irradiation. Neutron-irradiated samples (at lower NIEL fluence) show a noticeably higher noise hit rate than proton-irradiated ones. No data is available for proton-irradiated samples at fluences below $3 \times 10^{15}\,\mathrm{n_{eq}\,cm^{-2}}$.

for various bias voltages at different NIEL fluences. Across all samples, an increase in noise hit rate for higher bias voltages is observed due to the larger leakage currents (see Figure 7.1). In the case of proton-irradiated samples, the noise hit rate increases with fluence level. While the same is expected for the neutron-irradiated chips, the $1 \times 10^{15}\,\mathrm{n_{eq}\,cm^{-2}}$ fluence sample performs worse compared to the $2 \times 10^{15}\,\mathrm{n_{eq}\,cm^{-2}}$ fluence one in this regard. Likely, this is explained by chip-to-chip variations and difficulties in finding the optimal operational settings for the $1 \times 10^{15}\,\mathrm{n_{eq}\,cm^{-2}}$ fluence sample. Furthermore, neutron-irradiated samples show a significantly higher noise hit rate compared to the proton-irradiated ones, considering the NIEL fluences shown in Figure 7.9 are higher for the latter.

As discussed in Section 6.2.3, noise hits in the DUT can affect the analysis of the hit-detection efficiency. Calculations of the overestimation of the hit-detection efficiency for different beam and noise hit rates are discussed in detail in [28]. In this publication, an overestimation of around 0.01 % is estimated for an event window of 10 µs and a noise hit rate around 5×10^{-9} per pixel per 25 ns at typical beam rates. The shorter event association time cut of 1 µs for the LF-Monopix2 data stream yields an overestimation of less than 0.01 % for even higher noise hit rates up to 1×10^{-7} per pixel per 25 ns. Consequently, the high noise hit rates (especially after neutron irradiation) only marginally alter the uncertainty of the efficiency calculation and the estimated overall systematic uncertainty of 0.05 % remains dominant.

Hit-detection efficiency after NIEL irradiation

Based on the measured depletion depth curve for each NIEL fluence, the optimized performance of each front-end variant implemented in LF-Monopix2 can be compared. The applied bias voltage is configured such that the sensitive volume is fully depleted for each irradiation level. The results across all fluences and front-end variants are summarized in Table 7.5. Apart from the mean hit-detection efficiency, the ratio of hits detected within a 25 ns time window after the trigger signal (labeled as in-time ratio), the noise hit rate, and the applied bias voltage are listed for each front-end variation. The corresponding threshold and ENC of each measurement are shown in Table 7.2. As in the previous analysis, the hit-detection efficiency was determined from the activated pixels only. It must be considered that deviations in threshold result in changes of performance. Especially after irradiation, it was not always possible to precisely match the threshold between different front-ends.

Table 7.5 shows that all front-ends except Matrix 1-34 maintain a very good hit-detection efficiency larger than 99 % after irradiation to the highest fluence. For all front-end variants, the induced bulk damage at higher fluences is counteracted by increasing the bias voltages from 60 V up to 400 V as confirmed in the depletion depth study. At $1\times10^{15}\,\mathrm{n_{eq}\,cm^{-2}}$ fluence, the measured hit-detection efficiency was above 99 % across all front-end variations and irradiation particle types. This constitutes an improvement to the predecessor LF-Monopix1, which achieved 98.9 % hit-detection efficiency at this NIEL fluence [114]. The main reason for this is the reduced pixel pitch (see Section 5.1), which results in a smaller detector capacitance and larger signal-to-noise ratio (see Section 5.1). The degradation in hit-detection efficiency to below 98 % for Matrix 1-34 at the highest NIEL fluence is partially explained by high threshold of $(2631 \pm 214)\,\mathrm{e^-}$. While a threshold increase at this fluence is observed for all front-end variants, the matrices with unidirectional discriminator tuning also suffer a more severe degradation in threshold dispersion. Despite this drop, the hit-detection efficiency of Matrix 1-34 measured at $5\times10^{15}\,\mathrm{n_{eq}\,cm^{-2}}$ NIEL fluence is still very promising, since this fluence exceeds the design target by more than a factor of three (see Section 3.4). At lower fluences, only Matrix 1-2 irradiated to $3\times10^{15}\,\mathrm{n_{eq}\,cm^{-2}}$ fluence exhibits a hit-detection efficiency of less than 99 %. This decline may be explained by a not optimized front-end configuration and deviations in the operational conditions during this complex measurement. The least degradation is observed for Matrices 1-1 and 3 where the hit-detection efficiency is above 99.5 % across all fluences.

For the three largest matrices (Matrix 1-34, Matrix 2, and Matrix 3), the corresponding noise hit rates of the different irradiated samples follow the same pattern as discussed in the previous section. In the case of Matrix 1-1 and Matrix 1-2, no data is available for the neutron-irradiated samples. Furthermore, Matrix 1-2 is the only front-end that detected a larger noise hit rate at $3\times10^{15}\,\mathrm{n_{eq}\,cm^{-2}}$ NIEL fluence compared to $5\times10^{15}\,\mathrm{n_{eq}\,cm^{-2}}$. This is consistent with the experienced difficulties in tuning that resulted in a higher threshold despite a larger amount of masked pixels for the lower fluence (see Table 7.2). Since the other front-end variants do

	Fluence / $n_{eq}\,cm^{-2}$	Hit-detection efficiency	In-time ratio	Noise hit rate / $25\,ns^{-1}pixel^{-1}$	Bias voltage / V
Matrix 1-1	0	99.60 %	99.49 %	$< 1 \times 10^{-12}$	60
	1×10^{15} (p)	99.79 %	99.72 %	N/A	150
	2×10^{15} (p)	99.82 %	99.75 %	N/A	300
	3×10^{15} (p)	99.67 %	99.54 %	1.72×10^{-11}	250
	5×10^{15} (p)	99.77 %	99.56 %	1.20×10^{-9}	400
	1×10^{15} (n)	99.84 %	99.80 %	N/A	250
	2×10^{15} (n)	99.61 %	98.75 %	N/A	250
Matrix 1-2	0	N/A	N/A	N/A	N/A
	1×10^{15} (p)	99.50 %	99.40 %	N/A	150
	2×10^{15} (p)	N/A	N/A	N/A	N/A
	3×10^{15} (p)	98.10 %	97.89 %	1.61×10^{-9}	250
	5×10^{15} (p)	99.70 %	99.57 %	1.36×10^{-10}	400
	1×10^{15} (n)	99.79 %	99.73 %	N/A	250
	2×10^{15} (n)	99.29 %	98.59 %	N/A	250
Matrix 1-34	0	99.59 %	99.43 %	6.70×10^{-11}	60
	1×10^{15} (p)	99.47 %	99.15 %	N/A	150
	2×10^{15} (p)	99.66 %	98.45 %	N/A	275
	3×10^{15} (p)	99.27 %	96.80 %	4.90×10^{-10}	400
	5×10^{15} (p)	97.84 %	93.64 %	4.50×10^{-9}	400
	1×10^{15} (n)	99.57 %	98.63 %	8.65×10^{-9}	150
	2×10^{15} (n)	99.04 %	96.86 %	2.37×10^{-9}	250
Matrix 2	0	99.85 %	99.76 %	$< 1 \times 10^{-12}$	60
	1×10^{15} (p)	99.66 %	99.55 %	N/A	150
	2×10^{15} (p)	99.69 %	99.57 %	N/A	300
	3×10^{15} (p)	99.28 %	99.21 %	5.01×10^{-10}	250
	5×10^{15} (p)	99.46 %	99.38 %	7.39×10^{-10}	400
	1×10^{15} (n)	99.73 %	99.64 %	5.10×10^{-9}	250
	2×10^{15} (n)	99.46 %	98.95 %	2.46×10^{-10}	250
Matrix 3	0	99.63 %	99.58 %	1.05×10^{-12}	60
	1×10^{15} (p)	99.73 %	99.65 %	N/A	150
	2×10^{15} (p)	99.74 %	99.60 %	N/A	250
	3×10^{15} (p)	99.72 %	99.67 %	1.67×10^{-10}	250
	5×10^{15} (p)	99.71 %	99.63 %	3.90×10^{-10}	400
	1×10^{15} (n)	99.82 %	99.79 %	1.82×10^{-9}	250
	2×10^{15} (n)	99.58 %	99.11 %	5.27×10^{-10}	250

Table 7.5: Mean hit-detection efficiency and in-time ratio for the individual matrices implemented in LF-Monopix2 (see Table 5.1) at all available NIEL fluences. Proton (p) and neutron (n) fluences are marked accordingly. All NIEL-irradiated measurements were performed at $-20\,°C$ environmental temperature. A dominant systematic uncertainty of 0.05 % is estimated for all efficiency values.

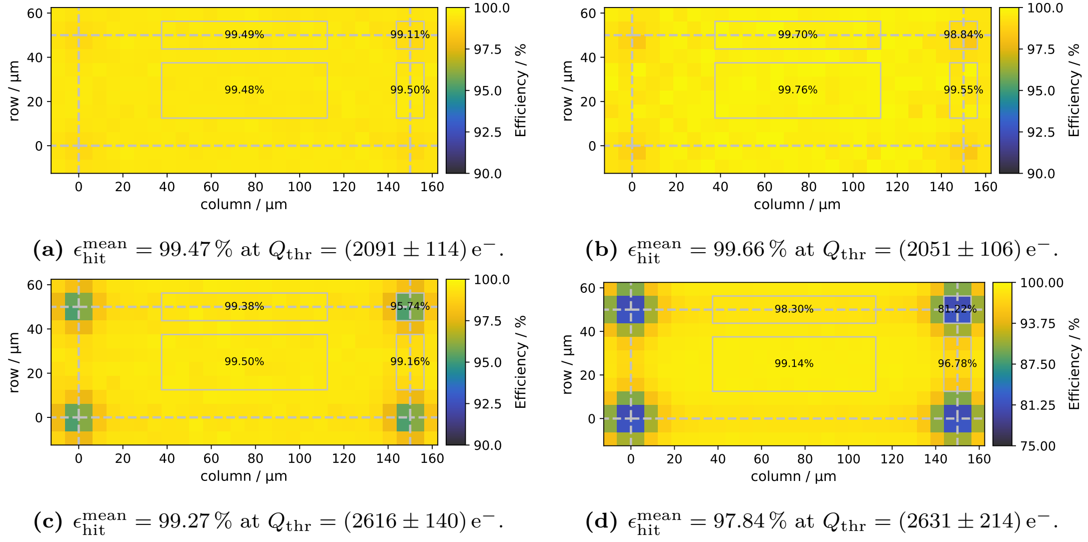

(a) $\epsilon_{\mathrm{hit}}^{\mathrm{mean}} = 99.47\,\%$ at $Q_{\mathrm{thr}} = (2091 \pm 114)\,\mathrm{e}^{-}$.

(b) $\epsilon_{\mathrm{hit}}^{\mathrm{mean}} = 99.66\,\%$ at $Q_{\mathrm{thr}} = (2051 \pm 106)\,\mathrm{e}^{-}$.

(c) $\epsilon_{\mathrm{hit}}^{\mathrm{mean}} = 99.27\,\%$ at $Q_{\mathrm{thr}} = (2616 \pm 140)\,\mathrm{e}^{-}$.

(d) $\epsilon_{\mathrm{hit}}^{\mathrm{mean}} = 97.84\,\%$ at $Q_{\mathrm{thr}} = (2631 \pm 214)\,\mathrm{e}^{-}$.

Figure 7.10: Hit-detection efficiency of LF-Monopix2 projected onto a single pixel cell for in-pixel studies for 1×10^{15}, 2×10^{15}, 3×10^{15}, and $5 \times 10^{15}\,\mathrm{n_{eq}\,cm^{-2}}$ NIEL fluence from (a) to (d). The respective bias voltages are 150, 275, 400, and 400 V. Here, only proton-irradiated samples are shown. The displayed results are measured with Matrix 1-34 but represent the trend for all front-end variants. While the pixel centers remain very efficient at all fluences, the hit-detection efficiency in the pixel corners decreases significantly with radiation level. Note that the lower limit of the color scale changed from 90 % to 75 % in (d).

not share this behavior, the aforementioned explanation of an insufficiently optimized front-end configuration is corroborated. Nevertheless, the short event association time cut reduces the contribution to the efficiency uncertainty of noise hits in the DUT to less than 0.01 % across all samples and front-end variants. Therefore, no adjustment of the estimated overall systematic uncertainty of 0.05 % is required for any measurement point.

Asymmetries and non-uniformity in the in-pixel layout can cause deviations in the response of the detector, depending on the precise particle-track intersection with respect to the position within a pixel cell of the DUT. To evaluate the hit-detection efficiency within a pixel cell, the telescope setup must provide sufficient spatial resolution and a large amount of data is required. To shorten the data-taking duration, the collected data of all enabled pixels is combined and projected onto a single pixel cell in the case of LF-Monopix2. Figure 7.10 displays the hit-detection efficiency within a pixel cell for all available NIEL fluences after proton irradiation. The mean efficiencies of the center, side, and corner regions of a single pixel cell are included for each graph. Since Matrix 1-34 exhibits the most pronounced performance deterioration, the respective in-pixel projections are chosen as representative example. The qualitative observation is the same for all front-end variants. As discussed, the mean efficiency decreases with increasing radiation level. The in-pixel projections show that the performance degradation is significantly worse in the pixel corners. After proton irradiation to $1 \times 10^{15}\,\mathrm{n_{eq}\,cm^{-2}}$ fluence, the performance

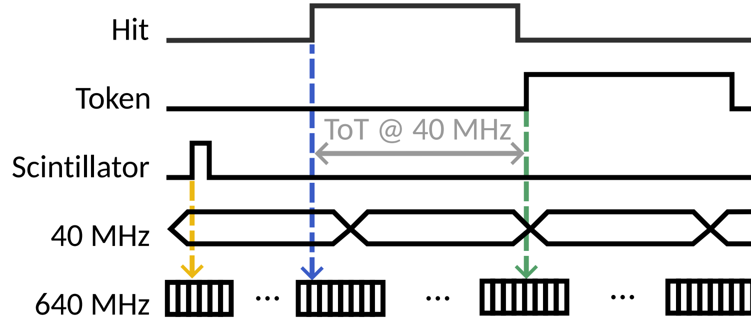

Figure 7.11: Schematic illustration of the measured and calculated timestamps needed to estimate the in-time ratio of LF-Monopix2. The scintillator (yellow) and `Token` (green) timestamps are measured with 640 MHz resolution. Using the time-over-threshold information with 40 MHz resolution, the leading-edge timestamp (blue) can be calculated with 640 MHz resolution.

of LF-Monopix2 is very uniform across a single pixel cell. Already at a NIEL fluence of $2 \times 10^{15}\,\mathrm{n_{eq}\,cm^{-2}}$, the hit-detection efficiency at the pixel corners drops below 99 %, although the mean efficiency is still (99.66 ± 0.05) %. At $5 \times 10^{15}\,\mathrm{n_{eq}\,cm^{-2}}$ NIEL fluence, the center of a pixel still detects (99.14 ± 0.05) % while the pixel corners only register (81.22 ± 0.05) % of hits. Since charge sharing with neighboring pixels is more likely at the pixel edges, the individually measured charge per pixel is typically less than the deposited charge in the sensor. For such events, a low threshold configuration is essential. Furthermore, the drift distance from the pixel corner to the collection electrode is the longest distance within a pixel cell. Thus, charge carriers generated at this position have the highest trapping probability after irradiation. The combination of shared charges between pixels and high trapping probabilities due to long drift distances explains the more severe drop in performance observed in the pixel corners. The corresponding results for the best performing front-ends Matrix 1-1 and Matrix 3 are shown in the appendix in Figure 9.2 after irradiation to $5 \times 10^{15}\,\mathrm{n_{eq}\,cm^{-2}}$ NIEL fluence. In both cases, the hit-detection efficiency stays above 99 % in the pixel corners.

In-time ratio of efficient events

For triggerless devices like the Monopix2 chips, the estimation of the in-time efficiency within a given time window is not trivial. In the case of LF-Monopix2, the scintillator signal associated with a traversing particle is sampled with 640 MHz resolution in the FPGA using the auxiliary inputs of the DAQ hardware. Similarly, the timestamp of the `Token` signal (see Section 5.1 and Section 9.1) is also sampled with 640 MHz resolution. Using this high-resolution `Token` timestamp and the time-over-threshold information sampled with 40 MHz resolution, the actual hit arrival time (leading edge) is calculated. Thus, a reliable time-over-threshold information is essential for this analysis. The time difference between scintillator timestamp and calculated leading edge is applied to assign a phase (with 640 MHz resolution) relative to the 40 MHz sampling clock to each hit. A schematic illustration of this method is shown in Figure 7.11.

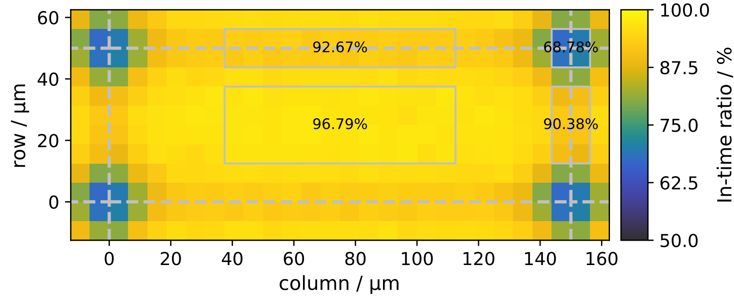

Figure 7.12: In-time ratio of Matrix 1-34 of LF-Monopix2 projected onto a single pixel cell for in-pixel studies at $5 \times 10^{15}\,\mathrm{n_{eq}\,cm^{-2}}$ NIEL fluence. The mean in-time ratio across the matrix is 93.64 % measured at a mean threshold of $Q_{\mathrm{thr}} = (2631 \pm 214)\,\mathrm{e}^-$. Due to a higher probability of charge sharing and resulting time-walk effects, the most severe drop in in-time ratio is observed in the pixel corners.

The resulting phase distribution allows one to identify the phase at which the majority of hits are registered within a selected time interval. This analysis provides a good estimation of the ratio of hits arriving within a chosen 25 ns time window (corresponding to the LHC collision frequency).

The in-time ratios measured with LF-Monopix2 are listed in Table 7.5 and indicate that Matrix 1-34 performs the worst with an in-time ratio of 99.43 % before irradiation. Since this front-end is equipped with a 5 fF feedback capacitance, the pre-amplifier gain is small compared to the other front-end variants (see Figure 7.5), which directly decreases the rise time of the analog signal. Already at $2 \times 10^{15}\,\mathrm{n_{eq}\,cm^{-2}}$ NIEL fluence, the in-time ratio drops below 99 %. After irradiation to $5 \times 10^{15}\,\mathrm{n_{eq}\,cm^{-2}}$ NIEL fluence, a decrease below 94 % is observed. Figure 7.12 shows the respective in-time ratio projected onto a single pixel cell. The severe drop below 70 % in the pixel corners is explained by the previously discussed reasons of charge sharing and trapping probability after irradiation. If the created charge is close to the threshold of a pixel, time-walk effects cause delayed hit detection on the discriminator level. Consequently, charge sharing is even more relevant for timing measurements and the degradation towards the pixel edges is more pronounced compared to the hit-detection efficiency.

The hit-detection efficiencies measured with Matrix 1-34 ($>$ 99 % up to $3 \times 10^{15}\,\mathrm{n_{eq}\,cm^{-2}}$ fluence) confirm that the events are still detected, but the charge collection duration increases with NIEL fluence. Thus, the low gain of this front-end cannot compensate the slower charge collection due to bulk damage. Unexpectedly, this behavior is not observed for Matrix 1-2, which features the same feedback capacitance and similar gain. As long as the respective thresholds are reasonably close to each other, which is the case here, the different discriminator tuning circuits implemented in these two matrices are not expected to affect the in-time performance. However, no corrections regarding signal propagation delays relative to the pixel position (along columns and rows) were considered in this analysis. If large areas of the matrix are enabled, the readout scheme as one large super column (see Section 5.1) may cause delays in the registration

of a hit. Since Matrix 1-34 is eight times larger than Matrix 1-2 (see Table 5.1), this could explain the unexpected difference in in-time ratio. It would also imply that the in-time ratio of Matrix 1-34 improves if corrected for the respective pixel position delays. However, this hypothesis still needs to be confirmed.

All other front-end variants accomplished in-time ratios larger than 98.5 % at all fluences. The only exception is Matrix 1-2 at a NIEL fluence of $3 \times 10^{15}\,\mathrm{n_{eq}\,cm^{-2}}$, where also the hit-detection efficiency does not match the general tendency. It is likely that this measurement was affected by external factors such as short-term instabilities in the cooling. The evaluated in-time ratios pose a significant improvement compared to the predecessor LF-Monopix1, which measured an in-time ratio of 83 % at $1 \times 10^{15}\,\mathrm{n_{eq}\,cm^{-2}}$ NIEL fluence [114]. Similar to the hit-detection efficiency, this enhancement is facilitated by the smaller pixel pitch and, thus, lower detector capacitance. As Matrix 3 has the highest gain, it also shows the best in-time performance with ratios larger than 99 % across all fluences. Furthermore, all front-ends show a degradation in in-time ratio with increasing NIEL fluence. For the same reasons as previously discussed, the pixel corners are affected the most by this decrease. The increasing trapping probability and decreasing charge collection efficiency caused by bulk damage slow down the charge collection and decrease the total collected charge. Since the in-time ratio is even more sensitive to delays in drift duration and time-walk effects of different signal amplitudes, the degradation is more severe. Similar to previous observations, the measured in-time ratios do not align with the NIEL hypothesis. Based on the results in Table 7.5, irradiation with neutrons causes a larger declination of the in-time ratio.

Hit-detection efficiency after X-ray irradiation

Due to limitations of available beam time slots at both test-beam facilities, it was only possible to measure the X-ray-irradiated LF-Monopix2 chip at a TID of 400 Mrad. As surface damage does not affect the sensitive volume and, thus, charge generation, no depletion depth or bias voltage studies were conducted with this sample. Due to time constraints during the corresponding test-beam campaign, it was only feasible to measure front-end variants Matrix 1-34 and Matrix 3. Figure 7.13 shows the hit-detection efficiency projected onto a single pixel cell of LF-Monopix2 at 400 Mrad TID. The applied bias voltage of 200 V ensures full depletion of the sensitive volume. The front-ends were tuned to a threshold of $(1865 \pm 142)\,\mathrm{e^-}$ in the case of Matrix 1-34 and $(2123 \pm 53)\,\mathrm{e^-}$ in the case of Matrix 3. Both front-end variants show a mostly uniform performance with a mean hit-detection efficiency above 99 %, although the efficiency drops below 99 % in the pixel edges. The corresponding noise hit rates were below 1×10^{-9} hits per pixel per 25 ns, which implies a negligible contribution to the efficiency overestimation. Based on the tuning results presented in Section 7.1.2 at the final TID, the other front-end variants are expected to perform similarly well. Only Matrix 1-2 experienced a substantial increase in threshold above $2800\,\mathrm{e^-}$ (see Table 7.4). Accordingly, also a degradation in the hit-detection efficiency is expected for this front-end.

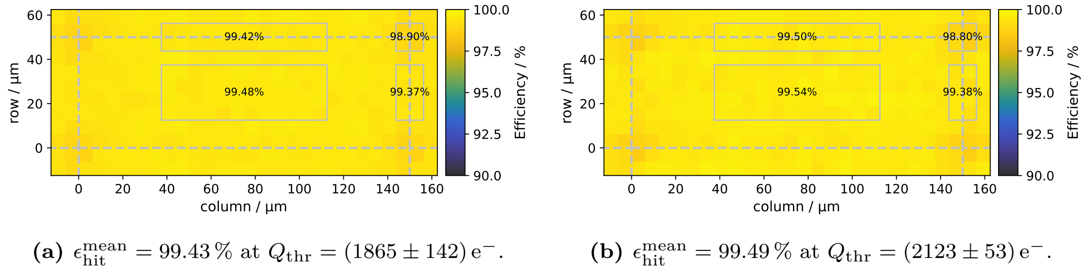

(a) $\epsilon_{\mathrm{hit}}^{\mathrm{mean}} = 99.43\,\%$ at $Q_{\mathrm{thr}} = (1865 \pm 142)\,\mathrm{e}^{-}$.

(b) $\epsilon_{\mathrm{hit}}^{\mathrm{mean}} = 99.49\,\%$ at $Q_{\mathrm{thr}} = (2123 \pm 53)\,\mathrm{e}^{-}$.

Figure 7.13: In-pixel efficiency of LF-Monopix2 after irradiation to 400 Mrad TID for (a) Matrix 1-34 and (b) Matrix 3. A bias voltage of 200 V was supplied in both cases.

Since the injection capacitance was only recalibrated after 100 Mrad TID (see Section 7.1.2), it is possible that this value changed with the continuation of the X-ray irradiation. Consequently, the thresholds might be larger than the measured values, which would explain the observed efficiency drop in the pixel corners. Another recalibration measurement after 400 Mrad could confirm this assumption. Furthermore, an estimation of the in-time ratio after X-ray irradiation is not possible. Due to surface damage, overflow of the leading- and trailing-edge counters cannot be prevented since the feedback current could not be adjusted reliably anymore. Thus, the time-over-threshold measurement, which is required for the estimation of the in-time ratio, is no longer trustworthy. Despite these uncertainties, the performance of LF-Monopix2 after 400 Mrad TID is very convincing considering that it is four times the targeted dose (see Section 3.4).

7.1.4 Conclusion

The performance of LF-Monopix2 after irradiation to the initial design targets of $1\times10^{15}\,\mathrm{n_{eq}\,cm^{-2}}$ NIEL fluence and 100 Mrad TID was proven. Furthermore, the successful operation of the chip at irradiation levels beyond these design goals up to $5\times10^{15}\,\mathrm{n_{eq}\,cm^{-2}}$ NIEL fluence and 400 Mrad TID has been verified. While a systematic increase in ENC with NIEL fluence was measured, the scaling between proton and neutron irradiation was not in accordance to the NIEL hypothesis. This is explained by the difference in ratio between point-like and clustered defects for proton and neutron irradiation. Front-end variants equipped with the bidirectional tuning circuit were verified to maintain a better threshold dispersion at the cost of larger ENC. Towards the largest available NIEL fluences, the differences in ENC performance decreased between the two discriminator circuits, while the advantage in threshold dispersion remained. The same behavior was observed after X-ray irradiation. The increased leakage currents after NIEL irradiation complicated the tuning procedure of LF-Monopix2 at especially high bias voltages, which required a growing amount of masked pixels with fluence. In the worst case across all front-end variants, this lead to an increase of almost 37 % in threshold configuration at the highest fluence.

The enhanced bias voltage capabilities of LF-Monopix2 compared to the predecessor facili-

tate to reach full depletion of 100 µm thick samples after irradiation to $3 \times 10^{15}\,\mathrm{n_{eq}\,cm^{-2}}$ NIEL fluence. With increasing bias voltage, the larger noise hit rates confirmed the observation of higher noise levels during the tuning procedure of the laboratory measurements. Consequently, the implementation of a leakage current compensation circuit at the cost of additional power consumption was identified as an effective improvement method for a possible further iteration. Neutron-irradiated samples revealed a significantly higher noise hit rate and required larger bias voltages to achieve full depletion, which posed another disagreement with the NIEL hypothesis. The aforementioned different likelihood of point-like and clustered defects between proton and neutron irradiation causes distinctive changes in effective doping concentration, which is not accurately described by the NIEL hypothesis. At the highest NIEL fluence, hit-detection efficiencies above 99 % were measured for all but one front-end variants. Estimation of the in-time ratio of events within a 25 ns window verified the better timing performance of front-ends with higher amplifier gain. These variants maintained an in-time ratio larger than 99 % across all fluences. The degradation in efficiency was found to be more severe in pixel corners due to charge sharing and longer drift distances. The respective in-time ratio confirmed this observation. The presented results validate a performance enhancement compared to the predecessor LF-Monopix1 and verified the functionality of LF-Monopix2 after NIEL irradiation above the initial design target. Across all available NIEL fluences, the front-end variant with the largest gain was identified to experience the least degradation.

After X-ray irradiation up to 400 Mrad TID, a decrease in power consumption of the digital and analog matrix domains below 25 % of the original power was measured for the largest front-end variant. Between 1 and 10 Mrad ionizing dose, a spike and subsequent rebound effect in the digital power domain characteristic for NMOS devices of this technology feature size was observed. The relative change in digital power consumption behaved uniformly for all front-end variants independent of the matrix size, while the relative change in analog power consumption scaled with the number of columns per variant. No degradation in the pre-amplifier gain was detected up to an ionizing dose of 200 Mrad. In the case of the front-ends with larger gain, a degradation in gain was identified to begin close to the maximum tested TID. Adjustments to the DAC reference current rendered an effective compensation of the received surface damage. For all but one front-end variants, threshold configurations similar to the non-irradiated case were achieved at 400 Mrad TID and after annealing. The very good hit-detection efficiencies above 99.4 % measured for two matrices at this ionizing dose verified the functionality of LF-Monopix2 after X-ray irradiation above the initial design target of 100 Mrad TID.

The demonstrated radiation hardness of LF-Monopix2 up to $5 \times 10^{15}\,\mathrm{n_{eq}\,cm^{-2}}$ NIEL fluence and 400 Mrad TID in the scope of this thesis demonstrates the advancements of monolithic pixel sensors in recent years. Although the confirmed radiation tolerance does not yet meet the requirements of the harshest environment such as faced in the ATLAS ITk inner layer (see Table 3.1), it is on par with many (including current) hybrid detector solutions. The presented results prove the feasibility of developing and employing DMAPS for high-radiation and high-

Sample	Fluence / $n_{eq}\,cm^{-2}$	Particle energy and type	Irradiation facility
G	5×10^{14}	14 MeV protons	Bonn isochronous cyclotron
H	1×10^{15}	14 MeV protons	Bonn isochronous cyclotron

Table 7.6: Overview of available NIEL-irradiated TJ-Monopix2 samples. The received TID is assumed to be negligible since all chips were not powered during the irradiation. Each sample was annealed for 80 min at 60 °C after the irradiation.

rate environments in future high-energy physics applications.

7.2 Characterization of TJ-Monopix2

To evaluate the radiation tolerance of the TJ-Monopix2 DMAPS, samples were irradiated separately up to 100 Mrad TID and $1 \times 10^{15}\,n_{eq}\,cm^{-2}$ NIEL fluence. The X-ray irradiation setup introduced in Section 6.1 is employed to inflict surface damage. To investigate bulk damage, TJ-Monopix2 chips are irradiated with protons at the Bonn isochronous cyclotron [150]. Persistent wire-bonding difficulties were faced for TJ-Monopix2, which remain unsolved at the time of writing and limited the available number of modules for characterization. Consequently, the chip could not be measured over the full range of NIEL fluences initially foreseen. Furthermore, only samples fabricated on an epitaxial layer and equipped with the n-gap modification (see Section 5.2 and Figure 5.3) were irradiated in the scope of this thesis. Detailed studies comparing the different materials and modifications types have already been performed with the predecessor chip as well as the MALTA project [117, 152]. Bare TJ-Monopix2 samples have been irradiated with neutrons to a fluence of $1.5 \times 10^{15}\,n_{eq}\,cm^{-2}$ at the TRIGA Mark II research reactor in Ljubljana [151]. Due to the unsolved wire-bonding issues, they are yet to be wire-bonded successfully and could not yet be tested. The two proton-irradiated TJ-Monopix2 samples characterized in the following are listed in Table 7.6. Both samples were annealed for 80 min at 60 °C after the irradiation.

In Section 7.2.1, laboratory measurements of the NIEL-irradiated TJ-Monopix2 samples are discussed. In addition, a threshold fluctuation caused by the distribution of the time reference clock is characterized based on non-irradiated chips. The change in performance due to X-ray irradiation is discussed in Section 7.2.2.

7.2.1 Laboratory characterization

For the characterization after NIEL irradiation, only the DC-coupled front-end variants are compared since they offer more pixels, and thus more data. The samples were annealed before all measurements and cooled to −10 °C during the measurement procedure. Table 7.7 summarizes

	NIEL fluence / $n_{eq}\,cm^{-2}$	Threshold / e^-	ENC / e^-	Leakage current[3] / µA
Standard	0	244 ± 4	6 ± 1	10
	5×10^{14}	318 ± 6	15 ± 2	280
	1×10^{15}	268 ± 6	15 ± 2	480
Cascoded	0	230 ± 7	6 ± 1	10
	5×10^{14}	280 ± 6	14 ± 2	280
	1×10^{15}	267 ± 5	15 ± 2	480

Table 7.7: Mean threshold, ENC, and leakage current after tuning for the DC-coupled front-end variants implemented in TJ-Monopix2 (see Table 5.3) and all available NIEL fluences. The leakage current was measured while -6 V was applied to the substrate and shielding p-wells. All irradiated measurements are conducted at $-10\,°C$ and after annealing for 80 min at 60 °C.

the change in mean threshold, ENC, and leakage current with increasing NIEL fluence. As for LF-Monopix2, the uncertainties are based on the threshold dispersion and the width of the ENC distribution, respectively. As discussed in Section 5.2, one of the main improvements of TJ-Monopix2 is the reduction in ENC by mitigating the tail towards larger values above $10\,e^-$ before irradiation [28].

While for both front-end variants the mean ENC increases by more than a factor of two after irradiation to $5 \times 10^{14}\,n_{eq}\,cm^{-2}$ NIEL fluence, the absolute value remains below $20\,e^-$. This degradation is explained by the large increase in leakage current of more than 200 µA due to bulk damage (see Section 4.1) and a corresponding rise in shot noise. Irradiation to $1 \times 10^{15}\,n_{eq}\,cm^{-2}$ NIEL fluence did not yield further degradation in the mean ENC, although the leakage current continued to grow. This observation is not yet fully understood, but it is assumed that adjustments to the chip configuration depending on radiation level explain the behavior. The largest rise with regard to the threshold is observed after irradiation to $5 \times 10^{14}\,n_{eq}\,cm^{-2}$ fluence. An increase of roughly 30 % and 22 % was measured for the standard and cascoded front-end, respectively. However, at this fluence the cascoded front-end suffered from very noisy pixels, which required masking a total of 1.3 % of pixels to render the chip operational. All other measurements required masking of less than 0.1 % of pixels. For the higher NIEL fluence, the threshold increased only by about 10 % and 16 % for the two front-end variants, respectively, compared to the non-irradiated results.

Figure 7.14 shows the normalized threshold distribution for both DC-coupled front-end variants of TJ-Monopix2 at all available NIEL fluences. While the fitted threshold dispersion did not degrade substantially after irradiation, the threshold is no longer Gaussian distributed towards the outer edges. The limited variable range of the register controlling the local tuning

[3] The non-irradiated results were measured at room temperature and scaled to $-10\,°C$ using Equation (8.62) in [7] for better comparison.

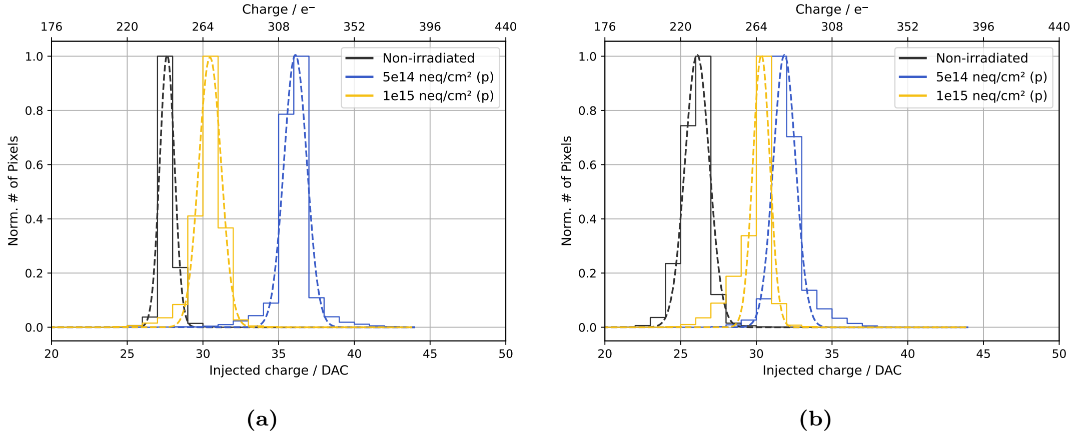

(a)

(b)

Figure 7.14: Normalized threshold distribution of the DC-coupled TJ-Monopix2 (a) standard and (b) cascoded front-end variants at different NIEL fluences.

step size and the limited 3-bit local tuning DAC cannot compensate the greater variations between pixels due to radiation damage. Even before irradiation, the former is already operated close to the maximum capacity. Outliers towards smaller thresholds limit the lowest achievable threshold, as these pixels reach the noise limit sooner and begin to detect noise hits continuously. Increasing the dynamic range of the respective register would provide a more uniform threshold performance and, possibly, a lower mean threshold also after irradiation. Although the measured ENC is the same for both NIEL fluences, fewer outlier pixels with very low threshold after irradiation to $1 \times 10^{15}\,\mathrm{n_{eq}\,cm^{-2}}$ fluence facilitate tuning the chip to lower thresholds. This is particularly noticeable for the standard front-end in Figure 7.14. For the cascoded front-end at $5 \times 10^{14}\,\mathrm{n_{eq}\,cm^{-2}}$ NIEL fluence, the distribution is skewed by the neglected 1.3 % masked pixels. These noisy pixels have lower thresholds with respect to the distribution and discarding them causes the observed asymmetry in the outliers. At all fluences, the measured thresholds pose a significant performance increase compared to values between 400 and 500 $\mathrm{e^-}$ achieved with the predecessor TJ-Monopix1 before and after irradiation [28, 117].

Threshold fluctuation

Laboratory measurements verified an improved performance of TJ-Monopix2 before and after irradiation in threshold and ENC compared to its predecessor [28]. However, periodic fluctuations in threshold were observed during the characterization even for non-irradiated chips. Extensive investigations [153] revealed that the threshold varies with the arrival time of a hit relative to the leading- and trailing-edge counter, in the following referred to as `BCID` counter. As described in Section 5.2, the corresponding 40 MHz sampling rate, in the following referred to as `BCID` clock, is derived on chip from the 160 MHz command clock. Utilizing the phase-adjustable injection circuit, the time of injection can be fixed to a chosen phase relative to

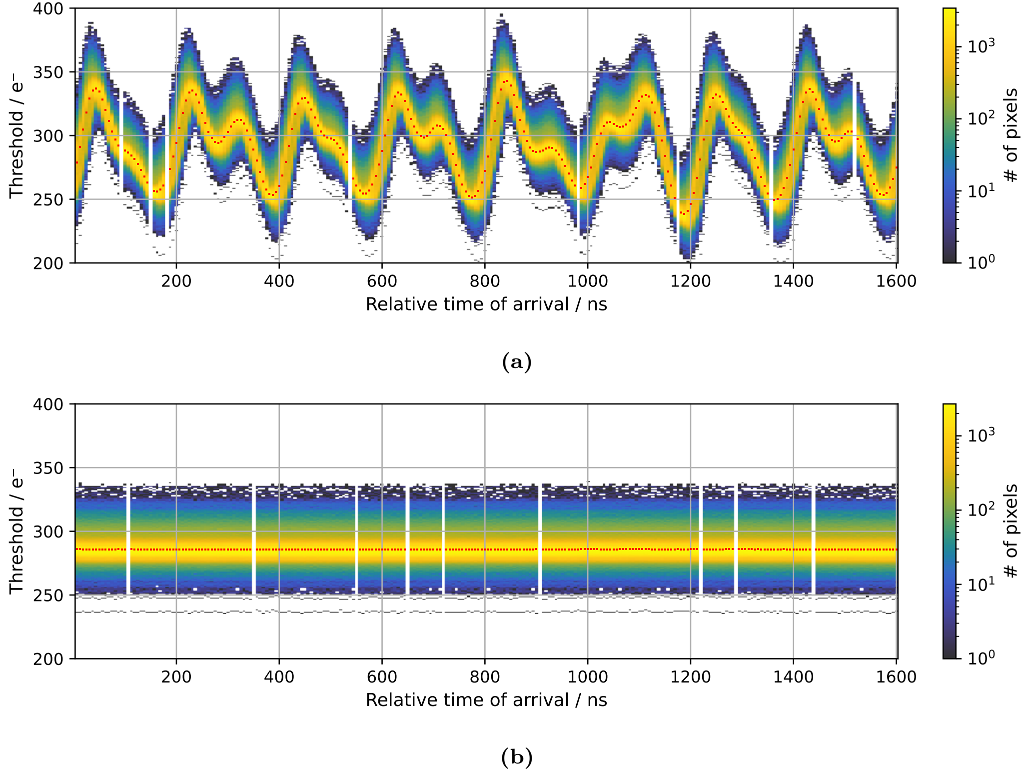

Figure 7.15: Threshold fluctuation with respect to the relative arrival time of a hit observed in TJ-Monopix2 (a) with and (b) without `BCID` clock distribution across the matrix. Each data point corresponds to a threshold scan of a single pixel at a fixed arrival time. The fluctuation was measured for $\mathcal{O}(30000)$ pixels across half of the available 7 bit counter length. Red dots indicate the mean threshold of all enabled pixels. The relative arrival time is calculated from the mean leading edge of the respective threshold scan. Without the distribution of the `BCID` clock the threshold fluctuations disappears entirely. Since in this case no leading edge is recorded by the chip, the same parameterization of (a) is used for (b).

resetting of the `BCID` counter. Figure 7.15a shows the periodic threshold fluctuation relative to a fixed arrival time across half of the available 7-bit `BCID` counter in TJ-Monopix2. For this measurement, the phase between counter reset and injection was fixed for and shifted between each individual threshold scan. In total, $\mathcal{O}(30000)$ pixels were measured. The mean threshold per fixed phase is visualized in red. The maximum mean threshold deviation of about $100\,e^-$ across the full counter resolution exceeds the initial threshold dispersion of $4\,e^-$ after tuning by orders of magnitude. No significant correlation between pixel position on the chip and impact on the amplitude of the fluctuation is observed. The corresponding map of each pixel's maximum threshold difference across the full counter is displayed in Figure 7.16a. Studies after irradiation showed no change in amplitude or pattern of the fluctuation.

Additional tests revealed that the fluctuation is introduced by cross-talk from the `BCID`

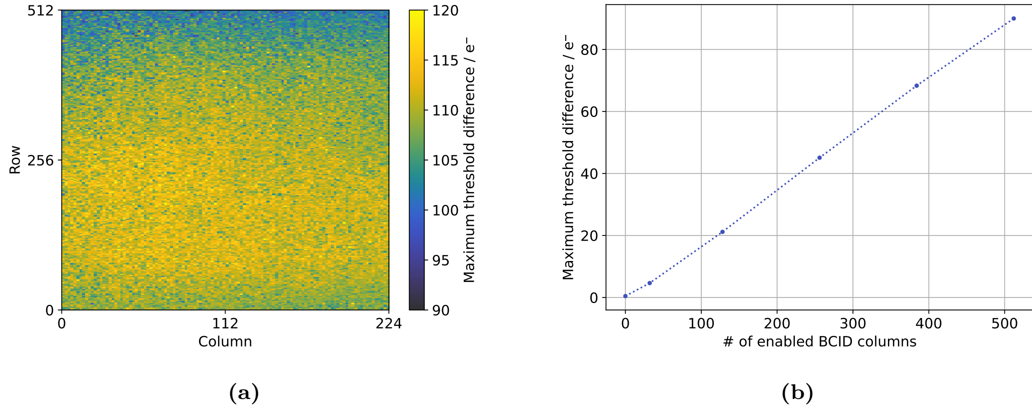

Figure 7.16: (a) Map of the maximum threshold difference across the 7-bit counter period while the BCID clock was distributed to the entire matrix. Only every fourth pixel is enabled to minimize the scan duration while maintaining reasonable data set. A slight gradient towards the top of the chip is visible, although the maximum change remains in the order of $100\,e^{-}$. No significant other correlations between fluctuation and relative position within the matrix were identified across multiple chips. (b) The scaling of the maximum threshold difference with the number of enabled BCID clock columns is averaged over all $\mathcal{O}(30000)$ enabled pixels. The maximum threshold fluctuation can be substantially attenuated by decreasing the number of columns to which the BCID clock is distributed. As shown in Figure 7.15b, no threshold fluctuation is observed in case the BCID clock is not distributed at all.

counter, which is distributed across the matrix. Figure 7.15b shows the same measurement when disabling the BCID clock, where the threshold remains constant across all hit arrival times. Since leading-edge information is no longer available in this case, the same parameterization between injection phase and relative hit-arrival time as before is used. Furthermore, the correlation of the amount of columns, to which the BCID counter is distributed, and the fluctuation amplitude was analyzed. Figure 7.16b depicts the measured linear increase of the maximum threshold difference across the 7-bit counter period for more columns to which the BCID counter is distributed. Measuring different pixel positions relative to a group of enabled BCID columns verified that pixels in columns with disabled BCID clock distribution are equally impacted. No modification in the fluctuation amplitude with increasing distance between pixel and enabled BCID columns was observed. This confirms that the periodic threshold fluctuation is a global effect across the entire chip without any local dependency.

Slowing down the BCID clock by reducing the command clock frequency alters the pattern of the threshold fluctuation. The change in fluctuation pattern for a BCID clock range from 40 to 5 MHz is shown in Figure 7.17 for an exemplary pixel. Further reduction of the clock frequencies is not possible since the chip no longer functions properly at lower command clock speeds and complex scan procedures cannot be performed. In this case, the mean hit arrival time is given as the leading-edge information which remains equal across all clock frequencies. In addition, the leading edge is depicted in form of the gray-encoded BCID counter setting to highlight the toggling of individual bits. It must be noted that the absolute time axis changes for

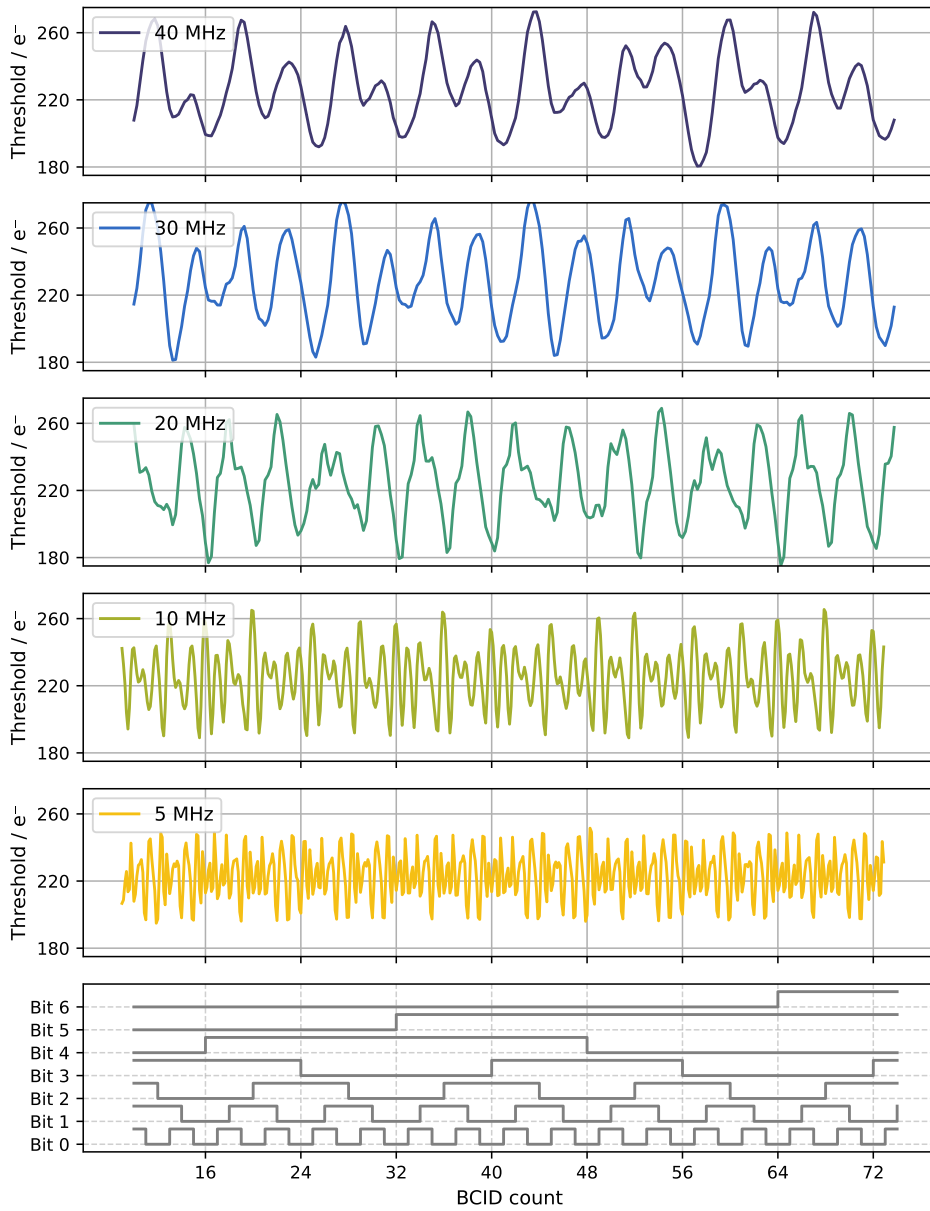

Figure 7.17: Dependency of the threshold fluctuations in TJ-Monopix2 on the frequency of the clock, which is distributed across the matrix, shown for an exemplary pixel. The mean hit arrival time is shown below in form of the gray-encoded counter bit setting corresponding to the respective leading edge. It has to be considered that a slower clock effectively changes the absolute time axis of each subplot. For higher clock frequencies, the distortions generated by the toggling of individual counter bits overlap and create the initially observed periodic pattern.

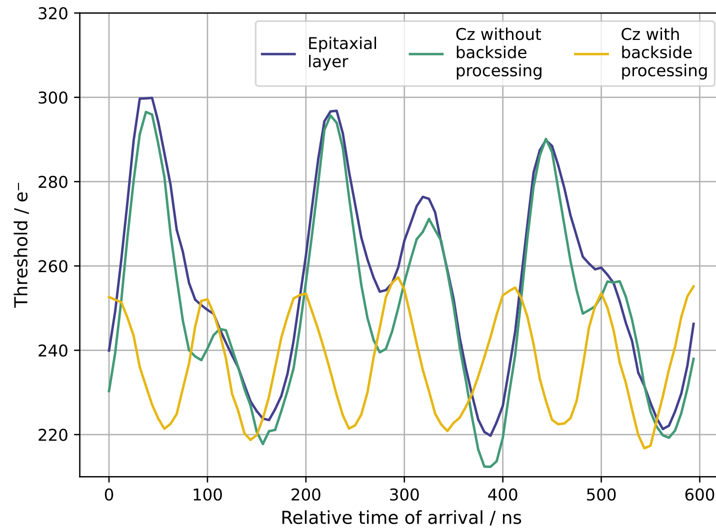

Figure 7.18: Dependency of the threshold fluctuations in TJ-Monopix2 on the wafer material shown for an exemplary pixel. While no significant difference is observed between chips fabricated on 30 µm epitaxial layers or 100 – 300 µm Czochralski wafers, the backside processing of the Czochralski wafer reduces the fluctuation amplitude noticeably. This indicates that the distortions from individual bit toggles couple into the non-depleted backside of the chip where it spreads globally. Fixing the backside potential (by adding backside metallization) restricts this coupling.

each subplot according to the different bit toggling frequencies. For smaller `BCID` clock speeds, it becomes noticeable that each bit toggle causes a distortion in threshold irrespective of the specific counter bit. This gets even more prominent when investigating the analog front-end signals on an oscilloscope at an even lower `BCID` clock frequency of 1.25 MHz[4] (see Figure 9.3). In this case, it is possible to assign distortions based on their shapes to separate counter bits. The amplitude of each individual distortion is significantly lower than the initial magnitude of more than 100 e^-. These separately generated distortions overlay for faster `BCID` clock speeds creating the initially observed periodic pattern and extent of the fluctuation.

Subsequent studies focused on the impact of the fabrication material on the threshold fluctuation. Here, chips fabricated on a 30 µm epitaxial layer and 100 µm or 300 µm Czochralski wafers were tested. For the latter, chips with and without backside processing are available. The dependency between threshold fluctuation and fabrication material is shown in Figure 7.18 for one exemplary pixel per chip. Only minor differences in pattern and amplitude are observed between chips fabricated on epitaxial layers and Czochralski wafers without backside processing. However, backside processing and metallization of the Czochralski wafer reduces the fluctuation amplitude by a factor of two. This result suggests that the cross-talk originating from the `BCID` counter bit toggling couples from the chip periphery into the non-depleted backside

[4] At such low clock frequencies, it was no longer feasible to run complex scan procedures with TJ-Monopix2.

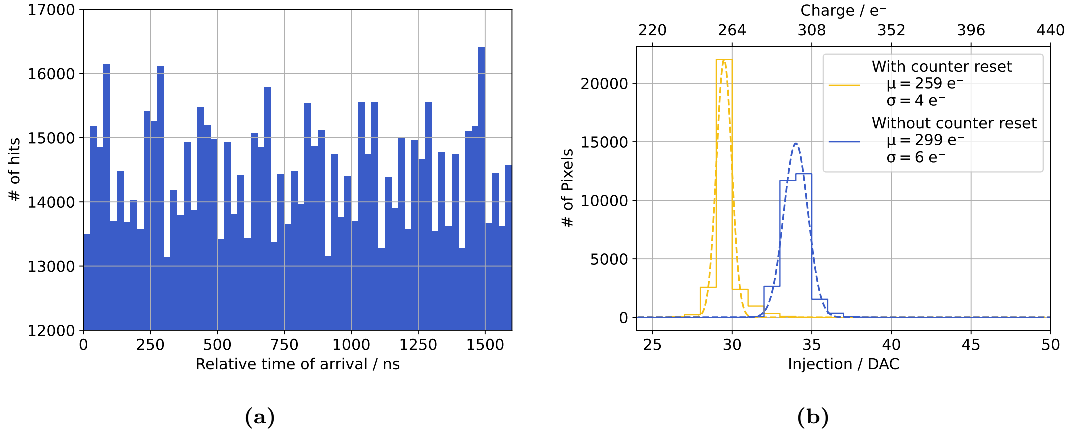

(a) **(b)**

Figure 7.19: Impairments caused by the threshold fluctuations observed for non-injection-based measurements without control over the hit arrival time. (a) The relative hit arrival time distribution measured in a beam test shows the same periodic pattern as observed in the threshold fluctuation of Figure 7.15a. Thus, the fluctuations are no artifact introduced by the injection circuit but affect the actual threshold of a pixel. (b) The comparison of a threshold scan with and without a fixed timing relation between injection and `BCID` counter reset were measured with the same chip and identical front-end settings. It highlights the difference between the injection-based measurements at optimal laboratory conditions and the effective threshold that is present on average during source or test-beam measurements.

of the chip. The distortion couples globally into all pixels of the chip from there. Backside metallization allows to fix the potential to either ground or the substrate voltage, which allows for restricting the cross-talk coupling into the backside. A schematic illustration of the coupling path is shown in Figure 9.4 for a chip manufactured on an epitaxial layer and a Czochralski wafer with backside processing. Without metallization, the oxidation of silicon in air passivates the backside and prevents a conductive contact. Due to the low-ohmic substrate wafer needed for chips fabricated on epitaxial layers, backside metallization is only effective for Czochralski wafers. Thus, TJ-Monopix2 chips fabricated on epitaxial layers were not backside metallized and the respective impact on the threshold fluctuation cannot be studied here.

While the threshold fluctuation can be bypassed in injection based measurements, the cross-talk is unavoidable in source or beam tests with relevant timing information. For injection-based scans, the `BCID` counter is reset before every injection and a fixed injection-phase corresponding to a local minimum in Figure 7.15a is set. This workaround is applied for all threshold and ENC measurements presented in this thesis. However, particle-induced signals arrive at randomly distributed times relative to the `BCID` counter. Consequently, the hits are discriminated against an arrival-time-dependent threshold. Figure 7.19a shows the hit arrival time relative to the `BCID` counter measured in a beam test. In contrast to the expected uniform distribution, the same periodic pattern as seen in the threshold fluctuation can be identified. In the non-irradiated case, the charge MPV generated by a traversing MIP is around $2500\,e^-$ for $30\,\mu m$ epitaxial

layers and around 3000 e^- for Czochralski wafers [28, 154]. Consequently, each pixel collects as few as 650 e^- in the event where the generated charge is shared equally among four neighboring pixels. Typical front-end settings operate at thresholds in the range of 200 to 300 e^-, not including the unexpected threshold fluctuation of more than 100 e^-. Especially in combination with degraded charge collection efficiencies, the magnitude of this threshold fluctuation can degrade the performance after irradiation to high fluences larger than $1 \times 10^{15}\,n_{eq}\,cm^{-2}$. In case the charge is unevenly distributed across a cluster, Figure 7.19a indicates that the threshold fluctuation causes a loss of hits as part of a cluster even before irradiation. Despite this, studies of non-irradiated TJ-Monopix2 chips confirmed an excellent hit-detection efficiency due to the very low threshold [28]. It needs to be emphasized that only individual hits within a cluster may stay undetected but not the entire event.

Furthermore, the beam tests verified that the threshold fluctuation is not an artifact of the injection circuit and affects non-injection-based data taking. On average, the effective threshold seen by particles differs from the injection-based, tuned one as visualized in Figure 7.19b. Here, the effective threshold was measured without a fixed injection phase imitating random hit arrival times relative to the `BCID` counter. The same chip with identical front-end settings was used. An increase in both mean threshold and threshold dispersion is observed for the latter. Since the successor chip of TJ-Monopix2 will consist of almost 900 columns to which the `BCID` clock is distributed, the extent of the fluctuations will only increase (see Figure 7.16b). Thus, a change in design of the clock distribution across the matrix is required to reduce this cross-talk and not risk a performance loss. This is realized by implementing low-voltage `BCID` drivers that minimize the cross-talk per bit toggle as shown by simulations. In addition, this adjustment will also reduce the power consumption of the chip.

7.2.2 X-ray irradiation of TJ-Monopix2

TJ-Monopix2 was irradiated to 100 Mrad TID at the X-ray irradiation setup introduced in Section 6.1. Similar to the procedure of LF-Monopix2, the campaign was split into 16 irradiation steps logarithmically distributed across the TID range. After each irradiation step, a standardized short-term annealing and measurement routine was performed (see Section 4.2.2). Upon reaching the final ionizing dose, the sample was annealed for 80 min at 60 °C to replicate the post-irradiation procedure of NIEL-irradiated chips. The chip was cooled to 0 °C during the entire irradiation campaign and the subsequent measurements.

The power consumption of all low-voltage power domains was measured after each irradiation step to evaluate the respective susceptibility to surface damage. In the case of TJ-Monopix2, four low voltages (nominally set to 1.8 V) are supplied to the digital and analog readout electronics as well as to the chip periphery and DAC registers. Figure 7.20 shows the change in power consumption for each domain up to 100 Mrad TID. The chip periphery draws the most power, which is primarily required for the distribution of the 40 MHz clock across the matrix [28]. Both

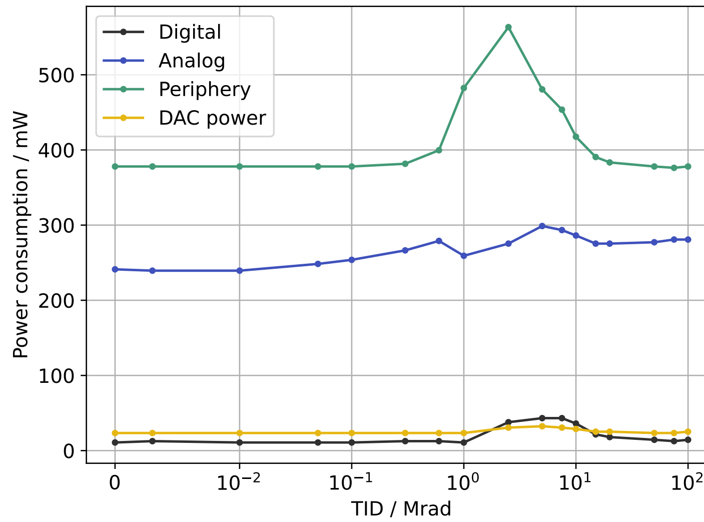

Figure 7.20: Power consumption of the different low-voltage power domains supplied to TJ-Monopix2 at different ionizing doses. The entire pixel matrix and reference clock distribution to all columns were enabled for this measurement.

the digital power domain and the periphery exhibit an increase in power consumption between 1 Mrad and 10 Mrad. As described in Section 4.2.3, this is characteristic for NMOS transistors of the used technology feature size, which was also observed for LF-Monopix2 (see Section 7.1.2). The largest relative increase is measured for the digital power domain as the power consumption quadruples between 2.5 Mrad and 7.5 Mrad. The biggest absolute contributor remains the chip's periphery at all times. No substantial changes in power consumption are observed for the analog and DAC power domains during the entire irradiation. For ionizing doses larger than 10 Mrad, the power consumption reduces again, and the rebound effect described in Section 4.2.3 is observed [102]. Up to the maximum ionizing dose, the combined power consumption of all power domains remains around 7 % higher than before irradiation.

To estimate the effect of the received surface damage on the detector performance, a threshold configuration specified for the non-irradiated chip is re-measured after each irradiation step. As discussed in Section 7.1.2, this analysis is only of qualitative nature since the time-consuming optimization of front-end parameters to counteract the radiation damage is only done after the entire irradiation campaign. In this case, also no re-tuning of the threshold configuration is done after each irradiation step. Figure 7.21a visualizes the results for both DC-coupled front-end variants, which follow the same pattern. The error bars on the threshold are defined by the respective threshold dispersion. Apart from a large fluctuation at 2.5 Mrad ionizing dose, a continuous degradation with increasing TID is observed. The measurement step, at which the fluctuation occurred, is equivalent to the ionizing dose, at which the power consumption spikes the highest (see Figure 7.20). Thus, both results support the conclusion that the effects

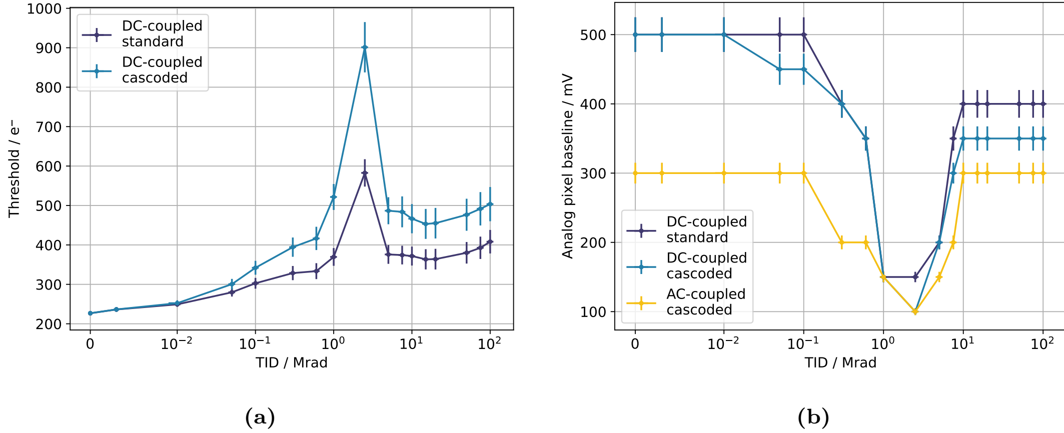

(a) **(b)**

Figure 7.21: (a) Re-measured threshold of the initially tuned configuration before the campaign and (b) baseline of the analog monitoring pixels after each irradiation step. The former is only measured for the DC-coupled front-end variants. The analog monitoring data included the AC-coupled cascoded circuit and shows the output signal baseline of the pre-amplifier. Matching the change in power consumption (see Figure 7.20), the re-measured threshold observed the worst degradation between 5 to 10 Mrad. The drop in the baseline of the analog output signal of the pre-amplifier confirms that the degradation occurs in the analog front-end electronics.

of surface damage are most severe around this ionizing dose. To identify which circuit of the front-end is most affected, the response of the analog monitoring pixels to injected charge is sampled with an oscilloscope. Figure 7.21b shows the analog output signal baseline behind the pre-amplifier stage for both DC-coupled variants and the cascoded AC-coupled front-end. The stated uncertainties are given by the resolution of the oscilloscope settings. Starting at 1 Mrad TID, the signal baseline of all front-end variants begins to decrease. Similar to the previous observations, the largest degradation to below 40 % of the initial baseline is observed between 1 Mrad and 5 Mrad TID. For increasing ionizing doses, the baseline recovers. However, the initial baseline is only reached in the case of the AC-coupled front-end variant. For the DC-coupled front-ends, the baseline only rebounds to 70 % and 80 % of the initial value for the cascoded and standard version, respectively. A similar behavior was observed for gain measurements with the predecessor TJ-Monopix1 [127]. This also matches the larger degradation in the re-measured threshold configuration with the DC-coupled cascoded front-end at the maximum TID. The prominent drop of the analog signal baseline at the pre-amplifier output implies that the pre-amplifier circuit is particularly susceptible to surface damage.

Upon completion of the irradiation to 100 Mrad and annealing of the TJ-Monopix2 sample, optimizations of the front-end settings to counteract the radiation damage were investigated. An increase of the bias current of the pre-amplifier input transistor by 80 % restores most of its degraded performance after irradiation. Table 7.8 compares the measured mean threshold and ENC at 0 Mrad and 100 Mrad after re-tuning of the threshold configuration. Again, the threshold dispersion and the width of the ENC distribution are used to quantify the uncertain-

Front-end		TID / Mrad	Threshold / e^-	ENC / e^-
DC	Standard	0	227 ± 5	5 ± 1
		100	245 ± 6	13 ± 2
	Cascoded	0	227 ± 5	6 ± 1
		100	275 ± 6	13 ± 2
AC	Cascoded	0	292 ± 6	6 ± 1
		100	296 ± 7	10 ± 2
	Standard	0	291 ± 7	6 ± 1
		100	244 ± 6	11 ± 2

Table 7.8: Mean threshold and ENC results after tuning for each front-end variant implemented in TJ-Monopix2 (see Table 5.3) after X-ray irradiation to 100 Mrad TID. All measurements are conducted at 0 °C and after annealing of 80 min at 60 °C.

ties, respectively. For all front-end variants, an increase in ENC between 66.6 % and 116.6 % after the irradiation is observed. Due to the very small ENC of non-irradiated TJ-Monopix2, the absolute increase remains small. In contrast to LF-Monopix2, no degradation in threshold dispersion and, thus, the tuning circuit is observed for TJ-Monopix2. Despite the good performance in ENC and threshold dispersion at 100 Mrad TID, the threshold increased by 7.9 % and 21.1 % for the DC-coupled front-ends. In the case of the AC-coupled front-end variants, similar or even better threshold configurations were achieved[5]. A recalibration of the injection circuit after irradiation to 100 Mrad confirmed no alteration. This was expected due to the implementation of the test injection circuit based on two separate voltage registers (see Section 5.2) that experience a similar degradation.

7.2.3 Beam test results of TJ-Monopix2

In this section, the performance of irradiated TJ-Monopix2 chips in beam tests is discussed. A focus is put on maintaining the excellent hit-detection efficiency evaluated for non-irradiated modules [28]. Based on the results, the radiation tolerance of TJ-Monopix2 up to the tested fluences and ionizing doses is assessed. The measurement campaigns were performed at the DESY test-beam facility [138]. Utilizing the portable cooling setup introduced in Section 6.2.1, NIEL-irradiated samples were cooled to −10 °C while the X-ray-irradiated sample was cooled to 0 °C to reduce the increased leakage current after irradiation.

Hit-detection efficiency after NIEL irradiation

After NIEL irradiation, the change in effective doping concentration and, therefore, resistivity of the sensitive volume facilitates to apply larger depletion voltages to the substrate without

[5] It must be emphasized that the initial tuning configuration was not chosen close to the noise limit. Thus, this improvement is not entirely unexpected.

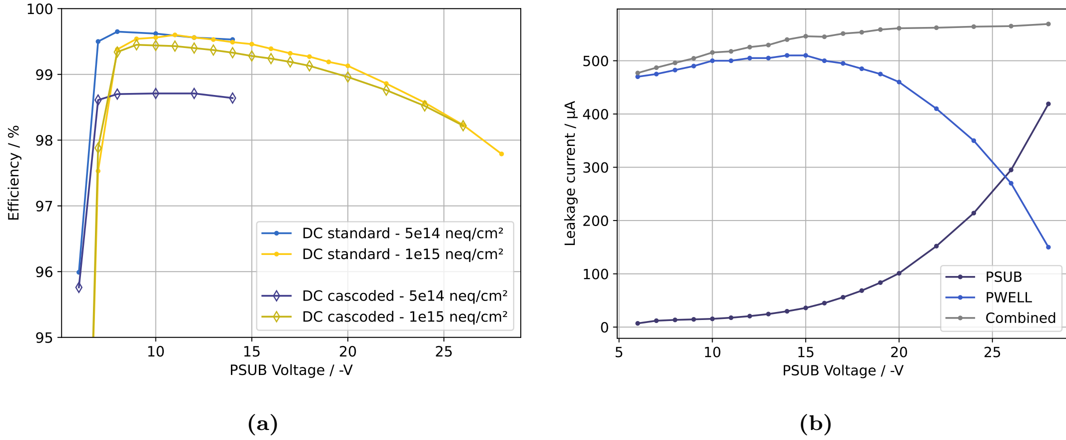

(a) (b)

Figure 7.22: (a) Hit-detection efficiency and (b) leakage current versus substrate voltage of DC-coupled TJ-Monopix2 front-end variants at different NIEL fluences. The latter is only shown for $1 \times 10^{15}\,\mathrm{n_{eq}\,cm^{-2}}$ NIEL fluence. The drop in efficiency towards higher substrate voltages is caused by a change in leakage current path from substrate (PSUB) to the electronics shielding p-well (PWELL). This yields a change in the working point at the amplifier input node and, thus, a change (in this case an increase) in threshold.

experiencing punch-through effects to the shielding p-well. Figure 7.22a shows the hit-detection efficiency of the DC-coupled front-end variants for increasing substrate voltages after NIEL irradiation. As discussed in Section 7.2.1, the $5 \times 10^{14}\,\mathrm{n_{eq}\,cm^{-2}}$ NIEL fluence sample required masking of around 1.3 % of pixels for the DC-coupled cascoded front-end, which are neglected in this analysis. At the nominal bias voltage of $-6\,\mathrm{V}$, the hit-detection efficiency drops below 97 % after irradiation to $5 \times 10^{14}\,\mathrm{n_{eq}\,cm^{-2}}$ fluence. Before irradiation, the DC-coupled front-end variants detected more than 99.9 % for the given n-gap modification and epitaxial layer [28]. After irradiation, the increase of the depletion voltage applied to the substrate counteracts the performance degradation due to bulk damage. The p-wells for shielding the electronics are kept at $-6\,\mathrm{V}$. At $5 \times 10^{14}\,\mathrm{n_{eq}\,cm^{-2}}$ NIEL fluence, $-7\,\mathrm{V}$ biasing voltage are sufficient to recover the hit-detection efficiency to above 99.5 % for both front-ends. After irradiation to $1 \times 10^{15}\,\mathrm{n_{eq}\,cm^{-2}}$ NIEL fluence, a substrate voltage of $-9\,\mathrm{V}$ is required to achieve efficiencies close to 99.5 %. For further increases of the biasing voltage, a decrease in the hit-detection efficiency is observed. It is particularly noticeable for the sample with the higher NIEL fluence and substrate voltages above $-20\,\mathrm{V}$. At this point, the efficiency dropped below 99 % for both front-end variants again. The same pattern was observed for MALTA2 samples[6] irradiated to the same fluence [155]. This degradation is explained by a shift in the mean threshold of the chip towards larger values caused by the change in biasing conditions. Figure 7.22b visualizes the leakage current measured in the substrate and the shielding p-wells for different substrate voltages at $1 \times 10^{15}\,\mathrm{n_{eq}\,cm^{-2}}$ NIEL

[6] MATLA2 is the second iteration of a large scale DMAPS designed by the MALTA project and equipped with the same pixel layout as TJ-Monopix2 (see Section 5.2).

Front-end		Fluence / $n_{eq}\,cm^{-2}$	Hit-detection efficiency	Noise hit rate / $25\,ns^{-1}pixel^{-1}$	Substrate voltage / V
DC	Std.	0	99.96 %	$< 1 \times 10^{-13}$	−6
		5×10^{14}	99.65 %	2.67×10^{-12}	−8
		1×10^{15}	99.60 %	6.25×10^{-13}	−11
	Casc.	0	99.94 %	$< 1 \times 10^{-13}$	−6
		5×10^{14}	99.76 %	5.69×10^{-11}	−8
		1×10^{15}	99.45 %	9.47×10^{-12}	−9

Table 7.9: Hit-detection efficiency of the DC-coupled front-end variants of TJ-Monopix2 at all available NIEL fluences. The listed noise hit rates are calculated per number of enabled pixels. Similar to LF-Monopix2, the uncertainty on the evaluated hit-detection efficiencies is dominated by a systematic uncertainty of 0.05 % (see Section 6.2.2). All measurements after irradiation are conducted at −10 °C and after annealing of 80 min at 60 °C. The non-irradiated values are taken from [28].

fluence. Upon reaching −15 V depletion voltage, the leakage current flow begins to change from substrate to shielding p-well. At −26 V substrate voltage, more leakage current is measured in the p-well domain than in the substrate. This additional leakage current within the shielding p-well alters the operating points within the in-pixel readout electronics, which in return shifts the threshold of the chip. Furthermore, the change of dominant leakage current path through the p-well above −25 V depletion voltage indicates that the bias setting is close to sustaining a punch through from substrate to p-well.

The hit-detection efficiency and noise hit rate at different NIEL fluences are compared in Table 7.9 for both DC-coupled front-end variants at the best bias settings, respectively. The corresponding threshold configurations are listed in Table 7.7. Since the noise hit rates of all measurements are low enough to disregard an overestimation of the efficiency [28], a dominant systematic uncertainty of 0.05 % as discussed in Section 6.2.2 is assumed. Up to a NIEL fluence of $1 \times 10^{15}\,n_{eq}\,cm^{-2}$, both front-end variants maintain a very good hit-detection efficiency larger than 99.4 % and no significant difference in performance is observed. In the case of the cascoded front-end at $5 \times 10^{14}\,n_{eq}\,cm^{-2}$ fluence, the large number of masked pixels was disregarded again. Taking these pixels into account in the test-beam analysis tool reduced the hit-detection efficiency to (98.70 ± 0.05) % for this data point. While the efficiency drops below 99 %, this is still a good result considering that around 1.3 % of pixels were disabled. The small pixel pitch facilitates charge sharing between pixels, which compensates disabled pixels to a certain extent. In this case, more than 17 % of all events had a cluster size of at least two, which corresponds to a mean cluster size of 1.28.

For the standard front-end, no degradation within the error margin is observed between the irradiation from 5×10^{14} to $1 \times 10^{15}\,n_{eq}\,cm^{-2}$ NIEL fluence. This is explained by the higher threshold configuration at the lower fluence (see Table 7.7). The measured efficiencies

after proton irradiation to $1 \times 10^{15}\,\mathrm{n_{eq}\,cm^{-2}}$ fluence pose a significant improvement over the predecessor. For the same sample type (n-gap modification fabricated on epitaxial layer) of TJ-Monopix1, hit-detection efficiencies slightly above 87 % were measured after neutron irradiation to the same fluence [28, 117]. For the extra deep p-well modification fabricated on Czochralski substrate, the efficiency measured with TJ-Monopix1 increases to above 98 % at the same NIEL fluence. The primary reason for this improvement in TJ-Monopix2 is the reduction of the ENC as described in Section 5.2, which facilitates tuning of the chip to considerably lower thresholds. The irradiated TJ-Monopix1 samples were tuned to thresholds around 450 to 500 $\mathrm{e^-}$ compared to thresholds around 270 $\mathrm{e^-}$ for TJ-Monopix2. However, NIEL scaling does not apply with respect to such complex measurements, as observed for LF-Monopix2 (see Section 7.1.3). Still, it can be assumed that TJ-Monopix2 performs better due to the discussed improvements in threshold performance. Once the available neutron-irradiated samples will be successfully assembled, this assumption will need to be confirmed.

Furthermore, Table 7.9 shows that the cascoded front-end variant is more prone to noise. The largest noise hit rate was measured for the cascoded front-end after irradiation to $5 \times 10^{14}\,\mathrm{n_{eq}\,cm^{-2}}$ NIEL fluence, which is in alignment with the difficulties during tuning encountered for this sample. For the standard front-end variation, the observed noise hit rate was also higher at the lower NIEL fluence. The reason for this is assumed to be chip-to-chip variations, but cannot be confirmed due to the shortage in successfully assembled TJ-Monopix2 samples. Despite the increase, the noise hit rates remain sufficiently low to not affect the overestimation of the efficiency, according to the analysis in [28].

In the case of TJ-Monopix2, the hit-detection efficiency within a pixel cell is evaluated by projecting the combined data of all enabled pixels onto a 2×2 pixel matrix. This format is chosen to investigate deviations corresponding to the 2×2 core pixel layout of TJ-Monopix2 (see Section 5.2). Figures 7.23 and 7.24 show the hit-detection efficiency after NIEL irradiation projected onto such a core pixel for the standard and cascoded DC-coupled front-ends, respectively. Already at $5 \times 10^{14}\,\mathrm{n_{eq}\,cm^{-2}}$ NIEL fluence, a slight degradation in efficiency towards the pixel corners is visible, although it remains above 99 % for both front-end variants. After irradiation to $1 \times 10^{15}\,\mathrm{n_{eq}\,cm^{-2}}$ NIEL fluence, the hit-detection efficiency drops below 99 % in this region. The long drift distances combined with the increased probability of charge trapping due to bulk damage (see Section 4.1) cause this degradation. Due to the small-collection-electrode design, the effect is more prominent compared to LF-Monopix2, which maintained a better hit-detection efficiency in the pixel corner region at this fluence (see Section 7.1.3). At the larger fluence, a marginal asymmetry in the performance of laterally and vertically neighboring pixels (with respect to the orientation of the figure) is also measured. This was already observed for TJ-Monopix1 [28] and is explained by corresponding asymmetries in the core pixel layout [126].

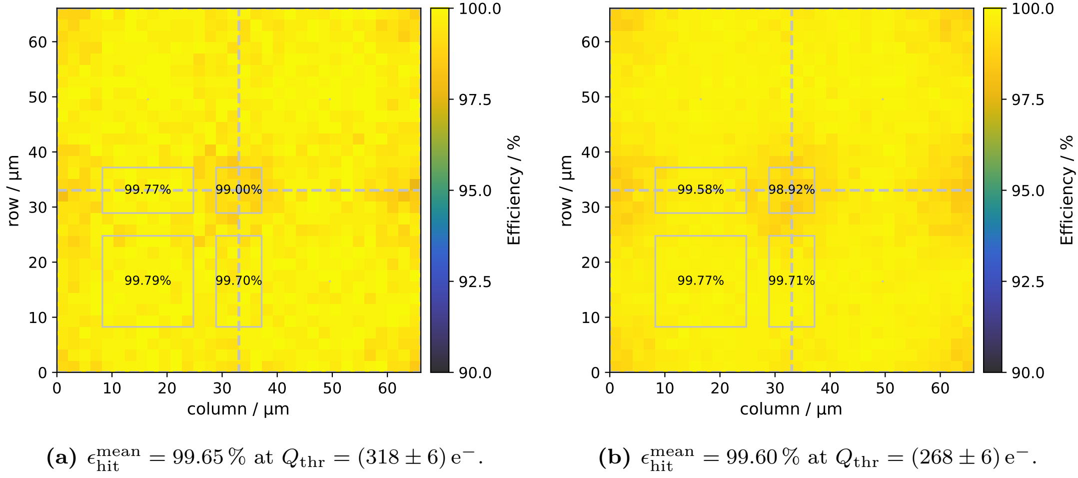

(a) $\epsilon_{\mathrm{hit}}^{\mathrm{mean}} = 99.65\,\%$ at $Q_{\mathrm{thr}} = (318 \pm 6)\,\mathrm{e}^-$. **(b)** $\epsilon_{\mathrm{hit}}^{\mathrm{mean}} = 99.60\,\%$ at $Q_{\mathrm{thr}} = (268 \pm 6)\,\mathrm{e}^-$.

Figure 7.23: Hit-detection efficiency of the DC-coupled TJ-Monopix2 standard front-end variant after NIEL irradiation to (a) 5×10^{14} and (b) $1 \times 10^{15}\,\mathrm{n_{eq}\,cm^{-2}}$ NIEL fluence. The data is projected onto a 2×2 pixel matrix to investigate the in-pixel response.

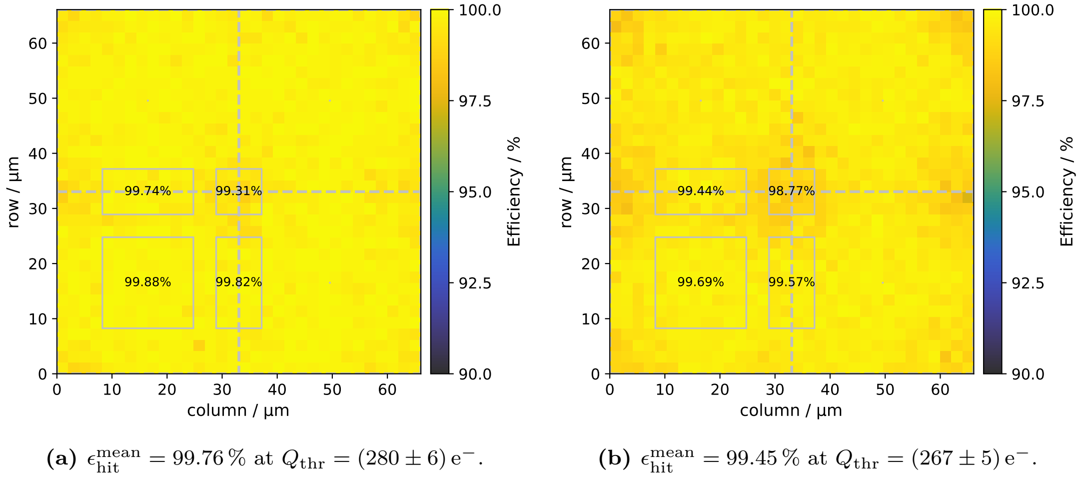

(a) $\epsilon_{\mathrm{hit}}^{\mathrm{mean}} = 99.76\,\%$ at $Q_{\mathrm{thr}} = (280 \pm 6)\,\mathrm{e}^-$. **(b)** $\epsilon_{\mathrm{hit}}^{\mathrm{mean}} = 99.45\,\%$ at $Q_{\mathrm{thr}} = (267 \pm 5)\,\mathrm{e}^-$.

Figure 7.24: Hit-detection efficiency of the DC-coupled TJ-Monopix2 cascoded front-end variant after irradiation to (a) 5×10^{14} and (b) $1 \times 10^{15}\,\mathrm{n_{eq}\,cm^{-2}}$ NIEL fluence. The data is projected onto a 2×2 pixel matrix to investigate the in-pixel response.

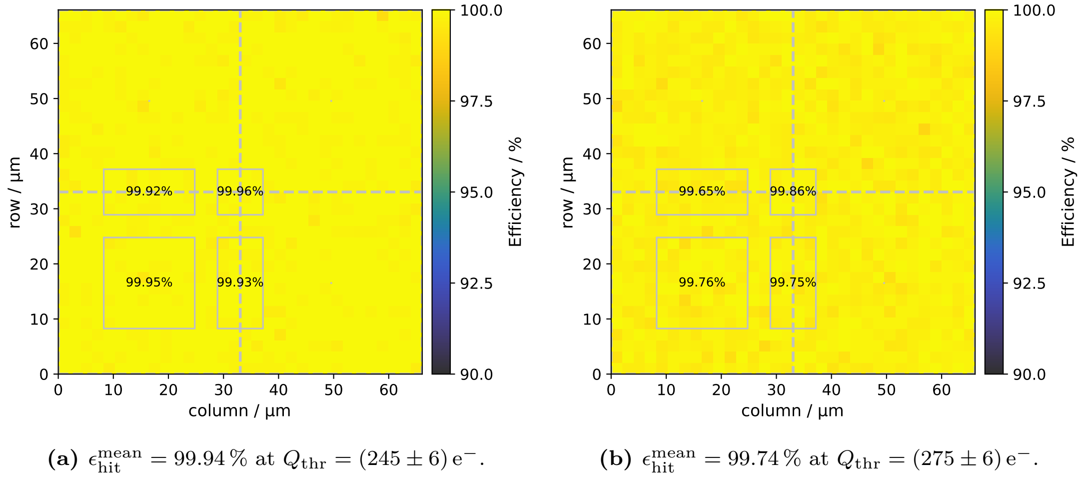

(a) $\epsilon_{\mathrm{hit}}^{\mathrm{mean}} = 99.94\,\%$ at $Q_{\mathrm{thr}} = (245 \pm 6)\,\mathrm{e}^-$.

(b) $\epsilon_{\mathrm{hit}}^{\mathrm{mean}} = 99.74\,\%$ at $Q_{\mathrm{thr}} = (275 \pm 6)\,\mathrm{e}^-$.

Figure 7.25: Hit-detection efficiency of the (a) standard and (b) cascoded DC-coupled TJ-Monopix2 front-end variants after irradiation to 100 Mrad TID projected onto a 2×2 pixel matrix.

Hit-detection efficiency after X-ray irradiation

Investigations of the X-ray-irradiated TJ-Monopix2 sample in beam conditions were conducted at the DESY test-beam facility. Utilizing the portable cooling setup described in Section 6.2.1, the chip was cooled to 0 °C throughout the whole measurement. Since no bulk damage is expected from X-ray irradiation, the hit-detection efficiency is investigated for the same biasing conditions as in the non-irradiated case. Figure 7.25 shows the hit-detection efficiency of both DC-coupled front-end variants after irradiation to 100 Mrad TID at a bias voltage of −6 V. The front-ends were tuned to a threshold of $(331 \pm 50)\,\mathrm{e}^-$ and $(347 \pm 52)\,\mathrm{e}^-$ for the standard and cascoded versions, respectively. In both cases, homogeneous hit-detection efficiencies larger than 99.7 % across the 2×2 pixel core were measured. For the AC-coupled standard and cascoded variations, mean hit-detection efficiencies of $(99.95 \pm 0.05)\,\%$ and $(99.90 \pm 0.05)\,\%$ were derived at thresholds of $(240 \pm 36)\,\mathrm{e}^-$ and $(279 \pm 42)\,\mathrm{e}^-$, respectively. The corresponding noise hit rates below 1×10^{-11} per pixel per 25 ns for all measurements imply a negligible overestimation of the efficiency. These results verify the functionality of TJ-Monopix2 up to a TID of 100 Mrad and indicate a substantially higher X-ray radiation tolerance. The latter would need to be investigated in a separate irradiation campaign. However, the confirmed X-ray radiation tolerance up to 100 Mrad of TJ-Monopix2 would sufficient for operation in the Belle II VTX environment (see Table 3.1), which the successor chip will face.

7.2.4 Conclusion

The radiation tolerance of TJ-Monopix2 was verified up to the design targets of $1 \times 10^{15}\,\mathrm{n_{eq}\,cm^{-2}}$ NIEL fluence and 100 Mrad total ionizing dose. The ENC was measured to increase by a factor

of 2.5 after NIEL irradiation to $1 \times 10^{15}\,\mathrm{n_{eq}\,cm^{-2}}$ fluence. An absolute value below $20\,\mathrm{e^-}$ was maintained due to the very low ENC before irradiation. For the DC-coupled front-end variants, an increase in threshold up to 30 % was observed at a NIEL fluence of $5 \times 10^{14}\,\mathrm{n_{eq}\,cm^{-2}}$. After irradiation to $1 \times 10^{15}\,\mathrm{n_{eq}\,cm^{-2}}$ NIEL fluence, the degradation in the threshold was reduced to 16 % or less compared to the non-irradiated case. Higher noise hit rates for the sample, which received the lower fluence of $5 \times 10^{14}\,\mathrm{n_{eq}\,cm^{-2}}$, were identified as the cause for this unexpected behavior. While the quantified threshold dispersion remained constant across all NIEL fluences, deviations from the Gaussian threshold distribution towards both tails were noticed. For the lower NIEL fluence, pixels corresponding to the outliers towards lower thresholds prevent further reduction of the mean threshold. Investigations showed that the available dynamic range of the local tuning circuit is insufficient to maintain the Gaussian threshold distribution after irradiation.

For non-irradiated TJ-Monopix2 chips, the distribution of the time reference (`BCID`) clock across the matrix and the corresponding bit toggling of the `BCID` counters were identified as the origin of a periodic threshold fluctuation relative to the arrival time of a hit. The extent of the threshold variation was established to scale with the amount of columns, which receive the time reference clock, and showed no spatial dependency to a relative pixel position. In case the clock is distributed across the entire matrix, a maximum threshold variation of around $100\,\mathrm{e^-}$ was quantified. Reduction of the clock frequency stretched out the periodic pattern, which allowed to assign individual bit toggles of the `BCID` counter to distinguishable cross-talk signals. Studies on the dependency of the fabrication material suggested that the cross-talk propagates through the non-depleted backside of the chip. Backside metallization of chips fabricated on Czochralski substrate was found to mitigate the extent of the threshold fluctuation by a factor of two. A workaround of fixing the relative arrival time for injection-based measurements was successfully examined. Analysis of test-beam data confirmed that the threshold fluctuation is no artifact introduced by the injection circuit.

TJ-Monopix2 maintained a very good hit-detection efficiency after NIEL irradiation up to $1 \times 10^{15}\,\mathrm{n_{eq}\,cm^{-2}}$ NIEL fluence. Across both available NIEL fluences, efficiencies larger than 99.4 % were measured for the DC-coupled front-end variants at the optimal bias settings. This improvement compared to the predecessor was confirmed to result from the enhancement in threshold performance by more than $200\,\mathrm{e^-}$. A notably high noise hit rate of the cascoded DC-coupled front-end of the TJ-Monopix2 sample irradiated to $5 \times 10^{14}\,\mathrm{n_{eq}\,cm^{-2}}$ fluence required masking of more than 1 % of the total pixels. It was verified that an increased depletion voltage at the p-type substrate compensates the charge collection degradation due to bulk damage. The observed performance decrease for substrate voltages above $-20\,\mathrm{V}$ was explained by the shift in leakage current through the shielding p-wells. This change in current flow altered the operating point of the in-pixel electronics and caused a shift in the mean threshold. Due to the long drift distances of charges created in the pixel corners to the small collection electrode, this in-pixel region was identified as most susceptible to bulk damage. At $1 \times 10^{15}\,\mathrm{n_{eq}\,cm^{-2}}$ NIEL fluence,

the hit-detection efficiency in the pixel corners remained close to or above 99 % for both tested front-end variants.

TJ-Monopix2 displayed full functionality during and after X-ray irradiation to 100 Mrad TID. The characteristic spike and rebound effect in power consumption for NMOS devices in this technology feature size was observed between 1 and 10 Mrad ionizing dose for the peripheral and digital power domain. The peripheral domain was verified as biggest contributor to the overall power consumption across all ionizing doses. At 100 Mrad TID, an increase of 7 % in the total power consumption was measured. The change in performance of a threshold configuration tuned before irradiation was used to estimate the degradation with surface damage. The front-end electronics were most affected at 2.5 Mrad ionizing dose. Studies of the analog pre-amplifier signal confirmed that the pre-amplifier is particularly susceptible to surface damage. The baseline of the pre-amplifier output was measured to drop below 40 % throughout the irradiation campaign and only recovers fully for the AC-coupled front-ends. Increasing the bias current of the pre-amplifier input transistor was identified as an effective compensation method for the received surface damage. After irradiation to 100 Mrad TID and annealing, all front-end variants remained configurable to thresholds below 300 e^- and maintained ENC values below 15 e^-. Beam-test measurements confirmed a very good hit-detection efficiency larger than 99.7 % for all front-end variants at the maximum ionizing dose.

Due to the chip assembly difficulties, the absolute limits of the radiation tolerance of TJ-Monopix2 could not be tested. For the same reason, studies on performance differences between various fabrication materials, modification types, and doping concentrations after irradiation remain pending. The results presented in the scope of this thesis demonstrated that the requirements of the initial design target of the ATLAS ITk outer layer were fulfilled. Furthermore, the results are promising with respect to the performance of TJ-Monopix2 after irradiation to higher TID and NIEL fluences.

7.3 Performance comparison

The Monopix2 chips constitute two conceptually different design approaches of DMAPS for tracking applications in high-energy physics environments. Since both chips are designed with the ATLAS ITk outer layer requirements in mind (see Table 3.1), the advantages and disadvantages of their respective design approaches are compared. Table 7.10 summarizes key properties and performance characteristics of LF-Monopix2 and TJ-Monopix2.

Although LF-Monopix2 is only half as wide, both DMAPS share the same column length relevant for the implemented readout architecture described in Section 9.1. Adjustments to the width of LF-Monopix2 should not affect the functionality of the chip which facilitates a larger matrix size for a possible successor chip. One of the obvious distinctions between the two chips is the pixel pitch as a consequence of the chosen collection electrode size (see Section 3.3.3). The pixel size of LF-Monopix2 exceeds the one of TJ-Monopix2 by almost a factor of seven, which

	LF-Monopix2	TJ-Monopix2
Collection-electrode design approach	Large	Small
Pixel pitch	$150\,\mu m \times 50\,\mu m$	$33.04\,\mu m \times 33.04\,\mu m$
Matrix size	56×340 pixels	512×512 pixels
Detector capacitance	$\mathcal{O}(100\,fF)$	$\mathcal{O}(1\,fF)$
Analog power consumption	$5.5 - 14.9\,\mu W/pixel$	$0.61 - 0.92\,\mu W/pixel$
Digital power consumption	$0.71 - 6.90\,\mu W/pixel$	$0.04 - 0.08\,\mu W/pixel$
Depletion depth (non-irradiated)	$85\,\mu m$	$25 - 40\,\mu m$ [28]
Charge MPV of traversing MIP	$6000\,e^-$	$2200 - 3000\,e^-$
Operational threshold	$1900 - 2500\,e^-$	$200 - 300\,e^-$
ENC (non-irradiated)	$88 - 128\,e^-$	$5 - 6\,e^-$
ENC (at $1 \times 10^{15}\,n_{eq}\,cm^{-2}$)	$121 - 142\,e^-$	$10 - 13\,e^-$
ENC (at 100 Mrad)	$120 - 147\,e^-$	$14 - 15\,e^-$
NIEL fluence tolerance	$> 5 \times 10^{15}\,n_{eq}\,cm^{-2}$	$> 1 \times 10^{15}\,n_{eq}\,cm^{-2}$
TID tolerance	$> 400\,Mrad$	$> 100\,Mrad$

Table 7.10: Characteristics and performance comparison of LF-Monopix2 and TJ-Monopix2 with respect to radiation tolerance. All values for LF-Monopix2 are measured with a 100 µm thin sample. For power and ENC related properties, the stated range corresponds to the different front-end variants of the respective chip. The operational threshold describes the range of threshold achieved before and after irradiation.

directly affects the spatial resolution of the detector. For cylindrical detector systems (such as the ATLAS experiment), the rectangular formed pixels of LF-Monopix2 can compensate this to a certain extent. In this case, the chip would be oriented such that the shorter pixel side is aligned in the direction that requires more precise spatial information from the experimental point of view. As discussed in Section 3.3.3, a large collection electrode not only limits the minimum pixel size but also introduces a detector capacitance, that is orders of magnitude larger compared to the alternative design approach. Consequently, LF-Monopix2 consumes substantially higher analog and digital power per pixel to counteract the respective deterioration in noise and timing performance. This elevated power consumption requires additional cooling efforts in the context of an entire detector system. In contrast, the very low power consumption of TJ-Monopix2 facilitates cooling for large-scale detector systems.

Due to the small collection electrode and the implemented voltage amplifier, TJ-Monopix2 benefits from very low noise levels before and after irradiation. Despite an unexpected threshold

fluctuation with significant magnitude due to cross-talk effects from the time reference counters (see Section 7.2.1), the low ENC facilitates operation of the chip at thresholds below 300 e^- even after irradiation. In comparison, the threshold and ENC measured with LF-Monopix2 exceeds these values by one order of magnitude. While the relative increase in ENC with radiation level is larger for TJ-Monopix2, the absolute values remain negligible compared to the ENC measured with LF-Monopix2. The considerably higher threshold, at which LF-Monopix2 needs to be operated, is compensated by a larger depleted volume that results in a larger charge signal for traversing particles. In this aspect, TJ-Monopix2 is limited by the applicable biasing voltage as well as the substrate material. The corresponding created charge range given in Table 7.10 refers to chips manufactured on a 30 µm epitaxial layer or a 100 µm Czochralski substrate. Since the maximum achievable depletion depth is around 40 µm, TJ-Monopix2 chips can be thinned below 100 µm without losing necessary charge signal, which would minimize the material budget. Due to the small threshold of TJ-Monopix2, the generated signal by a traversing MIP exceeds the operational threshold by almost a factor of ten, compared to around three in the case of LF-Monopix2. However, the large pixel size and uniform electric field of the latter reduces the likelihood of charge sharing between pixels. Both DMAPS have demonstrated that their respective generated-charge-to-threshold ratio is sufficient to measure very high hit-detection efficiencies above 99 % before and after irradiation to $1 \times 10^{15}\,n_{eq}\,cm^{-2}$ NIEL fluence.

While the maximum radiation tolerance of both chips has not yet been investigated, LF-Monopix2 was successfully tested at substantially larger radiation levels in the scope of this thesis. As explained in Section 3.3.3, the large collection electrode facilitates a uniform electric field across the depleted volume and short drift distances. The large bias voltage capabilities of the LF-Monopix2 ensure full depletion of 100 µm thick chips up to $3 \times 10^{15}\,n_{eq}\,cm^{-2}$ NIEL fluence. These features are essential for efficient and fast charge collection after NIEL irradiation. While both DMAPS preserved their excellent hit-detection efficieny after irradiation to their initial design goal of $1 \times 10^{15}\,n_{eq}\,cm^{-2}$ NIEL fluence, LF-Monopix2 remained very efficient up to $5 \times 10^{15}\,n_{eq}\,cm^{-2}$ NIEL fluence. The radiation tolerance with respect to X-ray irradiation solely depends on the chosen CMOS technology. Consequently, the DMAPS design approach with respect to the size of the collection electrode is irrelevant for surface damage. Both chips proved full functionality and very good hit-detection efficiency above 99.4 % after irradiation to the initial design target of 100 Mrad TID. While LF-Monopix2 demonstrated very good results after 400 Mrad ionizing dose, the performance of TJ-Monopix2 after 100 Mrad TID strongly indicates a similar tolerance to surface damage.

Comparing the implementation of the different design approaches in the Monopix2 chips reveals that both DMAPS are suitable detectors for high-energy physics tracking applications. Within the scope of this thesis, the latest iteration of both development lines was confirmed to meet the necessary radiation tolerance with respect to their initial design target. The large-collection-electrode design approach features a higher NIEL radiation tolerance at the cost of a larger pixel capacitance and, thus, larger power consumption. Furthermore, this design approach

limits the minimum pixel size. The high bias voltage capabilities, uniform electric field, and short drift distances of LF-Monopix2 render the large-collection-electrode design particularly suitable for the application of monolithic pixel detectors in very-high-radiation environments. In contrast, the very low noise and power operation is advantageous for the small-collection-electrode design approach. The design facilitates small pixel sizes while long drift distances within a pixel restrict the radiation tolerance. The possibility of thinning chips to less than 100 µm without relevant signal loss is ideal to reduce the material budget of a detector. Based on these characteristics, the small-collection-electrode design is especially fitting for experiments focussing on precision measurements with restricted exposure to radiation such as lepton collider experiments. Due to this suitability and its demonstrated performance, TJ-Monopix2 constitutes the basis for the development of a new DMAPS as part of the VTX upgrade of the Belle II experiment [67, 70]. For the small-collection-electrode design approach, the hypothetical extension of the depletion depth to levels around 100 µm and above is not expected to significantly enhance the NIEL radiation tolerance. The achieved signal-to-threshold ratio of TJ-Monopix2 is already sufficient, such that a larger generated signal would not make a substantial difference. In addition, the hypothetical even longer drift distances would also increase susceptibility to charge carrier trapping after irradiation.

8 Summary

Over the last decades, the accessibility of commercial CMOS technologies propelled developments of monolithic pixel detectors for tracking applications, which combine readout electronics and sensor volume in one entity of silicon. The reduced material budget and simplified production procedure without a complex interconnection step is at the expense of no separate optimization of readout ASIC and sensor. Increased availability of high-resistivity substrates and large bias voltage capabilities in these commercial CMOS processes improved the fast charge collection abilities of monolithic detectors. This renders such depleted monolithic active pixel sensors a feasible alternative to hybrid devices in high-rate and high-radiation environments. In this thesis, the radiation tolerance of two conceptually different implementations of large-scale DMAPS was studied.

The $1\,\mathrm{cm} \times 2\,\mathrm{cm}$ LF-Monopix2 chip comprises 56×340 pixels with a pitch of $150\,\mu\mathrm{m} \times 50\,\mu\mathrm{m}$. The utilized large-collection-electrode design approach facilitates a homogeneous electric field and short drift distances across a pixel at the expense of a large detector capacitance. A relatively high power consumption of up to $22\,\mu\mathrm{W}$ per pixel is required to compensate impairments caused by the large detector capacitance. Before irradiation, typical operational thresholds of around $2000\,\mathrm{e}^-$ at ENC values between 90 and $130\,\mathrm{e}^-$ have been measured depending on the front-end variation. In the case of $100\,\mu\mathrm{m}$ thin, backside metallized chips, full depletion of the sensitive volume ensures sufficient charge generation by traversing MIPs to reach hit-detection efficiencies above $99.5\,\%$ before irradiation. After proton and neutron irradiation up to $5 \times 10^{15}\,\mathrm{n_{eq}\,cm^{-2}}$ and $2 \times 10^{15}\,\mathrm{n_{eq}\,cm^{-2}}$ NIEL fluence, respectively, the increased leakage current generated higher ENC up to $200\,\mathrm{e}^-$ in the worst case. This led to a degradation in mean operational thresholds up to $2600\,\mathrm{e}^-$ for individual radiation levels and front-end variants only. The enhanced bias voltage capabilities of LF-Monopix2 facilitate full depletion of the sensitive volume up to $3 \times 10^{15}\,\mathrm{n_{eq}\,cm^{-2}}$ NIEL fluence before charge carrier trapping begins to dominate. For all tested NIEL fluences, hit-detection efficiencies above $99\,\%$ were measured for at least four of the implemented front-end variants. The most severe efficiency degradation due to bulk damage was identified in the pixel corners due to higher charge sharing probabilities. The enhanced timing performance achieved through larger pre-amplifier gain was also confirmed after NIEL irradiation. For the respective front-end variants, the ratio of events measured within a $25\,\mathrm{ns}$ time interval remained above $99\,\%$ at the highest NIEL fluence. Differences in performance after neutron and proton irradiation were observed that do not conform to the NIEL hypothesis. This is expected, since NIEL scaling does not accurately account for differences in impact between

point-like and clustered defects on certain sensor properties. Furthermore, the functionality of LF-Monopix2 was verified up to a TID of 400 Mrad. The chip maintained typical operational thresholds after 100 Mrad and 400 Mrad and annealing despite an increase in ENC by 83.8 % in the worst case. Beam tests confirmed the good performance with hit-detection efficiencies above 99.4 % at the highest ionizing dose.

TJ-Monopix2 is a 2 cm × 2 cm DMAPS that contains 512 × 512 pixels with a pitch of 33.04 µm × 33.04 µm. The chosen small-collection-electrode design approach assists the very low power consumption below 1 µW per pixel but renders electric field shaping more difficult. Benefitting from this design approach, the very low ENC around 5 e^- yields operational thresholds around 200 e^- for non-irradiated chips. A global fluctuation of the threshold relative to the arrival time of a hit with a maximum deviation of up to 100 e^- was observed. Toggling of the leading and trailing edge counter bits was identified as the origin of this cross-talk. Studies of backside metallized samples verified the coupling path of this cross-talk through the non-depleted volume of the chip. Proton-irradiated TJ-Monopix2 chips were measured up to a fluence of $1 \times 10^{15}\,\mathrm{n_{eq}\,cm^{-2}}$. A degradation in the mean ENC up to 15 e^- and the mean operational threshold above 300 e^- was observed after NIEL irradiation. Still, beam tests demonstrated hit-detection efficiencies above 99.4 % after irradiation to the highest fluence. The most severe performance degradation was located in the pixel corners due to the long drift distance and high charge sharing probability. The tolerance of TJ-Monopix2 to X-ray irradiation was validated up to a total ionizing dose of 100 Mrad. The pre-amplifier was identified to be particularly susceptible to surface damage. After irradiation to the highest TID and annealing, an increase in ENC up to 13 e^- was measured while the operational threshold remained below 300 e^- for all front-end variants. Hit-detection efficiencies above 99.7 % confirmed the very good performance of TJ-Monopix2 at 100 Mrad ionizing dose.

In summary, the radiation tolerance of both Monopix2 DMAPS was verified to comply with or even exceed the initial design goal of $1 \times 10^{15}\,\mathrm{n_{eq}\,cm^{-2}}$ NIEL fluence and 100 Mrad TID of the ATLAS ITk outer layer environment. LF-Monopix2 demonstrated a tolerance to significantly larger radiation levels, which were only achievable by hybrid devices previous to the rapid development of monolithic pixel detectors. TJ-Monopix2 proved high radiation tolerance while maintaining a low power consumption and very low noise operation. This combination lead to the development of a successor chip by the VTX collaboration for an all-silicon tracker upgrade of the Belle II experiment [67, 70]. The absolute limitations of both Monopix2 DMAPS with respect to radiation tolerance still remain to be investigated.

9 Appendix

9.1 Synchronous column-drain readout architecture

The column-drain readout architecture implemented in both Monopix projects is based on the ATLAS FE-I3 readout ASIC [156]. It provides a fast readout with time-over-threshold information and high rate capabilities (>100 MHz/cm^2), while offering a simple and not space-consuming implementation. Once a hit is processed in the analog front-end and digitized by the discriminator, the discriminator output triggers the readout logic. Figure 9.1 shows the timing diagram of the most important signals of the column-drain readout architecture. The leading and trailing edge (LE/TE) of the discriminated signal generate two pulses, which are sampled in 40 MHz and stored in memory cells. The trailing edge pulse sets a hit flag register, which triggers the propagation of the `Token` signal to the readout controller. Upon receiving the `Token`, the readout controller sends the `Freeze` signal to the respective column stopping any new hits from disturbing the readout procedure. Subsequently, the readout controller sends the `Read` and `ReadInt` signals to the column. The latter allows the hit and pixel information to be written into the column data bus for readout and clears the hit flag register afterwards. In case multiple hits are recorded within a column, the procedure repeats until all hits are read out, while the top-most pixel of the column is prioritized. Since all Monopix chips are trigger-less, no trigger memory is necessary and the buffer depth of the readout architecture is one in this scenario.

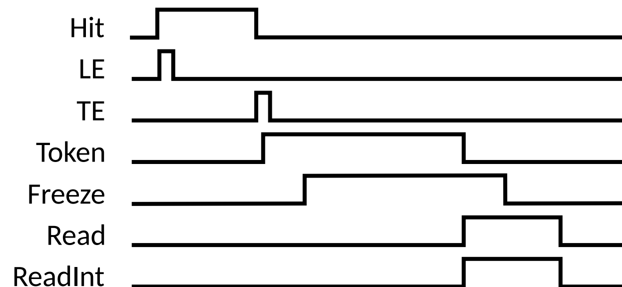

Figure 9.1: Timing diagram of the different signals in the column-drain readout logic.

9.2 Supplementary figures on irradiated LF-Monopix2 results

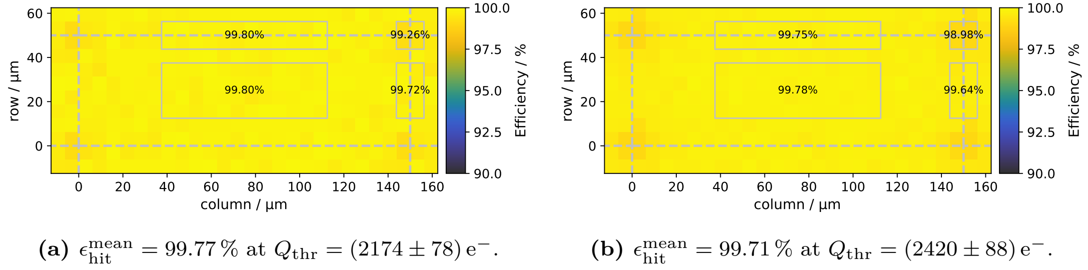

(a) $\epsilon_{\text{hit}}^{\text{mean}} = 99.77\,\%$ at $Q_{\text{thr}} = (2174 \pm 78)\,\text{e}^-$. **(b)** $\epsilon_{\text{hit}}^{\text{mean}} = 99.71\,\%$ at $Q_{\text{thr}} = (2420 \pm 88)\,\text{e}^-$.

Figure 9.2: Hit-detection efficiency of (a) Matrix 1-1 and (b) Matrix 3 of LF-Monopix2 projected onto a single pixel cell for in-pixel studies at $5 \times 10^{15}\,\text{n}_{\text{eq}}\,\text{cm}^{-2}$ NIEL fluence. In both cases, the applied bias voltages was 400 V. The hit-detection efficiency stayed close to or above 99 % in the pixel corners.

9.3 Supplementary information on threshold fluctuation of TJ-Monopix2

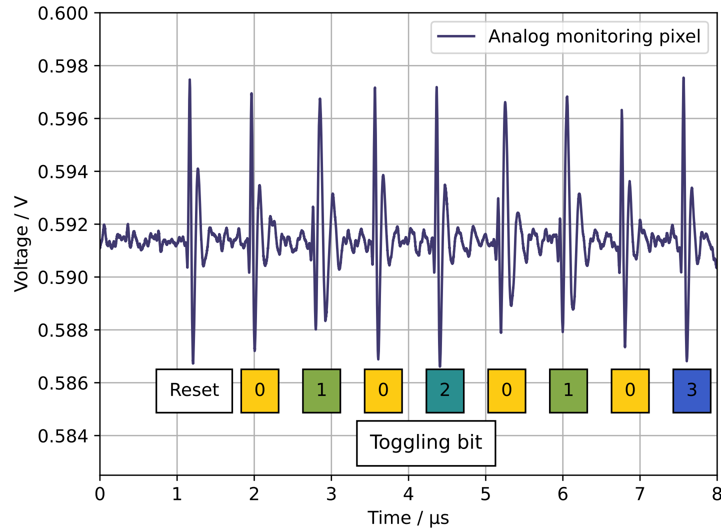

Figure 9.3: Distortion measured at the analog amplifier output induced by individual bit toggling in TJ-Monopix2. The first pulse is caused by the reset of the `BCID` counter. According to the gray-coded counter, subsequent distortions can be assigned to toggling of individual bits based on the pulse shape.

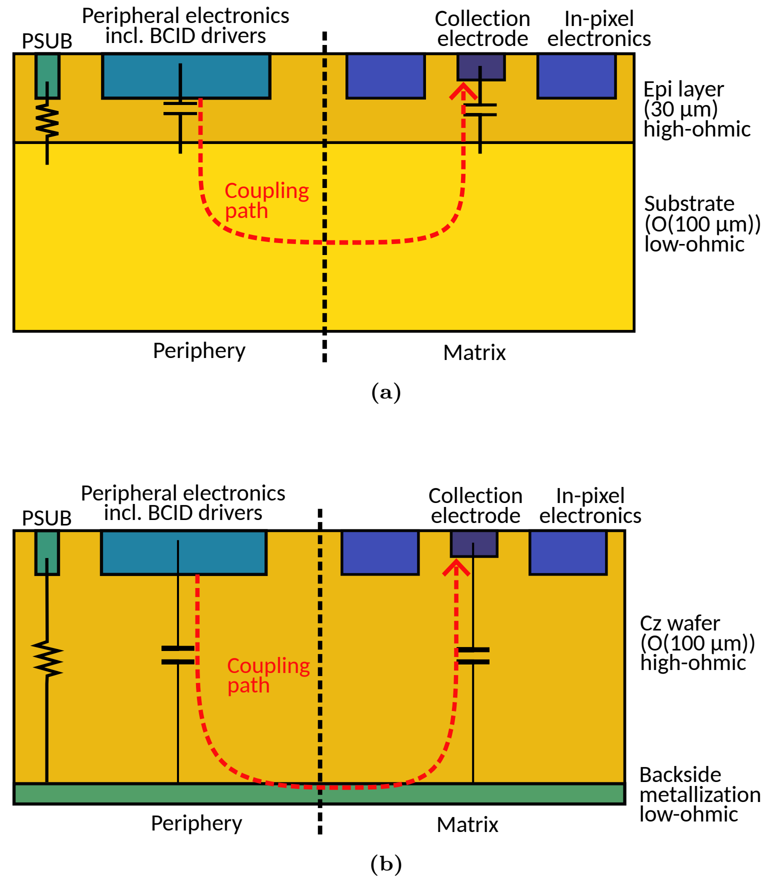

Figure 9.4: Schematic illustration of the coupling path of the threshold-shifting cross-talk for chips manufactured on (a) epitaxial layers and (b) Czochralski wafers. The threshold fluctuation originates from potential distortions caused by `BCID` counter bit toggling in the periphery. These distortions couple capacitively from the periphery into the non-depleted backside of the chip, and into the collection electrode from there. Backside metallization of high-ohmic Czochralski wafers facilitates the fixation of the potential in the non-depleted volume, which attenuates the cross-talk. Due to the low-ohmic substrate required for chips manufactured on epitaxial layers, the effectiveness of backside metallization in this case is difficult to assess.

Bibliography

[1] A. Salam and J.C. Ward. "Electromagnetic and weak interactions." In: *Physics Letters* 13.2 (1964), pp. 168–171. DOI: 10.1016/0031-9163(64)90711-5.

[2] Peter W. Higgs. "Broken Symmetries and the Masses of Gauge Bosons." In: *Phys. Rev. Lett.* 13 (1964), pp. 508–509. DOI: 10.1103/PhysRevLett.13.508.

[3] Steven Weinberg. "A Model of Leptons." In: *Phys. Rev. Lett.* 19 (1967), pp. 1264–1266. DOI: 10.1103/PhysRevLett.19.1264.

[4] H. Fritzsch, M. Gell-Mann, and H. Leutwyler. "Advantages of the color octet gluon picture." In: *Physics Letters B* 47.4 (1973), pp. 365–368. DOI: 10.1016/0370-2693(73)90625-4.

[5] G. Aad et al. "Observation of a new particle in the search for the Standard Model Higgs boson with the ATLAS detector at the LHC." In: *Physics Letters B* 716.1 (2012), pp. 1–29. DOI: 10.1016/j.physletb.2012.08.020.

[6] Lyndon Evans and Philip Bryant. "LHC Machine." In: *Journal of Instrumentation* 3.08 (Aug. 2008), S08001. DOI: 10.1088/1748-0221/3/08/S08001.

[7] Hermann Kolanoski and Norbert Wermes. *Particle Detectors: Fundamentals and Applications.* Oxford University Press, June 2020. DOI: 10.1093/oso/9780198858362.001.0001.

[8] H. Bethe. "Zur Theorie des Durchgangs schneller Korpuskularstrahlen durch Materie." In: *Annalen der Physik* 397.3 (1930), pp. 325–400. DOI: 10.1002/andp.19303970303.

[9] F. Bloch. "Zur Bremsung rasch bewegter Teilchen beim Durchgang durch Materie." In: *Ann. Phys.* 408.3 (Jan. 1933), pp. 285–320. DOI: 10.1002/andp.19334080303.

[10] John David Jackson. *Classical Electrodynamics.* 3rd ed. Wiley, 1999.

[11] R. L. Workman et al. "Review of Particle Physics." In: *PTEP* 2022 (2022), p. 083C01. DOI: 10.1093/ptep/ptac097.

[12] Dr. William R. Leo. *Techniques for nuclear and particle physics experiments: a how-to approach.* 2nd ed. Springer, 1994.

[13] M.J. Berger et al. *ESTAR, PSTAR, and ASTAR: Computer Programs for Calculating Stopping-Power and Range Tables for Electrons, Protons, and Helium Ions.* Version 1.2.3. National Institute of Standards and Technology, Gaithersburg, MD. 2005. (Visited on May 11, 2023).

[14] Donald E. Groom, Nikolai V. Mokhov, and Sergei I. Striganov. “Muon stopping power and range tables 10-MeV to 100-TeV.” In: *Atom. Data Nucl. Data Tabl.* 78 (July 2001), pp. 183–356. DOI: 10.1006/adnd.2001.0861.

[15] Lev Davidovich Landau. “On the energy loss of fast particles by ionization.” In: *J. Phys.* 8.4 (1944), pp. 201–205.

[16] Gert Moliere. “Theorie der Streuung schneller geladener Teilchen I. Einzelstreuung am abgeschirmten Coulomb-Feld.” In: *Zeitschrift für Naturforschung A* 2.3 (1947), pp. 133–145. DOI: 10.1515/zna-1947-0302.

[17] Gert Moliere. “Theorie der Streuung schneller geladener Teilchen II Mehrfach- und Vielfachstreuung.” In: *Zeitschrift für Naturforschung A* 3.2 (1948), pp. 78–97. DOI: 10.1515/zna-1948-0203.

[18] Hans Bichsel. “Multiple Scattering of Protons.” In: *Phys. Rev.* 112.1 (Oct. 1958), pp. 182–185. DOI: 10.1103/PhysRev.112.182.

[19] Virgil L. Highland. “Some practical remarks on multiple scattering.” In: *Nuclear Instruments and Methods* 129.2 (Aug. 1975), pp. 497–499. DOI: 10.1016/0029-554X(75)90743-0.

[20] Gerald R. Lynch and Orin I. Dahl. “Approximations to multiple Coulomb scattering.” In: *Nuclear Instruments and Methods in Physics Research Section B: Beam Interactions with Materials and Atoms* 58.1 (1991), pp. 6–10. DOI: 10.1016/0168-583X(91)95671-Y.

[21] Claude Leroy and Pier-Giorgio Rancoita. *Principles of radiation interaction in matter and detection*. 2nd ed. Singapore: World Scientific, 2009.

[22] M.J. Berger et al. *XCOM: Photon Cross Sections Database*. National Institutue of Standards and Technology. DOI: 10.18434/T48G6X.

[23] J. A. BEARDEN. “X-Ray Wavelengths.” In: *Rev. Mod. Phys.* 39.1 (Jan. 1967), pp. 78–124. DOI: 10.1103/RevModPhys.39.78.

[24] O. Klein and Y. Nishina. “Über die Streuung von Strahlung durch freie Elektronen nach der neuen relativistischen Quantendynamik von Dirac.” In: *Zeitschrift für Physik* 52.11 (1929), pp. 853–868. DOI: 10.1007/BF01366453.

[25] H. Bethe and W. Heitler. “On the stopping of fast particles and on the creation of positive electrons.” In: *Proc. R. Soc. Lond.* 146 (856 1934), pp. 83–112. DOI: 10.1098/rspa.1934.0140.

[26] Marius Grundmann. *The Physics of Semiconductors: An Introduction including Nanophysics and Applications*. 2nd ed. Springer, 2010.

[27] J.-P. Colinge and C.A. Colinge. *Physics of Semiconductor Devices*. Springer, 2005.

[28] Christian Bespin Valero. "Characterization of Depleted Monolithic Active Pixel Sensors for High-Energy Physics Experiments." PhD thesis. Rheinischen Friedrich-Wilhelms-Universität Bonn, 2024. DOI: `10.48565/bonndoc-427`.

[29] S.M. Sze; K.K. Ng. *Physics of Semiconductor Devices*. 3rd ed. John Wiley & Sons, Ltd, 2007.

[30] Gerhard Lutz. *Semiconductor Radiation Detectors: Device Physics*. New York: Springer, 1999.

[31] W. Shockley. "The Theory of p-n Junctions in Semiconductors and p-n Junction Transistors." In: *Bell System Technical Journal* 28.3 (1949), pp. 435–489. DOI: `10.1002/j.1538-7305.1949.tb03645.x`.

[32] D. M. Caughey and R. E. Thomas. "Carrier mobilities in silicon empirically related to doping and field." In: *Proceedings of the IEEE* 55.12 (1967), pp. 2192–2193. DOI: `10.1109/PROC.1967.6123`.

[33] Helmuth Spieler. *Semiconductor detector systems*. Oxford: Oxford Univ. Press, 2005. DOI: `10.1093/acprof:oso/9780198527848.001.0001`.

[34] W. Shockley. "Currents to Conductors Induced by a Moving Point Charge." In: *Journal of Applied Physics* 9.10 (May 1938), pp. 635–636. DOI: `10.1063/1.1710367`.

[35] S. Ramo. "Currents Induced by Electron Motion." In: *Proceedings of the IRE* 27.9 (1939), pp. 584–585. DOI: `10.1109/JRPROC.1939.228757`.

[36] Leonardo Rossi et al. *Pixel Detectors. From Fundamentals to Applications*. Springer, 2006. DOI: `10.1007/3-540-28333-1`.

[37] E. Belau et al. "Charge collection in silicon strip detectors." In: *Nuclear Instruments and Methods in Physics Research* 214.2 (1983), pp. 253–260. DOI: `10.1016/0167-5087(83)90591-4`.

[38] B. Hyams et al. "A silicon counter telescope to study short-lived particles in high-energy hadronic interactions." In: *Nuclear Instruments and Methods in Physics Research* 205.1 (1983), pp. 99–105. DOI: `10.1016/0167-5087(83)90177-1`.

[39] J.-L Agram et al. "The silicon sensors for the Compact Muon Solenoid tracker-design and qualification procedure." In: *Nuclear Instruments and Methods in Physics Research Section A: Accelerators, Spectrometers, Detectors and Associated Equipment* 517.1 (2004), pp. 77–93. DOI: `10.1016/j.nima.2003.08.175`.

[40] Yoshinobu Unno et al. *Specifications and Pre-production of n^{+}-in-p Large-format Strip Sensors fabricated in 6-inch Silicon Wafers, ATLAS18, for the Inner Tracker of the ATLAS Detector for High-Luminosity Large Hadron Collider*. Tech. rep. CERN, 2023. DOI: `10.1088/1748-0221/18/03/T03008`.

[41] S Albergo, A Alberigi, and Erik H M Heijne. *RD19: status report on activities in 1996-1997. Development of hybrid and monolithic semiconductor micropattern pixel detectors.* Tech. rep. Geneva: CERN, 1997. URL: http://cds.cern.ch/record/345010.

[42] Yannick Dieter. "Development and Characterisation of Passive CMOS Sensors for Pixel Detectors in High Radiation Environments." PhD thesis. Rheinische Friedrich-Wilhelms-Universität Bonn, Oct. 2022. URL: https://hdl.handle.net/20.500.11811/10346.

[43] M. Mironova and on behalf of the RD53 collaboration. "X-ray irradiation measurements of the radiation tolerance of the ITkPixV1 ATLAS pixel readout chip." In: *Journal of Instrumentation* 17.02 (Feb. 2022), p. C02028. DOI: 10.1088/1748-0221/17/02/C02028.

[44] J. Lange et al. "Radiation hardness of small-pitch 3D pixel sensors up to a fluence of 3×1016 neq/cm2." In: *Journal of Instrumentation* 13.09 (Sept. 2018), P09009. DOI: 10.1088/1748-0221/13/09/P09009.

[45] Ronald Lipton. "3D Integration of Sensors and Electronics." In: *PoS* Vertex 2017 (Aug. 2018). DOI: 10.22323/1.309.0025.

[46] Steve Holland. "Fabrication of detectors and transistors on high-resistivity silicon." In: *Nuclear Instruments and Methods in Physics Research Section A: Accelerators, Spectrometers, Detectors and Associated Equipment* 275.3 (1989), pp. 537–541. DOI: 10.1016/0168-9002(89)90741-9.

[47] Sherwood Parker. "A proposed VLSI pixel device for particle detection." In: *Nuclear Instruments and Methods in Physics Research Section A: Accelerators, Spectrometers, Detectors and Associated Equipment* 275.3 (1989), pp. 494–516. DOI: 10.1016/0168-9002(89)90736-5.

[48] P. Ahlburg et al. "The new and complete Belle II DEPFET pixel detector: Commissioning and previous operational experience." In: *Nuclear Instruments and Methods in Physics Research Section A: Accelerators, Spectrometers, Detectors and Associated Equipment* 1068 (Nov. 2024). DOI: 10.1016/j.nima.2024.169763.

[49] Jean-Pierre Colinge. "An overview of CMOS-SOI technology and its potential use in particle detection systems." In: *Nuclear Instruments and Methods in Physics Research Section A: Accelerators, Spectrometers, Detectors and Associated Equipment* 305 (3 Aug. 1991), pp. 615–619. DOI: 10.1016/0168-9002(91)90164-L.

[50] R Turchetta et al. "A monolithic active pixel sensor for charged particle tracking and imaging using standard VLSI CMOS technology." In: *Nuclear Instruments and Methods in Physics Research Section A: Accelerators, Spectrometers, Detectors and Associated Equipment* 458.3 (2001), pp. 677–689. DOI: 10.1016/S0168-9002(00)00893-7.

[51] W. Snoeys et al. "A new integrated pixel detector for high energy physics." In: *IEEE Transactions on Nuclear Science* 39.5 (1992), pp. 1263–1269. DOI: 10.1109/23.173188.

[52] Giacomo Contin et al. "The STAR MAPS-based PiXeL detector." In: *Nuclear Instruments and Methods in Physics Research Section A: Accelerators, Spectrometers, Detectors and Associated Equipment* 907 (Nov. 2018), pp. 60–80. DOI: 10.1016/j.nima.2018.03.003.

[53] M. Mager. "ALPIDE, the Monolithic Active Pixel Sensor for the ALICE ITS upgrade." In: *Nuclear Instruments and Methods in Physics Research Section A: Accelerators, Spectrometers, Detectors and Associated Equipment* 824 (2016). Frontier Detectors for Frontier Physics: Proceedings of the 13th Pisa Meeting on Advanced Detectors, pp. 434–438. DOI: 10.1016/j.nima.2015.09.057.

[54] Ivan Perić. "A novel monolithic pixelated particle detector implemented in high-voltage CMOS technology." In: *Nuclear Instruments and Methods in Physics Research Section A: Accelerators, Spectrometers, Detectors and Associated Equipment* 582.3 (2007). VERTEX 2006, pp. 876–885. DOI: 10.1016/j.nima.2007.07.115.

[55] J. D. Segal et al. "Second generation monolithic full-depletion radiation sensor with integrated CMOS circuitry." In: *IEEE Nuclear Science Symposium & Medical Imaging Conference* (Nov. 2010), pp. 1896–1900. DOI: 10.1109/NSSMIC.2010.5874104.

[56] Ivan Berdalovic et al. "MALTA: a CMOS pixel sensor with asynchronous readout for the ATLAS High-Luminosity upgrade." In: *2018 IEEE Nuclear Science Symposium and Medical Imaging Conference Proceedings (NSS/MIC)*. 2018, pp. 1–4. DOI: 10.1109/NSSMIC.2018.8824349.

[57] T. Wang et al. "Depleted fully monolithic CMOS pixel detectors using a column based readout architecture for the ATLAS Inner Tracker upgrade." In: *Journal of Instrumentation* 13 (Mar. 2018). DOI: 10.1088/1748-0221/13/03/c03039.

[58] Andre Schoening et al. "MuPix & ATLASpix: Architectures and Results." In: *Proceedings of The 28th International Workshop on Vertex Detectors — PoS(Vertex2019)*. Vol. 373. 2020, p. 024. DOI: 10.22323/1.373.0024.

[59] Y. Degerli et al. "CACTUS: a depleted monolithic active timing sensor using a CMOS radiation hard technology." In: *Journal of Instrumentation* 15.06 (June 2020). DOI: 10.1088/1748-0221/15/06/P06011.

[60] Sinuo Zhang. "Investigation of Breakdown Behaviour andImprovement of Spatial Resolution for SiliconPixel detectors." PhD thesis. Rheinischen Friedrich-Wilhelms-Universität Bonn, 2025. DOI: 10.48565/bonndoc-592.

[61] T. Wang et al. "Development of a Depleted Monolithic CMOS Sensor in a 150 nm CMOS Technology for the ATLAS Inner Tracker Upgrade." In: *Journal of Instrumentation* 12.01 (Jan. 2017), p. C01039. DOI: 10.1088/1748-0221/12/01/C01039.

[62] E. Vilella et al. "RD50-MPW4: a thin backside-biased High Voltage CMOS pixel chip for high radiation tolerance." In: *Journal of Instrumentation* 20.03 (Mar. 2025), p. C03044. DOI: 10.1088/1748-0221/20/03/C03044.

[63] W. Snoeys et al. "A process modification for CMOS monolithic active pixel sensors for enhanced depletion, timing performance and radiation tolerance." In: *Nuclear Instruments and Methods in Physics Research Section A: Accelerators, Spectrometers, Detectors and Associated Equipment* 871 (2017), pp. 90–96. DOI: 10.1016/j.nima.2017.07.046.

[64] Heinz Pernegger. "Depleted CMOS sensors for HL-LHC." In: *PoS* VERTEX2018 (2019), p. 041. DOI: 10.22323/1.348.0041.

[65] K. Moustakas et al. "CMOS monolithic pixel sensors based on the column-drain architecture for the HL-LHC upgrade." In: *Nuclear Instruments and Methods in Physics Research Section A: Accelerators, Spectrometers, Detectors and Associated Equipment* 936 (Aug. 2019), pp. 604–607. DOI: 10.1016/j.nima.2018.09.100.

[66] ATLAS. *Technical Design Report for the ATLAS Inner Tracker Pixel Detector*. Tech. rep. CERN, 2017. DOI: 10.17181/CERN.FOZZ.ZP3Q.

[67] Francesco Forti. *Snowmass Whitepaper: The Belle II Detector Upgrade Program*. 2022. eprint: 2203.11349. DOI: 10.48550/arXiv.2203.11349.

[68] R. Boudagga et al. "Upgrade of the Belle II vertex detector with depleted monolithic CMOS active pixel sensors." In: *Nuclear Instruments and Methods in Physics Research Section A: Accelerators, Spectrometers, Detectors and Associated Equipment* 1080 (2025), p. 170677. DOI: 10.1016/j.nima.2025.170677.

[69] K. Arndt et al. "Technical design of the phase I Mu3e experiment." In: *Nuclear Instruments and Methods in Physics Research Section A: Accelerators, Spectrometers, Detectors and Associated Equipment* 1014 (2021). DOI: 10.1016/j.nima.2021.165679.

[70] M. Babeluk et al. "The OBELIX chip for the Belle II VTX upgrade." In: *Nuclear Instruments and Methods in Physics Research Section A: Accelerators, Spectrometers, Detectors and Associated Equipment* 1067 (2024), p. 169659. DOI: 10.1016/j.nima.2024.169659.

[71] P. V. Dressendorfer. *Basic mechanisms for the new millennium*. Sept. 1998. URL: https://www.osti.gov/biblio/658465.

[72] Michael Moll. "Radiation damage in silicon particle detectors: Microscopic defects and macroscopic properties." PhD thesis. Universität Hamburg, 1999. DOI: 10.3204/PUBDB-2016-02525.

[73] Y. Shi; D. X. Shen; F. M. Wu; K. J. Cheng. "A numerical study of cluster center formation in neutron-irradiated silicon." In: *Journal of Applied Physics* 67.2 (Jan. 1990), pp. 1116–1118. DOI: 10.1063/1.345799.

[74] V A.J. Van Lint et al. *Mechanisms of radiation effects in electronic materials. Vol. 1.* Wiley-Interscience,New York, NY, Jan. 1980. URL: https://www.osti.gov/biblio/6854931.

[75] M. Huhtinen. "Simulation of non-ionising energy loss and defect formation in silicon." In: *Nuclear Instruments and Methods in Physics Research Section A: Accelerators, Spectrometers, Detectors and Associated Equipment* 491 (May 2002), pp. 194–215. DOI: 10.1016/S0168-9002(02)01227-5.

[76] Frank Hartmann. *Evolution of Silicon Sensor Technology in Particle Physics.* Springer, 2017. DOI: 10.1007/978-3-319-64436-3.

[77] Michael Moll. "Displacement Damage in Silicon Detectors for High Energy Physics." In: *IEEE Transactions on Nuclear Science* 65.8 (2018), pp. 1561–1582. DOI: 10.1109/TNS.2018.2819506.

[78] G. Kramberger; V. Cindro; I. Dolenc; I. Mandić; M. Mikuž; M. Zavrtanik. "Performance of silicon pad detectors after mixed irradiations with neutrons and fast charged hadrons." In: *Nuclear Instruments and Methods in Physics Research Section A: Accelerators, Spectrometers, Detectors and Associated Equipment* 609 (Aug. 2009), pp. 142–148. DOI: 10.1016/j.nima.2009.08.030.

[79] J. Lindhard and V. Nielsen. "Nuclear collisions and ionisation fluctuations in charged particle detectors." In: *Physics Letters* 2.5 (Oct. 1962), pp. 209–211. DOI: 10.1016/0031-9163(62)90229-9.

[80] Pascal Wolf. "Development and Characterization of an Irradiation Site for Radiation Damage Studies of the ATLAS ITk Pixel Detector." PhD thesis. Rheinische Friedrich-Wilhelms-Universität Bonn, July 2025. DOI: 10.48565/bonndoc-609.

[81] W. Shockley and W. T. Read. "Statistics of the Recombinations of Holes and Electrons." In: *Phys. Rev.* 87 (5 Sept. 1952), pp. 835–842. DOI: 10.1103/PhysRev.87.835.

[82] R. N. Hall. "Electron-Hole Recombination in Germanium." In: *Phys. Rev.* 87 (2 July 1952), pp. 387–387. DOI: 10.1103/PhysRev.87.387.

[83] G Lindström et al. "Radiation hard silicon detectors—developments by the RD48 (ROSE) collaboration." In: *Nuclear Instruments and Methods in Physics Research Section A: Accelerators, Spectrometers, Detectors and Associated Equipment,* 466.2 (July 2001), pp. 308–326. DOI: 10.1016/S0168-9002(01)00560-5.

[84] Renate Wunstorf. "Systematische Untersuchungen zur Strahlenresistenz von Silizium-Detektoren für die Verwendung in Hochenergiephysik-Experimenten." PhD thesis. University of Hamburg, Oct. 1992. URL: https://bib-pubdb1.desy.de/record/153817.

[85] G Kramberger et al. "Determination of effective trapping times for electrons and holes in irradiated silicon." In: *Nuclear Instruments and Methods in Physics Research Section A: Accelerators, Spectrometers, Detectors and Associated Equipment* 476.3 (Jan. 2002), pp. 645–651. DOI: 10.1016/S0168-9002(01)01653-9.

[86] T.R. Oldham and F.B. McLean. "Total ionizing dose effects in MOS oxides and devices." In: *IEEE Transactions on Nuclear Science* 50.3 (June 2003), pp. 483–499. DOI: 10.1109/TNS.2003.812927.

[87] James R. Schwank et al. "Radiation Effects in MOS Oxides." In: *IEEE Transactions on Nuclear Science* 55.4 (Aug. 2008), pp. 1833–1853. DOI: 10.1109/TNS.2008.2001040.

[88] J. M. Benedetto and H. E Boesch. "The Relationship between 60Co and 10-keV X-Ray Damage in MOS Devices." In: *IEEE Transactions on Nuclear Science* 33.6 (Dec. 1986), pp. 1371–1323. DOI: 10.1109/TNS.1986.4334599.

[89] B.E. Deal. "Standardized terminology for oxide charges associated with thermally oxidized silicon." In: *IEEE Transactions on Electron Devices* 27.3 (Mar. 1980), pp. 606–608. DOI: 10.1109/T-ED.1980.19908.

[90] D.M. Fleetwood. "'Border traps' in MOS devices." In: *IEEE Transactions on Nuclear Science* 39.2 (Apr. 1992), pp. 269–271. DOI: 10.1109/23.277495.

[91] E. H. Snow;A. S. Grove;B. E. Deal;C. T. Sah. "Ion Transport Phenomena in Insulating Films." In: *Journal of Applied Physics* 36.5 (May 1965), pp. 1664–1673. DOI: 10.1063/1.1703105.

[92] R. C. Hughes. "Charge-Carrier Transport Phenomena in Amorphous SiO_2: Direct Measurement of the Drift Mobility and Lifetime." In: *Physical Review Journals* 30.26 (June 1973), pp. 1333–1336. DOI: 10.1103/PhysRevLett.30.1333.

[93] R. C. Hughes. "Hole mobility and transport in thin SiO2 films." In: *Applied Physics Letters* 26.8 (Nov. 1975), pp. 436–438. DOI: 10.1063/1.88200.

[94] Elliott W. Montroll; George H. Weiss. "Random Walks on Lattices. II." In: *Journal of Mathematical Physics* 6.2 (Feb. 1965), pp. 167–181. DOI: 10.1063/1.1704269.

[95] H. Scher and M. Lax. "Stochastic Transport in a Disordered Solid." In: *Phys. Rev. B* 7 (10 May 1973), pp. 4491–4502. DOI: 10.1103/PhysRevB.7.4491.

[96] H. Edwin Boesch and F. Barry McLean. "Hole Transport and Trapping in Field Oxides." In: *IEEE Transactions on Nuclear Science* 32.6 (1985), pp. 3940–3945. DOI: 10.1109/TNS.1985.4334047.

[97] Frank J. Feigl, W.Beall Fowler, and Kwok L. Yip. "Oxygen vacancy model for the E1′ center in SiO2." In: *Solid State Communications* 14.3 (1974), pp. 225–229. DOI: 10.1016/0038-1098(74)90840-0.

[98] J. R. Schwank et al. "Physical Mechanisms Contributing to Device "Rebound"." In: *IEEE Transactions on Nuclear Science* 31.6 (Dec. 1984), pp. 1434–1438. DOI: 10.1109/TNS.1984.4333525.

[99] M. Simons and H. L. Hughes. "Short-Term Charge Annealing in Electron-Irradiated Silicon Dioxide." In: *IEEE Transactions on Nuclear Science* 18.6 (1971), pp. 106–112. DOI: 10.1109/TNS.1971.4326420.

[100] P. M. Lenahan and P. V. Dressendorfer. "Hole traps and trivalent silicon centers in metal/oxide/silicon devices." In: *Journal of Applied Physics* 55.10 (Nov. 1983), pp. 3495–3499. DOI: 10.1063/1.332937.

[101] P. J. McWhorter; P. S. Winokur. "Simple technique for separating the effects of interface traps and trapped-oxide charge in metal-oxide-semiconductor transistors." In: *Applied Physics Letters* 48.2 (Jan. 1986), pp. 133–135. DOI: 10.1063/1.96974.

[102] Giovanni Faccio Federico; Cervelli. "Radiation-induced edge effects in deep submicron CMOS transistors." In: *IEEE Transactions on Nuclear Science* 52.6 (Jan. 2006), pp. 2413–2420. DOI: 10.1109/TNS.2005.860698.

[103] M.R. Shaneyfelt et al. "Interface-trap building rates in wet and dry oxides." In: *IEEE Transactions on Nuclear Science* 39.6 (Dec. 1992), pp. 2244–2251. DOI: 10.1109/23.211427.

[104] P. S. Winokur et al. "Total-Dose Failure Mechanisms of Integrated Circuits in Laboratory and Space Environments." In: *IEEE Transactions on Nuclear Science* 34.6 (Dec. 1987), pp. 1448–1454. DOI: 10.1109/TNS.1987.4337496.

[105] L. Gonella et al. "Total Ionizing Dose effects in 130-nm commercial CMOS technologies for HEP experiments." In: *Nuclear Instruments and Methods in Physics Research Section A: Accelerators, Spectrometers, Detectors and Associated Equipment* 582.3 (Dec. 2007), pp. 750–754. DOI: 10.1016/j.nima.2007.07.068.

[106] K. Dette. "Total Ionising Dose effects in the FE-I4 front-end chip of the ATLAS Pixel IBL detector." In: *Journal of Instrumentation* 11.11 (Nov. 2016). DOI: 10.1088/1748-0221/11/11/C11028.

[107] I. Caicedo et al. "Development and testing of a radiation-hard large-electrode DMAPS design in a 150 nm CMOS process." In: *Nuclear Instruments and Methods in Physics Research Section A: Accelerators, Spectrometers, Detectors and Associated Equipment* 1040 (2022), p. 167224. DOI: 10.1016/j.nima.2022.167224.

[108] A. Scarpa et al. "Ionizing radiation induced leakage current on ultra-thin gate oxides." In: *IEEE Transactions on Nuclear Science* 44.6 (Dec. 1997), pp. 1818–1825. DOI: 10.1109/23.658948.

[109] L. Larcher et al. "A model of radiation induced leakage current (RILC) in ultra-thin gate oxides." In: *IEEE Transactions on Nuclear Science* 46.6 (1999), pp. 1553–1561. DOI: 10.1109/23.819120.

[110] M. Ceschia et al. "Radiation induced leakage current and stress induced leakage current in ultra-thin gate oxides." In: *IEEE Transactions on Nuclear Science* 45.6 (Dec. 1998), pp. 2375–2382. DOI: 10.1109/23.736457.

[111] J R Srour and J M McGarrity. "Radiation effects on microelectronics in space." In: *Proc. IEEE; (United States)* 76.11 (Nov. 1988). DOI: 10.1109/5.90114.

[112] Toko Hirono et al. "Characterization of fully depleted CMOS active pixel sensors on high resistivity substrates for use in a high radiation environment." In: *2016 IEEE Nuclear Science Symposium, Medical Imaging Conference and Room-Temperature Semiconductor Detector Workshop (NSS/MIC/RTSD)* (2016), pp. 1–4. DOI: 10.1109/NSSMIC.2016.8069902.

[113] Y. Degerli et al. "Pixel architectures in a HV-CMOS process for the ATLAS inner detector upgrade." In: *JINST* 11.12 (2016), p. C12064. DOI: 10.1088/1748-0221/11/12/C12064.

[114] Toko Hirono. "Development of depleted monolithic active pixel sensors for high rate and high radiation experiments at HL-LHC." PhD thesis. Rheinische Friedrich-Wilhelms-Universität Bonn, July 2019. URL: https://hdl.handle.net/20.500.11811/7933.

[115] Piotr Rymaszewski. "Design and characterization of pixel IC electronics and sensors for new pixel detector generations." PhD thesis. Rheinische Friedrich-Wilhelms-Universität Bonn, Mar. 2022. URL: https://nbn-resolving.org/urn:nbn:de:hbz:5-65954,.

[116] Ivan Caicedo et al. "Improvement in the Design and Performance of the Monopix2 Reticle-Scale DMAPS." In: *JPS Conf. Proc.* 42 (2024), p. 011021. DOI: 10.7566/JPSCP.42.011021.

[117] J. Dingfelder et al. "Progress in DMAPS developments and first tests of the Monopix2 chips in 150 nm LFoundry and 180 nm TowerJazz technology." In: *Nuclear Instruments and Methods in Physics Research Section A: Accelerators, Spectrometers, Detectors and Associated Equipment* 1034 (July 2022), p. 166747. DOI: 10.1016/j.nima.2022.166747.

[118] M. Barbero et al. "Radiation hard DMAPS pixel sensors in 150 nm CMOS technology for operation at LHC." In: *Journal of Instrumentation* 15.05 (May 2020), P05013. DOI: 10.1088/1748-0221/15/05/P05013.

[119] M. Bazes. "Two novel fully complementary self-biased CMOS differential amplifiers." In: *IEEE Journal of Solid-State Circuits* 26.2 (1991), pp. 165–168. DOI: 10.1109/4.68134.

[120] R. Cardella et al. "MALTA: an asynchronous readout CMOS monolithic pixel detector for the ATLAS High-Luminosity upgrade." In: *Journal of Instrumentation* 14.06 (June 2019), p. C06019. DOI: 10.1088/1748-0221/14/06/C06019.

[121] M. Dyndal et al. "Mini-MALTA: radiation hard pixel designs for small-electrode monolithic CMOS sensors for the High Luminosity LHC." In: *Journal of Instrumentation* 15.02 (Feb. 2020), P02005. DOI: `10.1088/1748-0221/15/02/P02005`.

[122] H. Pernegger et al. "First tests of a novel radiation hard CMOS sensor process for Depleted Monolithic Active Pixel Sensors." In: *Journal of Instrumentation* 12.06 (June 2017), P06008. DOI: `10.1088/1748-0221/12/06/P06008`.

[123] Ruth Magdalena Muenker. "Test beam and simulation studies on High Resistivity CMOS pixel sensors." PhD thesis. Rheinische Friedrich-Wilhelms-Universität Bonn, Sept. 2018. URL: `https://hdl.handle.net/20.500.11811/7634`.

[124] I. Caicedo et al. "The Monopix chips: depleted monolithic active pixel sensors with a column-drain read-out architecture for the ATLAS Inner Tracker upgrade." In: *Journal of Instrumentation* 14.06 (June 2019), p. C06006. DOI: `10.1088/1748-0221/14/06/C06006`.

[125] M. Munker et al. "Simulations of CMOS pixel sensors with a small collection electrode, improved for a faster charge collection and increased radiation tolerance." In: *Journal of Instrumentation* 14.05 (May 2019), p. C05013. DOI: `10.1088/1748-0221/14/05/C05013`.

[126] Konstantinos Moustakas. "Design and Development of Depleted Monolithic Active Pixel Sensors with Small Collection Electrode for High-Radiation Applications." PhD thesis. Rheinische Friedrich-Wilhelms-Universität Bonn, Sept. 2021. URL: `https://hdl.handle.net/20.500.11811/9315`.

[127] C. Bespin et al. "DMAPS Monopix developments in large and small electrode designs." In: *Nuclear Instruments and Methods in Physics Research Section A: Accelerators, Spectrometers, Detectors and Associated Equipment* 978 (2020), p. 164460. DOI: `10.1016/j.nima.2020.164460`.

[128] D. Kim et al. "Front end optimization for the monolithic active pixel sensor of the ALICE Inner Tracking System upgrade." In: *Journal of Instrumentation* 11.02 (Feb. 2016), p. C02042. DOI: `10.1088/1748-0221/11/02/C02042`.

[129] C. Gao et al. "A novel source–drain follower for monolithic active pixel sensors." In: *Nuclear Instruments and Methods in Physics Research Section A: Accelerators, Spectrometers, Detectors and Associated Equipment* 831 (2016). Proceedings of the 10th International "Hiroshima" Symposium on the Development and Application of Semiconductor Tracking Detectors, pp. 147–155. DOI: `10.1016/j.nima.2016.03.074`.

[130] Roberto Cardella et al. "LAPA, a 5 Gb/s modular pseudo-LVDS driver in 180 nm CMOS with capacitively coupled pre-emphasis." In: *Proceedings of Topical Workshop on Electronics for Particle Physics — PoS(TWEPP-17)*. Sissa Medialab, Mar. 5, 2018. DOI: `10.22323/1.313.0038`.

[131] Maurice Garcia-Sciveres, Flavio Loddo, and Jorgen Christiansen. *RD53B Manual*. Tech. rep. Geneva: CERN, 2019. URL: `http://cds.cern.ch/record/2665301`.

[132] A. X. Widmer and P. A. Franaszek. "A DC-Balanced, Partitioned-Block, 8B/10B Transmission Code." In: *IBM Journal of Research and Development* 27.5 (1983), pp. 440–451. DOI: 10.1147/rd.275.0440.

[133] M. Daas et al. "BDAQ53, a versatile pixel detector readout and test system for the ATLAS and CMS HL-LHC upgrades." In: *Nuclear Instruments and Methods in Physics Research Section A: Accelerators, Spectrometers, Detectors and Associated Equipment* 986 (2021), p. 164721. DOI: 10.1016/j.nima.2020.164721.

[134] Silizium Labor Bonn. *basil - A data acquisition framework in Python and Verilog.* Aug. 18, 2025. URL: https://github.com/SiLab-Bonn/basil (visited on Aug. 18, 2025).

[135] Silizium Labor Bonn. *LF-Monopix2 DAQ.* Aug. 19, 2025. URL: https://github.com/SiLab-Bonn/lf-monopix2-daq (visited on Aug. 19, 2025).

[136] Silizium Labor Bonn. *tj-monopix2-daq.* Aug. 19, 2025. URL: https://github.com/SiLab-Bonn/tj-monopix2-daq (visited on Aug. 19, 2025).

[137] Ahmed Qamesh. "X-ray Irradiation and Calibration of the RD53A Pixel Read-out Chip." MA thesis. Universtät Bonn, Feb. 2019.

[138] R. Diener et al. "The DESY II test beam facility." In: *Nuclear Instruments and Methods in Physics Research Section A: Accelerators, Spectrometers, Detectors and Associated Equipment* 922 (2019), pp. 265–286. DOI: 10.1016/j.nima.2018.11.133.

[139] Dennis Proft. "Optimierung des Beschleunigerbetriebs für Experimente zur Hadronen- und Detektorphysik an der Elektronen-Stretcher-Anlage ELSA." PhD thesis. Rheinische Friedrich-Wilhelms-Universität Bonn, July 2019. URL: https://hdl.handle.net/20.500.11811/8054.

[140] I. Rubinskiy. "An EUDET/AIDA Pixel Beam Telescope for Detector Development." In: *Physics Procedia* 37 (2012), pp. 923–931. DOI: 10.1016/j.phpro.2012.02.434.

[141] J. Baudot et al. "First test results Of MIMOSA-26, a fast CMOS sensor with integrated zero suppression and digitized output." In: *2009 IEEE Nuclear Science Symposium Conference Record (NSS/MIC).* 2009, pp. 1169–1173. DOI: 10.1109/NSSMIC.2009.5402399.

[142] Hendrik Jansen et al. "Performance of the EUDET-type beam telescopes." In: *EPJ Techniques and Instrumentation* 3.1 (2016), p. 7. DOI: 10.1140/epjti/s40485-016-0033-2.

[143] M. Garcia-Sciveres et al. "The FE-I4 pixel readout integrated circuit." In: *Nuclear Instruments and Methods in Physics Research Section A: Accelerators, Spectrometers, Detectors and Associated Equipment* 636.1, Supplement (2011), S155–S159. DOI: 10.1016/j.nima.2010.04.101.

[144] Emily Anne Thompson. *ATLAS ITk Pixel Detector Overview.* Tech. rep. CERN, 2025. URL: https://cds.cern.ch/record/2928802.

[145] David Cussans. *Description of the JRA1 Trigger Logic Unit (TLU), v0.2c.* Sept. 11, 2009. URL: https://www.eudet.org/e26/e28/e42441/e57298/EUDET-MEMO-2009-04.pdf (visited on Aug. 9, 2023).

[146] Houdaifa Lahbil. "Charakterisierung und Optimierung eines Stickstoffkühlsystems für Detektortestanwendungen." BA thesis. Universität Bonn, Dec. 2022.

[147] Yannick Dieter, Jens Janssen, and David-Leon Pohl. *Beam Telescope Analysis.* Aug. 19, 2025. URL: https://github.com/SiLab-Bonn/beam_telescope_analysis.

[148] D. Dannheim et al. "Corryvreckan: a modular 4D track reconstruction and analysis software for test beam data." In: *Journal of Instrumentation* 16.03 (Mar. 2021), P03008. DOI: 10.1088/1748-0221/16/03/P03008.

[149] David-Leon Pohl. "3D-Silicon and Passive CMOS Sensors for Pixel Detectors in High Radiation Environments." PhD thesis. Rheinische Friedrich-Wilhelms-Universität Bonn, Oct. 2020. URL: https://hdl.handle.net/20.500.11811/8743.

[150] Pascal Wolf et al. "A beam-driven proton irradiation setup for precision radiation damage tests of silicon detectors." In: *Nuclear Instruments and Methods in Physics Research Section A: Accelerators, Spectrometers, Detectors and Associated Equipment* 1064 (July 2024), p. 169358. DOI: 10.1016/j.nima.2024.169358.

[151] Luka Snoj et al. "A half-century of nuclear research, education and training: Story of the JSI TRIGA reactor." In: *Annals of Nuclear Energy* 214 (May 2025), p. 111122. DOI: 10.1016/j.anucene.2024.111122.

[152] Leyre Flores Sanz de Acedo. "Design and characterisation of monolithic CMOS detectors for high energy particle physics and SEU radiation tests for ATLAS Inner Tracker Upgrade readout chip." PhD thesis. University of Glasgow, Aug. 2023. DOI: 10.5525/gla.thesis.83781.

[153] Lars Schall et al. "Cross-talk of a large-scale depleted monolithic active pixel sensor (DMAPS) in 180nm CMOS technology." In: *Nuclear Instruments and Methods in Physics Research Section A: Accelerators, Spectrometers, Detectors and Associated Equipment* 1064 (July 2024), p. 169381. DOI: 10.1016/j.nima.2024.169381.

[154] Christian Bespin et al. "Development and characterization of a DMAPS chip in TowerJazz 180 nm technology for high radiation environments." In: *Nuclear Instruments and Methods in Physics Research Section A: Accelerators, Spectrometers, Detectors and Associated Equipment* 1040 (2022), p. 167189. DOI: https://doi.org/10.1016/j.nima.2022.167189.

[155] Milou van Rijnbach et al. "Radiation Hardness of MALTA2 Monolithic CMOS Sensors on Czochralski Substrates." In: *The European Physical Journal C* 84 (Mar. 2024). DOI: 10.1140/epjc/s10052-024-12601-3.

[156] Ivan Perić et al. “The FEI3 readout chip for the ATLAS pixel detector.” In: *Nuclear Instruments and Methods in Physics Research Section A: Accelerators, Spectrometers, Detectors and Associated Equipment* 565.1 (2006). Proceedings of the International Workshop on Semiconductor Pixel Detectors for Particles and Imaging, pp. 178–187. DOI: 10.1016/j.nima.2006.05.032.

List of Figures

2.1 Average energy loss of a pion in silicon as a function of the particle's $\beta\gamma = p/mc$. 5
2.2 Exemplary characteristic Landau-shaped probability of the energy deposited by a charged particle traversing matter. 8
2.3 Particle traversing matter and being deflected multiple times by Coulomb scattering. 9
2.4 Total attenuation of photons in silicon across the relevant energy range. 10
2.5 Schematic drawing of Compton scattering. 12

3.1 Schematic illustration of the band structures formed within a periodic potential. 14
3.2 Schematic illustration of the difference between direct and indirect semiconductors. 15
3.3 Schematic band structure of p- and n-type semiconductors as well as an abrupt p-n junction. 17
3.4 Change of characteristic properties across an abrupt p-n transition. 19
3.5 Schematic illustration of a generic MOSFET structure and its idealized drain current characteristics. 20
3.6 Two-dimensional simulation of the weighting potential and weighting field shaping of a segmented, multi-electrode configuration. 24
3.7 Signal current and normalized signal charge induced by charge movement and accumulation in an unsegmented silicon detector. 26
3.8 A generic analog front-end readout chain used for pixelated detector systems. . . 26
3.9 Time-over-threshold method utilized to measure the deposited charge. 27
3.10 Schematic visualization of segmented electrodes implemented in a single-sided micro-strip detector. 29
3.11 Schematic layout of hybrid pixel cells consisting of precisely aligned sensor- and readout pixel connected via a bump bond. 30
3.12 Cross-section of a monolithic active pixel cell. 32
3.13 Cross-section of a depleted monolithic active pixel cell designed with a large collection electrode. 34
3.14 Cross-section of a depleted monolithic active pixel cell designed with a small collection electrode. 35

4.1 Exemplary overview of point-like defects in the silicon lattice generated by displacement damage. 41

4.2 NIEL induced defect levels and their location within the silicon band gap. 42
4.3 *Current-related damage rate* α for different annealing temperatures and accumulated annealing times [72]. 47
4.4 Visualization of IEL caused defects and their propagation in a MOS structure. . 49
4.5 Schematically illustrated recovery of the threshold voltage of an n-channel MOS-transistor over time after an irradiation pulse. 52
4.6 Schematic example of the positive charge accumulation within a transistor. . . . 54

5.1 Schematic illustration of the LF-Monopix2 layout. 56
5.2 Schematic illustration of the low-dose n-type implant modification to the small collection electrode design. 60
5.3 Schematic illustration of the NGAP and XDPW modifications to the small collection electrode design. 61
5.4 Schematic illustration of the TJ-Monopix2 layout. 62
5.5 LF-Monopix2 data acquisition hardware. 66
5.6 TJ-Monopix2 data acquisition hardware. 66
5.7 Schematic illustration of the modular data acquisition software based around the `ScanBase` class. 68

6.1 Schematic illustration and picture of the X-ray irradiation setup. 70
6.2 Calibration of the X-ray irradiation setup using a commercial diode. 71
6.3 Schematic illustration of a beam telescope setup. 73
6.4 Schematic illustration of the portable cooling system. 75
6.5 Picture of the beam telescope setup including a DUT inside a cooling box. 75
6.6 Exemplary correlation between two telescope planes and unbiased residual of a single telescope plane. 77

7.1 I-V characteristics of LF-Monopix2 at different NIEL fluences. 83
7.2 Exemplary hit occupancy with increasing injected charge for multiple pixels and resulting threshold distribution measured with LF-Monopix2. 84
7.3 Normalized power consumption of all power domains of LF-Monopix2 throughout the X-ray irradiation measured with Matrix 1-34. 88
7.4 Normalized power consumption of the analog and digital power domain for all front-end variants of LF-Monopix2 throughout the X-ray irradiation. 89
7.5 Measured gain of all front-end variants of LF-Monopix2 throughout the X-ray irradiation. 90
7.6 Measured threshold dispersion of all front-end variants of LF-Monopix2 throughout the X-ray irradiation. 91

7.7 Exemplary charge spectrum of a 5 GeV electron beam measured with LF-Monopix2 and estimation of the number of generated electron-hole pairs by an impinging particle for different silicon thicknesses. 94
7.8 Depletion depth and corresponding hit-detection efficiency versus bias voltages for all available NIEL fluences. 95
7.9 Noise hit rate of Matrix 1-34 of LF-Monopix2 for different bias voltages after irradiation. 97
7.10 Hit-detection efficiency of LF-Monopix2 projected onto a single pixel cell for in-pixel studies for all NIEL fluences. 100
7.11 Schematic illustration of the measured and calculated timestamps needed to estimate the in-time ratio of LF-Monopix2. 101
7.12 In-time ratio of Matrix 1-34 of LF-Monopix2 projected onto a single pixel cell for in-pixel studies at $5 \times 10^{15}\,\mathrm{n_{eq}\,cm^{-2}}$ NIEL fluence. 102
7.13 In-pixel efficiency of LF-Monopix2 after irradiation to 400 Mrad TID. 104
7.14 Normalized threshold distribution of DC-coupled TJ-Monopix2 front-end variants at different NIEL fluences. 108
7.15 Threshold fluctuation with respect to the relative arrival time of a hit observed in TJ-Monopix2. 109
7.16 Map of the maximum threshold difference across the 7-bit counter period and scaling of it with the number of `BCID` clock columns enabled. 110
7.17 Dependency of the threshold fluctuations in TJ-Monopix2 on the frequency of the clock, which is distributed across the matrix. 111
7.18 Dependency of the threshold fluctuations in TJ-Monopix2 on the wafer material. 112
7.19 Impairments caused by the threshold fluctuations observed for measurements without control over the hit arrival time. 113
7.20 Power consumption of the different low-voltage power domains supplied to TJ-Monopix2 at different ionizing doses. 115
7.21 Re-measured threshold of the initially tuned configuration and baseline of the analog monitoring pixels after each irradiation step. 116
7.22 Hit-detection efficiency and leakage current versus substrate voltage of DC-coupled TJ-Monopix2 front-end variants at different NIEL fluences. 118
7.23 Hit-detection efficiency of the DC-coupled standard TJ-Monopix2 front-end variant after NIEL irradiation. 121
7.24 Hit-detection efficiency of the DC-coupled cascoded TJ-Monopix2 front-end variant after NIEL irradiation. 121
7.25 Hit-detection efficiency of the DC-coupled TJ-Monopix2 front-end variants after irradiation to 100 Mrad TID. 122

9.1 Timing diagram of the different signals in the column-drain readout logic. 131

9.2 Hit-detection efficiency of the best performing front-end variants of LF-Monopix2 projected onto a single pixel cell for in-pixel studies at $5 \times 10^{15}\,\mathrm{n_{eq}\,cm^{-2}}$ NIEL fluence. 132
9.3 Distortion measured at the analog amplifier output induced by individual bit toggling in TJ-Monopix2. 132
9.4 Schematic illustration of the coupling path of the threshold-shifting cross-talk for chips manufactured on epitaxial layers and Czochralski wafers. 133

List of Tables

3.1 Requirements to the silicon tracking detector of multiple planned experiments and upgrades. 37

5.1 Overview of the different pixel variants implemented in LF-Monopix2. 57
5.2 Bit-wise structure of the LF-Monopix2 serialized hit data. 59
5.3 Overview of the different pixel variations implemented in TJ-Monopix2. 63
5.4 Bit-wise structure of the TJ-Monopix2 digitized hit data. 64
5.5 Description of common scan routines between the Monopix2 chips. 68

7.1 Overview of available NIEL-irradiated LF-Monopix2 samples. 82
7.2 Mean threshold and ENC results after tuning for the individual matrices implemented in LF-Monopix2 at all available NIEL fluences. 85
7.3 Power consumption of the low-voltage power domains for all front-end variants in LF-Monopix2 before X-ray irradiation. 87
7.4 Mean threshold and ENC results after tuning for each front-end variant implemented in LF-Monopix2 after X-ray irradiation to 100 Mrad and 400 Mrad TID. 92
7.5 Mean hit-detection efficiency and in-time ratio for the individual matrices implemented in LF-Monopix2 at all available NIEL fluences. 99
7.6 Overview of available NIEL-irradiated TJ-Monopix2 samples. 106
7.7 Mean threshold, ENC, and leakage current after tuning for the DC-coupled front-end variants implemented in LF-Monopix2 and all available NIEL fluences. 107
7.8 Mean threshold and ENC results after tuning for each front-end variant implemented in TJ-Monopix2 after X-ray irradiation to 100 Mrad TID. 117
7.9 Hit-detection efficiency of the DC-coupled front-end variants of TJ-Monopix2 at all available NIEL fluences. 119
7.10 Characteristics and performance comparison of LF-Monopix2 and TJ-Monopix2 with respect to radiation tolerance. 125

Acronyms

ASIC application specific integrated circuit.

CMOS complementary metal-oxide-semiconductor.

DAC digital-to-analog converter.

DAQ data acquisition.

DMAPS depleted monolithic active pixel sensors.

DUT device under test.

ENC equivalent noise charge.

IEL ionizing energy loss.

ITk Inner Tracker.

LHC Large Hadron Collider.

LVDS low voltage differential signaling.

MAPS monolithic active pixel sensors.

MIP minimum-ionizing particle.

MOS metal-oxide-semiconductor.

MOSFET metal-oxide-semiconductor field-effect transistor.

MPV most probable value.

NIEL non-ionizing energy loss.

PCB printed circuit board.

PKA primary knock-on atom.

RILC radiation induced leakage current.

TDC time-to-digital converter.

TID total ionizing dose.

TLU trigger logic unit.

Danksagung

Zuerst möchte ich mich bei Prof. Jochen Dingfelder für die Möglichkeit und das Vertrauen bedanken, diese Forschungsarbeit in seiner Arbeitesgruppe durchführen zu können. Seine Betreuung und das durch ihn erschaffene Arbeitsumfeld ermöglichte mir eine selbstständige und freie Entwicklung im wissenschaftlichen Arbeiten, durch die ich viel lernen und mich neuen Herausforderungen stellen konnte. Des weiteren möchte ich Prof. Ingrid-Maria Gregor für ihre Bereitschaft und Zeit danken, als zweite Gutachterin meiner Dissertation zu amtieren.

Einen großen Dank möchte ich Jannes, Christian, Ivan, Pascal, Patrick, Yannick, Georgios, Niko, Botho, Sinuo, Rasmus, Paula, Tomek und allen weiteren Mitgliedern des SiLabs widtmen, die ich über die Jahre kennenlernen durfte. Egal ob fachliche Diskussionen oder Kaffeeklatsch, es hat immer Spaß gemacht mit euch und Freundschaften über die Arbeitswelt hinaus geschaffen. Einen speziellen Dank möchte ich unseren Technikern, Susanne und Wolfgang, aussprechen, die trotz kurzfristigsten Anfragen immer hilfsbereit waren, Chips zu bonden und technische Probleme mit Setups zu lösen. Außerdem möchte ich mich bei Ivan, Christian, Yannick, Rasmus und Pascal für die am Ende zahlreichen langen Nächte im Rahmen von Testbeam-Kampagnen bedanken, die ebenso viel Freude wie Frust verursachten. An dieser Stelle möchte ich besonders Ivan und Christian hervorheben, die mich bei meiner Forschung stets unterstützt und all ihr Wissen selbstverständlich mit mir geteilt haben, sowie zu jeder Zeit ein offenes Ohr für Fragen hatten. Ohne euch wäre diese Arbeit nicht möglich gewesen! Auch möchte ich mich bei meinen Freunden und ehemaligen Kommilitonen Hakan, Karl, Micha, Jonas und Fabian bedanken, die mich durch das Studium begleitet haben und der Grund waren, warum jede Vorlesung und jedes Praktikum Spaß gemacht hat.

Ein besonderer Dank gilt meiner Freundin Sina, die immer für mich da ist und diese Arbeit durch all die 'kleinen' alltäglichen Dinge unterstützt hat. Danke, dass du auf meinen Unmut und Frust bedingt durch unproduktive Schreibtage stets besonnen und motivierend reagiert hast! Abschließend möchte ich mich bei meinen Eltern und meinem Bruder bedanken, die ebenfalls immer für mich da sind und mir den Rücken stärken. Ohne all die Dinge, die ihr mir beigebracht habt, eure bedingungslose Unterstützung und vielseitigen Ratschläge seit Kindesalter wäre ich nicht an diesem Punkt angekommen. Dafür bin ich euch unendlich dankbar!